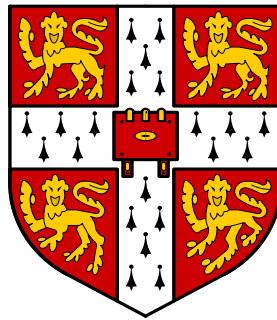


GROUND MOVEMENTS DUE TO EXCAVATION IN CLAY: PHYSICAL AND ANALYTICAL MODELS



A dissertation submitted for the degree of Doctor of Philosophy
at the University of Cambridge

Sidney Sze Yue Lam

Churchill College

October 2010

DECLARATION

I hereby declare that, except where reference is made to the work of others, the contents of this dissertation are a result of my own work and include nothing which is the outcome of work done in collaboration. This dissertation has not been submitted in whole or part for consideration for any other degree, diploma or other qualification to this University or any other institution, except where cited specifically.

This dissertation contains no more than 65,000 words, inclusive of appendices, references, footnotes, tables and equations, and has less than 150 figures.

Sidney Lam Sze Yue
September 2010

ABSTRACT

In view of the recent catastrophes associated with deep excavations, there is an urgent need to provide vital guidelines on the design of the construction process. To develop a simple tool for predicting ground deformation around a deep excavation construction for preliminary design and decision-making purposes, small scale centrifuge models were made to observe the complicated mechanisms involved.

A newly developed actuation system, with which the construction sequences of propping could be implemented, was developed, the new procedures were proven to give more realistic initial ground conditions before excavation with minimal development of pre-excavation bending moment and wall displacement. Incremental wall deformation profiles generally followed the O'Rourke cosine bulge equation and a new deformation mechanism was proposed with respect to wall toe fixity and excavation geometry. Validation of the conservation energy principle was carried out for the undrained excavation process. The total loss of potential energy was shown to be balanced by the total work done in shearing and the total elastic energy stored in structures with an error term of 30%.

An improved mobilizable strength method (MSD) method using observed mechanistic deformation patterns was introduced to calculate the displacement profile of a multi-propped undrained excavation in soft clay. The incremental loss in potential energy associated with the formation of settlement troughs was balanced by the sum of incremental storage of elastic energy and the energy dissipation in shearing. A reasonable agreement was found between the prediction by the MSD method and the finite element results computed by an advanced MIT-E3 model for wall displacements, ground settlement, base heave and bending moment on fixed base walls. For cases of excavations supported by floating walls, the effect of embedded wall length, depth of the stiff layer, bending stiffness of wall and excavation geometry and over-consolidation ratio of soils were found to have an influence on the maximum wall deflection. In general, the predictions fell within 30% of the finite element computed results.

A new chart ψ versus normalized system stiffness was used to demonstrate that MSD could correctly capture the trend of wall displacements increasing with the ratio of excavation depth to depth of stiff layer, which could be controlled by increasing wall stiffness for very stiff wall system only. The incorporation of a simple parabolic curve quantifying small strain stiffness of soil was proven to be essential to good ground movement predictions. A new dimensionless group has been defined using the MSD concepts to analyze 110 cases of excavation. The new database can now be used to investigate the relationship between structural response ratio S and soil-structure stiffness ratio R where this is shown on log-log axes to capture the enormous range of wall stiffness between sheet-piles and thick diaphragm walls. Wall stiffness was found to have a negligible influence on the magnitude of the wall bulging displacements for deep excavation supported by fixed-based wall with stiffness ranging from sheet pile walls to ordinary reinforced concrete diaphragm walls, whereas excavations supported by floating walls were found to be influenced by wall stiffness due to the difference in deformation mechanisms.

ACKNOWLEDGEMENTS

I would like to express my sincere gratitude to my supervisor Professor M.D. Bolton. With his encouragement, understanding and guidance, I am able to complete my work. His continuous encouragement throughout my research, especially in hard times, is much appreciated.

Special thanks go to Professor R.J. Mair who provides valuable suggestion on my research. I would like to thank Dr. Stuart Haigh, Dr. A.S Osman, Dr. M. Elshafie and Dr. A. Marshall, Dr. K. Joshi, Dr. G.B. Madabhushi for their valuable opinions on my project. I would also like to appreciate the help given by Prof. C.W.W. Ng, Prof. G.B. Lui and Dr. X.F. Ma in collection of data for analysis.

I would like to thank the technical staff, especially Chandler, S., Chandler, J.A., Pether, K., McGinnie, C., Ross, A. and especially Adams, R., in the Schofield centre and the geotechnical research laboratory for their assistance and technical supports. Thanks to Lowday, A for her assistance of the administrative issues during my research time.

I would like to thank K.H. Goh for his great contribution during my research time through detailed discussion about his wonderful engineering experience. I would like to take this chance to thank my friends Zheming Li, Christopher Lo, Andy Leung, Gue, C.S. and Fiona Kwok for their support and encouragement.

I would not have been able to finish this work without the financial support from Cambridge Overseas Trust, Cambridge University Engineering Department, and Churhcill College.

Finally, I would like to give my sincere words for my parents for their love and bearing of me for the past years. Thank them for giving me a wonderful life.

TABLE OF CONTENTS

DECLARATION	ii
ABSTRACT	iii
ACKNOWLEDGMENTS	iv
TABLE OF CONTENTS	v
LIST OF FIGURES	ix
LIST OF TABLES	xiv

CHAPTER 1 INTRODUCTION

1.1	Backgrounds	1-1
1.2	Objectives of studies	1-4
1.3	Outline of thesis	1-6

CHAPTER 2 LITERATURE REVIEW

2.1	Introduction	2-1
2.2	Calculation of Basal stability for deep excavation problem	2-2
2.3	Empirical observations	2-3
2.3.1	Predicting ground movement and apparent earth pressure	2-3
2.3.1.1	Peck's Method	2-4
2.3.1.2	Mana and Clough	2-7
2.3.1.3	Bowles' Method	2-8
2.3.1.4	Clough and O'Rourke's Method	2-9
2.3.1.5	Clough et al.'s Method	2-10
2.3.1.6	Hsieh and Ou's observation on shape of ground surface settlement	2-12
2.3.1.7	Ou et al.'s Method	2-13
2.3.1.8	Hsieh and Ou's Method	2-14
2.3.1.9	Long's Database	2-14
2.3.1.10	Moormann's Database	2-15
2.3.1.11	Stress paths method	2-17
2.4	Numerical studies	2-20
2.4.1	Effect of supporting structure	2-21
2.4.2	Effect of excavation geometry	2-22
2.5	Laboratory studies	2-25
2.5.1	Centrifuge testing	2-25
2.6	Centrifuge modelling of excavation	2-26
2.6.1	Method of simulating excavation	2-26
2.6.2	Centrifuge modeling of retaining wall propped at excavation level	2-29
2.6.3	Centrifuge modeling of doubly propped wall	2-29
2.6.4	Centrifuge modeling of retaining wall with soil improvement scheme	2-31

2.7	Earth pressure measurement	2-33
2.8	Image processing technique- Particle Image Velocimetry	2-35
2.9	Mobilizable strength design (MSD)	2-37
2.10	Summary and discussion	2-40

CHAPTER 3 DEVELOPMENT OF A NEW APPARATUS AND TESTING PROCEDURE

3.1	Introduction	3-1
3.2	In-flight excavator	3-4
3.3	Experimental setup	3-9
3.4	Cylinder support system and gate system	3-9
3.5	Preparation of model ground	3-13
3.6	Model making and instrumentation	3-16
3.7	Excavation test procedure	3-18
3.8	Test programme	3-20
3.9	Undrained compression tri-axial testing of core samples	3-21
	3.9.1. Measurement of stress strain behaviour by triaxial apparatus	3-21
	3.9.2. Triaxial apparatus and specimen installation	3-22
	3.9.3. Local strain measurement	3-28
	3.9.4. Pulse transmission system	3-32
	3.9.5. Small strain stiffness characterization by wave propagation technique and local strain measurement technique	3-37
	3.9.6. Comparison with published experimental data by Viggiani and Atkinson (1995)	3-40
	3.9.7. Power-law idealization	3-42
3.10	Summary and discussion	3-42

CHAPTER 4 OBSERVED CENTRIFUGE TEST PERFORMANCES FOR BOTH SHORT-TERM AND LONG-TERM

4.1	Introduction	4-1
4.2	Typical soil strength profile	4-1
4.3	Typical pre-excavation soil behaviour	4-3
	4.3.1 Pre-excavation responses	4-4
	4.3.1.1 Pore pressure response	4-5
	4.3.1.2 Ground settlement response	4-6
	4.3.1.3 Bending moment on research wall	4-8
4.4	Observed performance during deep excavation (Short term)	4-9
	4.4.1 Progress of excavation	4-9
	4.4.2 Short term excavation response	4-10
	4.4.2.1 Pore pressure response	4-10
	4.4.2.2 Apparent earth pressure	4-14
	4.4.2.3 Total earth pressure	4-16
	4.4.2.4 Stress paths	4-18
	4.4.2.5 Mobilization of shear strength	4-21
	4.4.2.6 Bending moment on retaining wall	4-22

4.4.2.7	Ground settlement and wall deflection	4-25
4.4.2.8	Proposed incremental deformation mechanism	4-42
4.4.3	Soil strains	4-44
4.4.3.1	Volumetric stain calculation	4-45
4.4.3.2	Engineering shear strain calculation	4-46
4.4.3.3	Validation of the energy conservation principle	4-52
4.5	Observed performance after excavation in long term	4-60
4.5.1	Pore pressure response	4-62
4.5.2	Wall deflection and ground settlement	4-66
4.6	Summary and discussion	4-74

CHAPTER 5 AN EXTENDED MOBILIZABLE STRENGTH DESIGN METHOD FOR DEEP EXCAVATION

5.1	Introduction	5-1
5.2	Application of MSD for deep excavation	5-3
5.3	Failure plastic mechanism	5-6
5.4	Geo-structural mechanism	5-9
5.4.1	Deformation pattern in different zones	5-12
5.5	Shear strength mobilized in mechanism	5-19
5.6	Incremental energy balance	5-20
5.7	Calculation procedures for fixed toe walls	5-22
5.8	Comparison with numerical finite element analysis	5-23
5.8.1	Wall deflection	5-25
5.8.2	Bending moment	5-26
5.8.3	Ground settlement and base heave	5-26
5.9	Validation MSD calculation with case histories in Singapore	5-27
5.10	Calculation procedures for excavation supported by floating walls	5-36
5.11	Comparison with numerical finite element analysis	5-39
5.11.1	Effect of width of excavation	5-39
5.11.2	Effect of bending stiffness of the wall	5-41
5.11.3	Effect of the depth of bearing stratum	5-43
5.11.4	Effect of clay stratum with different strength or OCR	5-45
5.11.5	Effect of embedded wall length	5-50
5.12	Comparison with observed results in centrifuge tests	5-52
5.13.	Summaries and discussions	5-53

CHAPTER 6 DATABASE OF MOVEMENTS DUE TO DEEP EXCAVATION IN SOFT SOIL

6.1	Introduction	6-1
6.2	Traditional interpretation of field data	6-2
6.3	Performance of MSD method in estimating deformations around deep excavations	6-6
6.4	Simplified relationship between wall deflections and mobilization of soil strength	6-6

6.5	Non-dimensionless analysis of deep excavation case histories	6-12
6.5.1	Normally consolidated clays	6-18
6.5.2	Over-consolidated clays	6-20
6.6	Implication of design on retaining wall	6-21
6.7	Conclusions	6-22

CHAPTER 7 CONCLUSIONS AND FUTURE DEVELOPMENTS

7.1	Introduction	7-1
7.2	Achievements	7-2
7.2.1	Development of a novel technique for deep excavation in centrifuge	7-2
7.2.2	Observations from small scale centrifuge model tests	7-2
7.2.3	Extended mobilizable strength design method for deep excavation	7-4
7.2.4	Database of ground movements of deep excavation in soft soil	7-6
7.3	Future developments	7-9

REFERENCES

APPENDIX A

LIST OF FIGURES

Figure 2.1	Summary of settlement adjacent to open cuts in various soils as function of distance from edge of excavation
Figure 2.2	Apparent pressure diagrams suggested by Terzaghi and Peck (1967) for computing strut loads in braced cuts
Figure 2.3	Excavation geometry and soil strength parameter for factors of safety
Figure 2.4	Analytically defined relationship between factor of safety against basal heave and non-dimensional maximum later wall movement (After Mana and Clough, 1981)
Figure 2.5	Method of Clough and O'Rourke (1990) for estimating ground movement
Figure 2.6	Lateral wall movements as a percentage of excavation depth versus system stiffness (After Clough, et al. 1989)
Figure 2.7	Definition of symbols by Moormann (2004)
Figure 2.8	Variation of maximum horizontal displacement with excavation depth following Moormann (2004)
Figure 2.9	Variation of normalized maximum horizontal displacement with system stiffness following Moormann (2004)
Figure 2.10	Location of soil elements around an excavation
Figure 2.11	(a) Effective stress paths and (b) Total stress path of soil elements located 10m behind diaphragm wall
Figure 2.12	Principle of PIV analyses
Figure 2.13	Flowchart of the GeoPIV analysis procedure
Figure 3.1	In-Flight Excavator
Figure 3.2	Schematic diagram of experimental setup with in-flight excavator
Figure 3.3	General arrangements of main apparatus
Figure 3.4	Propping and gate system (a) before and (b) after excavation
Figure 3.5	Modelling sequences of excavation
Figure 3.6	Positions of instruments (a) on model package (b) on model wall
Figure 3.7	Configuration of PIV cameras and Webcam (Front)
Figure 3.8	Progress of excavations
Figure 3.9	Layout of triaxial set-up
Figure 3.10	Local LVDT mount system after Cuccovillo and Coop (1997)
Figure 3.11	Results of undrained triaxial test on vertical core sample showing (a) mild concavity in stress-strain curve and (b) hump in stiffness degradation curve
Figure 3.12	stress strain curves and stiffness degradation curves for vertically and horizontally core sample.
Figure 3.13	Shear and compression waves received by bender elements in tests on dry Ticino sand (after Brignoli & Gotti,1992)
Figure 3.14	Calculated values of Vs using input-output and second arrival methods on samples with different Ltt to wavelength ratio. Figure 3.15 Results of

- bender element tests (a) input and output signals (b) Cross-correlation for Test 2 vertical core.
- Figure 3.16 Variation of G with mean stress and strain extracted from the present data and data from Viggiani and Atkinson (1995).
- Figure 3.17 Variation of soil shear secant stiffness with shear strain (Vertical sample)
- Figure 4.1 (a) Schematics of test set-up and (b) undrained shear strength and over-consolidation profile at 60g
- Figure 4.2 Development of pore pressure with time
- Figure 4.3 Dissipation of excess pore water pressure
- Figure 4.4 Excess pore pressure isochrones during reconsolidation
- Figure 4.5 Variation of (a) settlement data for SYL05 against root time (b) settlement data LVDT2 for all tests against time (c) settlement data LVDT2 for all tests against root time
- Figure 4.6 Displacement vectors of ground movement during consolidation
- Figure 4.7 Development of bending moment profile for test SYL05 during consolidation
- Figure 4.8 Progress of excavation
- Figure 4.9 Variation of pore water pressure during excavation with rigid props and wall (Test SYL04)
- Figure 4.10 Variation of excess pore water pressure during excavation with stiff props and wall (Test SYL04)
- Figure 4.11 Variation of water pressure at bottom of excavation site (PPT9)
- Figure 4.12 Variation of water pressure in middle of wall on retained side (PPT5)
- Figure 4.13 Development of apparent earth pressure with depth
- Figure 4.14 Variation of total earth pressure with excavation depth for Test SYL05 and SYL04
- Figure 4.15 Variation of total earth pressure with depth for Test SYL05
- Figure 4.16 Stress paths for soil elements near excavation
- Figure 4.17 Stress paths of soil elements in Tests SYL04 and SYL05
- Figure 4.18 Mobilization of undrained shear strength in Test SYL04 (Rigid wall rigid props)
- Figure 4.19 Mobilization of undrained shear strength in Test SYL05 (Flexible wall rigid props)
- Figure 4.20(a) Variation of bending moment with depth for excavation in deep clay with flexible wall (Test SYL05)
- Figure 4.20(b) Variation of bending moment with depth for excavation in shallow clay with flexible wall (Test SYL07)
- Figure 4.20(c) Variation of bending moment with depth for excavation in deep clay with rigid wall (Test SYL04)
- Figure 4.21 Development of wall deformation and ground settlement with progress of excavation (Test SYL05).
- Figure 4.22 Incremental deformation mechanisms for $H=0.96\text{m}$ and $H=5.4\text{m}$ for Test SYL05)
- Figure 4.23 Development of wall deformation and ground settlement with progress of excavation (Test SYL04)

- Figure 4.24 Variation of wall deformation with system stiffness (After Clough et al., 1989)
- Figure 4.25 Development of wall deformation and ground settlement with progress of excavation (Test SYL07)
- Figure 4.26 Incremental displacements for different stage of excavation for Test SYL07
- Figure 4.27 Total displacements for second and third stage of excavation for Test SYL07
- Figure 4.28 Development of wall deformation and ground settlement with progress of excavation (Test SYL06).
- Figure 4.29 Total deformation mechanism for the third stage of excavation (Test SYL06)
- Figure 4.30 Wall deflection and ground settlement profile for excavation using flexible wall (Test SYL05, SYL06 and SYL07)
- Figure 4.31 Variation of normalized incremental displacement with distance below the lowest prop
- Figure 4.32 Development of wall deformation and ground settlement with progress of excavation (Test SYL03).
- Figure 4.33 Deformation mechanism for excavation using rigid retaining wall with soft props at $H=5.4\text{m}$ (Test SYL03)
- Figure 4.34 A comparison of wall displacement and ground settlement on Tests with different prop stiffness
- Figure 4.35 Proposed deformation mechanism
- Figure 4.36 Mohr circle of strain
- Figure 4.37 Development of volumetric strain for excavation depth of 5.4m (Final stage of test SYL07)
- Figure 4.38 Engineering shear strain plots on active side for Excavation depth of $H=1.08\text{m}$, $H=3.24\text{m}$ and $H=5.40\text{m}$ for Test SYL07
- Figure 4.39 Engineering shear strain plots excavation depth of $H=5.40\text{m}$ for excavation in deep clay using flexible wall (Test SYL05)
- Figure 4.40 Engineering shear strain plots excavation depth of $H=5.40\text{m}$ for excavation in deep clay using flexible fixed-base wall (Test SYL06)
- Figure 4.42 Engineering shear strain plots excavation depth of $H=5.40\text{m}$ for excavation in deep clay using a rigid wall with soft props (Test SYL03)
- Figure 4.41 Engineering shear strain plots excavation depth of $H=5.40\text{m}$ for excavation in deep clay using a rigid wall with rigid props (Test SYL04)
- Figure 4.42 Work done in excavation depth of 1.08m , 3.24m and 5.40m for TEST SYL07
- Figure 4.43 Potential energy change for excavation depth of 1.08m , 3.24m and 5.40m for Test SYL07
- Figure 4.44 Work done and potential energy change for excavation depth of 5.40m for Test SYL05
- Figure 4.45 Work done and potential energy change for excavation depth of 5.40m for Test SYL06
- Figure 4.46 Variation of potential energy change with work done by the soil structural system

- Figure 4.47 Schematic diagram showing locations of PPTs
- Figure 4.48 Pore pressure responses after excavations for (a) Test SYL05 (b) Test SYL06 and (c) Test SYL07
- Figure 4.49 Pore pressure distributions against depth for (a) Test SYL05 (b) Test SYL06 and (c) Test SYL07
- Figure 4.50 Simplified flow nets for (a) Test SYL05 (b) Test SYL06 and (c) Test SYL07
- Figure 4.51 Development of long-term (a) lateral wall displacement and (b) ground surface settlement for Test SYL05
- Figure 4.52 Development of long-term (a) lateral wall displacement and (b) ground surface settlement for Test SYL07
- Figure 4.53 Development of long-term (a) lateral wall displacement and (b) ground surface settlement for Test SYL06
- Figure 4.54 Long term deformation mechanism (a) before wall toe kick out (b) after wall toe kick out
- Figure 5.1 Conventional basal stability mechanism and notation (after Ukritchon et al., 2003)
- Figure 5.2 Incremental displacements in braced excavation (after O'Rourke, 1993)
- Figure 5.3 Incremental displacement fields
- Figure 5.4 Mobilizable shear strength profile of an excavation stage in an layered soil
- Figure 5.5 Correlation between normalized average shear strain and excavation geometry for a narrow excavation
- Figure 5.6 Overlapping of deformation field
- Figure 5.7 Stress-strain response for K_0 consolidated undrained DSS tests on Boston blue clay (After Whittle, 1993)
- Figure 5.8 Comparison of MSD predicted and computed wall performance: MSD prediction compared with FEA by Jen (1998)
- Figure 5.9 Stress strain relationship of Singapore marine clay
- Figure 5.10 Soil profile along section 1-1
- Figure 5.11 MSD Prediction and measured lateral displacement (a) a long wall $L=25\text{m}$ (b) a short wall $L=12.5\text{m}$
- Figure 5.12 Properties of Marine clays from site investigation
- Figure 5.13 Predicted and measured displacement profile at different stage of excavation: MSD predictions compared with measurement and FEA prediction by FREW (Wallace et al., 1992)
- Figure 5.14 Marine clay properties
- Figure 5.15 Measured and predicted displacement profile at different stages of excavation: MSD predictions compared with measurement and FEA prediction by BILL (Nicholson, 1987)
- Figure 5.16 Modification to deformation mechanism after introduction of elastic energy stored in the wall to formulation
- Figure 5.17 Scope of studies carried by Jen (1998)
- Figure 5.18 Wall deflection profile of different excavation widths at $H = 17.5\text{m}$
- Figure 5.19 Deflection profiles of walls with various bending stiffness

- Figure 5.20 Wall deflection profiles of excavation with different depths to the firm stratum: solid lines- MSD prediction, Icons- FEA by Jen (1998) (a) shallow clay $C=37.5\text{m}$ (b) deep clay $C=50\text{m}$
- Figure 5.21 Deflection profiles of walls embedded in soil profiles of different stress histories
- Figure 5.22 Deflection profiles of diaphragm wall and sheet pile wall embedded in soil profiles of different stress histories
- Figure 5.23 Variation of normalized maximum wall deflection with system stiffness following Moormann (2004)
- Figure 5.24 Deflection profiles of diaphragm walls with different wall lengths embedded in soft soil
- Figure 5.25 Comparison of the deflection profiles by MSD predictions with actual measured displacement in centrifuge tests
- Figure 6.1 Normalized horizontal wall displacement with different support system
- Figure 6.2 Variation of normalized horizontal wall displacement following Mana and Clough (1981) approach
- Figure 6.3 Variation of maximum horizontal wall displacement with System stiffness defined by Clough et al. (1989) and factor of safety against base heave.
- Figure 6.4 Stress Strain relationship of soft clay worldwide (Mainly DSS data)
- Figure 6.5 Comparison between measured and predicted lateral wall displacement by MSD
- Figure 6.6 Variation of displacement factor with system stiffness defined by Clough (1989) (a) Data and MSD prediction for $\gamma_u=3\%$, (b) MSD prediction for $\gamma_u=1\%$, 3% and 5%
- Figure 6.7 Field data plotted on $\log S$ versus $\log R$
- Figure 6.8 Field data and MSD predictions plotted on $\log S$ versus $\log R$
- Figure 6.9 Field data plotted on normalized displacement factor versus structural system stiffness
- Figure 7.1 A summary of findings on the influence at wall stiffness EI in the cases of floating wall and fixed base walls

LIST OF TABLES

Table 3.1	Capability of the two axis actuator
Table 3.2	Properties of fraction E sand
Table 3.3	Mineralogy and properties of Speswhite Kaolin
Table 3.4	Summary of centrifuge testing programme
Table 3.5	Summary of bender element tests
Table 4.1	A summary of centrifuge testing programme
Table 4.2	A summary of calculated energy terms for different tests
Table 6.1	Summary of case histories (Reference list: Page R-10 & R-11)

CHAPTER 1

INTRODUCTION

1.1 Backgrounds

To optimize high land cost in urban development, underground space is commonly exploited, both to reduce the load acting on the ground and to increase the space available. Many deep excavation works have been carried out to construct various types of underground infrastructure such as deep basements, subways and service tunnels. The execution of these deep excavation works requires the use of appropriate retaining wall and bracing systems. Inadequate support systems are always a major concern, as any excessive ground movement induced during excavation could cause damage to neighboring structures, resulting in delays, disputes and cost overrun.

Efficient and safe design of multi-propped deep excavations is not easy. The responsible geotechnical engineer has to make some assumptions and he/she runs the risk of encountering surprises worldwide (Shirlaw, 2005). These circumstances are the inevitable result of dealing with natural materials such as soil and rock. Field monitoring the performance of deep excavations (Burland and Hancock 1977, O'Rourke 1981; Finno et al. 1989, Hansmire et al. 1989, Ulrich 1989; Whitman et al., 1991; Ikuta *et al.*, 1994;

Malone *et al.*, 1997a; Ng, 1998; Ng, 1999; Ou *et al.*, 2000; Liu *et al.* 2005; Wang *et al.*, 2005) is therefore necessary to provide a means by which the geotechnical engineer can verify the design assumptions and the contractor can execute the work with safety and economy. More importantly, the field data may also be assembled into a comprehensive case record that is then often used for checking the validity of any analytical and numerical models. Good agreement between back-analyzed values (or so called Class-C predictions (Lambe, 1973)) and field observations has frequently been reported in the literature. Although Class-C predictions can help to refine and improve our understanding, which in turn provides guidance for future designs, the ultimate challenge for designers is to make accurate design predictions prior to construction (i.e., Class-A predictions, Lambe (1973)). There are two common techniques for estimating wall deflections and soil settlements, either by interpolation from an empirical database or by numerical analysis such as finite element and finite difference methods. Recently, excellent case histories regarding the design analysis and observation of two multi-propped deep excavations were reported. Hsi and Yu (2005) reported and documented the design and construction of 20 m deep excavations in deep marine soft clays in Singapore. Prior to construction, two dimensional finite element (FE) analyses were carried out using very popular commercial software to assist in their design predictions. The soft soil was modeled as an elasto-plastic material with a Mohr-Coulomb failure criterion. Interfaces between the soil and various structural elements were simulated by using different strength reduction factors, depending on the soil and member types. However, details of how consolidation effects were incorporated were not clear. Although their class A prediction was not very consistent with the field data, lessons learnt from a genuine case

history should benefit research in the long run. On the other hand, even when a finite element analysis using an advanced soil model such as MIT-E3 predicts field results very well, the 23 modelling parameters require lots of undisturbed sample cores subjected to advanced laboratory testing over a long period of time. Thus, the practicality for real construction projects for very sophisticated soil models is still questionable.

Recently, Osman & Bolton (2004) showed that by combining statically admissible stress fields and kinematically admissible deformation mechanisms with distributed plastic strains, they could make displacement predictions based on knowing the stress-strain response of the soil. This application is different from the conventional applications of plasticity theory because it can approximately satisfy both safety and serviceability requirements by predicting stresses and displacements under working conditions by introducing the concept of “mobilizable soil strength”. The authors treat the stress-strain data of an element, representative of some soil zone, as a curve of plastic soil strength mobilized as strains develop. Designers enter these strains into a plastic deformation mechanism to predict boundary displacements. The particular case of a cantilever retaining wall supporting an excavation in clay is selected for a spectrum of soil conditions and wall flexibilities. The possible use of the mobilizable strength design (MSD) method in decision-making and design is explored and illustrated. The key advantage of the MSD method is that it gives designers the opportunity to consider the sensitivity of a design proposal to the nonlinear behaviour of a representative soil element. It accentuates the importance of acquiring reasonably undisturbed samples and of testing them with an appropriate degree of accuracy in the local measurement of strains (e.g.,

0.01%). The extra step of actually performing finite element analyses remains open, with the advantage that the engineer would then have an independent check on the answer to be expected, within a factor of about 2 on displacement. The new plastic solution provides simple hand calculations for nonlinear soil behaviour which can give reasonable results compared with those from complex finite element analyses. Osman & Bolton (2006) further extended the MSD method to predict ground movements for deep braced excavations in undrained clay but omitting the influence of system stiffness of the supporting struts and retaining wall, for simplicity. With the increasing use of commercial computer software by engineers and researchers for design analysis of deep excavations, simple hand calculations are vital to verify computer outputs from FEA software to avoid catastrophic disasters such as the recent collapse of the excavation for the Nicoll Highway in Singapore (Shirlaw, 2005). According to the report published by the Committee of Inquiry into the causes of the collapse at the Nicoll Highway, the misuse of commercial finite element software was one of the major reasons for the collapse. How to select and verify appropriate calculation procedures and model parameters for the design of deep excavations becomes an urgent issue to be addressed.

1.2 Summary of the research

This research project aims to improve the current understanding of the effect of deep excavation construction in clay and to develop a practical decision making tool for design. To achieve this goal, the following objectives were identified:

1. Deformation mechanisms due to multi-propped deep excavation in clays were studied. Centrifuge experiments were carried out to simulate deep excavation with different

excavation geometries. Since the deformation of soil is highly stress-dependent, it was of vital importance to model the process in the correct stress state in the centrifuge. The image processing technique, Particle image Velocimetry (PIV) developed by White and Take (2002), revealed the detailed deformation mechanism. Instrumentation produced further data such as earth pressure, pore water pressure and prop loads.

2. Simplified deformation mechanisms were embedded in an extended MSD method in which deformation predictions are made using global conservation of energy. The stiffness of the supporting structure is included, together with the sequence of constructions. Finite element analysis (FEA), previously published by others, are used to validate MSD prediction of settlement troughs, wall displacement profiles and collapse mechanisms.
3. A worldwide database of case histories of deep excavations was compiled from more than 150 cases histories, which is well-documented and published in international conference proceedings, national reports, geotechnical journals and dissertations. For each case, relevant information was extracted and analyzed within the newly built framework of MSD formulation considering major factors such as soil properties, groundwater conditions, stiffness of the support system, construction method and also ground deformation responses. Noticing the ineffectiveness of the traditional empirical analysis of field data, the author derived new non-dimensional groups of critical parameters, which generate more reliable interpretation of the field data. New design guidelines were advocated, accordingly.

1.3 Outline of thesis

This thesis contains six chapters. Chapter 1 describes the background, objectives and scope of the work. Chapter 2 reviews previous research and field observation of deep excavations. This includes an overview of the empirical methods, numerical studies, centrifuge experimental studies and some other important aspects of the current research such as earth pressure measurement and image processing technique (PIV). In addition, the mobilizable strength design concept is introduced. Chapter 3 discusses how centrifuge experiments for deep excavations were conducted. The excavation test development scheme involves the adaptation of a 2D actuator to be an in-flight excavator, the development of a hydraulic controlled propping system and the model preparation and testing procedures. Finally, the stress-strain behavior of the soil is described, with small strain stiffness measured in a triaxial apparatus with local strain measurement and by using bender elements to record seismic wave speeds. Results of the model tests including wall deformation profiles and ground movements for excavations with different excavation geometries and prop stiffness are presented in Chapter 4.

Chapter 5 gives a detailed explanation of how the Mobilizable Strength Design (MSD) method can be applied to predict wall deformation incrementally for staged construction, both for walls keyed in a stiff stratum and for those suspended in a deep clay stratum. On top of that, new elements such as consideration of bending stiffness and layered soil are included in the extended version of the MSD solution. Comparisons are made between predictions from the extended MSD method and the results computed by the highly non-linear MIT-E3 model. The effect of excavation geometry, bending stiffness of the wall, wall length and soil OCR profiles are addressed. Chapter 6 gives an overview of a new

database of field data of deep excavations from nine cities on soft clay and their back-analyses by the newly developed framework of MSD. New non-dimensionless groups are introduced to generalize trends and single out important factors governing deformations associated with deep excavation construction. Chapter 7 summarizes the contributions of each chapter and suggests a context for future research.

CHAPTER 2

LITERATURE REVIEW

2.1 Introduction

With the development of high rise buildings and other civil engineering constructions, foundation excavations get deeper and deeper. Some of them are over 15m in comparison to the normal depth of 5-7m. In order to ensure the stability of the excavation and reduce the effect on the neighbouring buildings and underground utilities caused by excavation, continuous wall structures are often used. In these cases, the use of a multi-strutted structural system is often desirable in order to reduce ground movements and to achieve relatively high economical benefits. There are two common techniques for predicting horizontal wall displacements and ground settlements using either interpolation from a published database of different areas of the world or numerical analysis using either finite element methods or finite difference methods. As soil is a complicated material that always shows non-linear or sometimes brittle behaviour, predictions of ground movements are difficult. Even though many different aspects of soil are incorporated into many numerical models, many of these models are usually complex and the parameters

do not have a clear physical meaning. In addition, these models require huge amount of computational resources. The parameters require special kind of testing technique and laboratory skills. Therefore, practising engineers try to avoid using them and tend to use design charts which relate wall deflections to soil properties only through the factor of safety against basal heave. In this section, a review of literature on field studies, analytical solutions, numerical solutions and laboratory studies is carried out with a main focus on prediction of movements of multi-strutted structures and ground deformations.

In the following section, observations from field studies, results from numerical analysis, empirical methods and findings from centrifuge tests are summarized.

2.2 Calculation of Basal stability for deep excavation problem

Conventional limit equilibrium analyses (Terzaghi, 1943; Eide *et al.*, 1972) assume the failure mechanisms associated with assumed values of the bearing capacity factor, N_c , the location of the vertical shear surface on the retained side, and the inclusion of shear traction along the shear plane. Some variable forms of the solution consider proximity of an underlying bearing layer and also contrast in undrained shear strength above and below the excavation grade. Some researchers (Clough and Hansen, 1981) further refine the solution to tackle strength anisotropy based on reference shear strengths measured at three orientations of the major principal stress (i.e. s_{u0} , s_{u45} and s_{u90}). Effect of wall embedment is taken into account in all previous approach on the assumption that the wall is rigid. O'Rourke (1993) assumes the wall embedment does not change the failure mechanism. The contribution of the elastic energy stored in wall flexure to stability of the

excavation is accounted for. The resulting stability number is a function of the yield moment and boundary conditions at the wall toe.

Ukritchon *et al.* (2003) performed short-term undrained stability analysis using upper bound and lower bound methods to work out stability number. The formulations include anisotropic yielding and strength contribution from flexure of the wall below the lowest support with careful consideration of mobilized strengths at shear strains in the range of 0.6 to 1%. Results match the predictions of highly non-linear finite element analysis and show how mechanism of failure for an embedded wall is governed by the ratio of their plastic moment capacity for the wall to the undrained strength of the clay and the embedded depth of the wall. However, further considerations on different failure modes of the structural support system, including prop failure and prop wall connection failure, need to be considered.

2.3 Empirical observations

2.3.1 Predicting ground movement and apparent earth pressure

Ground movements behind a supported wall occur as a result of unbalanced pressure due to removal of soil mass inside the excavation site. The magnitude and distribution of the settlement are related to many factors such as construction quality, soil and groundwater condition, excavation geometry, excavation sequences, duration of excavation, surcharge condition, existence of adjacent buildings, method of retaining wall construction, penetration depth, wall stiffness, type and installation of lateral support, spacing and stiffness of struts. A method derived purely from theoretical basis would be very complex.

Therefore, most of the existing predictive methods were obtained based on field measurements and local experiences. Several commonly used empirical methods in engineering practice are presented as follows:

2.3.1.1 Peck's Method

Peck (1969) summarized the field observations of ground surface settlement around excavations in a graphical form as shown in [Figure 2.1](#). This method may be suitable for the spandrel-type settlement profile. As shown in the figure, the settlement curve is classified into three zones, I, II and III, depending on the type of soil and workmanship. In [Figure 2.1](#), N_b represents the stability number, and N_{cb} represents the critical stability number for basal heave. The case histories used in the development of the figure are prior to 1969 and the excavations are supported by sheet pile or soldier piles with lagging. It is proposed that the maximum ground settlement for very soft to soft clay is about 1% of the maximum excavation depth. The lateral influence zone would extend up to two times the maximum excavation depth. With the use of newer technology, say the use of diaphragm wall, the maximum settlements are generally smaller than those defined in the figure. However, the method of Peck is the first practical approach to estimate ground surface settlement.

[Figure 2.2](#) shows the semi-empirical apparent pressure envelope by Terzaghi and Peck (1967) for predicting maximum strut load that may be expected in the bracing of a given cut. It does not represent the real distribution of earth pressure from which there could be calculated strut loads that might be approached but would not be exceeded in the actual

excavation. The method is evaluated by many different researchers such as Wong et al. (1997) and Ng (1998).

Ng (1998) has carried out field studies on a 10m deep multi-propped excavation in the over-consolidated and fissured Gault clay. Comparison of measured and Peck's design earth pressure is made. The measured values are close to the lower bound value of Peck's chart. The strut load of the lowest prop was found to be somewhat smaller due to the low lateral stress in the ground following the construction of the diaphragm wall.

Wong et al. (1997) found that the maximum apparent earth pressure for the upper 10% of H exceeded the trapezoidal boundary of the apparent earth pressure diagrams for both stiff clay and soft clay that were proposed by Terzaghi and Peck (1967). This may have been caused by the high position of the first prop level and the application of preload. It is also suggested that the apparent earth pressure diagram should be extended to the ground surface rather than decrease to zero. No significant difference in trend among the apparent earth pressure values of excavation supported by wall of different stiffness is found.

Following Goldberg et al.(1976), many researchers attempted to evaluate Peck's loading envelopes using finite element stimulations for different lateral earth support systems e.g. for stiff diaphragm walls and soil profiles. Recent evidence by Hashash and Whittle (2002) shows that the loading envelopes under-predict the apparent earth pressure acting on diaphragm walls. Apparent pressure on a more flexible sheet pile wall on the other hand agrees quite well with the design envelope.

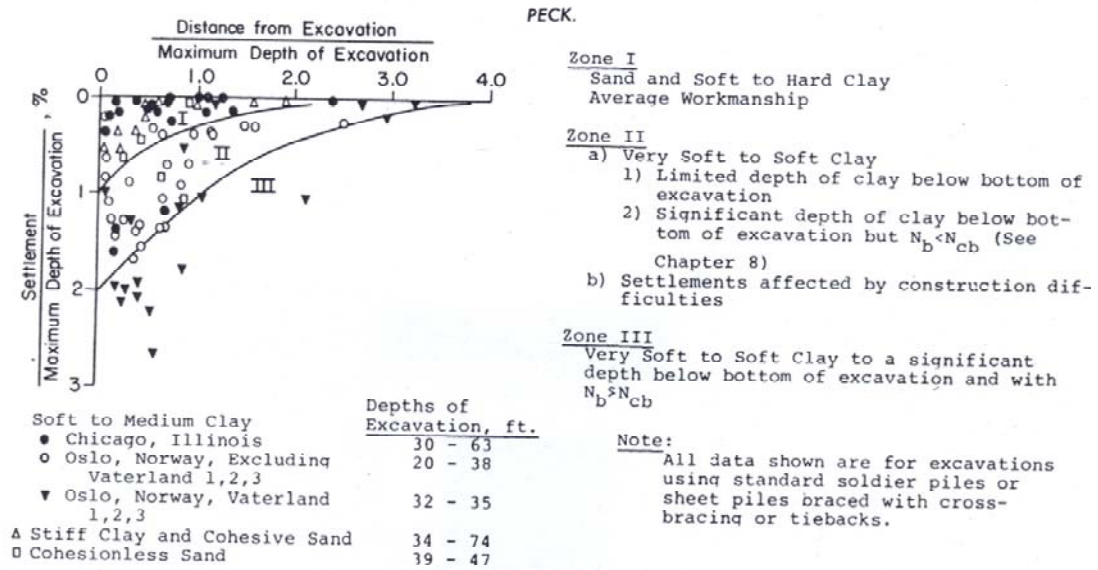


Figure 2.1 Summary of settlement adjacent to open cuts in various soils as function of distance from edge of excavation

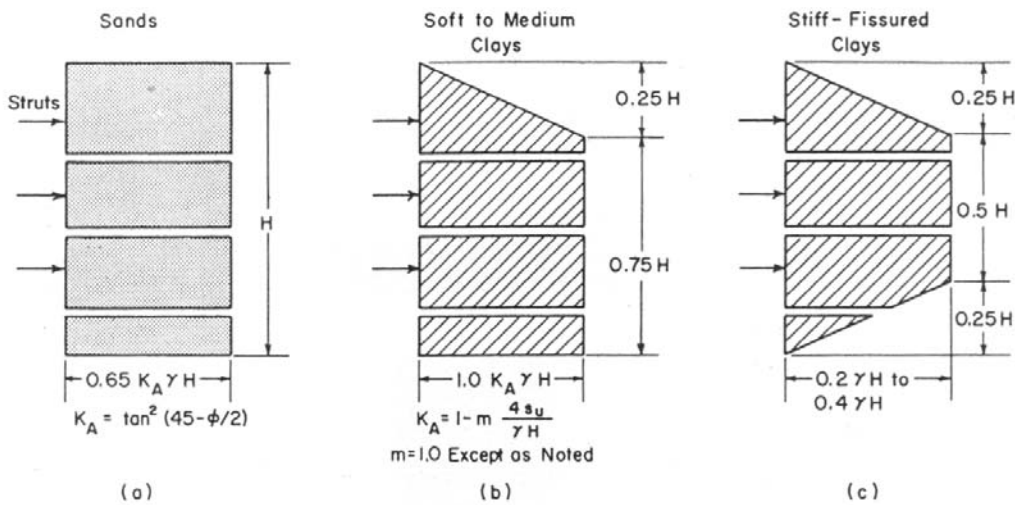


Figure 2.2 Apparent pressure diagrams suggested by Terzaghi and Peck (1967) for computing strut loads in braced cuts

2.3.1.2 Mana and Clough

In the studies of Mana and Clough (1981), 11 case histories were examined. The maximum observed movements for case histories are normalized by the excavation depth and correlated with the factor of safety against basal heave set out by Terzaghi(1943) as shown in Figure 2.3. As shown in Figure 2.4, the constant non-dimensional movement are at high safety factor is an indication of a largely elastic response. The rapid increases in movements at lower factor of safety are a result of yielding in the sub-soils. Upper and lower limits were suggested by authors for estimating expected level of movement.

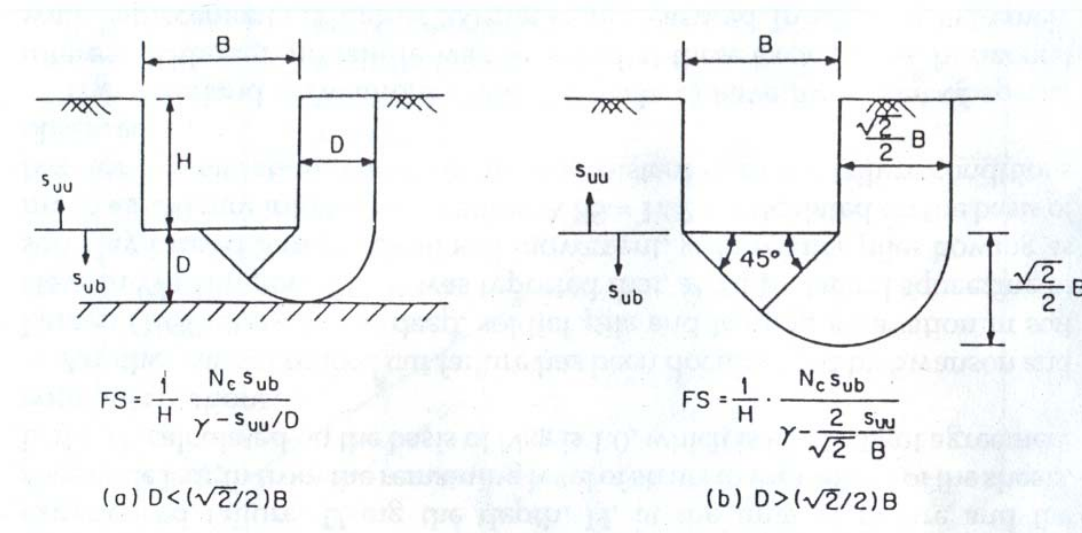


Figure 2.3 Excavation geometry and soil strength parameter for factors of safety

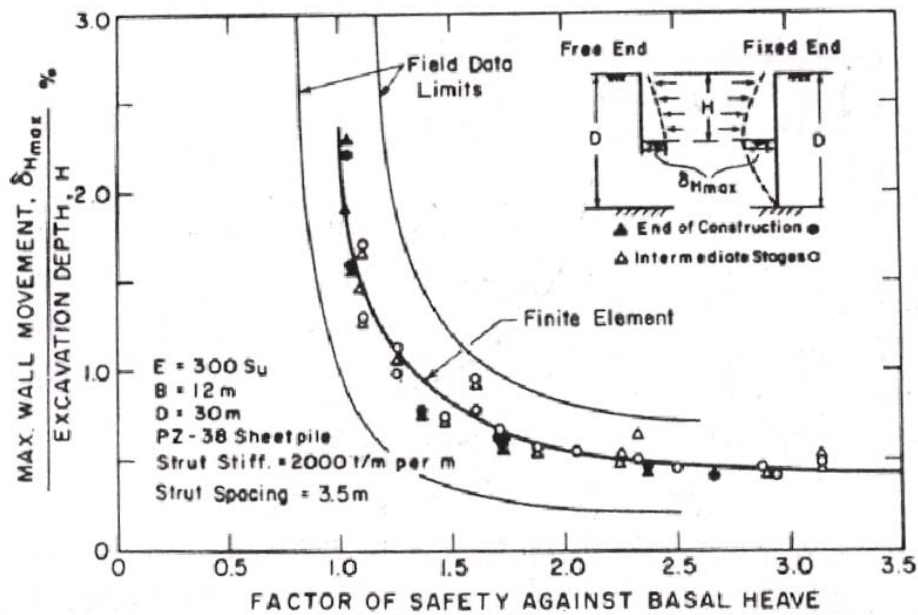


Figure 2.4 Analytically defined relationship between factor of safety against basal heave and non-dimensional maximum later wall movement (After Mana and Clough, 1981)

2.3.1.3 Bowles' Method

Bowles (1988) proposed a method for estimating the spandrel-type settlement profile induced by excavation. The steps are given as follows.

1. Lateral wall displacement is estimated.
2. Volume of lateral movement of soil mass is calculated.
3. The influence zone (D) using the method suggested by Caspe (1966) is adopted.

$$D = (H_e + H_a) \tan(45 - \phi'/2)$$

where H_e is the final excavation depth, ϕ' is the internal frictional angle of soil. For cohesive soil, $H_d=B$, where B =width of excavation; for cohesionless soil $H_d=0.5B \tan(45 + \phi'/2)$

4. By assuming that maximum ground settlement occurs at the wall, maximum ground settlement can be estimated by the following.

$$\delta_{vm}=4V_s/D$$

5. The settlement curve is assumed to be parabolic. The settlement (δ_v) at a distance from the supported wall (d) can be calculated as,

$$\delta_v=\delta_{vm}(x/D)^2$$

where $D-x$ is the distance from the wall.

2.3.1.4 Clough and O'Rourke's Method

Based on several case histories, Clough and O'Rourke (1990) suggested that the settlement profile is triangular for an excavation in sandy soil or stiff clay. The maximum ground surface settlement will occur at the wall. The non-dimensional profiles are given in [Figure 2.5\(a\) and 2.5\(b\)](#), which shows that the corresponding settlement extends to about $2H_e$ and $3H_e$ for sandy soil and stiff to very hard clays, respectively. For an excavation in soft to medium clay, the maximum settlement usually occurs at some distance away from the wall. The trapezoidal shape of the settlement trough is proposed as indicated in [Figure 2.5\(c\)](#). The influence zone extends up to 2 times the maximum excavation depth. If the δ_{vm} is known, the settlement at various locations can be estimated.

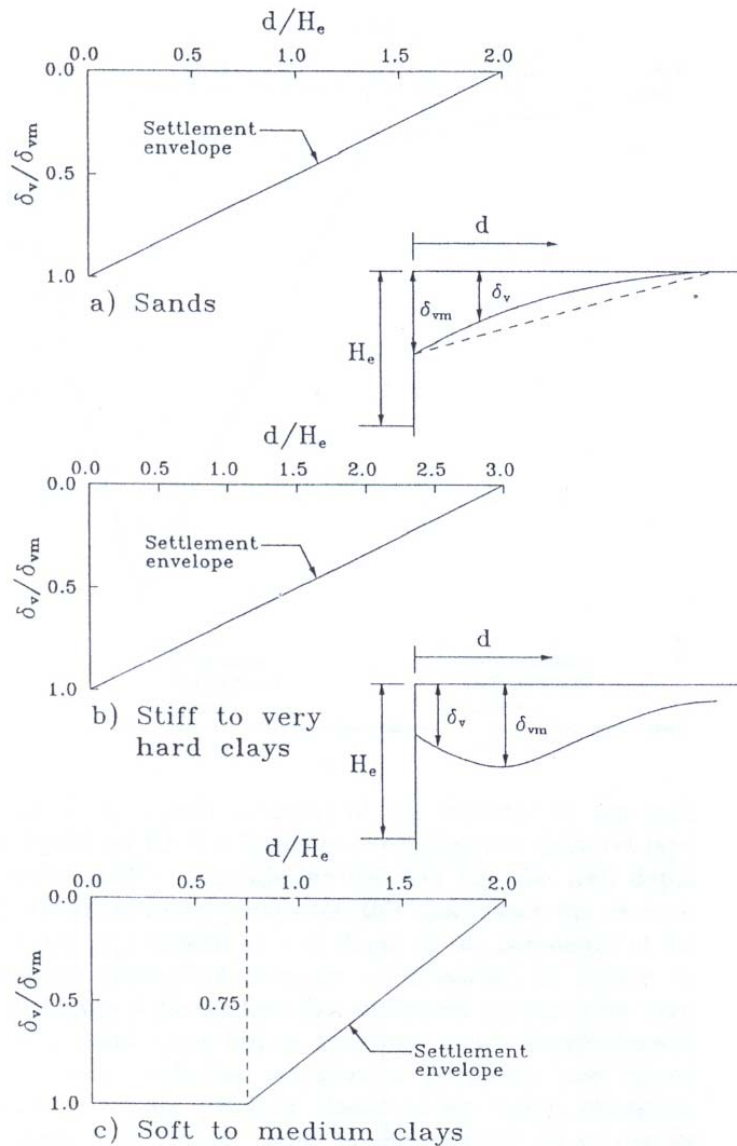


Figure 2.5 Method of Clough and O'Rourke (1990) for estimating ground movement

2.3.1.5 Clough et al.'s Method

Clough et al. (1989) proposed a semi-empirical procedure for estimating movement at excavations in clay in which the maximum lateral wall movement δ_{lm} is evaluated relative to factor of safety (FS) and system stiffness, which is defined as follows:

$$\text{System stiffness } (\eta) = EI/\gamma_w h^4$$

where EI is the flexure rigidity per unit width of the retaining wall, γ_w the unit weight of water and h the average support spacing.

The factor of safety (FS) is defined according to Terzaghi (1943), as shown in [Figure 2.3](#). It should be emphasized that FS is used as an index parameter. The system stiffness is defined as a function of the wall flexural stiffness, average vertical separation of supports, and unit weight of water, which is used as a normalizing parameter. [Figure 2.6](#) shows δ_{hm} plotted relative to system stiffness for various FS. The family of curves in the figure is based on average condition, good workmanship, and the assumption that cantilever deformation of the wall contributes only a small fraction of the total movement. A method for estimating cantilever movement is also recommended by Clough et al. to be added directly to those predicted by the [Figure 2.6](#).

Addenbrooke (2000) defined a new term, displacement flexibility, $\Delta=h^5/EI$, to quantify the effect of structural stiffness. Simple elastic-perfectly plastic finite element analysis was carried out to validate the idea. This allows engineers to consider different support options which meet the same wall displacement criteria. A more extensive validation by field cases histories was carried out later on by the creation of databases of deep excavation created by Long (2000) and Moormann (2004). However, no simple dependency was found between normalized displacement by excavation depth from field data i.e. δ_{max}/H and the displacement flexibility.

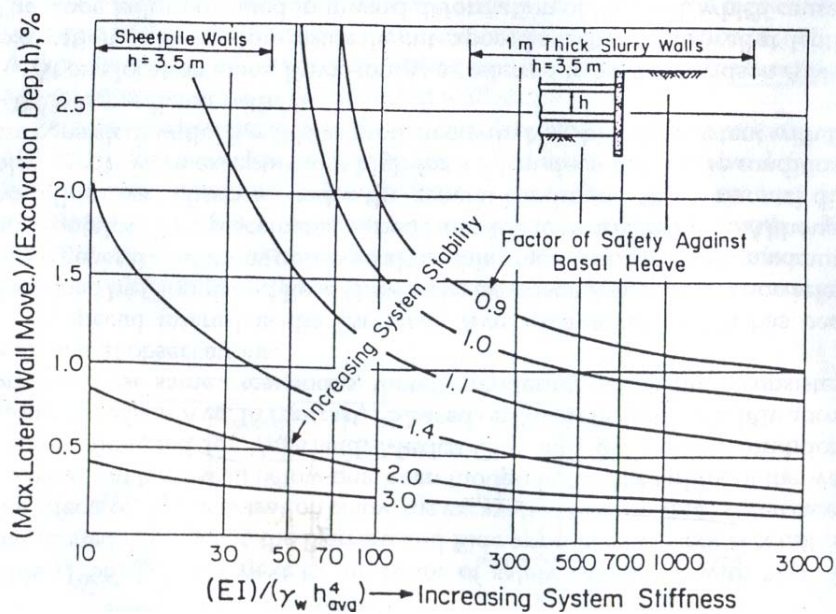


Figure 2.6 Lateral wall movements as a percentage of excavation depth versus system stiffness (After Clough, *et al.* 1989)

2.3.1.6 Hsieh and Ou's observation on shape of ground surface settlement

According to Hsieh and Ou (1998), there are two different types of settlement profile caused by excavation: (i) spandrel type, in which maximum surface settlement occurs very close to the wall, and (ii) concave type, in which maximum surface settlement occurs at a distance away from the supported wall. The magnitude and shape of wall deflection may result in different types of settlement profile. If a large amount of wall deflection occurs at the first stage of excavation and relatively small deflection occurs at subsequent stages of excavation, the spandrel type of settlement shape is likely. On the other hand, if a relatively small amount of wall deflection occurs at initial stages of excavation, compared with the amount of deflection at deeper levels, additional cantilever wall deflection, or deflection in the upper part of the wall, is restrained by installation of

support as the excavation proceeds to deeper elevations which translates to a ground settlement profile consistent with concave settlement profile.

2.3.1.7 Ou et al.'s Method

Based on 10 cases in Taipei, Taiwan, Ou et al. (1993) observed that the vertical movements of the soil behind the wall may extend to a considerable distance. The settlement at a limited distance behind the wall is not uniform and increases with excavation depth. Buildings within this distance may be damaged. The zone is thus defined as the apparent influence range (AIR). The settlement outside this AIR would be negligible. According to Ou et al. (1993), the AIR is approximately equal to the distance defined by the active zone. The upper limit is a distance equal to the wall depth, that is,

$$AIR = (H_e + H_p) \tan(45 - \phi/2) < (H_e + H_p)$$

Where H_e is the final excavation depth and H_p is the wall penetration depth.

Ou et al. (1993) also proposed a method for prediction of both spandrel and concave types of ground settlement profile. For the spandrel type, a bilinear line was suggested by averaging settlement profiles of 10 case histories in Taipei. For the concave type, it was proposed that the profile was represented by a tri-linear line, in which the maximum ground surface settlement occurred at a distance equal to half the depth where the maximum later wall deflection occurred.

2.3.1.8 Hsieh and Ou's Method

Following the findings from Ou et al. (1993), Hsieh and Ou (1998) setup a procedure for predicting ground deformation. The predicting procedures are listed as follows:

1. Predict the maximum lateral wall deflection (δ_{hm}) by performing lateral deformation analysis, e.g. finite element methods or beam on elastic foundation methods
2. Determine the type of settlement profile by calculating the cantilever area and deep inward area of predicted wall deflection. If $A_s \geq 1.6A_c$, concave type of settlement profile is adopted, where A_s and A_c refer to areas of deep inward movement and area of cantilever movement in the graph of wall horizontal displacement against depth, respectively.
3. Estimate the maximum ground settlement using empirical data. (e.g. relationship between maximum horizontal displacement and maximum ground settlement)
4. Calculate the surface settlement at various distances behind the wall using the profile suggested by Ou et al. (1993).

2.3.1.9 Long's Database

Long (2001) analyzed 296 case histories. His studies largely focus on validating results of Clough and O'Rourke (1990) for stiff soils with $\delta_{hm}/H=0.05-0.25\%$ and $\delta_{vm}/H=0-0.2\%$. For soft clay with low factor of safety against base stability, large movements of up to

$\delta_{hm}/H = 3.2\%$ may occur. These roughly followed the trends in Clough's chart despite scattering of the data. He stated that the deformations of deep excavations in non-cohesive soils as well as in stiff clay are independent of the stiffness of the wall and the support as well as the kind of support. The stiffness term only affect the deformation significantly when dealing with deep excavation in soft clays with a low factor of safety against base heave. Attempts were made by Long(2001) to validate the use of Addenbrooke's flexibility number for quantifying stiffness of the support system. Results again show a similar trend as found in Clough's approach with wide scatter.

2.3.1.10 Moormann's Database

Moormann(2004) had carried out extensive empirical studies by taking 530 case histories of retaining wall and ground movement due to excavation in soft soil ($c_u < 75\text{kpa}$) into account. It is concluded that the maximum horizontal wall displacement (δ_{hm}) lie between $0.5\% H$ and $1.0\% H$, on average at $0.87\% H$ (Figure 2.7 and Figure 2.8). The location of maximum horizontal displacement is at $0.5H$ to $1.0H$ below the ground. The maximum vertical settlement at the ground surface behind a retaining wall (δ_{vm}) lies in the range of $0.1\% H$ to $10\% H$, on average at $1.1\% H$. The settlement δ_{vm} occurs at a distance of less than $0.5\% H$ behind the wall, but there are cases in soft soil with this distance to be up to $2.0 H$. The ratio δ_{vm}/δ_{hm} varies mainly between 0.5 and 1.0. The ground conditions and the excavation depth H are found to be the most influential parameter for deformation due to excavation. The retaining wall and ground movements seem to be largely independent of the system stiffness of the retaining system. **Figure 2.9** shows the variation of normalized horizontal displacement with the system stiffness of the retaining

structures. The results are then compared with the previous prediction by O'Rourke (1993). Large scatter was observed. A calculated safety factor of about 1 could lead to observed maximum wall displacements w_{max}/H as low as 0.1%, even though the value expected by Clough et al. was about 1% even for the stiffest support system.

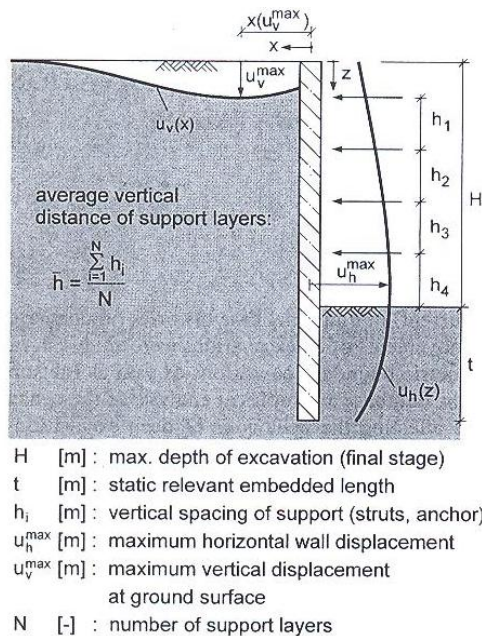


Figure 2.7 Definition of symbols by Moormann (2004)

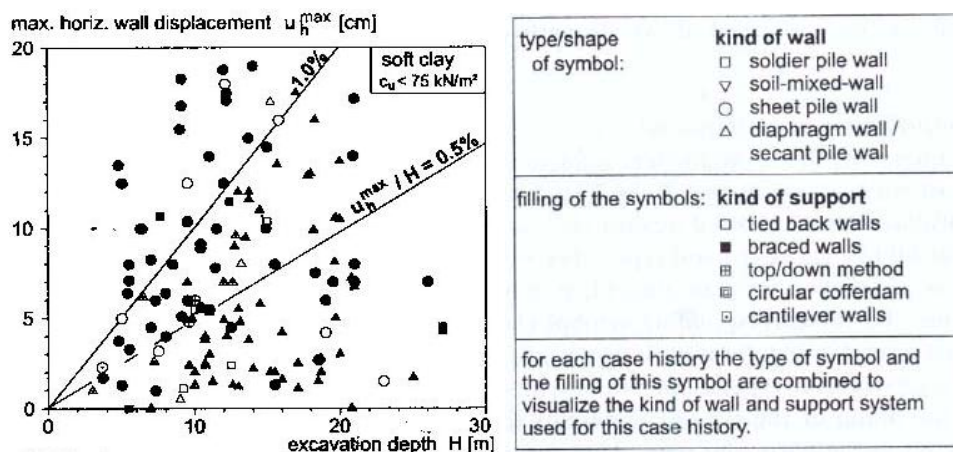


Figure 2.8 Variation of maximum horizontal displacement with excavation depth following Moormann (2004)

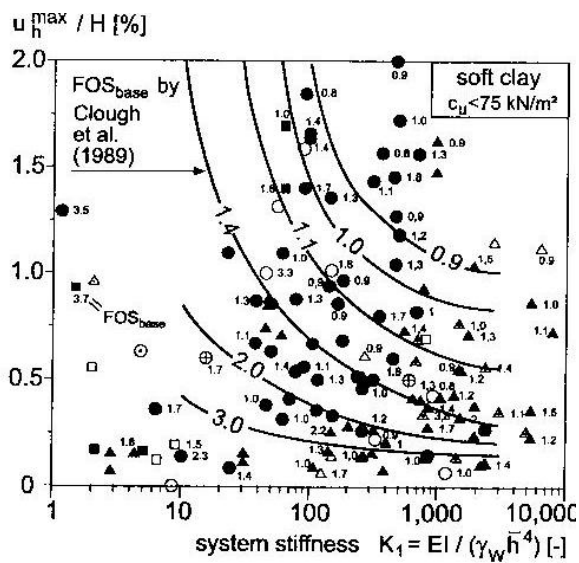


Figure 2.9 Variation of normalized maximum horizontal displacement with system stiffness following Moormann (2004) (For legend see figure 2.8)

2.3.1.11 Stress paths method

The stress path method introduced by Lambe (1967) provides a rational approach to the study of field and laboratory soil behaviour. Since the stability and deformation characteristics of an excavation in heavily over-consolidated material are influenced by stress history and stress state, anticipated field behaviour should be properly informed by laboratory tests for determination of shear strength and stiffness parameters. Ng (1999) agreed that the effective stress paths observed in a triaxial extension test were comparable with that experienced by the soil elements in front of the wall at the interface. Nevertheless, no particular correspondences between the field observations and laboratory undrained compression tests for soil elements behind the wall were found.

Hashash and Whittle (2002) demonstrated the evolution of an arching mechanism through plane strain finite element analyses. With the use of a complicated constitutive MIT-E3 soil model considering strength anisotropy, loading hysteresis and small strain non-linearity, the authors studied the stress changes in both effective and total stress space. It is shown in Figure 2.11(a) that the stress path experienced by a soil element in front of the wall (location of element shown in Figure 2.10) at the final excavation level follows typical path of plane strain passive mode of shearing (1E). On the other hand, the soil elements behind the wall on the retained side followed more complicated stress paths. For soil elements below the excavation level, all the elements shear towards the undrained shear envelope, whereas excavation below the level of the soil elements causes a large rotation of principal stress directions. This produces spiral shear stress paths, showing stress reversal induced by an arching mechanism in the retained soil mass.

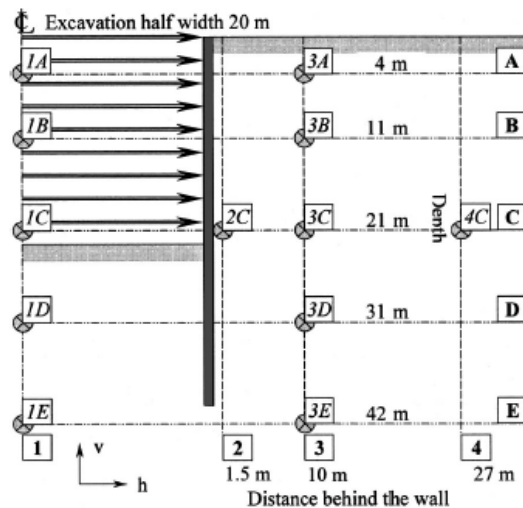
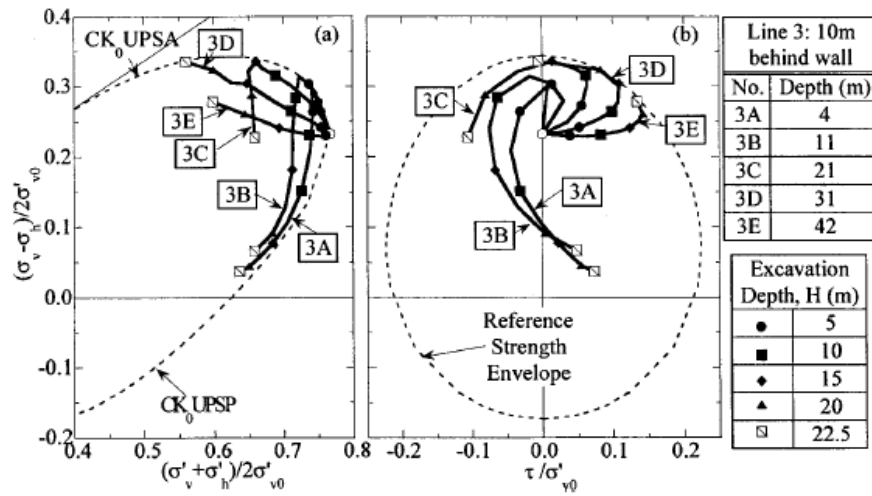
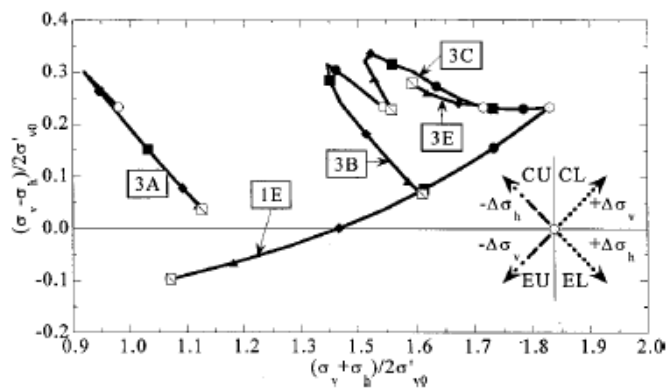


Figure 2.10 Location of soil elements around an excavation



(a)



(b)

Figure 2.11 (a) Effective stress paths and (b) Total stress path of soil elements located 10m behind diaphragm wall

Hashash and Whittle (2002) also plot total stress paths followed by soil elements around deep excavations in Figure 2.11(b). The behaviour of soil elements at the centreline of excavation can be explained by the reduction in vertical total stress with each stage of excavation and the shear induced pore pressures estimated from the effective stress path in the passive shear mode. This generally matches the explanation by Lambe (1970).

Shallow elements in the retained soil initially follow a stress path referred to as compression unloading paths, which correspond to decrease in horizontal total stress at constant vertical total stress. When excavation level goes below the element elevation, there is a stress reversal. The stress experienced is in a mode of extension loading, which refers to an increase in horizontal loading at either constant or reducing vertical total stress. The computed result shows that the stress reversal usually occurs in the range $0.6 \leq H/z \leq 0.85$, where H and z are the excavation depth and depth of the soil element, respectively.

2.4 Numerical studies

Currently, there are no standard design methods for estimating ground movement caused by deep excavations. Existing methods of predicting excavation performance are either based on empirical observations or numerical modelling. Because of the inherent complexities in staged excavations, the empirical methods cannot satisfactorily predict ground movements accurately. The influence of the individual factors cannot be extracted from an empirical database due to the limited number of excavations in similar soil and construction conditions. Although many existing numerical solutions tend to be site-specific and not available to generalized design, numerical methods still represent a viable route to understand the problem of deep excavation induced ground movement. However, the choice of competent constitutive models and model parameters remains a very important question for geotechnical engineers. In the following section, some of the key findings of previous numerical studies are presented.

2.4.1 Effect of supporting structure

Mana and Clough (1981) carried out parametric studies on the effect of wall stiffness and strut spacing, the effect of strut stiffness, and the effect of excavation geometry such as excavation width and depth of the underlying firm layer, the effect of strut preloading and calculation of elastic soil stiffness on excavation induced deformation. Increasing the wall bending stiffness or decreasing strut spacing decreases movement. This effect is more significant when the factor of safety is low. Increasing the strut stiffness reduces movement, though the effect shows diminishing return at very high stiffness. Movement increases as excavation width and depth to an underlying firm layer increases. Use of preloads in the struts reduces movement, although there is a diminishing returns effect at higher preloads. Movement levels are strongly influenced by the soil modulus. Higher modulus leads to smaller movement.

Powrie and Li (1991) have carried out a series of numerical analyses on excavations singly propped at the crest of the retaining wall. The effect of soil, wall and prop stiffness and pre-excavation pressure coefficient were investigated. As the structure investigated was very stiff, so the magnitude of soil and wall movements was governed by the stiffness of the soil rather than that of the wall. A reduction in soil stiffness by a factor of 2 resulted in an increase in wall deformation almost by the same order of magnitude. On the other hand, wall movement was little affected by a 40% reduction in bending stiffness when the thickness of the wall was reduced from 1.5m to 1.25m. The assumed pre-excavation lateral earth pressure significantly affected the prop loads and bending moment though the deformation would not increase much due to the accompanying

increase in soil stiffness. The connection of the base slab to the retaining wall had an important influence on the bending moment profile of the slab. The provision of a quasi-rigid construction joint reduced the bending moment in the wall and the hogging moment at the center of the prop slab, but introduced a sagging moment in the slab at the connection to the wall.

Addenbrooke et al. (2000) carried out 30 nonlinear finite element analyses of undrained deep excavations in stiff clay. A new displacement flexibility number ($\frac{EI}{h^5}$) in multi-propped retaining wall design was introduced by an extension of Rowe's flexibility number (Rowe, 1952). The effect of different initial stress regimes and various values of prop stiffness for the internal supports to the excavation were addressed. The results demonstrated that for a given initial stress regime and prop stiffness, support systems with the same displacement flexibility number gave rise to practically the same maximum lateral wall deflection and the same ground surface displacement profiles on completion of an undrained excavation in stiff clay. The number can be used as a part of the displacement control design scheme. Engineers can vary the wall types and balance the reduced material cost associated with necessary increase in propping levels that obstruct the excavation procedure.

2.4.2 Effect of excavation geometry

The effect of excavation geometry such as excavation width, depth of the firm stratum, the effect of wall stiffness and the effect of wall embedment depth have been carried out by various researchers such as Wong and Broms (1989) and Goh (1994) using the finite

element method. In addition, the use of non-linear elasto-plastic models (e.g. Ou et al.,1993; Ou et al., 1996; Ng et al.,1998) have been used to incorporate the small strain behaviour involved in deep excavation and compared against some case histories.

The most recent and comprehensive one was investigated using highly non-linear model (MIT-E3 model) by the geotechnical research group in MIT led by Professor Andrew Whittle.

Whittle et al. (1993) describe the application of a finite element analysis for modelling the top down construction of a seven-story, underground parking garage at post office square in Boston. The analysis incorporated coupled flow and deformation within real time simulation of construction activities. Predictions were evaluated through comparison with extensive field data, including settlement, wall deflection, and piezometric elevations. Good agreement was obtained but it was emphasized that adequate characterization of engineering properties for the entire soil profile was important.

Hashash and Whittle (1996) performed a series of numerical experiments, using the advanced finite element analyses, which investigated the effects of wall embedment depth, support conditions and stress histories profile on undrained deformation of braced excavations. Anisotropic stress strain of soft clay in undrained shearing, hysteretic behaviour and nonlinear stiffness properties at small shear strain were modelled. Wall length has a minimal effect on the pre-failure deformation for excavations in deep layers of clay, but does have a major effect on the location of failure mechanisms within the soil.

For very long walls, predicted improvements in base stability are offset by large bending moments that can cause flexure failure of the wall itself. The prediction for excavations with continuous bracing show that deep-seated soil movements occurring below grade level represent the principal mechanism controlling wall deflections and surface settlements. Additional basal movements occur as the support spacing increases; however, the importance of this parameter is closely related to the stress history profile of the clay. For OC clay profiles with constant OCRs= 2 and 4, there is not a trend for basal instability, and the computed maximum ground movements are independent of wall length and are linear functions of the excavation depth.

Jen (1998) carried out extensive parametric studies to investigate how predictions of excavation-induced ground movements are related to key parameters such as excavation geometry, support system and soil mass stress history profile. Depth of bedrock was found to be the key parameter affecting the distribution of ground movements, excavation width, excavation depth and uncertainties in the stress history profile and support stiffness were major factors contributing to the magnitude of the displacements. The computed settlement troughs in the retained soil are described as dimensional functions of excavation depth wall length, bedrock depth and soil profile. These equations offer a new approach for geotechnical engineers to preliminary design calculations of ground movement. The hypothetical simulation results are used in later chapters of this dissertation for calibration of the mobilizable strength design method.

Hashash and Whittle (2002) gave a detailed interpretation of stress paths from nonlinear finite element analyses providing new insight to explain the evolution of lateral earth pressure acting on well braced diaphragm walls for deep excavation in clay. The study related the deep-seated soil deformations and the arching of stress within the soil mass. These observations are consistent with mechanisms described elsewhere in the literature and apply to a wide range of soil profiles when the wall is not keyed into an underlying firm stratum. Results showed that lateral earth pressures can exceed the initial stress at elevations above the excavated grade, producing apparent earth pressures higher than those anticipated from empirical design method.

2.5 Laboratory studies

2.5.1 Centrifuge testing

To obtain reliable and controlled data that is essential to better understand the behaviour of soils during the process of excavation, the simulation should be realistic and reproducible. Though the field-instrumented excavation is the most straightforward and effective method, the major obstacle of using field data for mechanical study is the low degree of repeatability. The soil condition and construction sequence are different from one site to another site. This often makes correlation and comparison difficult. Furthermore, it is almost impossible to know the deformation mechanism of soils involved. However, field measurement remains important and should be used as a means of calibration and verification of physical and numerical models.

The most convenient method of analyzing the soil-structure interaction problem is to use the finite element method. It has been proven to be a very powerful tool to model

complex construction process and detailed site specific properties of the structural system. However, the ability to predict ground movement reliably is strongly related to the input parameters relating to material properties. Sensitivity analysis will provide the optimum condition but it is unlikely to be effective in furnishing the kind of database needed for studies unless the results are collated with other type of modelling results.

As an alternative method to simulate the prototype behaviour of an excavation, small-scale centrifuge model has been used. A centrifuge is used to create an artificial acceleration field to simulate the gravitational stress needed to ensure correct modelling of the problem in a small scale model. Centrifuge modelling provides a correctly scaled physical model to enable the simulation of the prototype behaviour of excavation so that it could effectively be used to investigate clearly soil deformation mechanisms during the excavation process. The beauty of the method is that the test can always be repeated and the excavation test can be tested until failure, which is abnormal to happen in the field. Even most finite element programmes will not be executable to such failure stage. Due to these facts, physical modelling in centrifuge has gained acceptance worldwide and it is therefore chosen as the main physical tool for this study.

2.6 Centrifuge modelling of excavation

2.6.1 Method of simulating excavation

To model an excavation in a centrifuge, a method of simulating the soil removal ideally has to be carried out in-flight. Currently, the following four methods are used to model an in-flight excavation in centrifuge:

1. Increasing centrifugal acceleration till failure (Lyndon and Schofield, 1970)

2. Draining of a heavy fluid (Powrie, 1986, Elshafie, 2008)
3. Removal of a bag of material from the excavation area (Azevedo, 1983)
4. An in-flight excavator (Kimura et al., 1993; Loh et al., 1998)

In the first method, soil in the excavation area is initially removed in 1g condition before being subjected to increasing centrifuge acceleration until failure. Although the overall total stress of model ground could be re-produced, the characteristics of the soil would have changed correspondingly to the increased g-level. This method may be suitable for modelling excavation in sand but not clayey soil. For sandy material, the effective stress can develop almost instantaneously with the increase in g-level, dissipation of excess pore pressure occurs almost immediately. However, one should bear in mind that soil behaviour such as soil stiffness and soil strength is always stress-dependent. This method would not give us the right failure mechanism. For clays with a much lower permeability, the consolidation process requires much longer period for the dissipation of excess pore pressure. Nevertheless, this method is the simplest and it can only be used to provide a quick preliminary result on the potential failure pattern of an immediate and undrained excavation for clayey material.

In the second method employed, the key idea is to replace the soil to be excavated by a fluid of identical density. This method was employed by a number of researchers (e.g. Powrie, 1986) working on excavation in heavily consolidated clay. The main setback of this method is that for a fluid, the coefficient of lateral stress is always one. For a heavily over-consolidated soil, the K is also expected to approach 1 and thus, this method is

considered a reasonable approximation to the excavation in such a soil. However, K_o value of 1 is not typical for normally consolidated clays, which falls within the range of 0.55 to 0.65 (Kimura et al., 1993). Even then, it is recognized that during the excavation, the K_o on the passive side still remains as 1, which is not consistent with what happen in the field where the K_o value will approach K_p .

The third method, soil bags were placed at the zone to be excavated and were removed during the excavation process. This method has advantage over the first two methods, as the modelling of stress history of the soil model is more realistic. Since the soil used in the bags is similar to the soil model, the coefficient of lateral stress is consistent. Nonetheless, the interaction behaviour between the interfaces of soil bags with the retaining wall would be very difficult to quantify.

Therefore, the first three methods cannot satisfactorily model a proper excavation in clayey soil in the centrifuge. This is because the actual excavation has not been carried out and the process of removing soil is not simulated properly in each case. In view of the problem, the forth method should be developed. A small scale robotic excavator is developed to remove the soil in-flight in the centrifuge.

A new 2D-servo actuator, which has two degree of freedom, was designed in the workshop of Engineering Department, Cambridge University. In vertical and horizontal directions, the actuator can apply a maximum load of 10kN with a maximum speed of 10mm/s at an in-flight acceleration up to 100g. The stroke of the equipment should allow

a maximum vertical displacement of 300mm and a maximum horizontal displacement of 500mm, monitored by encoders. The use of a 2D actuator to create an excavation and a hydraulic prop system to support retaining walls during excavation are detailed in Chapter 3.

2.6.2 Centrifuge modeling of propped retaining walls

Bolton and Stewart(1994) investigated the stability and serviceability of propped diaphragm walls in stiff clay, firstly just after excavation, secondly when long term ground water seepage developed and thirdly when the water table was raised. The work focused on the understanding of swelling clays in relation to swelling strain path tests. The stress path followed by kaolin in one-dimensional unloading was idealized as bilinear, which facilitated hand calculations for horizontal effective stress on a diaphragm wall propped at excavation level, providing a conservative method for checking of structural serviceability.

2.6.3 Centrifuge modeling of doubly propped wall

Kimura et al. (1994) reported centrifuge experiments on unsupported excavations, and excavations with sheet pile walls, with or without ties, in NC and OC clays. An in-flight excavator was used to simulate the excavation process. Deformations of the clay, pore water pressures and earth pressures on the wall, were measured. The ratio $\left(\frac{\sigma_h - \sigma_v}{2c_u} \right)$ was introduced to represent the extent of the mobilization of shearing strength in undrained clay. The active failure state was achieved at smaller strain than that of the passive side. In addition, a smaller mobilization of earth pressure on the passive side was

observed due to anisotropy. Negative pore water pressures induced near the retaining wall were partly cancelled by positive pore pressures generated by shear deformations of clay in the area.

Richards and Powrie (1998) presented centrifuge model testing of doubly propped embedded retaining walls in over-consolidated kaolin clay. The influence of groundwater regime, pre-excavation earth pressure coefficient, embedment depth and propping sequence on the ground movements, bending moments and prop-loads were investigated. Excavation of soil was simulated by draining heavy fluid (Zinc chloride solution) with a relative density of 1768kg/m^3 . In the reconsolidation process, some inevitable imperfections were found, such as the wall having been installed fractionally out of plumb and shear stresses induced on sliding the wall into place. So the authors restricted to discussing bending moments generated prior to excavation and changes in bending moment. Other perceived problems included the relatively low stiffness of reconstituted kaolin clay compared with natural clays, the reduced effective stress associated with a high groundwater table, and the time required for completing excavation. The maximum bending moment increased with depth of wall embedment. A delay of up to a year (at prototype scale) occurred after the end of excavation before the bottom prop load had increased to its maximum value. No advantage was found by increasing wall embedment in terms of limiting soil surface settlement has not been demonstrated. This is consistent with finite element results by Simpson (1992), who showed that shortening of the wall reduced bending moments without increasing soil settlement significantly. The major advantage of increasing embedment depth is that the load on the lowest prop reduces as

the resistance offered by the soil increases. Richard and Powrie also showed that the effect of lowering the groundwater behind the retaining wall was to reduce the bending moment and prop loads significantly. The maximum bending moments and prop loads in general increase with the pre-excavation lateral earth pressure coefficient above the excavated surface.

Takemura et al. (1999) investigated a vertical excavation in normally consolidated soft clay in which the construction sequence of a doubly tied wall for an open excavation was simulated properly in-flight with an excavator. Settlement of the ground surface, earth pressure on the wall strains along the wall and pore water pressure in the ground were measured during the test. The effect of propping and embedment of the retaining wall into the bottom sand layer on the behaviour of the wall and ground were carefully studied. Only 1m of embedment into the bottom sand could increase significantly the stability of the excavation. Propping can reduce settlement; however, it is very difficult to recover settlement once it has occurred by increasing the strutting force. Hysteresis and non-linear behaviour of soil are considered to be the main reasons for such irrecoverable deformations.

2.6.4 Centrifuge modeling of retaining wall with soil improvement scheme

Lim (2003) has carried out a series of centrifuge tests on excavations to investigate the composite ground resistance provided to a retaining wall when different configurations of soil improvement are applied to the soil on the excavated side below the formation level. The effect of the stiffness of the improved soil layer, the effect of a gap of untreated soil

between a diaphragm wall and an improved soil layer, and the effect of using a soil berm as a temporary support, were studied. The stiffness of an improved soil 'strut' is the key parameter for design. Nonetheless, a stiffer improved soil layer can result in a higher bending moment in the retaining wall. The existence of a gap between the retaining wall and the improved soil layer significantly increases the ground movement in the initial stage of excavation, though the ground deformation was limited eventually. The untreated soil in the gap significantly decreased the overall stiffness of the whole improved soil layer. Soil berms were an effective means to support a diaphragm wall during excavation especially for an excavation with a large width. Nevertheless, the way the berm transfers the lateral force from the retaining wall to the surrounding soil, which is by a combination of skin friction and end bearing, is totally different from the behavior of a strut. The berm stiffness was not important in controlling the deformation of the wall. However, catastrophic failure could happen if the berm was not designed properly.

McNamara and Taylor (2002) carried out a series of centrifuge tests to investigate the effectiveness of piles in reducing vertical and horizontal ground movements behind an embedded retaining wall in soft clay. Top-down basement construction with different pile layouts was simulated. At the end of excavation, the reduction of vertical settlement behind the retaining wall achieved by 1 and 2 rows of piles behind the wall was about 40% and 60%, respectively, in the short term. In the long term, 2 rows of piles would reduce the settlement more efficiently. The use of 5 piles in a row can reduce base heave by about 50% even without introduction of the heave reduction piles, while the use of 10 piles in 2 rows can reduce the movement by 70%. Horizontal soil displacement contours

show a general reduction in movement throughout the model. Reductions in settlement at the retained surface were most significant close to the retaining wall but less apparent further away.

2.7 Earth pressure measurement

It is well known that earth pressure remains one of the most difficult physical parameters to measure during physical testing. The sensitivity of stress conditions in soil is without doubt owing to the non-linearity of soil behaviour as a result of stress history and soil micro structures. Various factors affecting the measurement of soil pressure have been studied by Weiler and Kulhawy(1982) and grouped into 3 categories, namely:

1. Stress cell properties and geometry;
2. Properties of the soil in which the cell is instrumented;
3. Environmental conditions

The performance of an earth pressure sensor is indicated by the cell action factor (CAF), a concept introduced by Taylor(1947) to quantify the measurement error (Clayton and Bica, 1993). The CAF is the ratio of the value of normal stress measured by the cell and the value that would have been applied in its absence. A CAF of nearly 1 indicates an more accurate measurement of normal stress. A good system would also have a linear calibration characteristic, without inducing stress redistribution within the material. Arching of soil stress over the diaphragm of the pressure sensor is the main cause of earth pressure sensors under-registering the soil pressure. Trollope and Lee(1961) and Clayton and Bica(1993) ascribed this to the relative flexibility of the diaphragm. A design

criterion was introduced for the satisfactory performance of an earth pressure cell to be the ratio of the diameter of the diaphragm, $2R$, to the displacement δ at the centre shall be greater than some threshold value. Trollope and Lee (1961) reported that as long as the threshold value exceeded 2000, a sensibly linear curve can be obtained. Clayton and Bica also adopted a value ranging from 2000 to 5000. In addition, the accuracy of the stress measurement also depends on the stiffness of the granular material. Calibration tests conducted by Clayton and Bica (1993) showed that high modulus materials such as dense coarse sand produced the lowest measured values of CAF. The CAF of a cell that would be considered adequate for soft clay could be as low as 0.6 if the cell was used in dense coarse sand.

With a view to improving the design of pressure sensors for soil, Askegaard (1961) proposed a definition of flexibility ratio, F , which accounted for the effect of the stiffness of the pressure cell diaphragm and the granular material. F was defined as:

$$F = \frac{E_{soil} R^3}{E_{cell} t^3} \quad (2.1)$$

Where E_{soil} is the Young's Modulus of the soil

E_{cell} is the Young's Modulus of the cell

R is the radius of the diaphragm;

t is the thickness of the diaphragm

The CAF value increases with increasing diaphragm stiffness and decreases with increasing soil stiffness. To achieve a more accurate measurement, soil stiffness values should be evaluated by the use of local strain instrumentation and the construction of an appropriate stress path.

In later chapters the performance of an Entran EPL-series miniature pressure cell in soft clay will be studied.

2.8 Image processing technique- Particle Image Velocimetry (PIV)

PIV began as a velocity-measuring procedure originally developed in the field of experimental fluid mechanics, as reviewed by Adrian (1991). A MATLAB module was written by White and Take (2002) to implement PIV technology for measuring displacement fields for geotechnical testing purposes. GeoPIV uses the principles of PIV to gather displacement data from a sequence of digital images captured during geotechnical model and element tests. GeoPIV is a MATLAB module, which runs at the MATLAB command line. The development and performance of the software are described in detail by White (2002) and Take (2002). Concise details are presented in White *et al.* (2001a, 2001b and 2003).

The principles of PIV analysis are summarized in [Figure 2.12](#). The analysis process used in GeoPIV is indicated by the flowchart shown in [Figure 2.13](#). PIV operates by tracking the texture (i.e. the spatial variation of brightness) within an image of soil through a series of images. The initial image is divided up into a mesh of PIV test patches. Consider a single test patch, located at coordinates (u, v) in image 1 ([Figure 2.12](#)). To find the displaced location of this patch in a subsequent image, the following operation is carried out. The correlation between the patch extracted from image 1 (time = t_1) and a larger patch from the same part of image 2 (time = t_2) is evaluated. The location at which the

highest correlation is found indicates the displaced position of the patch (u_2, v_2). The location of the correlation peak is established to sub-pixel precision by fitting a bi-cubic interpolation around the highest integer peak. This operation is repeated for the entire mesh of patches within the image, and then repeated for each image within the series, to produce complete trajectories of each test patch.

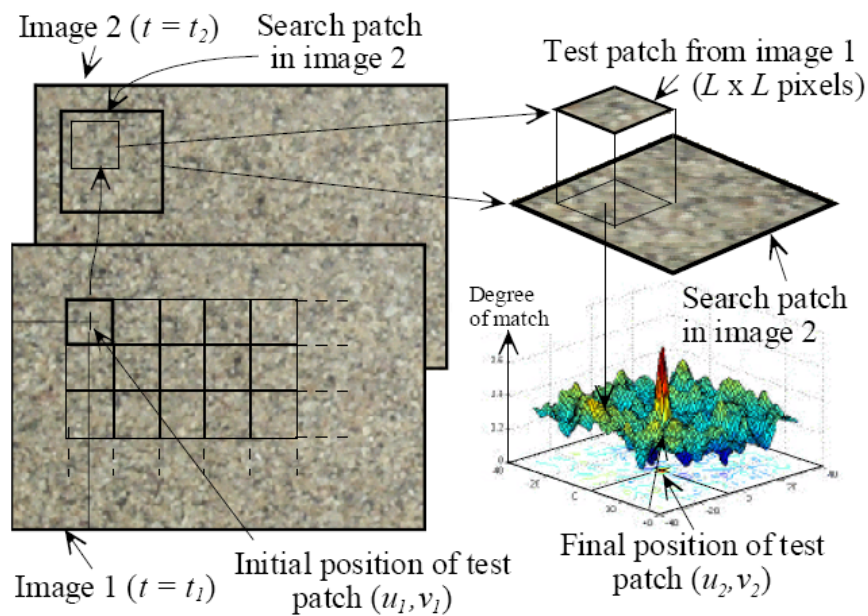


Figure 2.12 Principle of PIV analyses

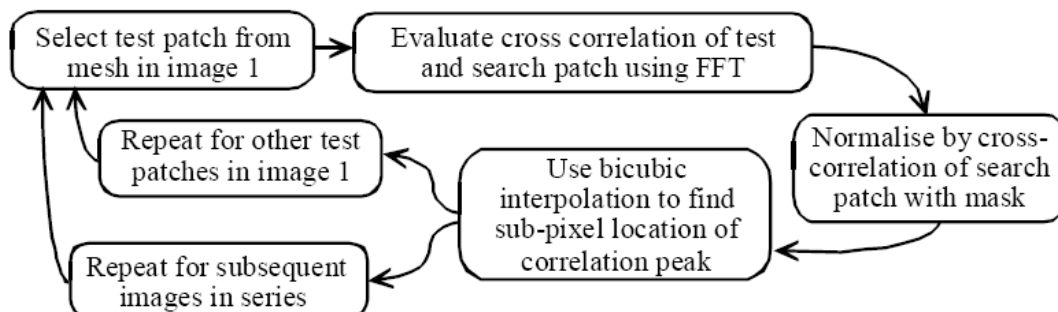


Figure 2.13 Flowchart of the GeoPIV analysis procedure

2.9 Mobilizable strength design (MSD)

The development of mobilizable strength design emerged from previous advances in the concept of ‘mobilized strength’ to predict displacement: (Milligan and Bransby,1975; Bolton and Powrie,1988; Bolton et al. 1989,1990a, 1990b). The method of MSD was introduced to achieve a general unified simple design methodology, which could satisfy both safety and serviceability in some simple steps of calculation, as an alternative to the standard limit state design methodology which separate design issues into stability problems and serviceability problems. In the MSD method, the design strength limiting the deformation and satisfying equilibrium is selected according to actual stress-strain data without the use of empirical factors. Basically, two concepts of the approach are:

1. Simple deformation mechanisms are used, which should represent the working state of the geotechnical problem. The mechanisms represent the equilibrium and displacement of the various soil bodies, especially at their junction with the superstructure.
2. Raw stress-strain data from soil tests on undisturbed samples taken from representative elements are used directly to link stress and displacements under working conditions. The use of constitutive laws and soil parameters are avoided.

The approach has been successfully implemented by Osman and Bolton on geotechnical problems such as shallow foundations, cantilever retaining walls, tunneling induced displacements and also deep excavations inducing wall displacements and ground deformation. This approach has the advantage that one can use a single stress-strain curve from a single soil test, together with a simple hand calculation, to estimate both stability and soil deformation without the need for complex computer simulation.

The MSD approach firstly requires the engineer to figure out the working states of the geotechnical problem by considering a simple mechanism which can represent both the equilibrium and displacements of the soil, dealing approximately with soil-structure interaction. Secondly, analysis of the deformation mechanism leads to a relationship between the average strain mobilized in the soil and the boundary displacements. Thirdly, the mobilized average shear strength can be found from an equilibrium analysis using a permissible stress field, or from an upper bound style of calculation balancing work and energies. Fourthly, the location of a representative soil element is selected considering the stress history, soil profile and geological history. Fifthly, the stress strain relationships are obtained from conventional laboratory tests on undisturbed soil samples taken from representative locations. The soil tests should shear the soil in direction consistent with the mechanism. Finally, the shear strength mobilized in the soil corresponding to the average mobilized strength calculated is set against the stress strain curve obtained in order to obtain the representative soil strain and thus the boundary displacement for the mechanism.

Osman and Bolton (2004) suggested that for the deep excavation problem the total wall deformation could be taken as the sum of the cantilever movement and the bulging movement. The method suggested by Osman and Bolton (2004) could be used for estimation of cantilever movement at early stage of an excavation. This considered the lateral earth pressure distribution for an embedded cantilever wall in equilibrium whilst rotating with respect to a point located distance above the toe of the wall in undrained

conditions. A simple mobilized strength ratio is introduced to characterize the degree of mobilization of the average undrained shear strength throughout the soil. Using horizontal force and moment equilibrium equations, the position of the pivot point and the mobilized strength ratio are obtained. Then, a mobilized strain value is read off from a suitable stress strain curve for a soil element at a representative depth for the mechanism. Taking the kinematics from a simple admissible mechanism for undrained condition, the mobilized strain value is converted to the rotation angle of the wall and thus the lateral displacement of wall. Similarly, the bulging movement is calculated by considering a new base heave plastic mechanism and by using the virtual work principle. The energy dissipated by shearing balanced the virtual loss in potential energy of the soil. A mobilized strength ratio can then be calculated. The mobilized shear strain is read off from the stress strain curve of a representative element in the mechanism. The deformation is estimated using the relationship between the boundary displacement and the average mobilized shear strain. The solution compares well with some numerical simulation using the advanced non-linear MIT-E3 model, and with some field data. However, the solution ignored the structural energy within the support system, which is generally considered to be an important factor determining ground deformation. In addition, the solution considers the total energy terms starting from the beginning of excavation so that it does not consider the progressive accumulation of mobilized shear strain at different depths in the ground. Only a rough estimation would be made of the effects of construction sequence, therefore, in view of the short comings, a more precise approach can be developed.

2.10 Summary and discussion

In the case of base heave in braced excavations, plastic solutions were originally derived from slip-line fields based on the method of characteristics. Such solutions comprise both slip surfaces, and plastic fans which distribute plastic strains over a finite zone in the shape of a sector of a circle. Notwithstanding these zones of disturbed strain, the additional presence of slip surfaces still restricts the application of these solutions to the prediction of failure. Furthermore, no such solution can be regarded automatically as an accurate predictor of failure, notwithstanding their apparent sophistication. The contribution of wall friction and wall bending remains controversial. Their use in practice can only be justified following back-analysis of actual failures, whether in the field or the laboratory.

Terzaghi (1943) suggested a mechanism consisting of a soil column outside the excavation which creates a bearing capacity failure. The failure is resisted by the weight of a corresponding soil column inside the excavation and also by adhesion acting along the vertical edges of the mechanism. Bjerrum and Eide (1956) assumed that the base of the excavation could be treated as a negatively loaded perfectly smooth footing. The bearing capacity factors proposed by Skempton (1951) are used directly in the stability calculations and are taken as stability numbers, $N = \gamma H/c_u$. O'Rourke (1993) further modified the basal stability calculations of Bjerrum and Eides' approach to include flexure of the wall below the excavation level. It was assumed that the embedded depth of the wall does not change the geometry of the basal failure mechanism. However, an increase in stability was anticipated due to the elastic strain energy stored in flexure. This

gave stability numbers that were functions of the yield moment and assumed boundary conditions at the base of the wall. Ukritchon et al. (2003) used numerical limit analysis to calculate the stability of braced excavations. Upper and lower bound formulations are presented based on Sloan and Kleeman (1995) and Sloan (1988), respectively. The technique calculates upper bound and lower bound estimates of collapse loads numerically, by linear programming, while spatial discretization and interpolation of the field variables are calculated using the finite element method. No failure mechanism needs to be assumed and failure both of the soil and the wall are taken care of. However, both soil and wall are again assumed to be rigid perfectly plastic so the failure mechanism includes a plastic hinge at the lowest level of support.

All these collapse limit analyses provide useful guidance on the possible geometry of plastic deformation mechanisms for service conditions. But the key requirement for MSD mechanisms is that displacement discontinuities (slip surfaces) must be avoided entirely. In that way, small but finite ground displacements are associated at every internal point with small but finite strains. Most importantly, the analytical solutions fail to predict performance of the support system.

Two important empirical databases of worldwide case histories by Long (2000) and Moormann (2004) showed the rather limited efficacy of current ways of presenting wall deformation data. The plot of maximum horizontal wall displacement against excavation depth demonstrated that the data scattered over a wide range. This once again confirmed that there was no simple linear dependency of horizontal wall displacement on excavation

depth. However, the method did show that the stiffness of the support system had a significant influence on the observed performance of the excavation. Following Clough (1989), Long(2000) and Moormann (2004) plotted the wall displacement normalized with excavation depth against system stiffness defined as ($\eta = \frac{EI}{\lambda_w h^4}$). Again the data for the cases scatters in a wide range with no simple dependency of the wall displacement on the system stiffness, although the chart suggested by Clough et al.(1989) may be roughly consistent with regard to the dual influence of the system stiffness and factor of safety against base heave. Apparently, the factor of safety against base heave or stability number is insignificant to quantify ground movements due to deep excavation, even when the wall stiffness is accounted for. Non-linear soil stiffness should additionally be accounted for. This is attempted in Chapter 5.

Existing methods of predicting excavation performance were based on numerical modelling. Because of the inherent complexities in staged excavation, the empirical methods cannot satisfactorily predict ground movement accurately. The influence of the individual factors could not be extracted from early databases due to the limited number of excavations in similar soil and construction conditions. Existing numerical solutions are generally site specific and not available to generalized design. Futhermore, the choice of constitutive models and model parameters remains a very important question for geotechnical engineer. Non-linear elastic plastic models usually predict wider and shallower settlement troughs than those found in the field. And the magnitude of ground movement is highly dependent on the choice of soil modulus.

The development of advanced soil models such as MIT-E3 model by the research group led by Prof. Whittle allows consideration of small strain non-linearity, soil anisotropy and the hysteretic behaviour associated with reversal of load paths. Hashash and Whittle (1996) and Jen(1998) performed a series of numerical experiments, using MIT-E3 in nonlinear finite element analyses, investigating the effects of wall embedment depth, support conditions and stress history profile on the undrained deformation of braced excavations. Promising validations and applications were made through case studies. However, the usage of the model is costly since many input parameters are required.

The MSD method has been applied to deep excavation problem by Osman and Bolton (2004) and this is very economical on input data requirements. However, the solution ignored the structural energy absorbed by the support system, which is considered to be an important factor of determining ground deformation. In addition, the solution did not correctly consider the accumulation of mobilized shear strain at different depths and the effect of sequential construction. This presented a research opportunity; an account of which can be found in Chapter 5.

New theories require validations and Chapter 3 will set out the details of centrifuge model simulations from which deformation mechanism can be obtained, and against which an extended version of MSD will be compounded.

Previous researchers drained heavy fluid on the excavation side to model vertical and lateral stress relief on centrifuges. However, this can not satisfactorily model earth

pressure varying during a real excavation in the centrifuge. In view of this problem, a new method had to be developed. In the past, other types of in-flight excavator have been developed for modeling open cuttings with retaining walls with or without ties (Loh et al.,1998; Takamura et al., 1999). These excavators produced very interesting results on the mechanical behaviour of an excavation. Nevertheless, the accurate physical modeling of construction sequences such as provision of props and wall installation needed to be accomplished. This provided a further research challenge, assisted by the recent development of a two-dimensional robotic manipulator for the Schofield Centre beam centrifuge. This development work will be described in Chapter 3 and the experimental results will be shown in Chapter 4.

CHAPTER 3

DEVELOPMENT OF A NEW APPARATUS AND TESTING PROCEDURE

3.1 Introduction

To obtain the reliable data that is essential to better understand the behavior of soils during the process of excavation, the simulation of that process should be realistic and reproducible. Although the instrumentation of actual excavations in the field is authoritative for the particular structure concerned, a major drawback to using field data in a scientific study is the difficulty of accurately characterizing the soils that are present. Soil conditions and construction sequence are different from site to site, and no experiment can ever be repeated. Furthermore, it would require an extraordinary array of inclinometers and extensometers to define the complete deformation mechanism of the ground. However, field measurements remain important as a means of calibration and verification of any calculations that emerge from physical and numerical model studies.

The most widely attempted method of assessing soil-structure interaction problems is by continuum numerical analysis, using finite element or finite difference computer programs. These offer powerful tools to model complex construction processes, with a chosen structural system progressively put in place within a detailed ground

stratigraphy. However, the ability to predict ground movements reliably is wholly dictated by the input of representative parameters for the various soils, and existing numerical codes are extremely demanding of such prior information. A more practical alternative is to discover simplified mechanisms of behavior, and to use those in decision-making. Such mechanisms universally form the basis of judgments that engineers make regarding possible collapse, but there has been relatively little information available on mechanisms that can be used to predict deformations under working conditions. The first step must be to observe them.

Small-scale centrifuge models can be used to simulate the prototype behavior of an excavation in soil. A centrifugal acceleration field is used in a small scale model to match the stresses induced by gravity in the prototype. The principal challenges are to design a test package to simulate the construction sequence of a braced excavation in the field, so that a cross-section can be used for the remote measurement of resulting ground movements. The advantage is that tests can be repeated with planned variations, and that the model can be observed continuously from the occurrence of small deformations up to complete collapse, which is not generally allowed to happen in the field.

To model an excavation in a centrifuge, some method must be found of simulating soil removal in flight. There are four typical methods for modeling deep excavation problem.

1. Increasing centrifugal acceleration until failure (Lyndon and Schofield, 1970).
2. Draining of a heavy fluid (Powrie, 1986; Bolton and Powrie, 1988).
3. Removal of a bag of material from the excavation area (Azevedo, 1983).

4. An in-flight excavator (Kimura et al., 1993; Loh et al., 1998; Takemura et al., 1999).

The first method involves removing soil in the excavation area during model-making at 1g, before the model is subjected to increasing centrifuge acceleration up to failure. Although the total vertical stress in a prototype can ultimately be reproduced, the scale factor continually changes with the increasing gravitational field, and it is not possible to simulate the progressive ground movements. For the second method, the key idea is to replace the soil to be excavated by a fluid of identical density retained in a rubber bag. The main drawback of simulation using a fluid is that the coefficient of lateral stress (K) is always one. This may approximate earth pressures adjacent to a cast-in-place wall (Richards, 2006), but it would not be an appropriate technique for sheet pile walls inserted into clays, whether normally consolidated ($K_o < 1$) or heavily overconsolidated ($K_o > 1$) so that pre-excavation bending moments induced on the wall and lateral displacement of the wall are inevitable. Even so it must be recognized that, during the excavation, K within the zone of future excavation will remain at unity in a heavy fluid, which is not consistent with what happens in the field where K below the excavation level may approach the passive earth pressure coefficient K_p . Thus, the technique of using liquid does not correctly reproduce the prototype deformations and stresses with respect to the progress of excavation. For the third method, soil bags were placed in the zone to be excavated and were removed during the excavation process. This has one advantage over the first two methods, as the modeling of stress history is more realistic. Since the soil used in the bags is similar to the soil in the rest of the model, the initial coefficient of lateral stress should be consistent. Nonetheless, the interaction between the interfaces of the soil bags and the retaining wall would be very difficult to quantify.

Therefore, the three methods cannot satisfactorily model a field excavation in clay soil in the centrifuge because the process of soil removal has not correctly been simulated. In view of this, in-flight excavation and bracing methods should be developed. Previous types of in-flight excavator modeled open cuttings with retaining walls, with or without ties that were placed initially at 1g: (Loh et al.,1998; Takamura et al., 1999). These excavators produced interesting results, but the modeling of more realistic construction sequences that include wall and prop installation in a single centrifuge flight remains a challenge for physical modelers.

3.2 In-flight excavator

A new two-axis servo actuator was designed for the Turner Beam Centrifuge at Cambridge University (Haigh et al., 2010). The actuator can apply a maximum load of 10kN in analogue vertical and horizontal directions, with a maximum speed of 5mm/s, at an in-flight acceleration up to 100g. The stroke of the equipment allows a maximum vertical displacement of 300mm and a maximum horizontal displacement of 500mm, monitored by encoders. The characteristics of the 2D servo actuator are summarized in **Table 3.1**. **Figure 3.1** shows the assembled excavator. The two DC servo-controlled motor-tacho units drive step-down gearboxes to increase the torque. Ball screws are used to convert these rotary motions into linear vertical and horizontal movements. The vertical screw system drives a ball nut carrier plate which slides along vertical guide rails, while the horizontal screw system shifts the whole actuator housing along horizontal guide rails. The whole frame was designed to be stiff enough to ensure good control of movements.

Table 3.1 Capability of the two axis actuator

Maximum operating g-level	100 g
---------------------------	-------

Actuator mass	150 kg
Horizontal Displacement	500 mm
Maximum horizontal maximum force	10 kN
Horizontal maximum velocity	5 mm/s
Vertical displacement	300 mm
Vertical maximum force	10 kN
Vertical maximum velocity	5 mm/s

Table 3.2 Properties of fraction E sand (Haigh and Madabhushi, 2002)

Properties	Value
Minimum void ratio	0.613
Maximum void ratio	1.014
Minimum dry unit weight	12.9 kN/m ³
Maximum dry unit weight	16.1 kN/m ³
Specific gravity of solids	2.65
D ₁₀	95µm
D ₅₀	140µm
D ₉₀	150µm

Table 3.3 Mineralogy and properties of Speswhite Kaolin

Mineralogy/ Properties	Value
SiO ₂	47%
Al ₂ O ₃	38%
300 mesh residue	0.02% maximum
≥ 10mm	0.5% maximum
≤ 2um	80±3%
Specific gravity	2.6
Surface area	14m ² /g
pH	5.0±0.5
Oil absorption	42g/100g
Water soluble salts content	0.2%

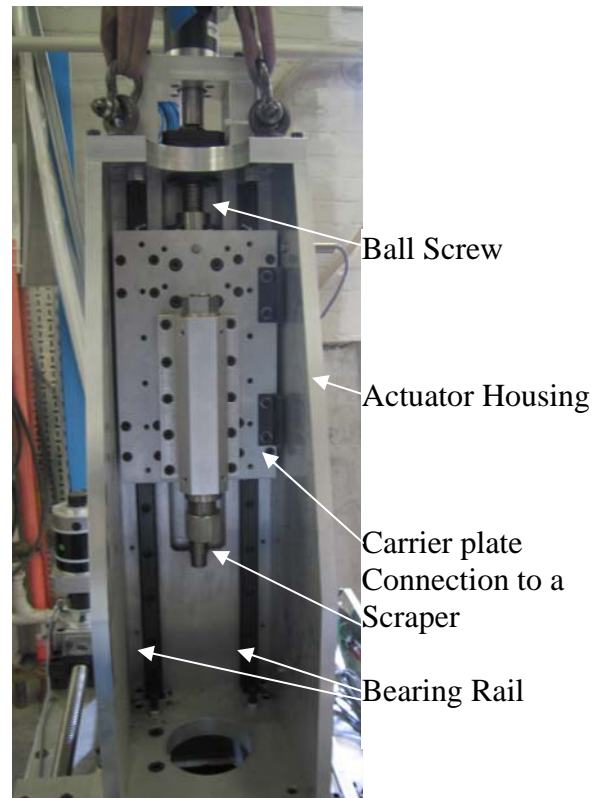


Figure 3.1 In-Flight Excavator

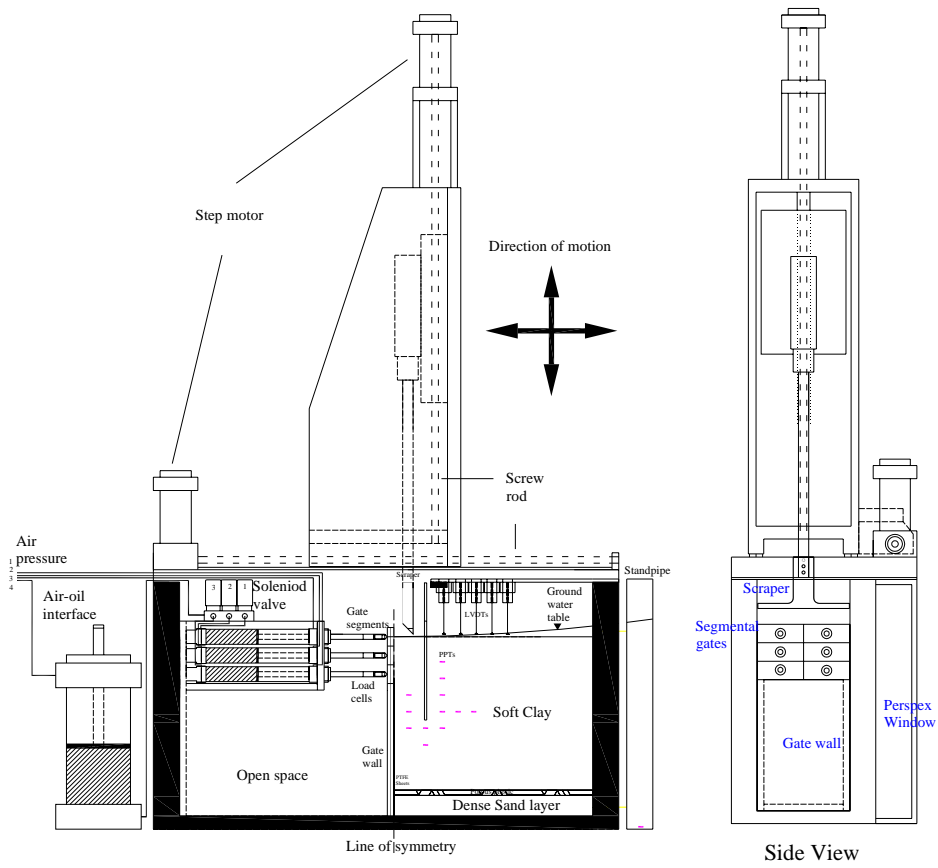


Figure 3.2 Schematic diagram of experimental setup with in-flight excavator

3.3 Experimental setup

Figure 3.2 shows the experimental setup of the present study. The rectangular model container is made of aluminum alloy with internal dimensions 790mm in length, 180mm in width and 470mm in depth. The front face of the container consists of a Perspex window, which enables the whole testing process to be monitored by cameras mounted in front. The back of the container has holes at specific locations with respect to the position of the retaining wall, for installation of pore pressure transducers and the provision of drainage. The servo actuator stands above the rim of the model container. The carrier plate of the actuator is connected through a screw fitting to an inverted T-shaped scraper which performs in-flight excavation at 60g.

Instrumentation comprising pore pressure transducers in the soil, earth pressure cells on the retaining wall, bending moment strain gauges on the wall, load cells on the props, laser sensors and linear variable transformers for displacement measurements were installed. Digital cameras were mounted in front of the Perspex window and LED arrays were situated to illuminate the clay cross-section without causing glare, or shadows.

3.4 Cylinder support system and gate system

The vertical plane through the center of an excavation can be regarded as a plane of symmetry. A “gate wall” (as shown in Figure 3.3) aims to represent this plane of symmetry, so that only one side of the excavation needs to be modeled. PTFE sheets were glued on the gate wall to minimize vertical friction, and steps are also taken to prevent its lateral movement prior to excavation.

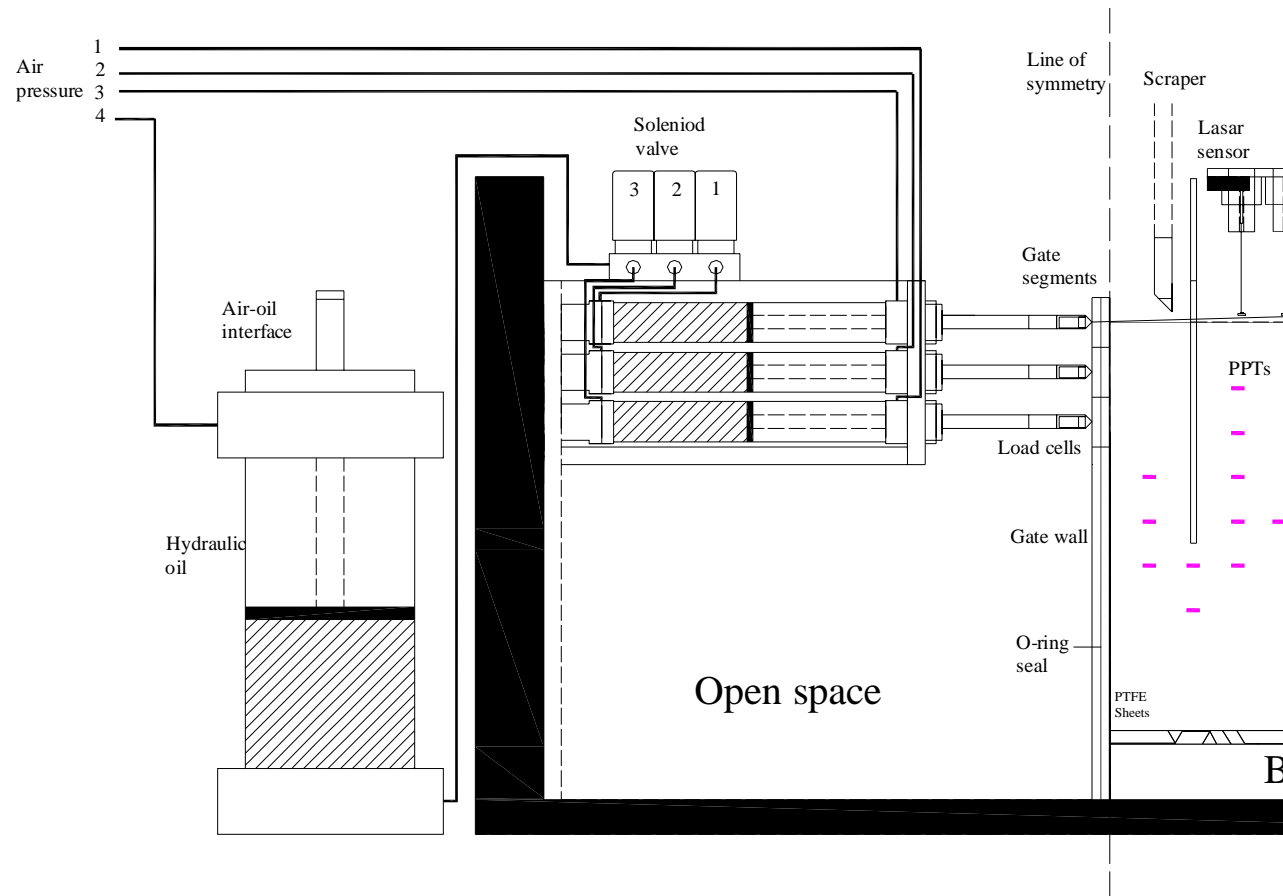


Figure 3.3 General arrangements of main apparatus

A prop installation sub-system was designed to provide in-flight support, initially to the gate wall and ultimately to the retaining wall, during the experiment. Three pairs of cylinders (FestoDSNU 25-125) are mounted on a rigid support frame and positioned at 0 mm, 36 mm and 72 mm below the initial clay surface. Props are driven via pistons in the cylinders which are actuated through a hydraulic/pneumatic control system. Backward pressure inlets are connected to a compressed air source for retreating the cylinders. Forward pressure inlets are connected to an oil pressure reservoir so that they can provide a similar propping force at each excavation level. Each level of props is controlled individually through solenoid valves. The oil supply manifold is connected to an air-oil interface through a needle valve which is used to control the rate of advance of each pair of props, in sequence. Compressed air acting on the front face of the pistons is transmitted from an external compressor and regulator, and is supplied to the centrifuge through a pneumatic coupling.

Before the experiment, the system is saturated with hydraulic oil. The prop stiffness is obtained by conducting axial-load displacement tests in a loading rig. The target stiffness of a fully-saturated prop is found to be about 1.66kN/mm. To begin with, all pressure sources are at atmospheric pressure. All solenoid valves are closed. The advancing of a pair of props is achieved by increasing air pressure at the air-oil interface and activating the solenoid valve for that specific pair of props. The propping force can be controlled by adjusting the air pressure at the air-oil interface. That solenoid valve is then closed and the associated props remain stiff due to the incompressibility of hydraulic oil. On the other hand, retreating the cylinders requires the reduction of air pressure at the air-oil interface and the increase in air pressure at the backward pressure inlet of the cylinders.

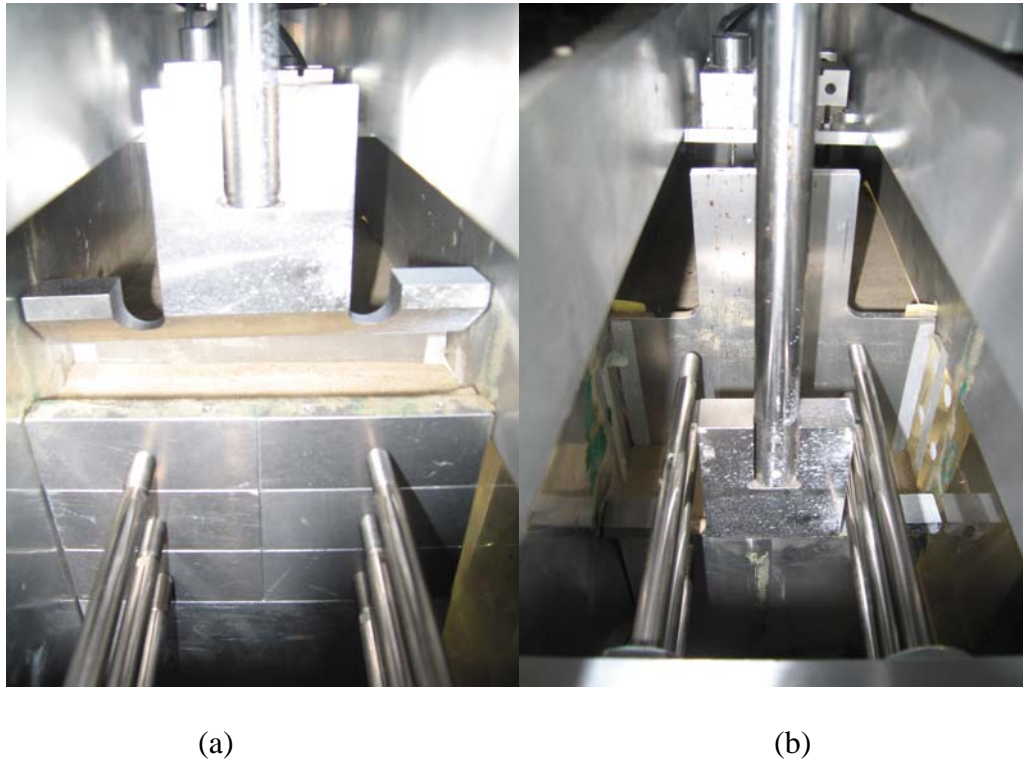


Figure 3.4 Propping and gate system (a) before and (b) after excavation

Figure 3.4 shows the gate system. At the start of the experiment, three pairs of sacrificial gates, each 36mm high, sit on the top of the gate wall. They act as a support to retain the soil to be excavated. The gates are temporarily supported by the pairs of cylinders throughout the initial reconsolidation stage before excavation. The forces required to support the gate segments are monitored by axial load cells attached at the end of each prop. **Figure 3.5** shows the sequence of the first excavation stage. At the start of excavation, the first pair of cylinders is retracted so that the first layer of gates is in an unstable condition and is easily knocked down by the scraper of the in-flight excavator. The in-flight excavator then makes a 4 mm cut into the soil, which is scraped off into the open space inside the cylinder support system. The scraper then returns to its initial position and makes another 4 mm cut, repeating until the excavation level reaches the top of the second level of gates. At that moment, the first level of props is pressurized again to support the retaining wall. The prop force

required can be adjusted by looking at the readings given by the prop load cells. This completes the first stage of excavation. As the scraper is specially made in an inverted T-shape, it can continue scraping below the first pair of props. The second and third stages of excavation can therefore proceed by repeating the same steps carried out for the first level.

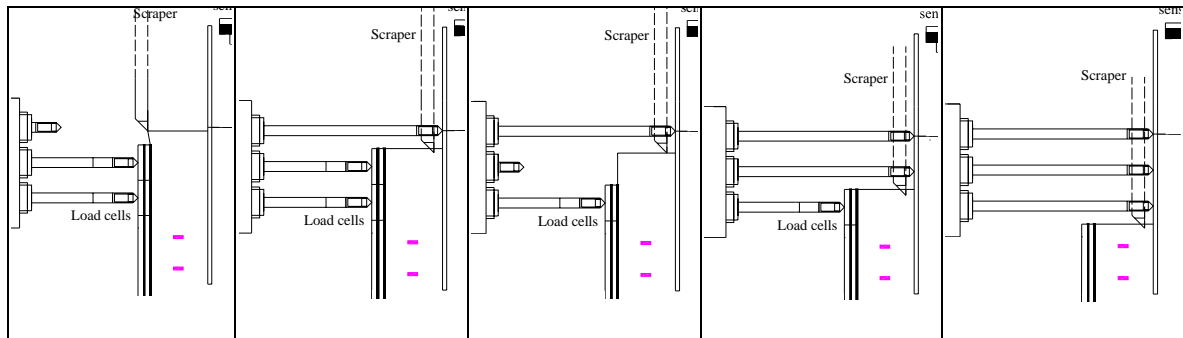


Figure 3.5 Modeling sequences of excavation

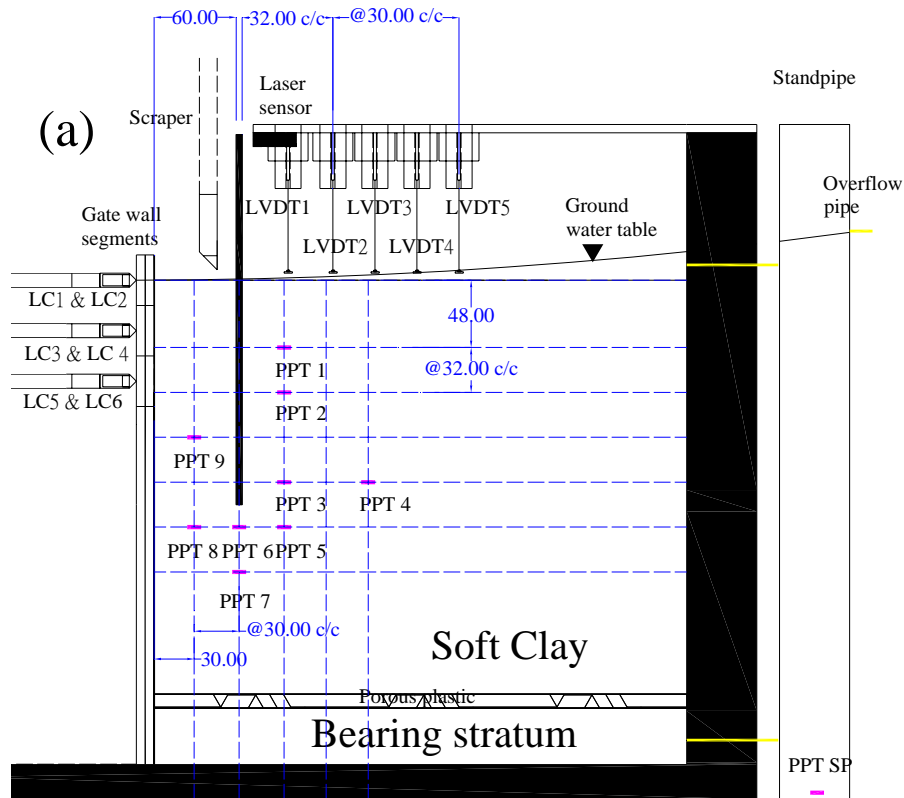
3.5 Preparation of model ground

Standardization of experimental procedures is very important as it determines the ability to reproduce similar soil stress states in each experiment. Both clay and sand were used in the present experiments.

A base layer of fine Fraction E sand was formed by pluviation using an automatic pouring machine (Madabhushi *et al.*, 2006; Zhao *et al.*, 2006). A constant fall-height of 600 mm was used to achieve a uniform layer with a relative density above 95% and a dry unit weight of 16.3 kN/m^3 . The properties of the sand, as quoted in Haigh and Madabhushi(2002), are shown in Table 3.2. Saturation of the sand was effected by connecting the bottom drainage hole to a standpipe filled with water.

Since the objective of these particular tests was to monitor excavation in soft clay and to compare different bracing schemes, lightly over-consolidated kaolin clay was used

in the models. A standard procedure was adopted to ensure repetitive reproduction of the model ground with similar strength profiles in each test. Speswhite kaolin clay was chosen for the tests because the parameters are well defined in the literature: some mineralogy and properties are given [Table 3.3](#). Clay powder was mixed with water to about twice the liquid limit (i.e. 120% moisture content), the mixing taking place under vacuum for at least two hours. The inner surface of the test container was coated with silicone grease to minimize friction against the clay. The clay slurry was carefully poured on the bearing layer, which consisted of a sheet of filter material placed over the base layer of sand. The final height of the slurry was 550mm. The container was placed in a hydraulic press, and pressure was applied to the clay in six loading steps (to 2 kPa, 5 kPa, 10 kPa, 20 kPa, 40 kPa and 80 kPa, and 160 kPa).



(b)

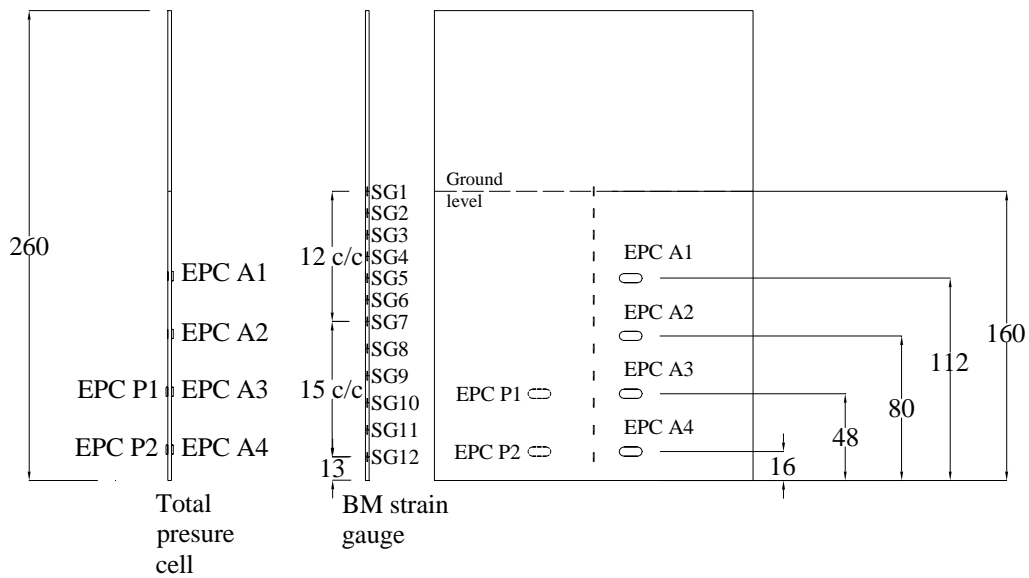


Figure 3.6 Positions of instruments (a) on model package (b) on model wall

The final pressure of 160 kPa was intended to achieve an estimated c_u of 25 kPa for the clay at mid-depth in the centrifuge model when it had swollen back into equilibrium at 60 g.

When the settlement of the clay in the press became steady for the pressure of 80 kPa, the clay was unloaded. Nine PPTs were inserted through pre-drilled openings in the back wall of the container. PPTs were installed through 90 mm long holes augured horizontally into the clay using a hand drill. Unconsolidated slurry was then injected to fill the holes, and the openings were sealed. The final locations of the PPTs are shown in [Figure 3.6\(a\)](#), The spacing between PPTs was about 30mm. After installation, loading was brought back to 80kPa. After equilibration, the consolidation pressure was further increased to 160kPa. After settlement was steady, the pressure was reduced again to 80 kPa and the clay was allowed to swell into equilibrium. Removal of this final pressure was known to be possible without drawing air into the clay.

3.6 Model making and instrumentation

The loading plate was removed. After trimming the clay surface, the resulting clay thickness was 295mm. The front wall of the model container was then removed. The clay and base layer were then removed from that half of the package that would contain the cylinder support system. An O-ring seal was placed along the edges of the gate wall to seal the gap at the side walls of the box. The retaining wall, in the particular test to be described here, is made of a 2mm thick aluminum alloy plate with

an equivalent stiffness (EI) of 10.4 MNm/m^2 at prototype scale. This wall simulates a sheet pile wall (US steel, PDA-27) in the field.

Aluminium alloy was chosen as it is stiff and light. This reduces the effect of excessive settlement of the wall in soft ground during self-weight consolidation. Six slots are made to accommodate total pressure cells (Entran EPL-D1-X-7BAR). The wall is instrumented with bending moment strain gauges arranged in Wheatstone bridges at 32 mm intervals. Greased wiper seals were used to prevent water from seeping past the sides of the wall and to ensure a free sliding condition with minimal friction. The wall was installed at a depth of 160 mm (equivalent to 9.6 m at prototype scale). A set of vertical guides and a cutter were used to dig a trench with the same thickness as the wall. The wall was then pushed into the trench using a vertical guide.

With the clay cross-section uppermost, grains of black-dyed fraction E sand were blown onto the clay to provide PIV texture. Lubricant was then applied to the Perspex window to reduce friction against the soil cross-section. The hollow frame, Perspex window and window frame were then bolted to the main body of the container.

LVDTs were assembled at 30 mm spacing intervals from the wall to measure the soil settlement profile. A laser sensor was used to monitor the lateral displacement of the top of the wall. Finally, the water table in the clay was to be maintained at the ground surface by permitting overflow from a stand pipe which would be supplied continuously throughout the experiment. Two 8 megapixels cameras took pictures throughout the experiment with the provision of suitable lighting. A CCTV camera and a webcam were used to observe the behaviour of the propping system during the

excavation. The detailed locations of the instrumentation are shown in [Figure 3.6](#) and [Figure 3.7](#).

3.7 Excavation test procedure

The in-flight excavator was bolted above the model container, and the integrated assembly was transferred onto the centrifuge swing platform. This was fixed to the torsion-bar catches which permit the package to rotate into a fixed-end condition at a centrifuge acceleration of about 10 g. The model was then brought to its scale acceleration of 60g. There are three test phases for a typical centrifuge test of deep excavation – reconsolidation, in-flight excavation, and long-term equilibration.

As an increase in soil self-weight leads to an increase in excess pore pressure, the model ground first had to undergo about 5 hours of reconsolidation until at least 90% of the consequential consolidation was achieved. The degree of consolidation was monitored by judging whether pore pressure transducer (PPT) readings were approaching their hydrostatic state.

The excavation was then started. The in-flight excavator operated at a rate of 10 mm/s horizontally and with 4 mm vertical increments. In order to ensure that realistic quasi-undrained responses were observed, the excavation process should be finished within a reasonably short period of time. [Figure 3.8](#) shows the progress of excavation in all tests. Excavation to an excavation depth of 5.5 m finished within 30-40 minutes (72-96 days at prototype scale), which is similar to the rate of excavation in the field. It is debatable, of course, whether a field profile in typical soft clay with sand and silt layers would be more or less permeable than the kaolin in the model.

Following excavation, the test was allowed to continue. The water table remained constant at the ground surface and excess pore pressures that had been generated by excavation dissipated as long term seepage conditions and thus deformations were monitored.

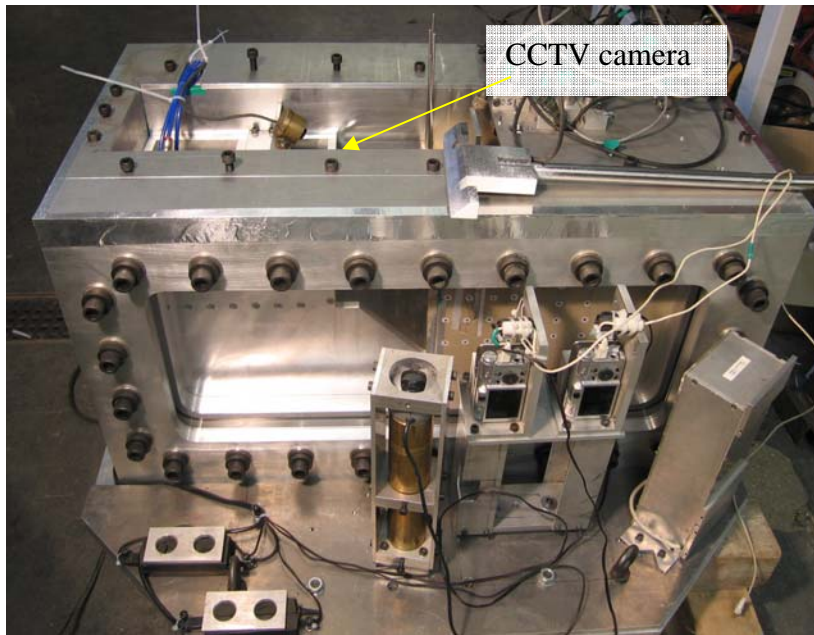


Figure 3.7 Configuration of PIV cameras and Webcam (Front)

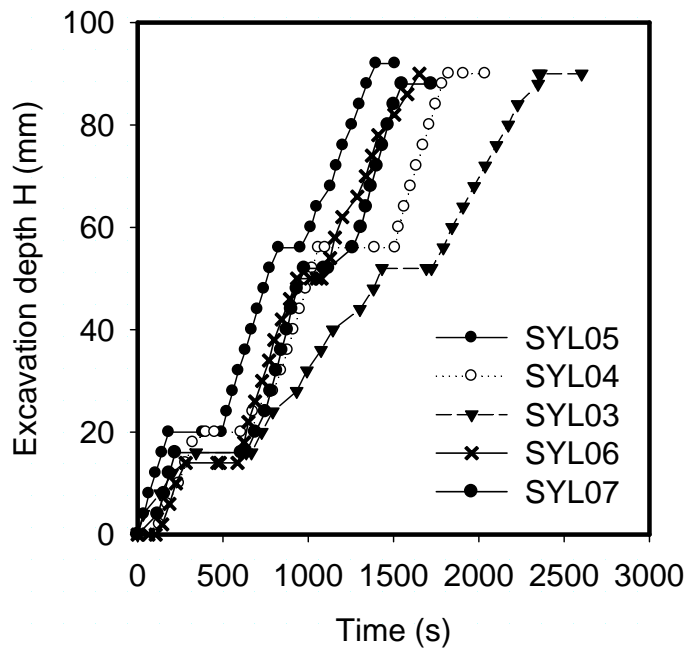


Figure 3.8 Progress of excavations

3.8 Test programme

Five centrifuge model tests were carried out to study the undrained (short-term) and consolidation (long-term) behaviour of excavation in soft clays. Test SYL04 investigated the behaviour of a floating rigid wall supported by stiff props. It acted as a reference test for comparisons. Test SYL05 studied the effect of wall flexibility on the deformation mechanism. Test SYL06 looked into the problem of using a base grout to fix the wall toe movement in bending and shear mode. Test SYL03 simulated a rigid wall supported by soft props to study the effect of soft propping on the changes in deformation pattern. Test SYL07 studied a case of excavation in shallow clay using a flexible wall. A summary of the test programme is given in Table 3.4.

Table 3.4 A summary of centrifuge testing programme

Centrifuge Tests	SYL04	SYL05	SYL06	SYL03	SYL07
	Floating Rigid wall with stiff props	Floating Flexible wall with stiff props	Fixed base Flexible wall with base grout	Floating Rigid wall with soft props	Fixed base Flexible wall in shallow clay
Objective	Baseline test	Wall stiffness	Fixed wall toe condition both BM and Shear	Prop stiffness	Clay thickness
Clay depth (mm) at model scale	300	300	300	300	160
Prop stiffness (kN/mm)	1.66	1.66	1.66	0.55	1.66
System stiffness $EI/\gamma_w s^4$	2860	106	106	2860	106
Toe fixity	Free	Free	Fixed	Free	Free

3.9 Undrained compression triaxial testing of core samples

3.9.1. Measurement of stress strain behaviour by triaxial apparatus

Triaxial apparatuses are the most common testing equipment to investigate the stress strain behaviour of a soil in the laboratory. Nevertheless, the results obtained from a conventional apparatus do not display the true stress strain behaviour of soils at very small strain levels. The stiffness obtained from conventional triaxial apparatus is usually far below the stiffness derived from back-calculation using measurements from the field. This discrepancy is thought to be caused by the errors incurred in testing and sample disturbance during sampling and transportation. However, it has been found that the stiffness of soils varies within a large range at different strain levels.

In the present studies, the stress strain behaviour of lightly over-consolidated speswhite kaolinite at small and intermediate strain levels was studied using a new local strain measurement and dynamic wave propagation system incorporated into a triaxial apparatus. Isotropically consolidated compression tests were carried out on vertically- and horizontally cut specimens. Burland (1989) suggests that ground beneath or adjacent to geotechnical structures such as excavations, pile foundations, footings and tunnels experiences a shear strain level of less than 1%. The routine conventional triaxial apparatus does not have the capability to achieve measurements at such a low strain level. External strain measurement leads to apparently linear initial stress strain behaviour with a very low stiffness. On the other hand, triaxial test, in which strain is measured locally on the specimen, shows much stiffer non-linear behaviour.

The main factors contributing to the under-estimation of soil stiffness at the initial stage of a triaxial experiment include the following:

1. Seating errors due to the closing of the gaps between the load cell on ram and the top cap and also those between the top cap or the base pedestal and soil sample.
2. Alignments error which may result from equipment and specimen non-uniformity and from non-perpendicularity of the end faces of the specimen to the vertical axis of symmetry.
3. Non-uniform strains along the specimen height resulting from lateral friction on the end platens.

For accurate measurement of stress strain stiffness, instrumentation capable of measuring strain to an accuracy of at $10^{-3}\%$ is ideally required. This degree of

accuracy can only be achieved by internal measurement within the triaxial cell. The strain measurement should be taken remotely away from the top cap and the base pedestal, normally within the middle one-third of the specimen.

3.9.2. Triaxial apparatus and specimen installation

The triaxial undrained compression tests were conducted in an automated set up provided by the GDS instruments with a computerized data logging system. **Figure 3.9** shows the layout of the triaxial setup. The assembly is described as follows:

1. A Bishop and Wesley type of cell was designed to withstand 17 bars of internal fluid pressure. It had a 50 mm diameter pedestal at the centre and a 50 mm diameter top cap. The base pedestal was connected to a bottom drainage line which was connected to a pore water pressure transducer and then to a back pressure/ volume controller. The top cap was connected to another drainage line which facilitated the flushing process.
2. A hydraulic piston at the bottom of the cell that can push the sample upwards in order to compress the sample against a load cell fixed at the top of the cell.
3. Three GDS controller pumps were set up to manage cell volume/pressure, back volume/pressure and volume/pressure for the piston at the bottom of the cell. All GDS controller pumps can control pressure to an accuracy of 1 kPa and volume within 1 mm³. The upper limit of its pressure and volumetric capacity is 20 bars and 20000mm³, respectively. They can be operated manually or under supervision of a pre-set computer program. The GDS controller pumps can communicate with each other through an integrated computer interface, which allows different settings of load conditions at various stages of the test.
4. A reservoir of de-aired water was used to fill the cell.

5. A submersible load cell is mounted on top of the top cap for axial load measurement. The load cell has a capacity of 4kN with a precision of 0.2N.
6. Two submersible linear variable differential transformers (LVDTs) were mounted vertically on a sample for evaluation of small strain stiffness over a gauge length of 40mm. The capacity of the device allows measurement accuracy of 0.0001mm and a measurement range of 10mm.
7. External LVDT can also be used to measure the overall movement of the sample with a measurement range of 50mm.
8. A pore pressure transducer is employed to record the pore water pressure change at the bottom of the specimen. The capacity of the transducer is 34bars.
9. Junction boxes was connected to all instruments to gather signals from the load cells, an external LVDT, two local LVDTs and GDS controller pumps.

A triaxial test involved a few stages of preparation and testing. The first stage was the installation of the sample. The samples were prepared by pushing very thin wall tubes with sharp edges either horizontally or vertically into a block of clay sample which was pre-consolidated at a pressure 160kPa in a consolidometer. All tests were carried out on 100mm high by 50mm diameter samples. The ends of the samples were trimmed with a thin wire saw with care to produce a flat and perfectly smooth surface to ensure vertical contact with the base pedestal and the top cap. The dimension and weight were measured using a digital vernier and a digital weighing balance, respectively, to determine its density, cross sectional area and axial strain for the compression stage of the experiment. Owing to the low strength of the sample, placement of the sample was carried out with the help of the thin wall tube and a plunger which was used for pushing the sample out of the tube and placing it properly on the base pedestal. Then, radial drainage filter paper strips were mounted on the

specimen. The sample was sandwiched by filter papers and porous stones to facilitate the consolidation process. The whole was then encased by a rubber member secured with the use of O-rings. Two submersible local LVDTs were then mounted at the middle of the specimen by glue and pins.

The next step of preparation involved flushing out air from the space between the specimen and the rubber membrane. A relatively low cell pressure of 10kPa was kept in the cell. A constant water flow was applied from the bottom pedestal to flush trapped air out of the system through the top drainage system. The back pressure was closely monitored in the process to ensure that the back pressure would not exceed the cell pressure to avoid swelling and separation of the rubber membrane. The flow was stopped when air bubbles were flushed out and the top drainage was close. The specimen was then ready for the experiment.

There were four main stages for a triaxial test. They are saturation, B-check, isotropic consolidation and swelling, and compression at constant confining pressure.

1. Saturation

All experiments were conducted under fully saturated conditions. Any degree of partial saturation would have affected the strength and stiffness of the soil specimen. The saturation process was achieved by increasing both back pressure inside the specimen and the cell pressure simultaneously. Throughout the process, the cell pressure was always 10 kPa higher than the back pressure to avoid separation of membrane from the specimen. The cell pressure was increased from an initial pressure of 10kPa to 370kPa, whereas the back pressure was increased from 2kPa to 360kPa. The whole process was carried out in 12 hours to allow the pore pressure within the specimen enough time to equilibrate.

2 B-value check

A B-value is a representation of saturation of the specimen. By closing all the drainage taps connected to the sample and then increasing the cell pressure, the back pressure should go up simultaneously. The B-value is the ratio of the change in pore pressure to the change in cell pressure. If a soft clay sample is fully saturated, then the increase in pore water pressure should be nearly equal to the increase in cell pressure with a B-value of 1. For this stage, the cell pressure was increased by 40 kPa and the back pressure valve was kept closed and the change in pore pressure was monitored. Normally, a B-value of 0.97 or above can be achieved easily with the current setup.

3 Consolidation and Swelling

The consolidation process brought the isotropic mean effective stress (p') of the sample back to the stress level of the sample experienced in the centrifuge. To trigger a consolidation stage, the cell pressure was increased to a desirable level above the back pressure in a short time. Excess pore pressure built-up in the sample was allowed to dissipate by draining out pore fluid. In the present study, the back pressure was maintained at 400kPa and the cell pressure was increased to 515kPa, which created an effective stress of 115kPa to mimic the stress level in the consolidometer. The excess fluid was drained out through the base pedestal to the GDS controller pump. Both back pressure system and cell volumes were closely monitored during the process. The process was finished when the pore volume remained unchanged for an hour. Then, the sample was allowed to swell back to a mean stress level (p') of 26kPa. This was done by decreasing the cell pressure to 426kPa. This mimicked the swelling of the sample at the mid-depth of the wall at the reconsolidation stage of the centrifuge

tests. Each of the consolidation and swelling processes took 24 hours to finish irrespective of confining pressure.

4 Compression

In this stage, the cell pressure was kept constant while the axial stress was increased until the sample failed. The specimen was loaded at a given rate of strain by means of the hydraulic piston driven by the GDS pump. The specimens were compressed at a rate of 0.017mm/min, which represents a strain rate of about 1% per hour, similar to that experienced by soil samples next to an excavation in the centrifuge. During the compression process, all drainage taps were kept closed to provide undrained conditions, for which water cannot move out or into the sample from the back pressure controller pump, as deformation took place at constant volume. As a result, excess pore water pressure was generated and monitored by a pore pressure transducer. The axial displacement was measured by an external LVDT and local submersible LVDTs attached to the surface of the sample. The axial load was measured using a submersible load cell and data were acquired at 3 second intervals. These data were then interpreted and used for calculation of stress, strain, stiffness, pore water pressure change and shear strength parameters.

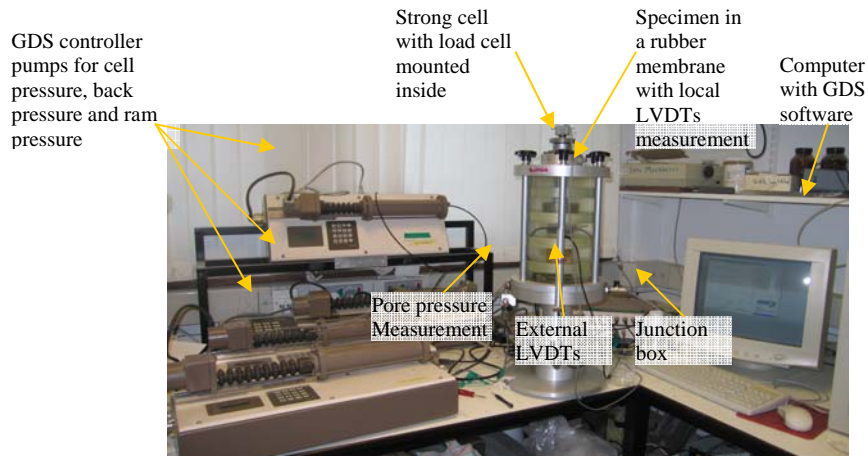


Figure 3.9 Layout of triaxial set-up

3.9.3. Local strain measurement

A small axial deformation of a triaxial sample can be measured by a local LVDT, a LDT, an electro-level inclinometer or a proximity transducer. Compared with other instruments, LVDTs have the advantage of high resolution, stability and easy calibration (Kok, 2006). In the present studies, two local submersible LVDTs were used to examine small strain axial stiffness during triaxial compression. They were mounted diametrically opposite to each other on the specimen using glue and pins during the specimen installation process. The armatures of the LVDTs were resting on lower mounting blocks that were attached on the specimen so that the armatures were free to move with respect to the deformation of the sample. The spacing between the two mounting blocks was 40mm and they were attached at the middle of the sample. The design was the same as the design by Cuccovillo and Coop (1997) as shown in [figure 3.10](#).

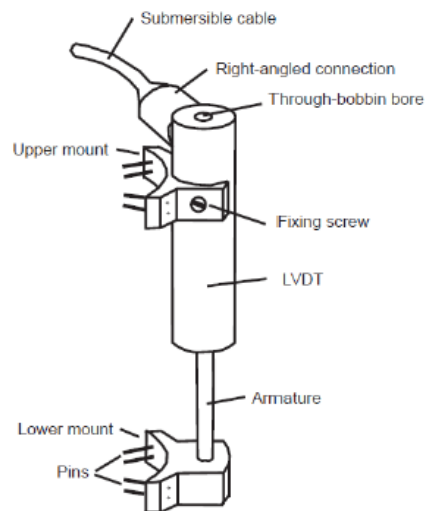


Figure 3.10 Local LVDT mount system after Cuccovillo and Coop (1997)

The local deformation data of four specimens was obtained from undrained compression tests on block soil samples pre-consolidated at 160 kPa for centrifuge tests SYL03 and SYL04. Both horizontal and vertical core samples were obtained and tested for each block sample. The deformation data from LVDTs were logged into a computer along with other triaxial data. The secant Young's modulus was then calculated as a ratio of the deviator stress and locally measured axial strain. Subsequently, the undrained shear modulus was derived by assuming a Poisson's ratio of 0.5. The secant shear modulus was plotted against local strain on a semi-log scale for the purpose of investigating the stiffness degradation for very small to large strain range.

Difficulties involved in mounting the local LVDTs were mainly related to the verticality of the LVDTs. The upper mount tended to twist owing to the relatively high stiffness of the submersible cable compared with the stiffness of the sample. It is reported by Cuccovillo and Coop (1997) that an inclination angle of 8 degree would give an error of 1%. The inclination angle could become bigger in the compression

process due to the stiff cable. The problem was resolved by softening the cable using a heat gun and also by rotating the instrument till the right angle connection of the cable was well aligned with the centreline of the sample instead of being tangential with the perimeter of the sample.

A major source of error is due to eccentric docking of the load cell in the conical notch of the top cap that can lead to concavity in the stress-strain response as discussed by Kok (2006). Any misalignment at the early stage of the specimen installation process would cause the sample to strain before the compression stage since the top cap along with the specimen would have to slide inside the notch to fit during the docking process. The slippage of the load cell will cause slow accumulation of stress against high axial strain during the initial compression stage. As a result, Kok (2006) recommended the use of a flat surfaced top cap without any recess. Although the eccentric load on the flat top cap would produce bending moment in the specimen, the small strain stiffness at the initial stage of the compression can still be revealed accordingly. This is considered a better alternative than forcing the specimen to comply, which would mask the measurement of small strain stiffness at initial stage of compression. **Figure 3.11** shows results of triaxial tests on samples using the top cap with a conical notch. The variation of deviator stress with axial strain shows that there was a mild concavity in the initial stage of the stress-strain curve. The resulting stiffness degradation curve displayed a hump at a strain level of about 0.07%. This problem would be due to misalignment of the specimen during installation, the inclined or irregular surface finish of the specimen or poor contact between the top cap and the specimen. The problem was resolved by an improvement in workmanship and sample handling techniques for later tests.

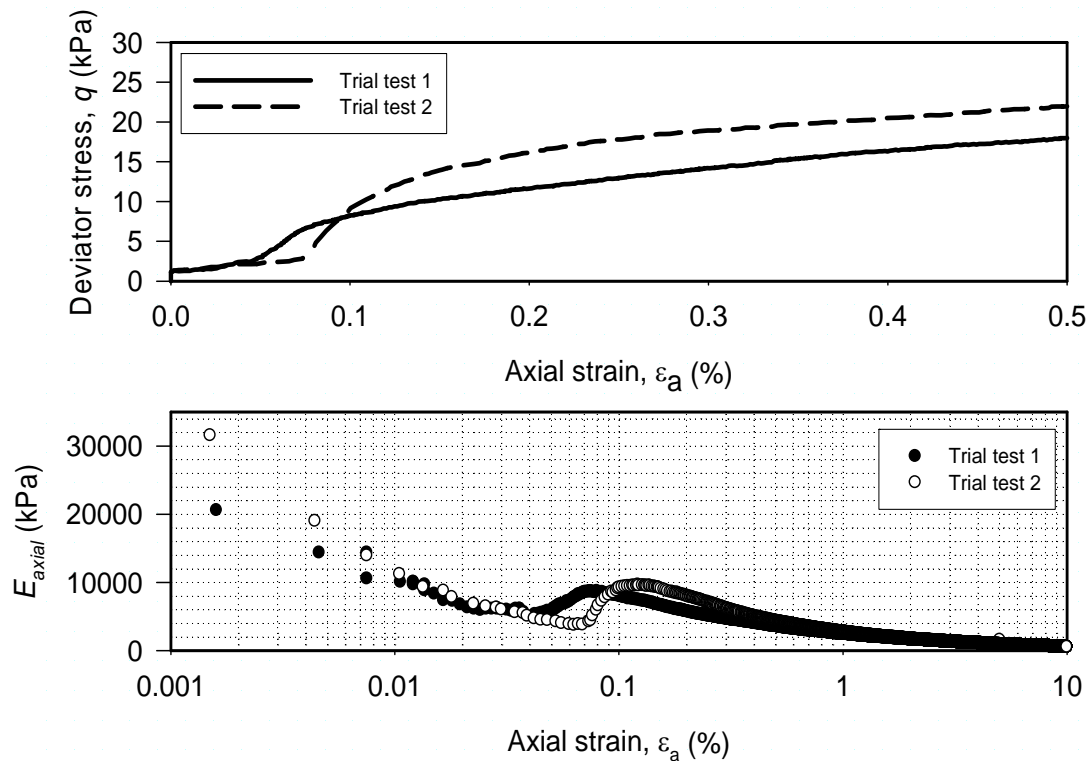


Figure 3.11 Results of undrained triaxial tests on vertical core samples showing (a) mild concavity in stress-strain curve and (b) hump in stiffness degradation curve

Results of the later experiments are shown in **Figure 3.12**. The deformation characteristics of the vertically and horizontally cored specimens in undrained conditions are developed. All specimens were initially isotropically consolidated to 125 kPa and then allowed to swell back to 26kPa before application of compressive load. Then, compressive load was applied within 8 hours at a rate of 0.16mm/hr. From the stress-strain curves and the stiffness degradation curve as shown in **Figure 3.12**, it can be seen that the horizontally cut specimen is mildly stiffer and stronger than the vertically-cut specimens. This could be ascribed to the direction of the bedding plane of clay particles formed during the deposition and one-dimensional consolidation stages.

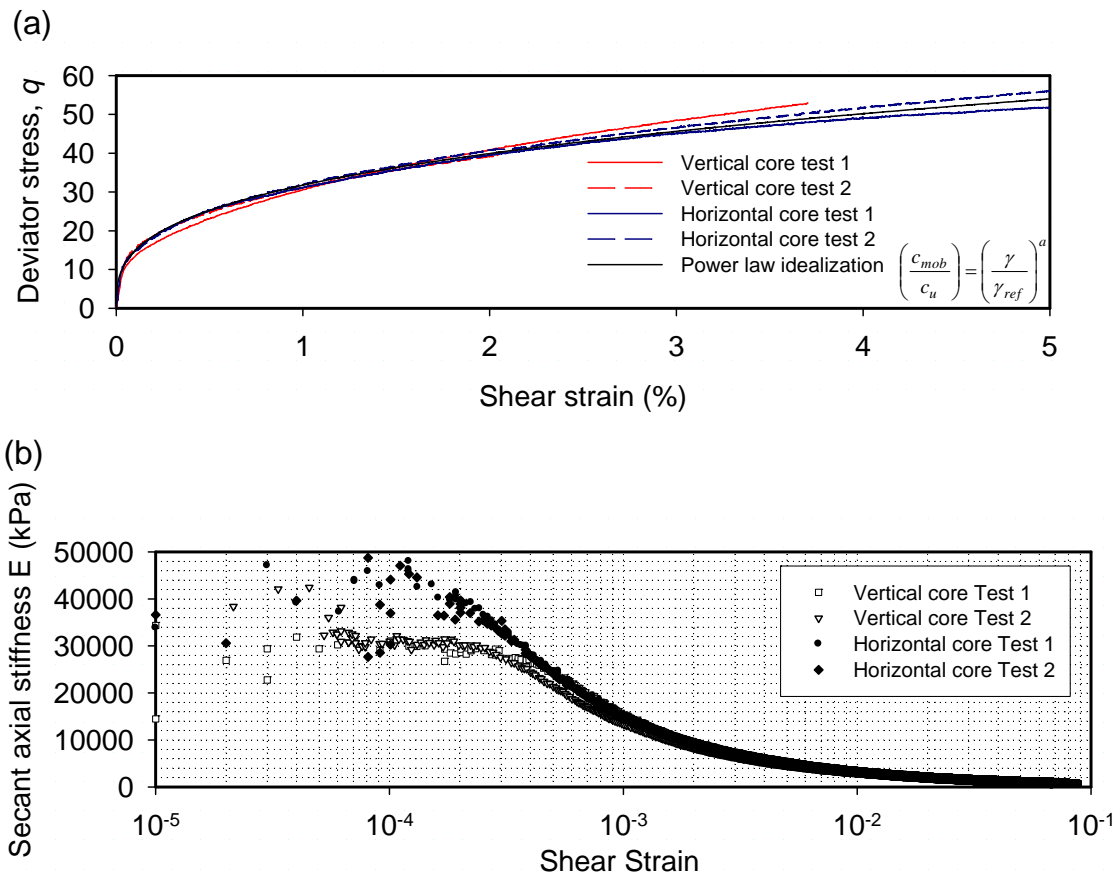


Figure 3.12 (a) Stress strain curves and (b) stiffness degradation curves for vertical and horizontal core sample.

3.9.4. Pulse transmission system

Evaluation of stiffness is not normally specified for structural wall design; however, it is an important criterion for estimating ground movements around a deep excavation. The realistic ground displacements would cause shear strains between 0.0001% and 1%. The shear modulus at a very low level of strain can be obtained by measuring shear wave velocity. Such value of stiffness is assumed to be the maximum possible modulus value of a material and it is normally called G_{max} or G_o .

After the innovation of using piezoceramic bender elements for generating and receiving shear waves in laboratory tests (Shirley, 1978), bender elements have found

their way into a number of geotechnical testing applications over the past two decades. Researchers (Viggiani and Atkinson(1995), Brignoli et al.(1996), Arulnathan et al.(1998) and Leong et al.(2005)) measured shear wave velocity in triaxial specimens using piezoceramic bender elements. Dyvik and Madhus(1985) measured small strain stiffness, G_o , of soil in resonant column, oedometer and direct simple shear apparatuses using bender elements. Despite the practicality of the equipment, there is no standardized procedure for interpretation.

The maximum shear modulus was measured from the velocity of propagation of S-waves through the triaxial specimen using bender elements. The bender elements used in this research were supplied by GDS instruments. The S-waves were triggered and recorded by a data acquisition system. The bender elements were fitted in the pedestal and top cap of the triaxial apparatus. The elements were 8mm long and 1mm thick and penetrate into the specimen by 2.25mm beyond the level surfaces of the pedestal and top cap. For measurement of shear wave velocity, the bender element on the top cap acts as a wave transmitter and the one on the base pedestal acts as a receiver. By measuring the travel time of the wave (t), the wave velocity V_s can be determined as follows:

$$V_s = \frac{L_{tt}}{t} \quad (3.1)$$

where L_{tt} is the tip to tip distance between the transmitter and the receiver and t is the travel time for the wave propagate from the transmitter to the receiver.

From the shear wave velocity, the shear stiffness G_{max} can be determined from the elastic wave propagation theory:

$$G_{max} = \rho V_s^2 \quad (3.2)$$

where ρ is the total density of the soil specimen.

Viggiani and Atkinson (1995) evaluated the sources of error in estimating G_{max} and concluded that the travel distance, L_{tt} , can reasonably be taken as the distance between the tips of the bender elements based on results obtained using samples of different length. They also concluded that the travel time, t , cannot be reliably taken as the time to first direct arrival of the shear wave because of near-field effects and that a more accurate calculation of travel time can be obtained by cross-correlation between the input and output signals. The use of characteristic points such as peaks on the input and output signals to identify travel time is a simpler way provided that it is first shown to be consistent with the more rigorous cross-correlation analyses for a given set of testing conditions.

Theoretical studies by Sanchez-Salinerio et al. (1986) show that the first recorded arrival may not correspond to the first arrival of the shear wave but to the arrival of the near-field component, which travels with the velocity of a compression wave and decays rapidly. For many typical values of shear wave velocity and excitation frequency in bender element tests, the near-field component masks the first arrival of the shear wave. [Figure 3.13](#) shows results of bender element tests on Ticino sand by Brignoli & Gotti (1992) in which both compression and shear waves were used simultaneously. The arrival of the near-field component for the shear wave coincides with the arrival of the compression wave component. The effect of the near-field compressive component from the shear wave on the first arrival of the shear wave signal is eminent. (Viggiani & Atkinson, 1995; Brignoli et al., 1996) Thus, the use of high frequency sinusoidal pulse was recommended to reduce the near-field effect as it ensures the separation of the near field coupled compression and shear waves. (Leong

et al. 2005). Leong et al. (2005) suggested that the ratio of the travel distance of the wave, L_{tt} to the wavelength should be at least 3.33 to improve the interpretation of results. **Figure 3.14** shows the calculated values of V_s by cross-correlation method in a numerical finite element study of a bender element test. It is seen that the results obtained are not uniquely correlated to the L_{tt}/λ ratio. The results suggested that an L_{tt}/λ ratio of more than 3 would give a consistent result for the shear wave velocity. As a result, in the present study a ratio of L_{tt}/λ of 9 is adopted for cross-correlation assessment.

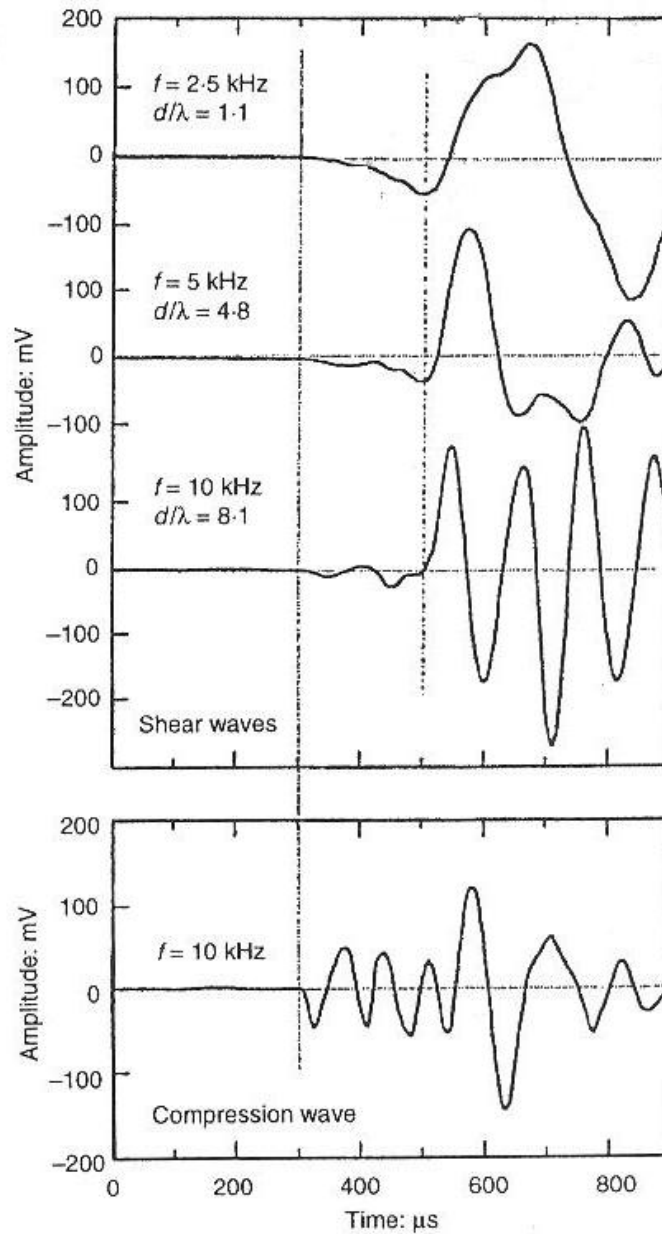


Figure 3.13 Shear and compression waves received by bender elements in tests on dry Ticino sand (after Brignoli & Gotti, 1992)

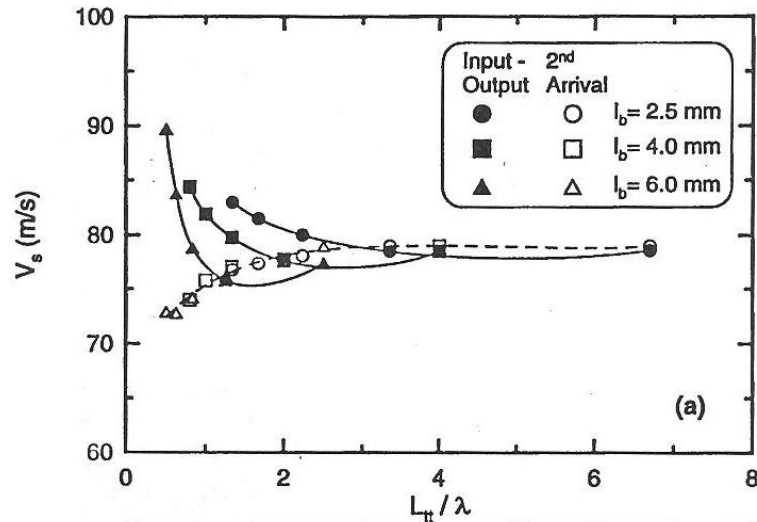


Figure 3.14 Calculated values of V_s using input-output and second arrival methods on samples with different L_{tt} to wavelength ratio.

3.9.5. Small strain stiffness characterization by wave propagation technique and local strain measurement technique

In this study, the method of cross-correlation would be used for interpreting bender element results. The cross-correlation function $CC_{xy}(t)$ is a measure of the degree of correlation of two signals $X(T)$ and $Y(T)$. The analytical expression of the cross-correlation is

$$CC_{xy}(t) = \lim_{T_r \rightarrow \infty} \frac{1}{T_r} \int_{T_r} X(T)Y(T+t)dT \quad (3.3)$$

where t is the time shift between signals. The solving procedures were given in Viggiani and Atkinson (1995).

Figure 3.15 shows the input-output response and the corresponding cross-correlation results for bender element test BT1 on a vertical core sample. The input signal had a period of 0.1ms. The output signal was obtained at a sampling frequency of 400 kHz.

A L_{tt} to λ ratio of 9.6 was used to avoid near-field effects. The best correlation was found at 340 intervals, which is 0.96ms. The shear wave velocity was calculated to be 97.4 (m/s), which gave a shear modulus G_{max} of 16456 kPa. Similarly, the shear stiffness of the horizontal cored samples in bender element tests of BT2 and BT3 was found to be 18030 and 18718, respectively. The results are summarized in [Table 3.5](#).

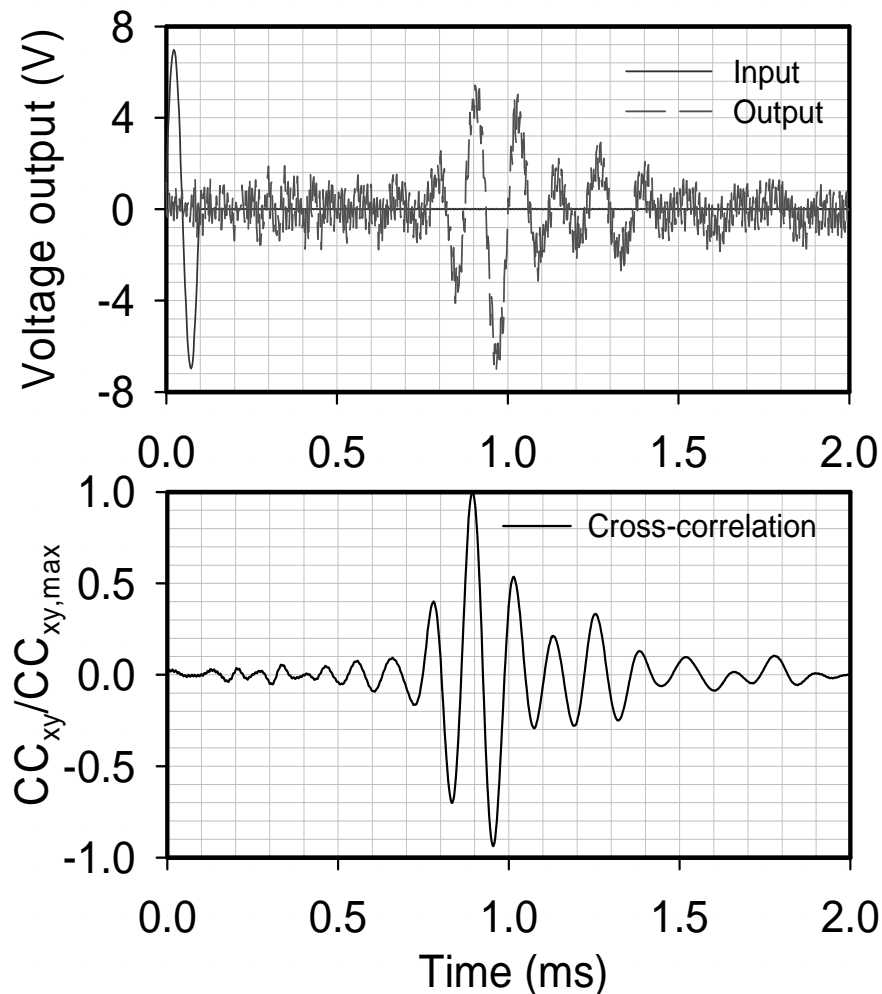


Figure 3.15 Results of bender element tests (a) input and output signals (b) Cross-correlation for Test 2 vertical core.

Viggiani and Atkinson (1995) conducted bender element tests on samples of kaolin clays at different states. By plotting the data in G_o/p_r and p'/p_r , both on a logarithmic

scale, where p_r is a reference pressure taken to be 1 kPa, the data points on the plot fell close to a single straight line given as follows:

$$\log\left(\frac{G_o}{p_r}\right) = \log A + n \log\left(\frac{p'}{p_r}\right) + m \log\left(\frac{p_{\max}}{p'}\right) \quad (3.4)$$

where A and n are non-dimensional soil parameters. The parameters A, n and m are found to be 2088, 0.653 and 0.194, respectively. The coefficient of correlation $r^2=0.82$ was obtained. For the present study, the calculated G_o by applying the empirical Equation 3.4 was found to be 22000kPa. The measured values obtained from bender element tests of the present study were within 20% of the prediction.

Table 3.5 A summary of bender element tests

Sampling frequency	400000	Hz	
Travelling path=	93.5	mm	
	Test BT3	Test BT2	Test BT1
	horizontal core	horizontal core	vertical core
Period(ms)	0.1	0.1	0.1
no of intervals	367	356	340
arrival time (s)	0.0009175	0.00089	0.00096
V_s (m/s)	101.91	105.06	97.40
Saturated			
density(N/m ³)	17348	16960	17362
G_{\max} (kPa)	18030	18718	16456
Wavelength (m)	1.0191E-02	1.0506E-02	9.7396E-03
L_{tt}/λ	9.175	8.9	9.6

3.9.6. Comparison with published experimental data by Viggiani and Atkinson (1995)

Figure 3.16 shows the values of stiffness at a particular strain extracted from the data of Figure 3.12, and plotted against mean effective stress, both axes being normalized with a reference pressure, p_r . The values obtained from the present study were obtained on samples tested at a very low mean stress level ($p'=26\text{kPa}$). The values compare well with extrapolated values using Viggiani and Atkinson (1995).

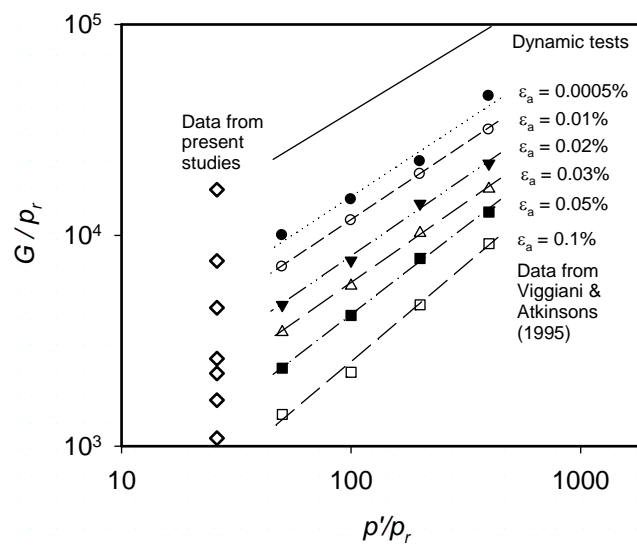


Figure 3.16 Variation of G with mean stress and strain extracted from the present data and data from Viggiani and Atkinson (1995).

Attempts have been made to write down a simple correlation relating secant shear modulus with shear strain. In this section, a hyperbolic function is introduced to make the best fit of the data of the present studies and Viggiani and Atkinson's data. The following expressions are used.

Viggiani and Atkinson (1995) suggested that G_o was a power-law function of the mean effective stress p' and the over-consolidation ratio from bender element testing of samples with different OCR ratio and p' .

$$\frac{G_o}{p_r} = 2088 \left(\frac{p'}{p_r} \right)^{0.65} \left(\frac{p_{\max}}{p'} \right)^{0.19} \quad (3.5)$$

A hyperbolic function is introduced to relate secant shear modulus with G_o , shear strain γ and the reference strain γ_{ref} . Reference strain γ_{ref} was assumed to be a linear function of void ratio following Vardanega and Bolton (2010).

Using the least square method, the coefficient of correlation was found to be 0.82. The parameters a and b in Equation 3.6 and 3.7 were found to be 0.69 and 2.3, respectively. The correlation is plotted together with the actual measurement for comparison in [Figure 3.17](#).

$$\frac{G}{G_o} = \frac{1}{1 + \left[\frac{\gamma}{\gamma_{ref}} \right]^a} \quad (3.6)$$

$$\gamma_{ref} = b e_o \times 10^{-3} \quad (3.7)$$

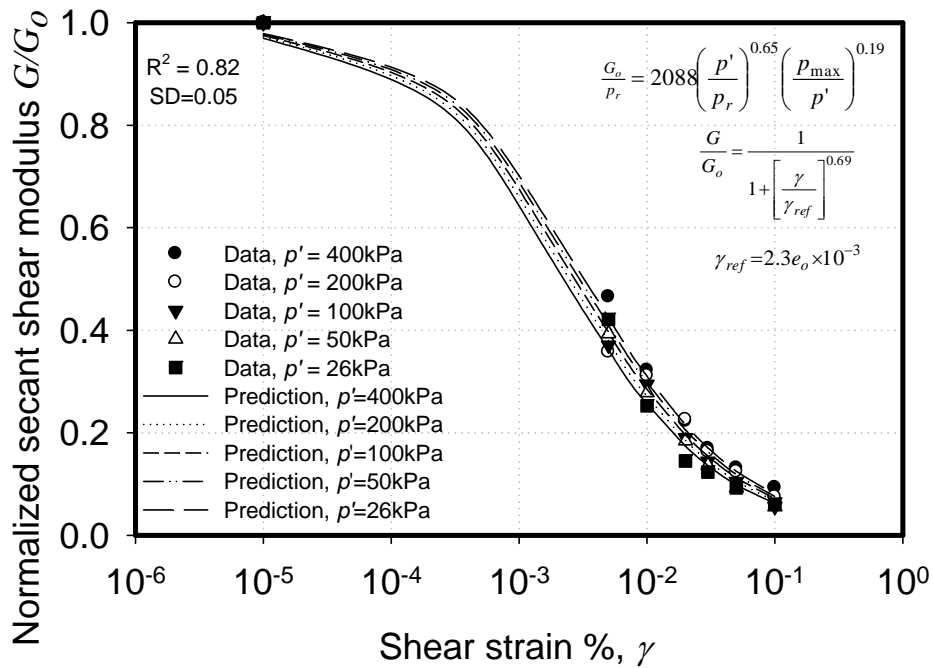


Figure 3.17 Variation of soil shear secant stiffness with shear strain (vertical sample)

3.9.7 Power-law idealization

The stress strain behaviour of the kaolin clay as shown in **Figure 3.12(a)** can be well-described by a power law. The following power law relationship describes it:

$$\frac{c_{mob}}{c_u} = \left(\frac{\gamma}{\gamma_u}\right)^a \tag{3.8}$$

By curve fitting, the γ_u and a are found to fit 5% and 0.33, respectively. The use of this simple stress strain power law relationship is used later on assisting in validation of the energy conservation principles using PIV data and MSD methods.

3.10 Summary and discussion

Centrifuge model tests of excavation in lightly over-consolidated clay were carried out using a newly developed actuation system, in which the construction sequence of

propping was precisely modelled. The new method provides the realistic initial ground conditions before excavation so that no pre-excavation bending moments develop during the reconsolidation stage. The actual removal of soils also provides a proper way of simulating passive resistance on the excavation side; whereas draining heavy fluid as a substitute of soil removal suffers from the setback of introducing pre-excavation lateral wall movement and bending moment and also a constant earth pressure coefficient of unity, which limits its applicability.

Undrained triaxial compression tests, controlled by the GDS triaxial computer-control system, were carried out to characterize the stiffness of soil sample cores obtained from the mid depth of the deformation mechanism. With the help of local strain measurements on the sample and geophysical soil characterization techniques, reliable stress-strain curves with a strain level below 0.1% can be obtained. The results are validated with published results by Viggiani and Atkinson (1995) and the comparisons are broadly consistent. A hyperbolic function is used to represent the actual stiffness data with a reasonable coefficient of correlation. The use of simple stress strain power law relationship is also used as a mean for a simple representation of the non-linear small strain behaviour of Kaolin. This result will assist in MSD analyses in Chapter 5.

CHAPTER 4

OBSERVED CENTRIFUGE TEST PERFORMANCES FOR BOTH SHORT- TERM AND LONG-TERM

4.1 Introduction

This chapter presents centrifuge test results and corresponding analyses that are related to the problem of greenfield excavation in soft clay. The centrifuge package used for testing was described in Chapter 3. The main objective of these tests is to observe excavation effects on ground deformations for the development of a simple analytical method for estimating maximum wall displacement and ground settlement profiles. The effect of wall stiffness, prop stiffness and wall toe propping are studied for both short and long term deformation. [Table 4.1](#) summarizes the objectives and test descriptions of the test programme.

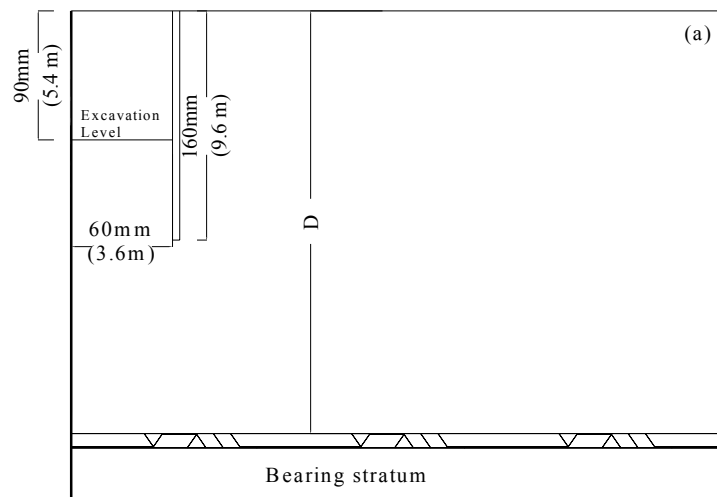
4.2 Typical soil strength profile

As described in the previous chapter, consolidated triaxial compression tests were carried out to characterize the undrained shear strength of the soil. The undrained shear strength was found to be 27.5kPa as shown in [Figure 4.1](#). (For details please refer to Chapter 3). In the same figure, a predicted and an estimated profile by using

an empirical relation suggested by Jamiolkowski et al.(1985), are also shown for comparisons. Jamiolkowski et al. (1985) related the c_u of the soil with the vertical effective stress of the soil and undrained strength ratio for normally consolidated clay and over-consolidation ratio. It is obvious that reasonably consistent results are obtained among the predictions.

Table 4.1 A summary of centrifuge testing programme

Centrifuge Tests	SYL04	SYL05	SYL06	SYL03	SYL07
	Floating Rigid wall with stiff props	Floating Flexible wall with stiff props	Fixed base Flexible wall with base grout	Floating Rigid wall with soft props	Fixed base Flexible wall in shallow clay
Objective	Baseline test	Wall stiffness	Fixed wall toe	Prop stiffness	Clay thickness
Depth of clay(mm) at model scale (D)	300	300	300	300	160
Prop stiffness (kN/mm)	1.66	1.66	1.66	0.55	1.66
System stiffness $EI/\gamma_w s^4$	2860	106	106	2860	106
Toe fixity	Free	Free	Fixed	Free	Free



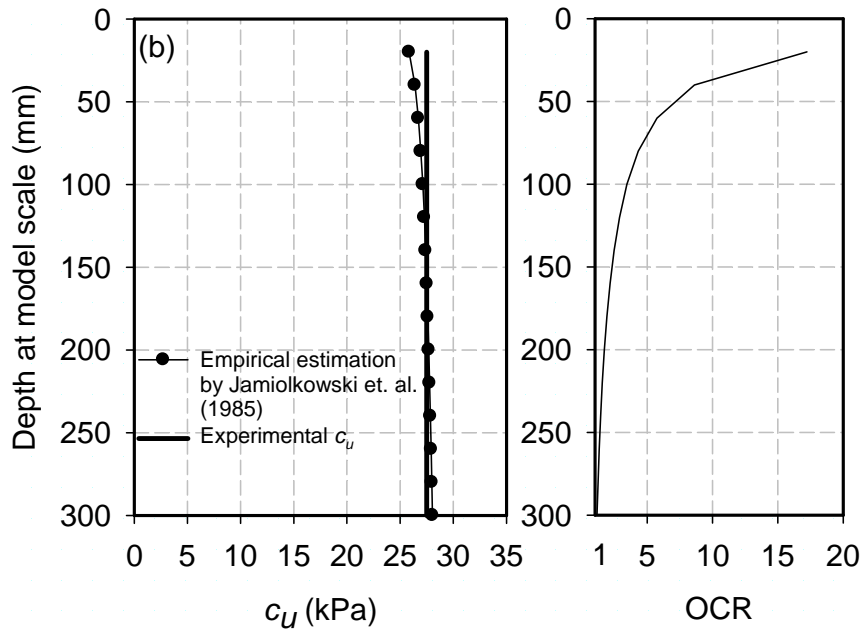


Figure 4.1 (a) Schematics of test set-up and (b) undrained shear strength and overconsolidation profile at 60g

4.3 Typical pre-excavation soil behaviour

There are three test phases for a typical centrifuge test of excavation. Firstly, the soil sample is allowed to reconsolidate under its enhanced self-weight. Then, in-flight excavation will be carried out. Finally, the soil sample is allowed to reconsolidate for dissipation of excess pore pressure generated from the excavation stage.

4.3.1 Pre-excavation responses

4.3.1.1 Pore pressure response

Figure 4.2 shows the response of pore water pressure with respect to time for a typical excavation test. During the swing-up, excess pore water pressure is generated due to the self-weight of the soil. The soil sample was allowed to consolidate and excess pore water pressure dissipated to reach a hydrostatic equilibrium as shown in Figure 4.3. At least 90% of the re-consolidation was achieved within 5.3 hours. Figure 4.4 shows the excess pore water pressure isochrones showing excess pore pressure dissipation under a double drainage condition.

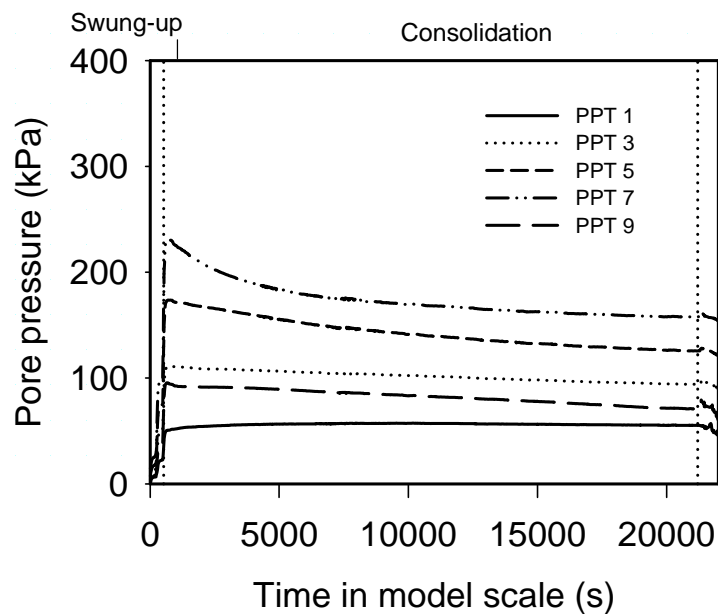


Figure 4.2 Development of pore pressure with time

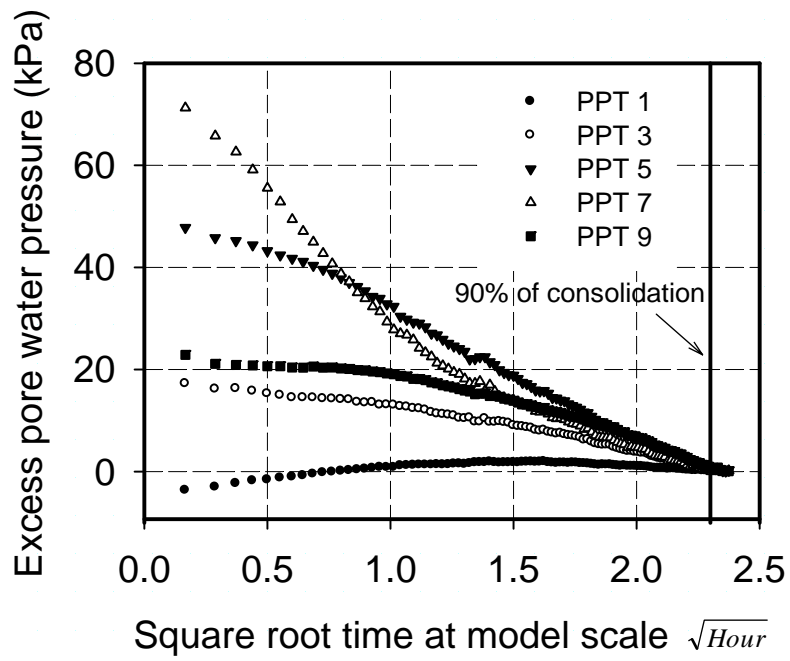


Figure 4.3 Dissipation of excess pore water pressure

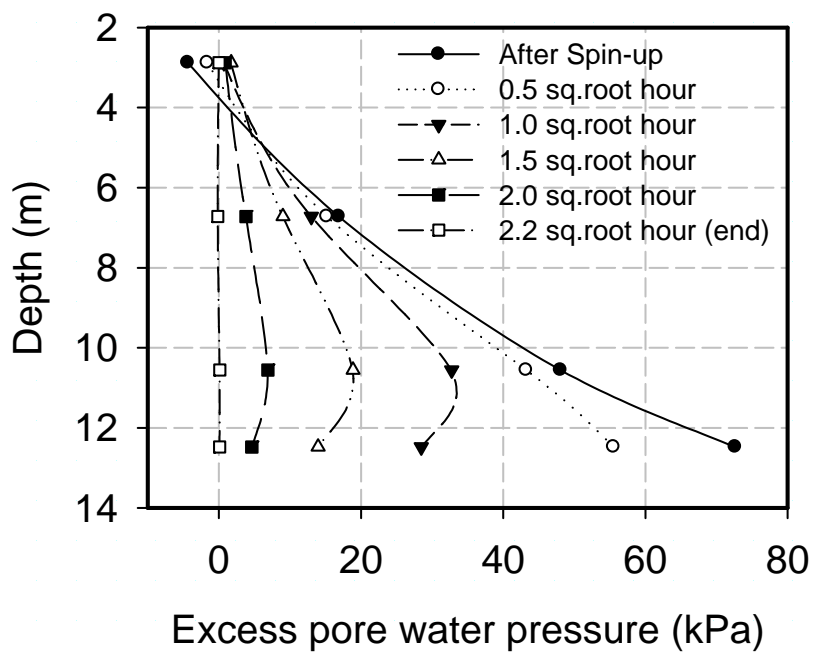


Figure 4.4 Excess pore pressure isochrones during reconsolidation

4.3.1.2 Ground settlement response

Figure 4.5(a) shows the development of ground settlement at model scale. The surface settlement develops in 4.8 hours after 90% dissipation of excess pore water pressure (Figure 4.5(a)). It was expected that the measured soil settlements at the end of the consolidation phase of the first four tests in this study would be fairly similar to each other (Figure 4.5(b)) because the soil sample preparation procedure was the same. However, the settlement in Test 5 was only 75% of the settlement in the other tests, due to the smaller thickness of the clay. Sub-surface consolidation settlement was observed by the PIV technique during the consolidation process (Figure 4.6). It is noted that the wall lateral displacement at this stage is less than 0.1mm at model scale whereas the pre-excavation wall movement using the technique of heavy fluid by Powrie (1986) was recorded to be about 1mm at model scale.

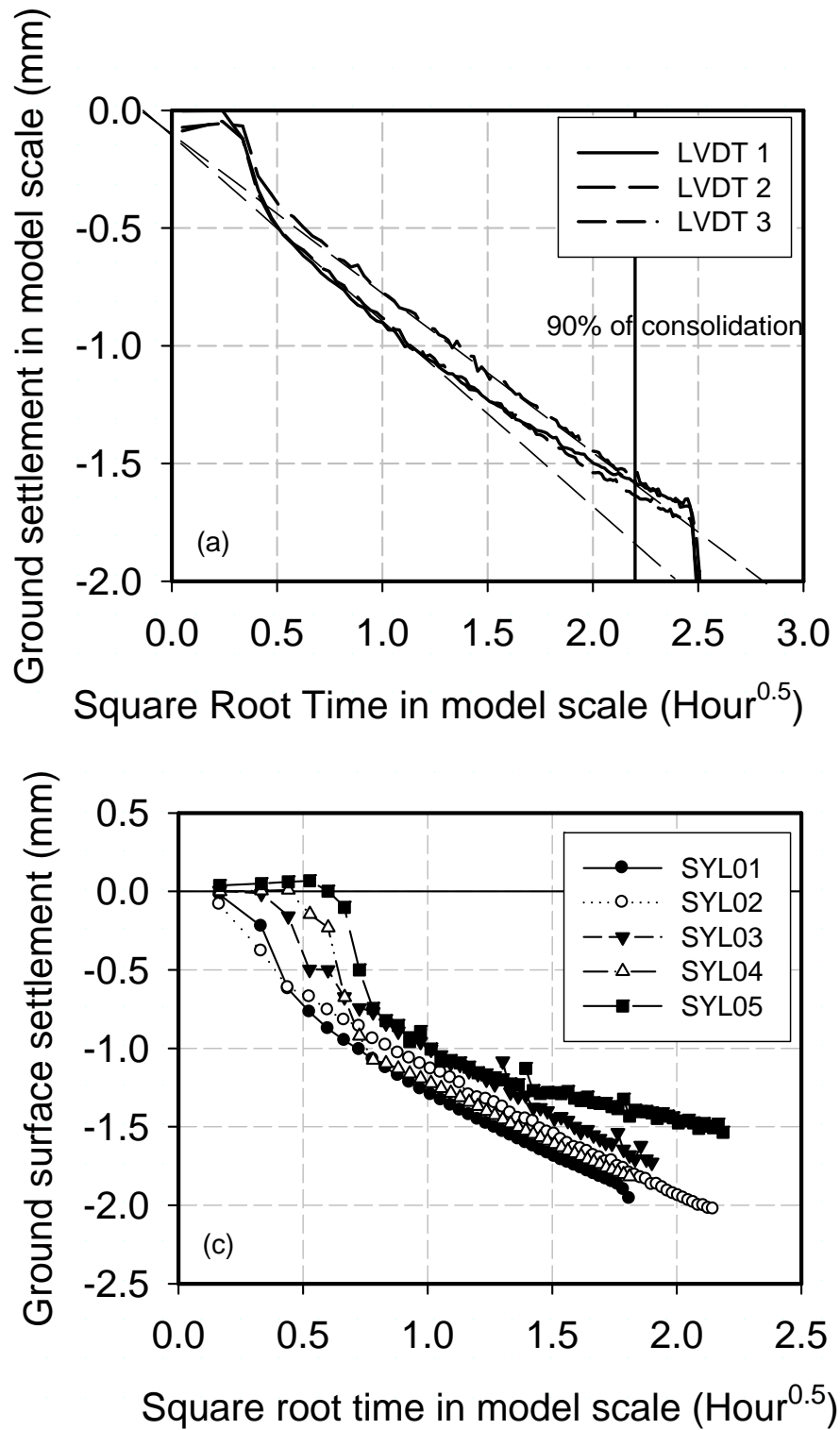


Figure 4.5 Variation of (a) settlement data for SYL05 against root time (b) settlement data LVDT2 for all tests against root time

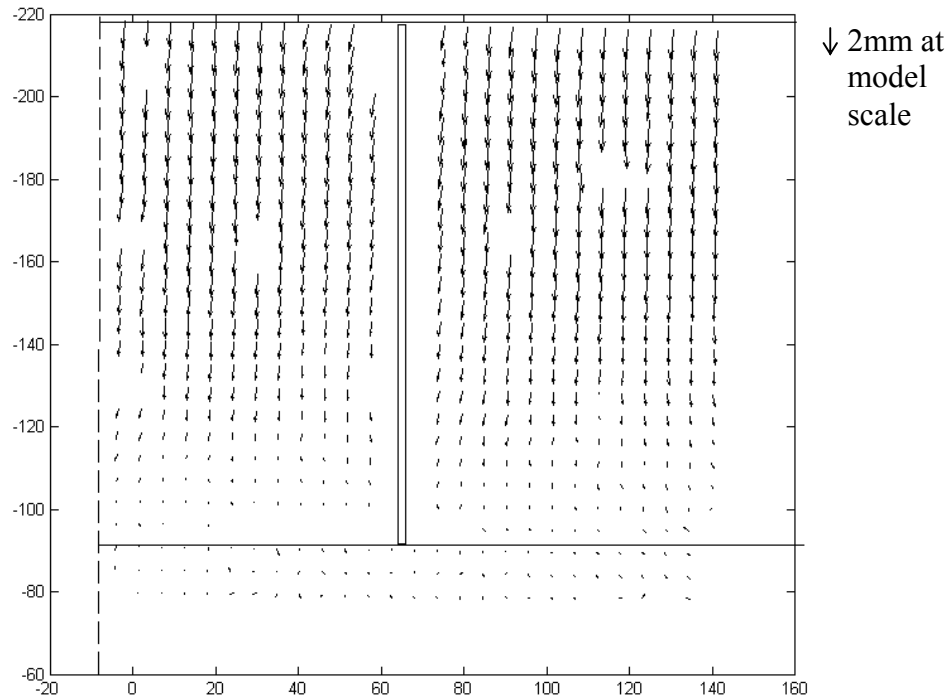


Figure 4.6 Displacement vectors of ground movement during consolidation

4.3.1.3 Bending moment in research wall

During the reconsolidation phrase, bending moments observed in the retaining wall are found to be minimal (only amounting to 1 % of excavation-induced bending moment), implying that the verticality of the retaining wall installed at 1g is not a problem (Figure 4.7). It was reported by some previous researchers (Richard and Powrie, 1998) that some bending moment was observed during the reconsolidation phrase before the start of excavation. The magnitude amounted to more than 20% of the excavation-induced bending moment. This was principally due to the mismatch between the total horizontal stress profile in the soil and the hydrostatic pressure in the heavy fluid used to support the wall. Thus, the wall retaining heavy fluid bends to fulfil the force equilibrium requirement. No such problem has occurred with the new actuation system.

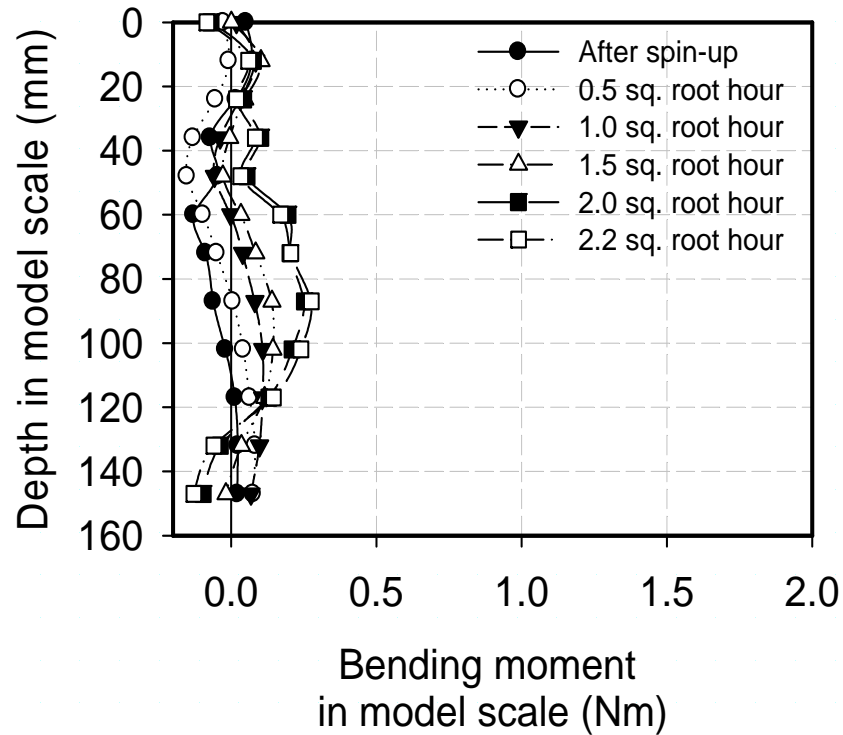


Figure 4.7 Development of bending moment profile for test SYL05 during consolidation

4.4 Observed performance during deep excavation (Short term)

4.4.1 Progress of excavation

One of the objectives of the tests of the current study is to investigate short term behaviour during an undrained excavation, which implies zero volumetric change for shearing. A typical excavation test finishes within 40minutes as seen in Figure 4.8 and PIV is used to check for the zero volume change conditions. The average volumetric strain was observed to be less than 1%.

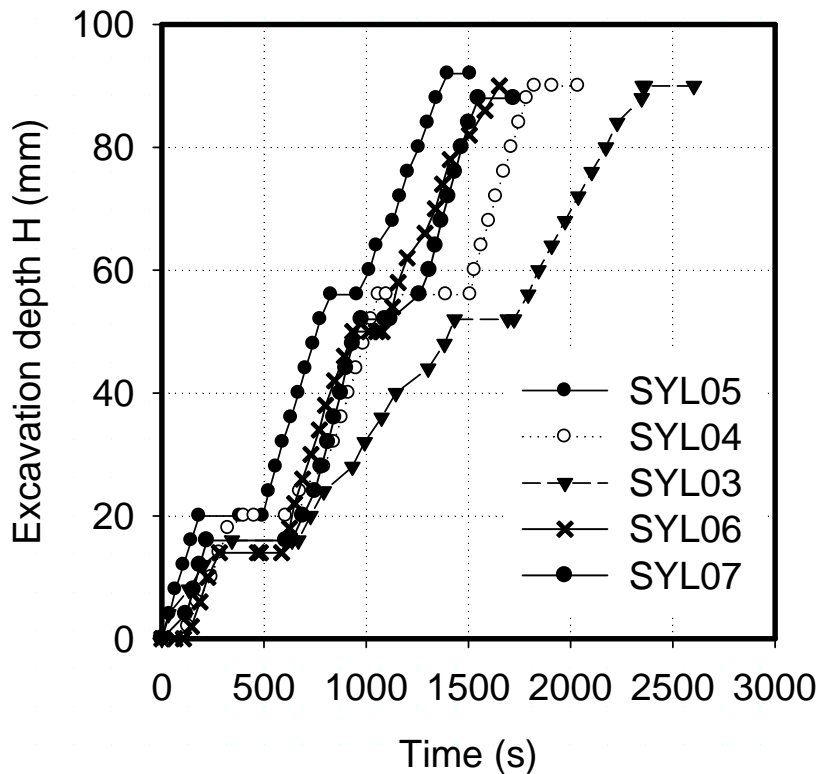


Figure 4.8 Progress of excavation

4.4.2 Short term excavation response

4.4.2.1 Pore pressure response

As the excavation proceeds, the ground water level in front of the wall was lowered simultaneously. The bottom drainage layer was connected to a standpipe which maintains a hydrostatic water pressure measured from the soil surface at the back of the wall throughout each test. Water flow past the sides of the wall was prevented by greased seals. Under such condition, downward seepage at the backside of the wall and upward seepage in front of the wall should be expected. Figure 4.9 and 4.10 show the variation of pore water pressure during excavation using a 6mm thick aluminium wall, which is equivalent to a 0.9m thick diaphragm wall in Test SYL04. In front of the wall, there was a negative pore pressure built-up (PPT 9 and PPT 8) due to the reduction in total mean stresses during excavation. The magnitude of the negative

pore pressures was smaller than the effective over-burden pressure lost in excavation. This is owing to the fact that negative pore pressures were cancelled somewhat by the positive pore pressures generated by shear deformation of clay. On the other hand, the change in pore pressure measured at the back of the retaining wall (PPT 1, PPT 2 and PPT 3) was relatively small because the stiff prop supports limited lateral wall deformation and thus limited the reduction in lateral horizontal stress.

Comparison of variation of pore water pressure underneath the excavation (PPT9) for different centrifuge tests is made in [Figure 4.11](#). The removal of overburden stress is plotted on the same graph for comparison. As described earlier, the negative pore pressure by removal of the over-burden stress is cancelled out by the generation of positive excess pore pressure by shear deformation of clay. The decrease in rate of pore pressure reduction for [Test SYL05, SYL06 and SYL07](#) is ascribed to more extensive excavation induced shear strain induced by flexible wall bulging and thus generation of positive excess pore water pressure. On the other hand, a similar comparison carried out for pore water pressure below the wall toe on the retained side (PPT5) ([Figure 4.12](#)) shows very similar rate of development of excess pore pressure for all cases.

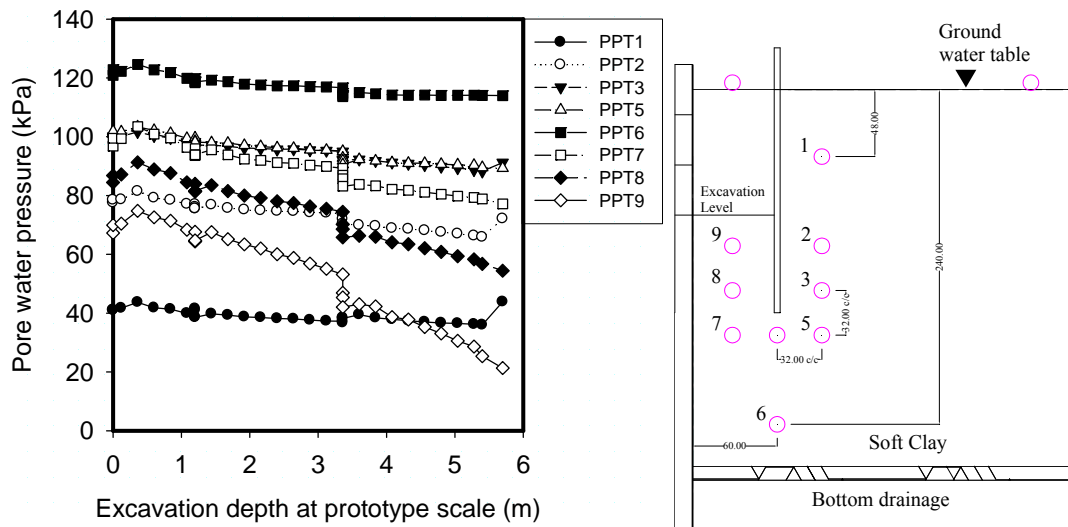


Figure 4.9 Variation of pore water pressure during excavation with rigid props and wall (Test SYL04)

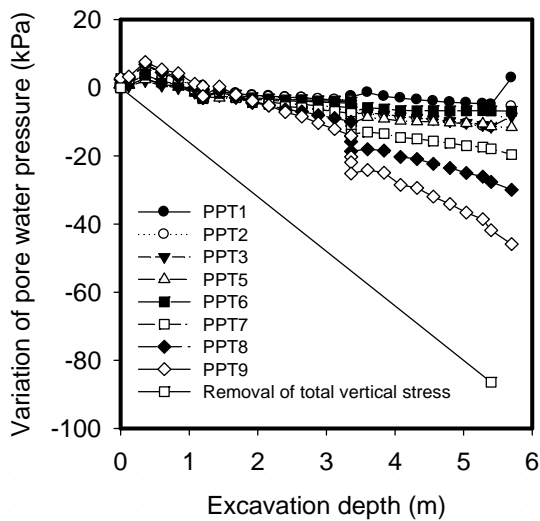


Figure 4.10 Variation of excess pore water pressure during excavation with stiff props and wall (Test SYL04) (For PPT positions, refer to Figure 4.9)

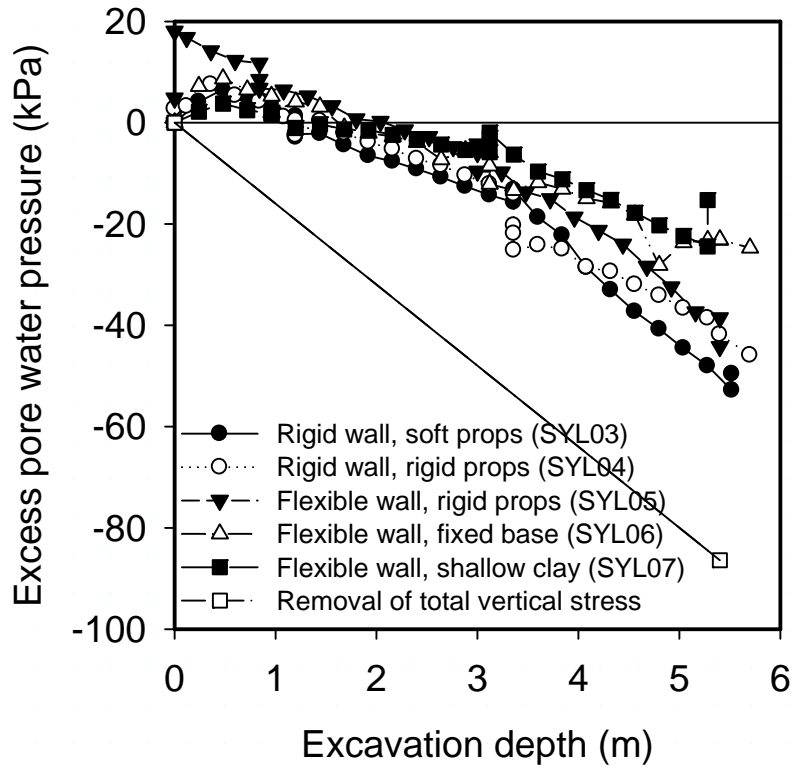


Figure 4.11 Variation of water pressure at bottom of excavation site (PPT9)

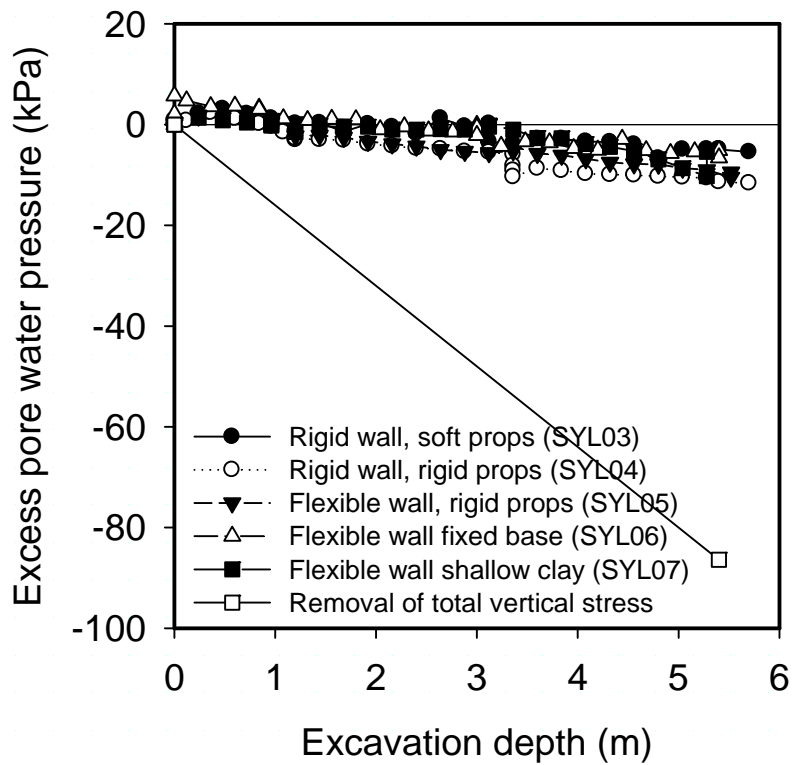


Figure 4.12 Variation of water pressure in middle of wall on retained side (PPT5)

4.4.2.2 Apparent earth pressure

The design of a bracing system usually involves the calculation of prop forces using apparent earth pressure envelopes developed empirically by Peck (1969) from field measurements of maximum strut forces and contributing areas of soil, which were obtained from early projects supported by sheet pile or soldier pile and lagging walls in the 1960s. **Figure 4.12** shows the development of apparent earth pressure with excavation depth for the case of a prototype excavation using either a sheet pile wall (**Test SYL05, SYL06**) or a 1.1m thick concrete diaphragm wall (**Test SYL03, SYL04**). The maximum strut force is usually observed at the lowest strut in the step before the installation of the next level of strut. The struts at previous levels would usually experience some relief. This phenomenon is observed to be more significant for excavations with flexible support systems. Hashash and Whittle (2002) propose that an arching mechanism forms for a deeper stage of excavation after installation of the latest strut. The major principal stresses are directed toward the lowest level of strut, while an underlying compressive arch transfers loads onto the embedded section of the wall. After installation of the lowest strut, a deeper arching mechanism forms due to the next stage of excavation. The lowest props therefore carry the majority of the supportive earth pressure removal in the subsequent stages of excavation. This agrees with the centrifuge observations that the apparent earth pressure drops after installation of the lowest prop. **Figure 4.13** shows the profile of apparent earth pressure with depth for an excavation depth of 5.5m. Comparisons between the measured pressure and the design recommendations are complicated by many factors such as stiffness of supporting structures. The maximum apparent earth pressure for depths beyond 25% of excavation depth according to Peck(1969), is specified as follows:

$$\sigma_h^A = K_a \gamma_t H \quad \text{with} \quad K_a = 1 - m \left(\frac{4s_u}{\gamma_t H} \right) \quad (4.1)$$

where $m=0.4$; s_u =undrained shear strength averaged over depth of excavation.

Results of the centrifuge tests, expressed at prototype scale in Figure 4.13, show that the recommended design values agree approximately with the measurements in the top 2m of soils for all cases. Nevertheless, the recommended values under-predict the measured values by 30% for the case of excavations supported by diaphragm walls. Similar observations were also reported in numerical studies of excavations supported by stiff embedded diaphragm wall by Goldberg(1976) and Hashash and Whittle (2002). On the other hand, reducing the bending stiffness of the retaining wall or the axial stiffness of the propping system causes a marked reduction in apparent earth pressures and close agreement with the design envelope as revealed in Figure 4.13.

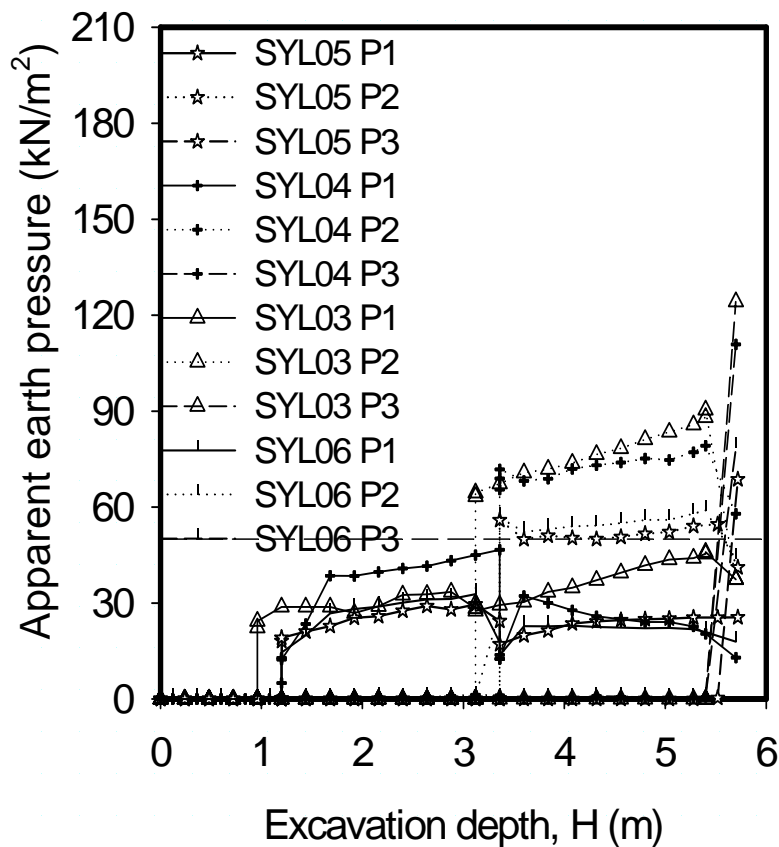


Figure 4.12 Development of apparent earth pressure with excavation depth

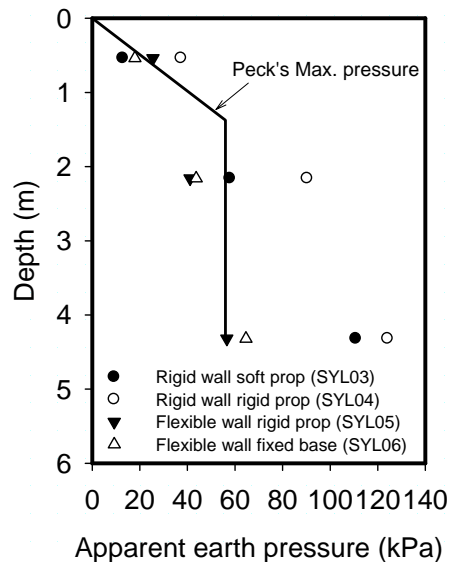


Figure 4.13 Development of apparent earth pressure with depth

4.4.2.3 Total earth pressure

Variation of measured total earth pressure with excavation depth, and the earth pressure distribution profile on both sides of the wall, is shown in [Figure 4.14](#) and [Figure 4.15](#), respectively. The locations of the earth pressure measurements were shown in [Figure 3.6](#). In [Figure 4.15](#), the pressure at K_0 condition before excavation and Rankine's active and passive pressures from excavation depth of 5.5m are also presented. In the calculation of Rankine's pressure, an undrained condition is assumed and an undrained shear strength of 27kPa was adopted. At the retained side of the wall, there is a gradual decrease in total pressure with excavation depth. As the excavation depth increases, a larger decrease in total pressure is observed at a greater depth. This is due to the fact that at later stage of the excavation, deep-seated soil movement developed below the lowest prop. At the front side of the wall, the decrease in total earth pressure in the clay layer is due to the removal of soil and thus total vertical stress. The variation is more significant than changes at the back side. As the excavation level goes deeper, the rate of decrease of total pressure becomes more

evident. This phenomenon reveals once again the importance of excavating real soil in-flight when simulating excavation, as discussed in the previous chapter.

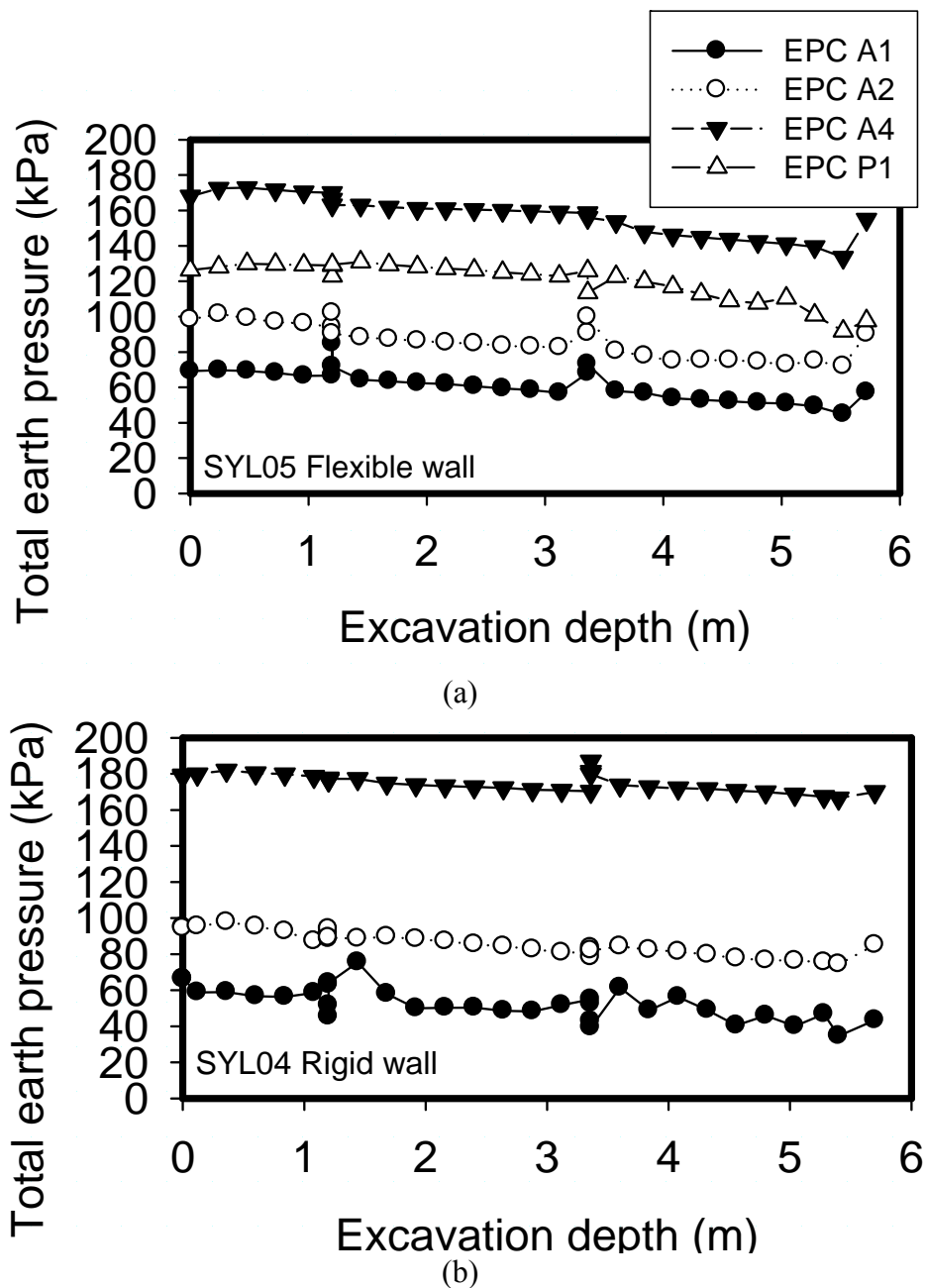


Figure 4.14 Variation of total earth pressure with excavation depth for **Test SYL05 and SYL04**

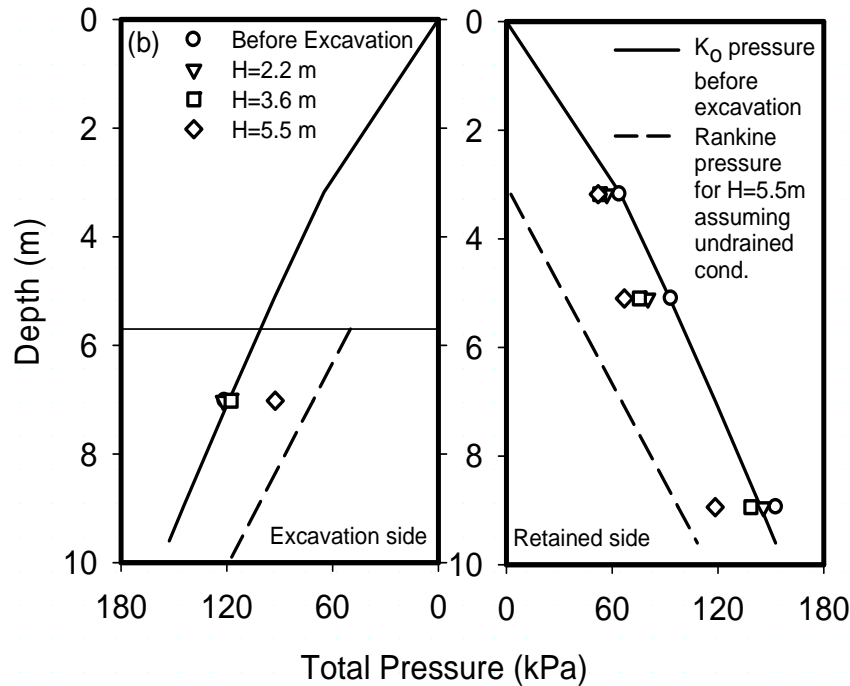


Figure 4.15 Variation of total earth pressure with depth for Test SYL05

4.4.2.4 Stress paths

Lambe (1970) presented the stress paths of soil elements around a deep excavation supported by a cantilever wall as shown in Figure 4.16. Soil elements in the retained soil side of excavation undergo a plane strain active (PSA) mode of shearing, whilst soil elements beneath the excavation experience a plane strain passive (PSP) mode of shearing. The analysis ignores shear stress components acting on the soil from soil structure interactions (i.e. No wall friction) and assumes constant total vertical stress on the retained side. During each excavation stage, soil elements on the retained side do experience significant reductions in total horizontal stress. The construction of the diaphragm wall and the excavation process is assumed to be rapid enough for the undrained assumption to be valid. The effective stress paths for the soil on the retained side should have a slope of 45 degree towards the PSA failure line if the soil is linear elastic and isotropic, while soil elements beneath the excavation suffer

removal of overburden stress and an increase in total horizontal stress leading to stress paths aiming towards the PSP failure line at a 45° slope.

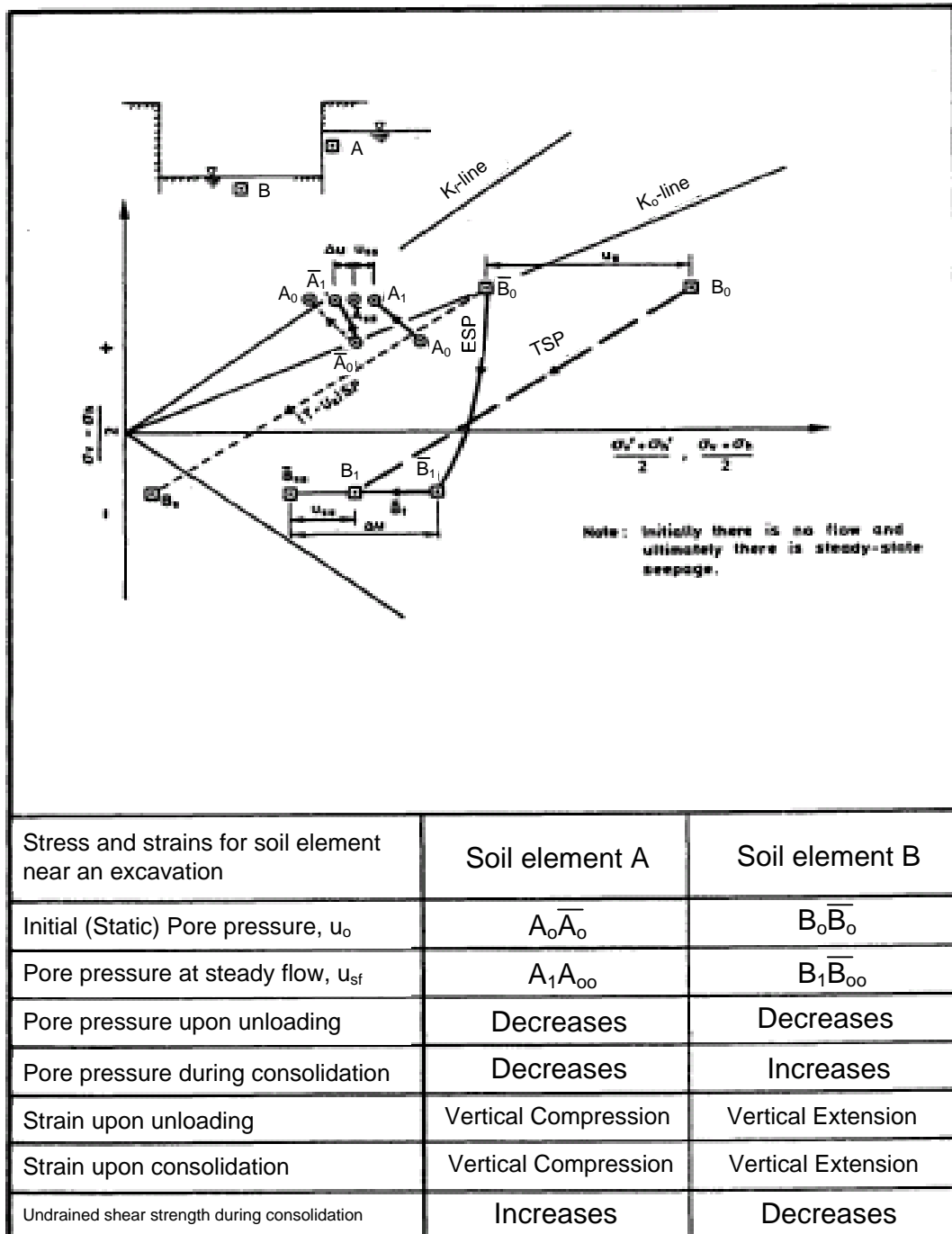


Figure 4.16 Stress paths for soil elements near excavation (Lamb, 1970)

Interpretation of centrifuge data using the stress path method requires the use of total earth pressure cell data (for calibration of EPCs, refer to Appendix A) and pore water pressure data with the assumption of vertical total stress controlled by the overburden

weight of soil, (i.e. $\sigma_v = \gamma z$, where z = depth of soil in the retained side and $z =$ depth of soil minus H on the excavation side). The detailed locations of the earth pressure measurement are given in Figure 3.6. The pore water pressure at each location is obtained by interpolation of readings from the nearest PPT locations. Figure 4.17 shows stress paths of soil elements next to either a stiff (SW, Test SYL04) or flexible (FW, Test SYL05) retaining wall supporting excavations. The initial stresses after reconsolidation are comparable to the K_o stress. The soil stress path (FW-EPC P1) on the passive side of the retaining wall follows very similar stress path as PSP stress path. The soil stress paths (FW EPC A1, FW EPC A2, FW EPC A3) on the active side of the retaining wall follow the PSA stress path initially, and then they experience a tendency of stress rotation. This provides partial evidence for development of an arching mechanism as described earlier.

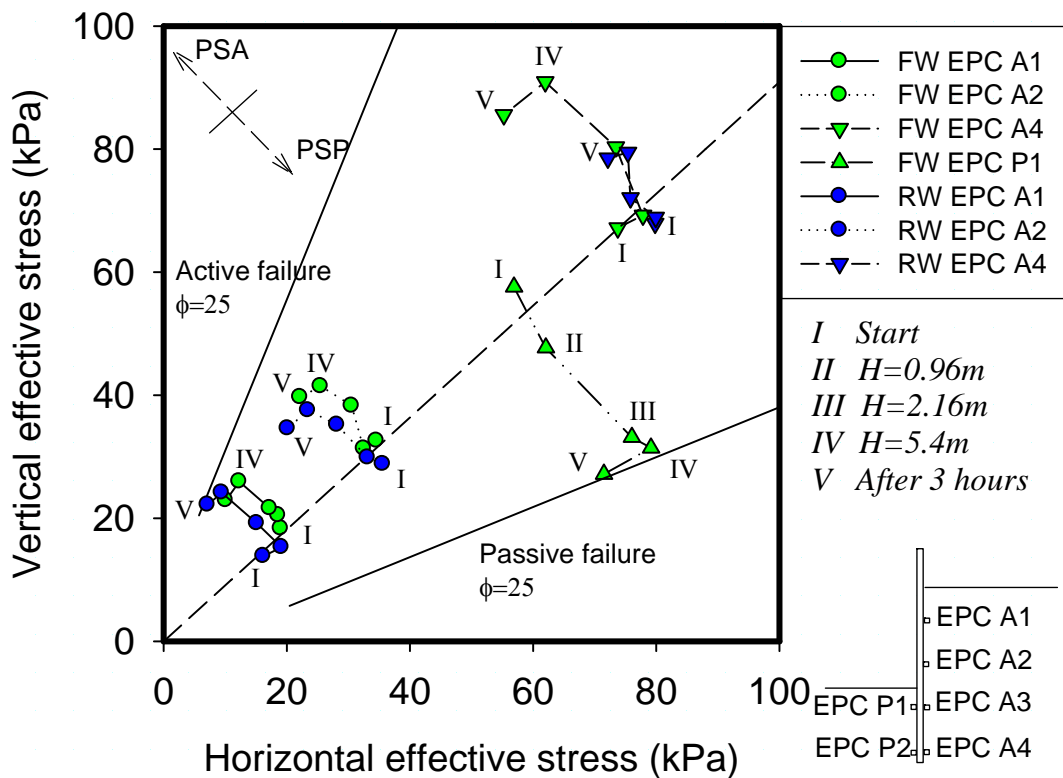


Figure 4.17 Stress paths of soil elements in Tests SYL04 and SYL05

4.4.2.5 Mobilization of shear strength

If the shear stress on vertical planes is neglected, the stabilized shear strength c_{mob} at any instant can be taken as $\frac{1}{2}(\sigma_v - \sigma_h)$, and the degree of mobilization can be expressed as $(\sigma_v - \sigma_h)/2c_u$. Data from tests SYL04 (Stiff wall) and SYL05 (Flexible wall) is utilized for plotting mobilization of soil strength at different locations around an excavation. It is observed that the insignificant rate of mobilization with excavation depths for soil elements at different depths supported by a stiff structural support system (Figure 4.18) is consistent with the restricted lateral displacement field experienced by the rigid wall. On the contrary, the rate of mobilization at mid-depth (EPC A2) of the wall using a flexible wall (Figure 4.19) is more apparent than that at shallower (EPC A1) and deeper (EPC A4) depths. This local development of strength mobilization is consistent with the bulging wall movements at mid-depth, to be shown later.

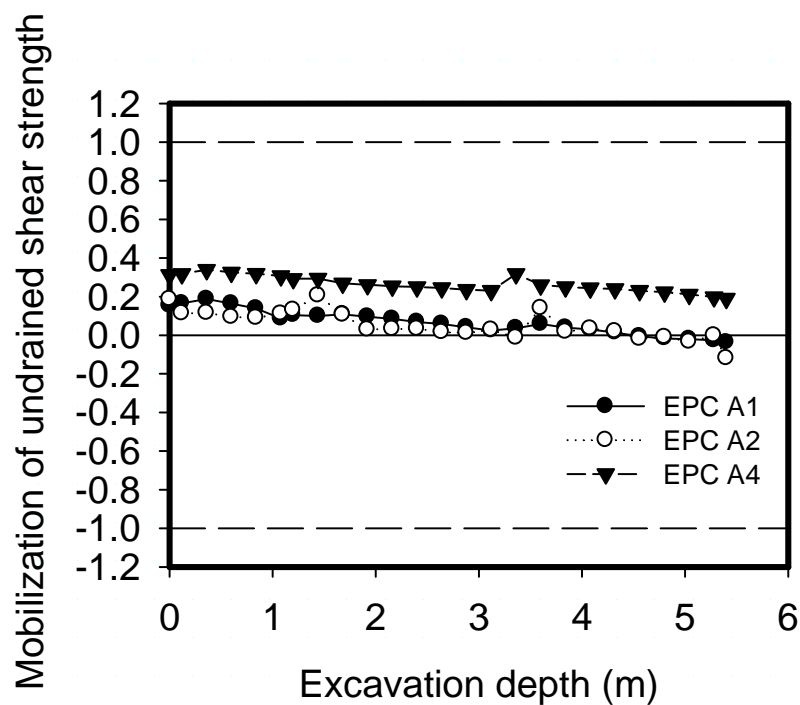


Figure 4.18 Mobilization of undrained shear strength in Test SYL04 (Rigid wall rigid props)

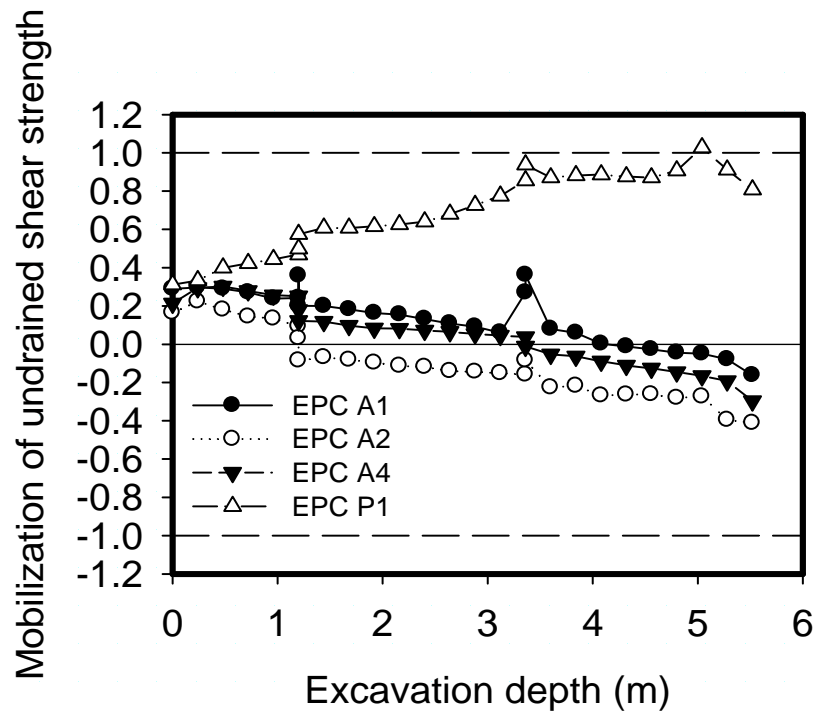


Figure 4.19 Mobilization of undrained shear strength in **Test SYL05** (Flexible wall rigid props)

4.4.2.6 Bending moments in retaining wall

Figure 4.20 (a) shows at prototype scale the development of bending moment per metre run during an in-flight excavation in a deep layer of clay using a flexible sheet pile wall (**SYL05**). For the first stage of the excavation, positive bending moment developed due to the cantilever movement into the excavation pit. After introduction of the first level of struts, the wall tends to budge beneath. Negative bending moment developed. On the other hand, installation of further level of props induced slight reductions of wall bending moment at the level of higher struts. As the excavation proceeded, the lateral restraint imposed by the support system on the retaining wall led to the development of a deep seated deformation mechanism beneath the lowest struts. This will be discussed in detail in section 4.4.2.7. Again, negative bending moment increases below the lowest props. The maximum bending moment induced by the undrained excavation was about 200 kNm/m at final excavation level. An

excavation in shallow clay using a flexible retaining wall e.g. **Test SYL07** (**Figure 4.20(b)**) showed only half the magnitude of induced bending moment due to the formation of a shallower deformation mechanism, which will be discussed in Section 4.4.2.7. On the other hand, an excavation case in deep clay with a stiff wall (**Test SYL04**) (**Figure 4.20(c)**) shows a bending moment profile similar to a beam simply supported at its ends, with a maximum magnitude only a quarter of the value for the deep clay case with a flexible wall(**Test SYL05**) Instead of bending, the stiff wall provoked a deep-seated deformation due to rotation and translate. This will be presented in Section 4.4.2.7.1.

In the long term, the magnitude of maximum bending moment decreased by 30% (to 150 kNm/m for **Test SYL05**) or by 50% of its original value (for **Test SYL07** and **SYL04**) as a result of clay softening and stress redistribution on the excavation side. Although the long term ultimate bending capacity of the retaining system is not crucial in this particular case, catastrophic collapse of a deep excavation can occur if there is a delay during excavation, permitting swelling and softening of the clay beneath the excavation.

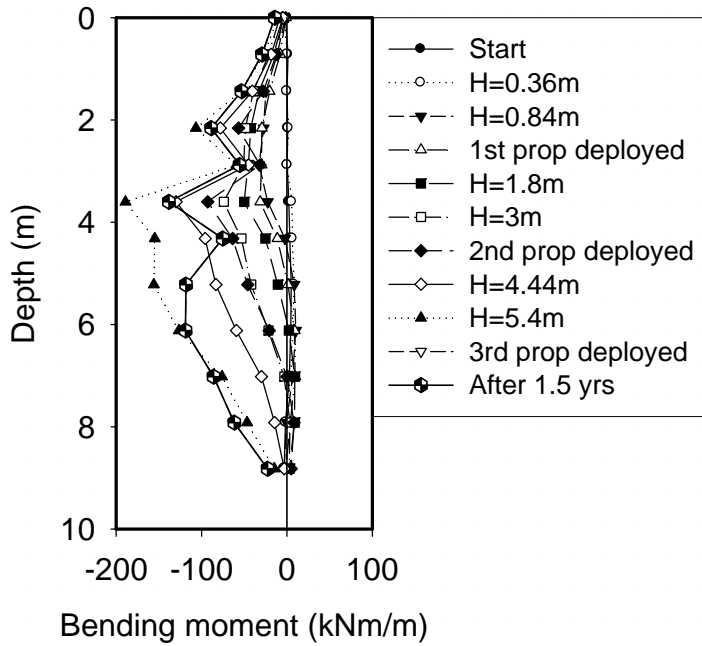


Figure 4.20 (a) Variation of bending moment with depth for excavation in deep clay with flexible wall (Test SYL05)

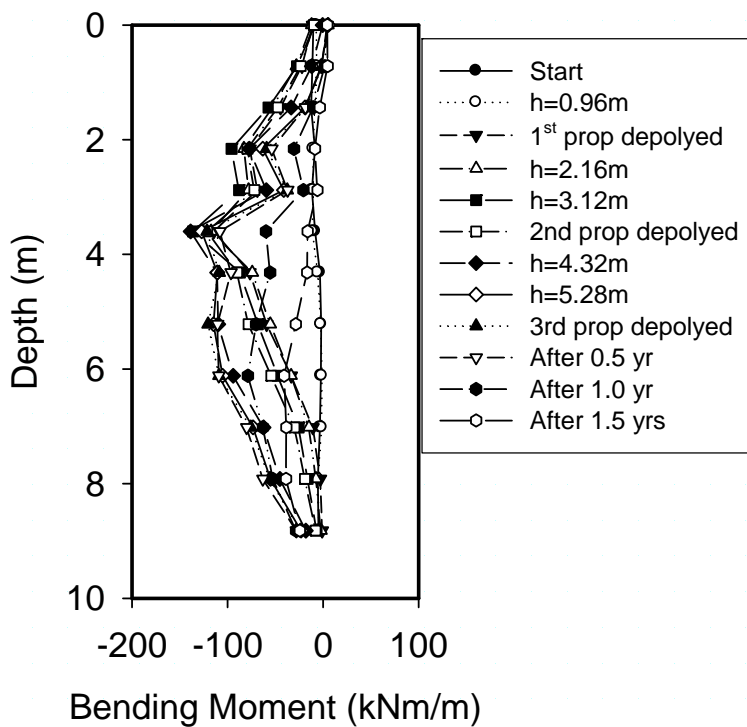


Figure 4.20 (b) Variation of bending moment with depth for excavation in shallow clay with flexible wall (Test SYL07)

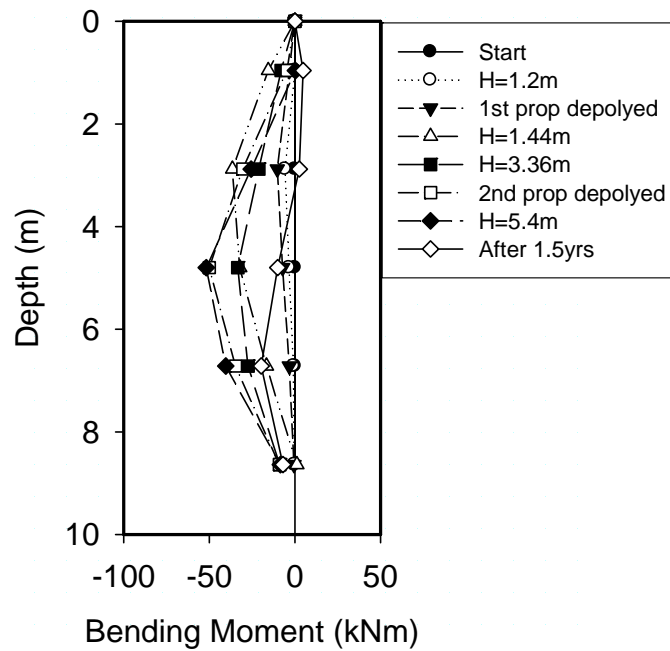


Figure 4.20 (c) Variation of bending moment with depth for excavation in deep clay with rigid wall (Test SYL04)

4.4.2.7 Ground settlement and wall deflection

The shape and magnitude of wall deflection and ground settlement during undrained excavation are vital in assessing the potential damage to neighbouring structures and buried services. In an ideal excavation process, the first support is installed at an early stage to minimize cantilever movement of the wall. However, this may not be always possible due to a variety of site constraints. In the present study, the excavation procedure began with a cantilever stage of excavation, which was then followed by singly propped and then multi-propped excavation. Ground movements were captured by the PIV technique. The ground settlement at certain discrete points away from the retaining wall was also monitored by LVDTs in Test SYL05. The results obtained by LVDTs and the PIV technique were comparable, as shown in Figure 4.21 which shows that the model behaved in a plane strain condition notwithstanding the possibility of friction against the window and the sealed wall.

Figure 4.21 shows the development of lateral wall displacement and ground settlement for a deep excavation supported by a flexible wall (SYL05). Consistent with results shown by Powrie (1986), the wall toe did not move, but in the present case the wall clearly bulges, whereas Powrie's much stiffer wall was seen to rotate about the toe in the cantilever excavation stage. A maximum incremental cantilever wall deflection of about 10mm (Figure 4.22(a)) at prototype scale was observed at the wall crest (0.167mm in model scale), which will be created by about 0.2% of average engineering shear strain in the 45° triangular soil zone behind the wall according to Osman and Bolton (2004).

Considering the incremental deformations of a multi-propped wall supporting a deep excavation in soft, undrained clay, at each stage of excavation the incremental displacement profile of the ground and the wall below the lowest prop was assumed to be a cosine function given by O'Rourke(1993):

$$\delta w = \frac{\delta w_{\max}}{2} \left(1 - \cos\left(\frac{2\pi y}{\lambda}\right) \right) \quad (4.2)$$

where δw is the incremental wall displacement at any distance y below the lowest support, δw_{\max} is its maximum value, and λ is the wavelength of the deformation.

O'Rourke (1993) defined the wavelength of the deformation as the distance from the lowest support level to the fixed base of the wall. Osman and Bolton (2006) suggested a definition for the wavelength of the deformation based on the wall end fixity such that $\lambda = \alpha s$. For walls embedded into a stiff layer beneath the soft clay, such that the wall tip is fully fixed in position and direction, the wavelength was set equal to the wall length ($\alpha = 1$). For short walls embedded in deep soft clay, the maximum wall displacement occurs at the tip of the wall so the wavelength was taken as twice the projecting wall length ($\alpha = 2$). Intermediate cases were described as restrained-end

walls ($1 < \alpha < 2$). For the excavation in deep soft clay layer, the α value is found to be 1.3-1.5. It should be noted that this value will be a function of soil-wall relative stiffness.

The settlement trough occurs at some distance away from the wall, which is slightly different from the roughly triangular pattern observed by Powrie (1986) for a cantilever wall. The later stages of excavation involve a deep-seated soil flow mechanism with bulging of the retaining wall below the lowest level of struts (Figure 4.22 (b)). The maximum incremental lateral wall displacement for the second and the third stages were 30mm and 90mm (0.5mm and 1.5mm in model scale), respectively. According to Bolton et al. (2008), these movements were equivalent to about 0.6% and 1.5% of average incremental engineering shear strain, respectively, within the deformation zone.

These findings once again showed the importance of the small to medium strain stiffness of over-consolidated soil on analyzing multi-propped excavation problems. The development of the settlement trough is complicated by the superposition of deep settlement trough increments near the wall with more widely spread settlement due to shallow excavation. This observation is consistent with the general observation given by Clough and O'Rourke (1990) that the settlement trough of a multi-propped excavation is bounded by a trapezoidal zone extended behind the wall by a distance of up to 2 times the maximum excavation depth. It is also noted that the areas underneath the two curves of wall displacement and settlement match within 10%, consistent with zero volumetric strain in undrained conditions.

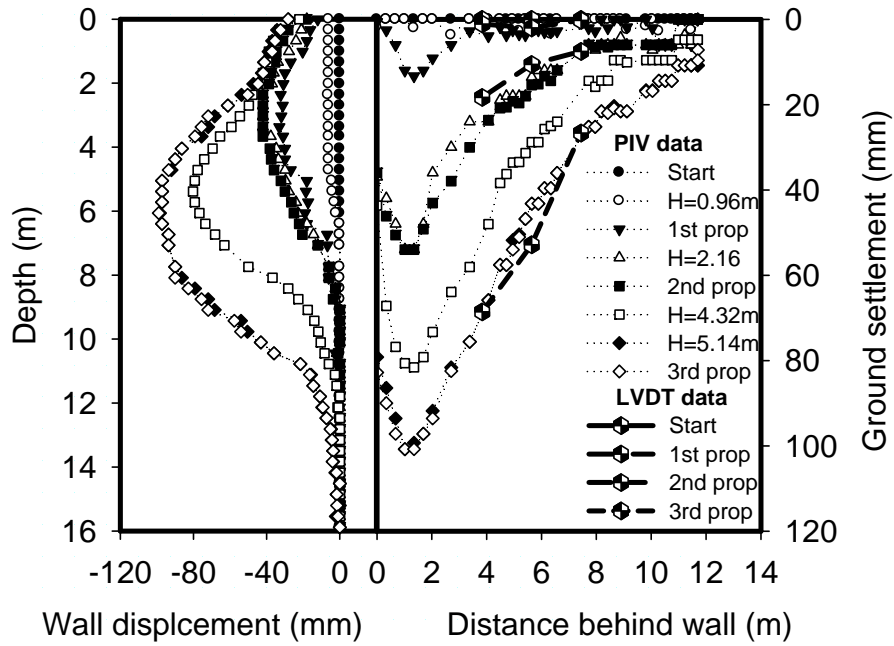
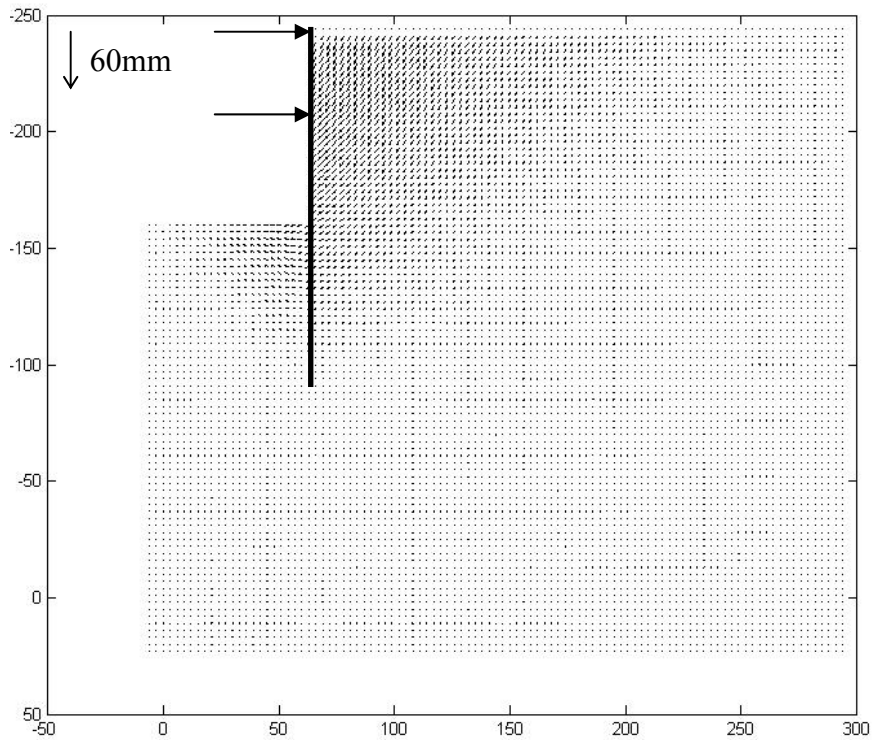
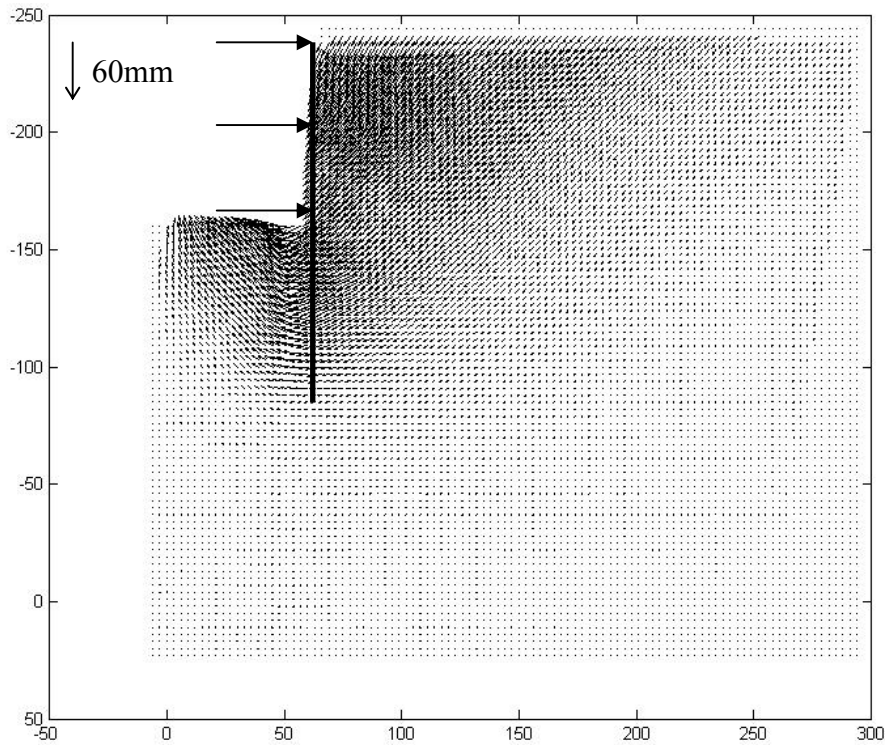


Figure 4.21 Development of wall deformation and ground settlement with progress of excavation (Test SYL05 at prototype scale).



(a) $H = 3.2\text{m}$



(b) H = 5.4m

Figure 4.22 Incremental deformation mechanisms for H=0.96m and H=5.4m for Test SYL05, at prototype scale)

4.4.2.7.1 Effect of wall stiffness for an excavation against a floating wall

Clough et al. (1989) proposed a semi-empirical procedure for estimating the wall movement due to excavations in clay, in which the maximum lateral wall movement; δ_{lm} is evaluated relative to factor of safety (FS) calculated ignoring the wall, and system stiffness, which is defined as follows:

$$\text{System stiffness } (\eta) = EI/\gamma_w h^4. \quad (4.3)$$

where EI is the flexural rigidity per unit width of the retaining wall, γ_w the unit weight of water and h the average support spacing.

It should be emphasized that FS is used as an index parameter. The system stiffness is defined as a function of the wall flexural stiffness, average vertical separation of supports, and unit weight of water, which is used as a normalizing parameter.

As a result, it is very interesting to know if the normalized wall deformation would change by varying system stiffness and keeping other parameters unchanged in a centrifuge test. The wall deformation profile is shown in [Figure 4.23](#).

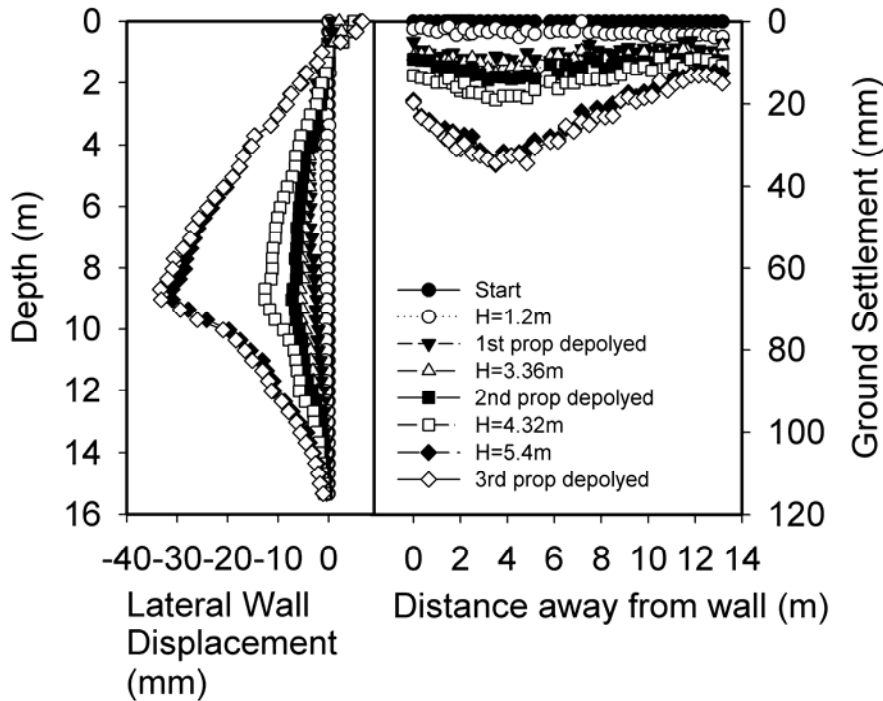


Figure 4.23 Development of wall deformation and ground settlement with progress of excavation ([Test SYL04 at prototype scale](#))

For [Test SYL04](#), the retaining wall thickness is increased by 3 times compared with [Test SYL05](#). Since the moment of inertia I term is proportional to the cube of the thickness of wall, the system stiffness is increased by a factor of 27. [Figure 4.24](#) shows w_{max} plotted relative to system stiffness for various values of FS. The factor of safety for the present excavation geometry ($H=5.4\text{m}$ at prototype scale) and soil profile is calculated by the following expression.

$$FS = \frac{(N_c)(c_u)}{H \left(\gamma - \frac{2}{\sqrt{2}} \frac{c_u}{B} \right)} = \frac{(6)(27)}{5.4 \left(16 - \frac{2}{\sqrt{2}} \frac{27}{12} \right)} = 2.34 \quad (4.4)$$

The system stiffness of the rigid wall is calculated to be 2850 whereas that of the flexible wall is 106. The black circles in [Figure 4.24](#) show the results of the present

study. This overestimation of wall deformation by a factor of about 2.3 shows the need for a more refined estimation procedure. The use of factor of safety to quantify wall deformation ignores small strain non-linear stiffness of the soil and also the incremental nature of the construction. This also points towards the controversial question of how much the stiffness of the wall matters in controlling ground deformations around deep excavation. In [Chapter 6](#), a detailed account for the effect of soil small to medium strain stiffness on wall deformation will be presented.

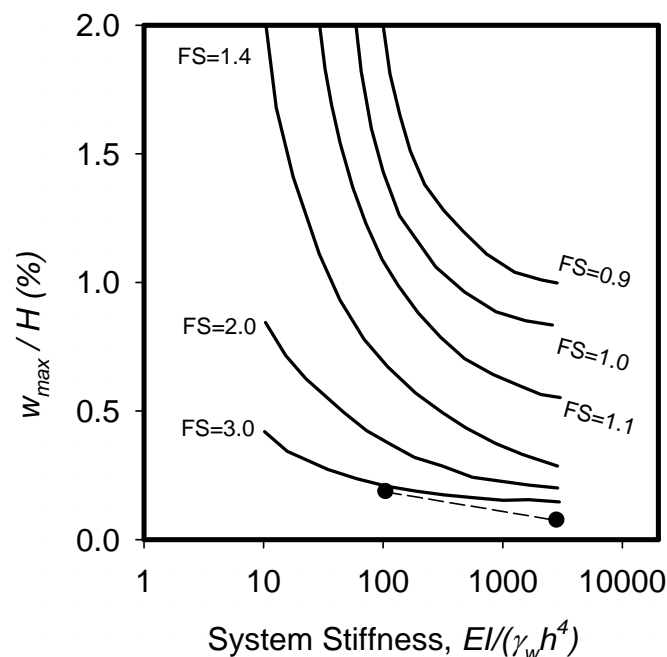


Figure 4.24 Variation of wall deformation with system stiffness (after Clough et al. 1989)

4.4.2.7.2 Effect of depth to stiff bearing stratum

Mana and Clough (1989) presented numerical parametric studies on the effect of the depth to the bearing stratum on the maximum lateral wall displacement for fixed base wall. Results showed that movements increase with excavation width and with depth to the bearing stratum. The magnitude of lateral wall displacement increased by a factor of 1.5 as the depth to the stiff layer doubled. However, soils were considered to be elastic which implies that the local development of plastic strain is not possible.

Jen (1998) investigated the same issue with a more sophisticated numerical constitutive model i.e. the MIT-E3 model. Parametric studies were carried out on the effect of depth to the hard stratum on lateral wall displacement for excavations using a floating wall. Results showed that the depth of end stratum only affects wall deflections below the excavation level, especially those at the wall toe. On the other hand, the depth of the clay layer has a stronger impact on the distribution of far-field ground settlement. As the location of the rigid base become shallower, the tail of the settlement trough tapers off much more rapidly. The distance for the tapering off is roughly equal to the depth of stiff stratum.

Figure 4.25 shows the development of wall displacement and ground settlement as excavation in shallow clay (Test SYL07) progresses. Since the wall toe is not fixed at the base, wall toe rotation and wall bulging movement are the major deformation features. The lateral wall deformation mode shape is very similar to that of Test SYL05 (See Figure 4.21) except that the length of the bulge is limited to the depth of soft layer.

The evolution of the soil displacement mechanism is illustrated in **Figure 4.26** for different stages of excavation. The introduction of the first pair of pre-loaded props induces inward displacement at the wall crest with cantilever bending as shown in **Figure 4.26(a)**, after further excavation and the deployment of the second level of props. The deformation mechanism changed to a bulging mode which is equivalent to loading a propped cantilever beam. It is the stage that wall rotation can be developed about the top, if the base of wall is free to translate (as shown in **Figure 4.26(b)**). After the introduction of the second prop, the wall length below the lowest prop is effectively moment restrained at the prop location. As an effect, not much wall rotation could be observed at the lowest prop location for excavation stage 3 (**Figure**

4.26(c)). Figure 4.27 shows the total displacement field for Test SYL07. The maximum lateral wall displacement for the second and the third stages were 45mm and 100mm, respectively. These movements were equivalent to about 0.9% and 2% of average overall engineering shear strain, respectively, within the deformation zone, according to Bolton et al. (2008).

Compared with the deformation mechanism of the equivalent excavation test (Test SYL05) in deep soft clay, two major points emerge. Firstly, the amount of maximum wall displacement is not affected by the depth to the stiff stratum. The difference in the two tests is within 10%. This is comparable to the observation on numerical simulations by Jen (1998) when suggested that the maximum wall movement would differ only by 20% when the depth to the stiff layer increased from 5m to over 50m below wall toe. Secondly, the settlement profile of the test (SYL07) does show a much more rapid tapering off with distance from the wall. This observation also echoes the results simulated in FEA by Jen (1998). This implies that an engineer who wants to control the extent of excavation-induced movement should have considered fixing the wall toe using ground improvement methods, if no hard stratum could conveniently be reached.

4.4.2.7.3 Effect of wall toe fixity conditions

For deep excavations in soft ground, the maximum deflection of the retaining wall usually occurs at the final excavation level. To restrict wall deflections at this location, ground improvement techniques (e.g. Jet-grouting) can be employed prior to excavation. A common approach is to improve the entire soil layer within the excavation zone below the excavation level to prop the wall toe. In the present study,

a centrifuge test (Test SYL06) was carried out to understand how an infinitely stiff fixed base grout layer at the wall toe would affect the deformation mechanism.

Figure 4.28 shows at prototype scale the variation of wall displacement and ground settlement as an excavation using a wall fixed at 9.6m depth (Test SYL06) progresses. Since the wall toe is fixed to the base, wall bulging is the deformation mode permitted. The lateral deformation mode shape is similar to that of Test SYL05 except that a bending moment restraint is being imposed at the wall toe. Figure 4.29 shows the total deformation mechanism of the fixed base retaining wall for an excavation depth of 5.4m. The maximum lateral wall displacement for the second and the third stages were 40mm and 65mm, respectively. These movements were equivalent to about 0.8% and 1.3% of average overall engineering shear strain, respectively, within the deformation zone. In effect, the wall toe fixity limited both the lateral soil deformations below the final excavation level and the lateral extent of the soil settlement trough.

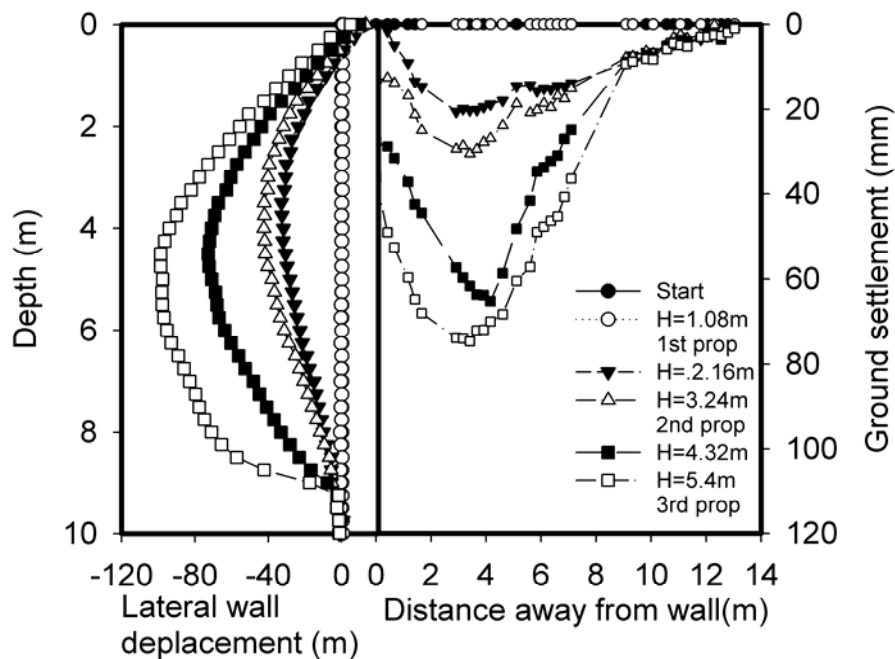


Figure 4.25 Development of wall deformation and ground settlement with progress of excavation (Test SYL07)

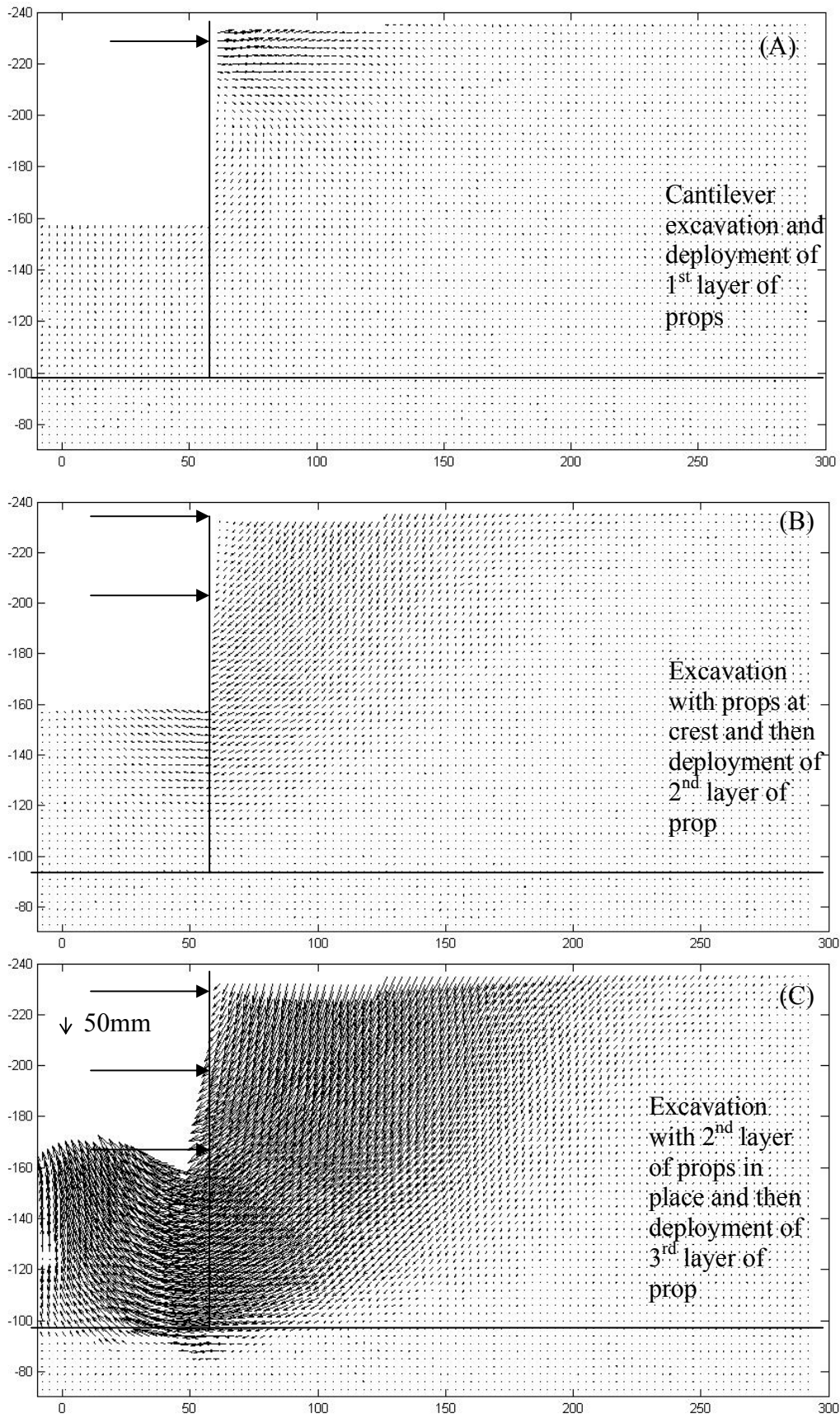


Figure 4.26 Incremental displacements for different stage of excavation for Test SYL07

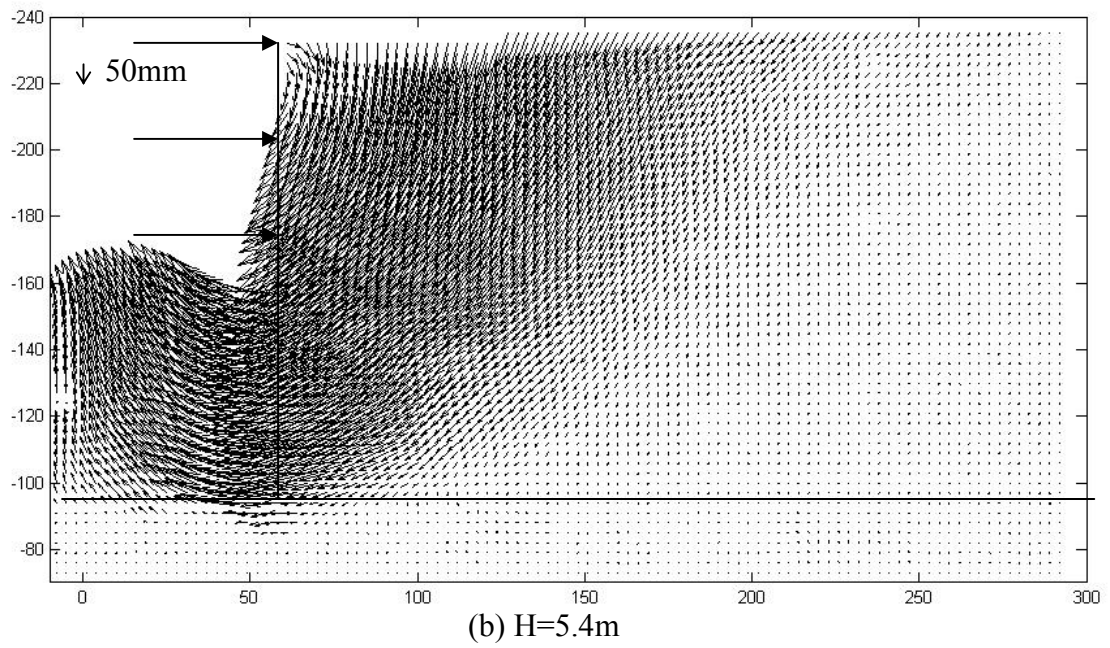
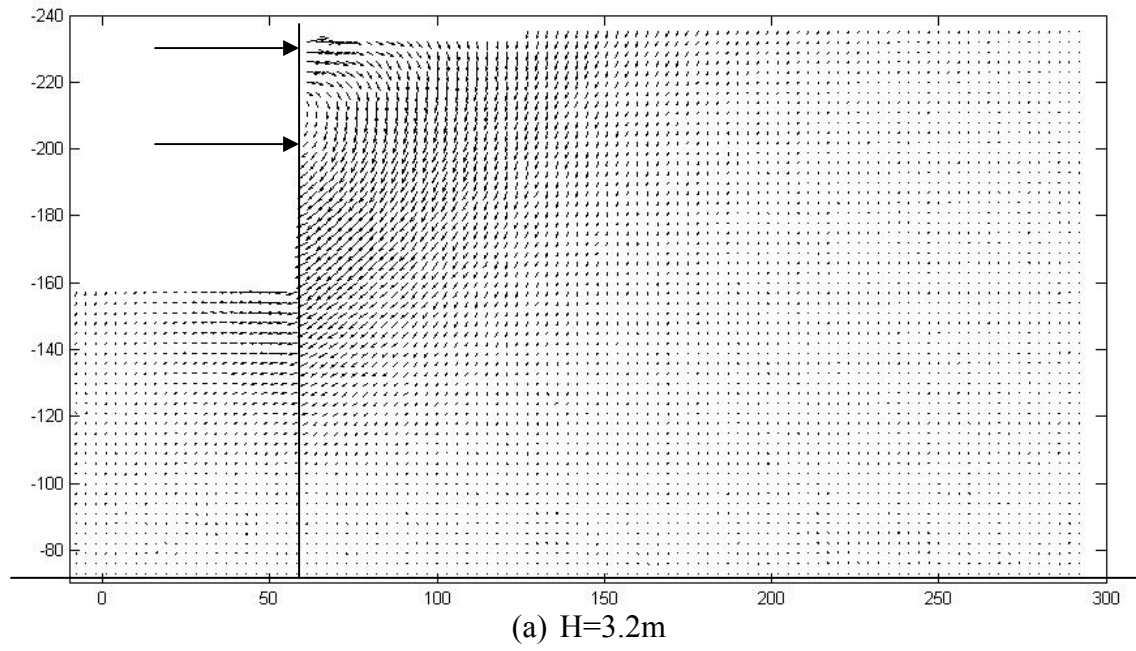


Figure 4.27 Total displacements after second and third stage of excavation for Test SYL07

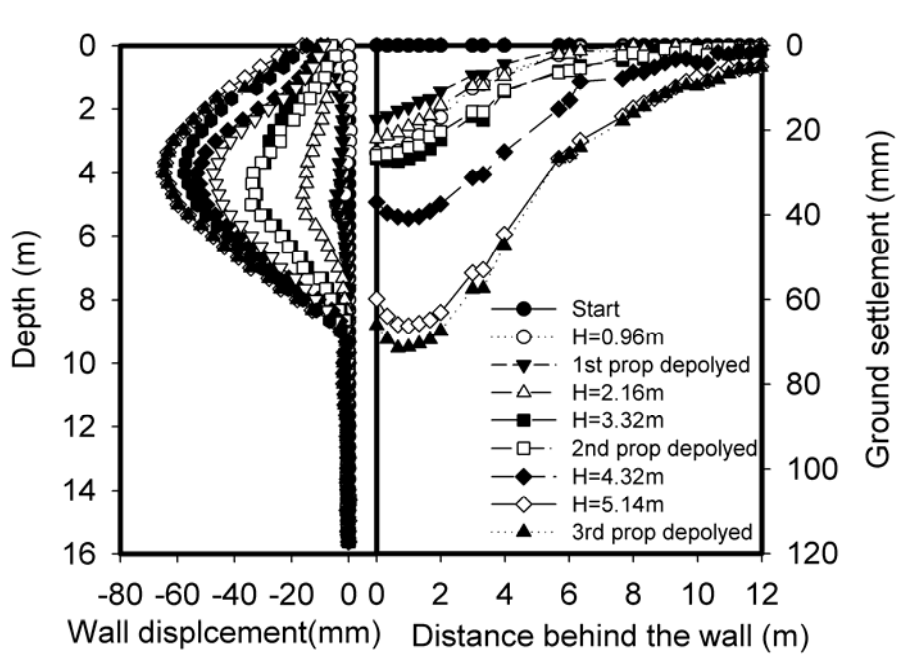


Figure 4.28 Development of wall deformation and ground settlement with progress of excavation (Test SYL06).

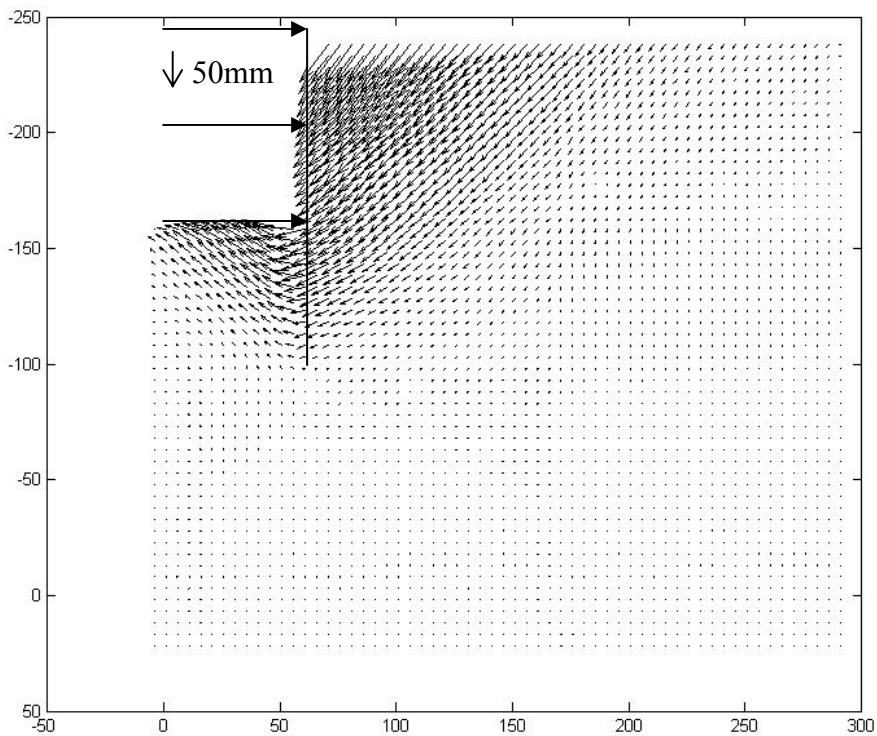


Figure 4.29 Total deformation mechanism for the third stage of excavation (Test SYL06)

Figure 4.30 compares the final wall deflection and ground settlement profiles of the excavation tests using the flexible wall. The following comments are made.

1. The depth to the stiff stratum does not have a significant effect on maximum wall displacement for floating walls.
2. The wall toe fixity condition is effective in controlling soil deformation below final excavation level and the lateral extent of ground surface settlement.
3. The wavelength of deformation is a function of depth to the stiff layer. For a fixed based wall, the wavelength is the same as the unsupported length of the wall below the lowest prop; whereas the wavelength for the floating wall is equal to 1.3-1.5 times the unsupported length of the wall below the lowest prop.

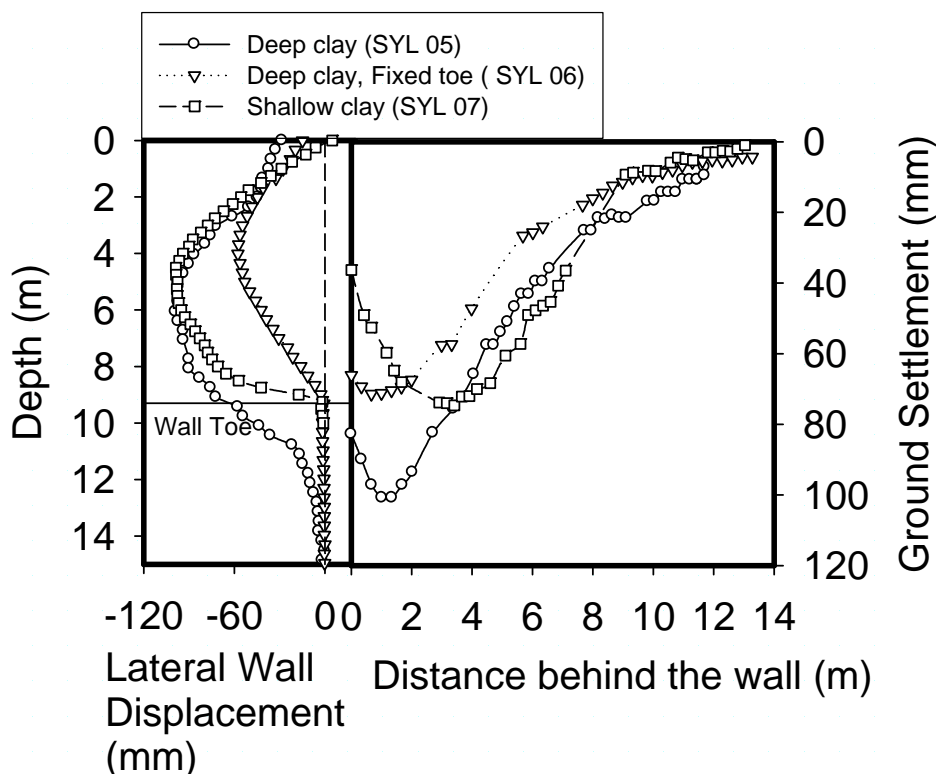


Figure 4.30 Wall deflection and ground settlement profile for excavation using flexible wall (Test SYL05, SYL06 and SYL07)

Following the approach of Clough et al.(1989), the incremental wall displacement can be normalized as a perspective of the maximum displacement in wall movement and plotted against depth below the lowest prop normalized against wavelength of the significant deformation as shown in Figure 4.31. Results show that the normalized curves for both floating (SYL05) and fixed base walls (SYL06) broadly follow the cosine curve. A cosine-shaped deformation mode shape is thereby proven to be a good representation of the typical wall bulging displacement profile below the lowest prop for multi-prop deep excavation stages.

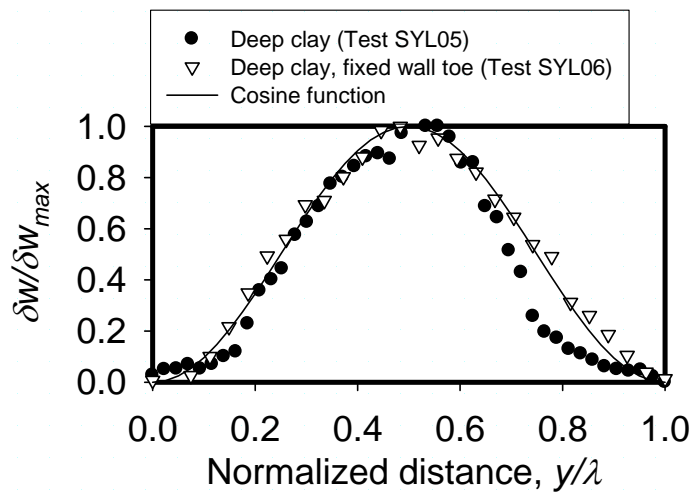


Figure 4.31 Variation of normalized incremental displacement with distance below the lowest prop

4.4.2.7.4 Effect of soft props deformation mechanism

According to Jen (1998), reductions in strut stiffness increases wall deflections occurring above excavation level, with the maximum wall deflection occurring closer to the excavated level whereas the lateral soil movement below the excavation level is not influenced by the stiffness of the prop system. As the props become more compressible, the maximum wall movement increases with negligible change in the extent of settlement trough. The reduction of prop stiffness also causes the soil to develop a shallower failure mechanism. A centrifuge experiment Test SYL03 was carried out to investigate the issue. The prop stiffness was measured by conducting axial-load displacement tests in a loading rig. The target stiffness of a fully-saturated prop is found to be about 1.66kN/mm at model scale or 100 kN/mm at prototype scale. For the present test, the prop stiffness was reduced by a factor of 3 to 550N/mm at model scale. Figure 4.32 shows the development of wall deformation and ground settlement with progress of excavation. The lateral wall deformation mode shape is similar to that of Test SYL04 except for the fact that the soft prop response allows rigid body displacement of the retaining wall into the excavation pit. Figure 4.33 shows the total deformation mechanism of the test. A triangular wedge mechanism (45 degree shear planes) is found to satisfy the deformation mechanism on the active side. The maximum lateral wall displacement for the second and the third stages were 37mm and 80mm, respectively. These movements were equivalent to about 0.74% and 1.6% of average overall engineering shear strain, respectively, within the deformation zone. Figure 4.34 compares the wall displacement and ground settlement profiles for excavations using a stiff wall with either softer or stiff props. Since the soft response of the props allows rigid body lateral displacement of the wall, soil on the active side is sheared at an angle 45 degree. A spandrel type settlement profile

occurs with a width equal to the depth of the wall. This extra soil strain developed on the active side will have induced additional reduction in soil stiffness, causing more soil deformation as the excavation goes deeper.

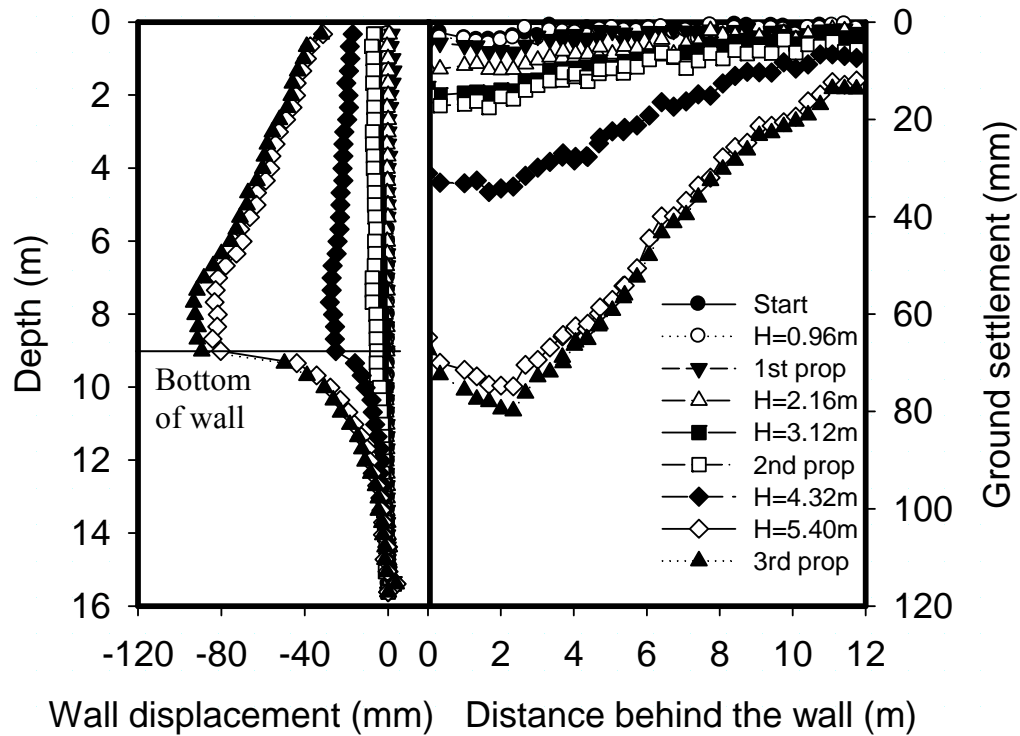


Figure 4.32 Development of wall deformation and ground settlement with progress of excavation (Test SYL03)

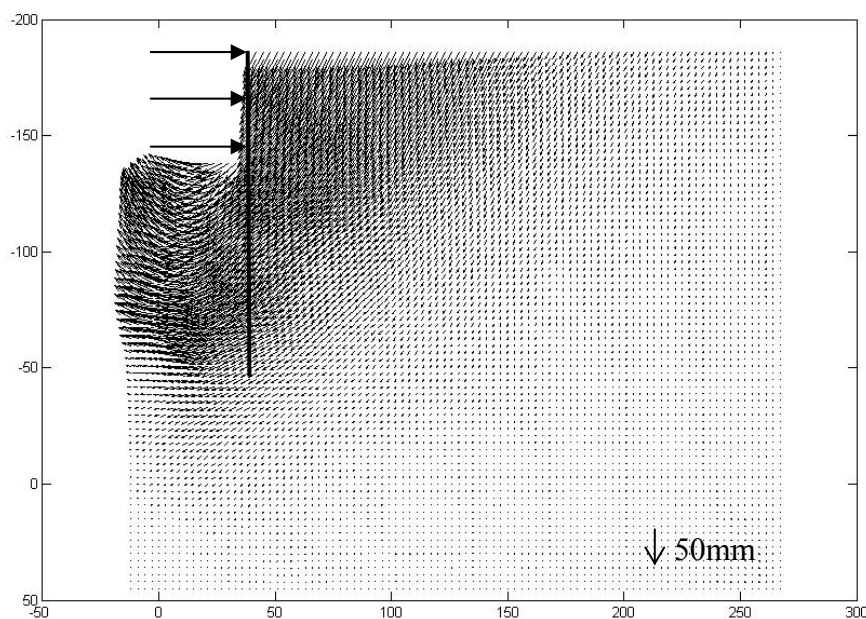


Figure 4.33 Deformation mechanism for excavation using rigid retaining wall with soft props at H=5.4m (Test SYL03)

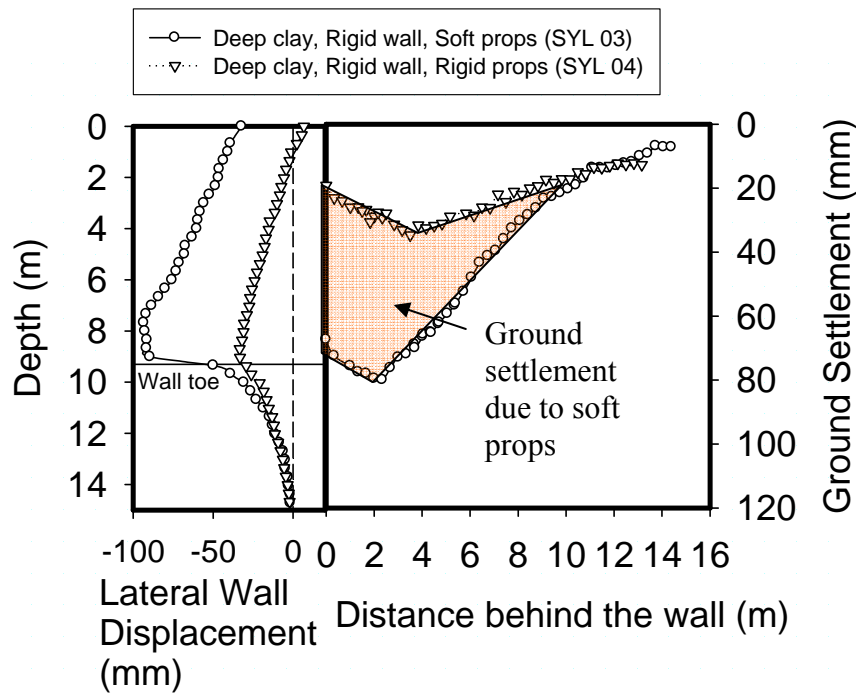
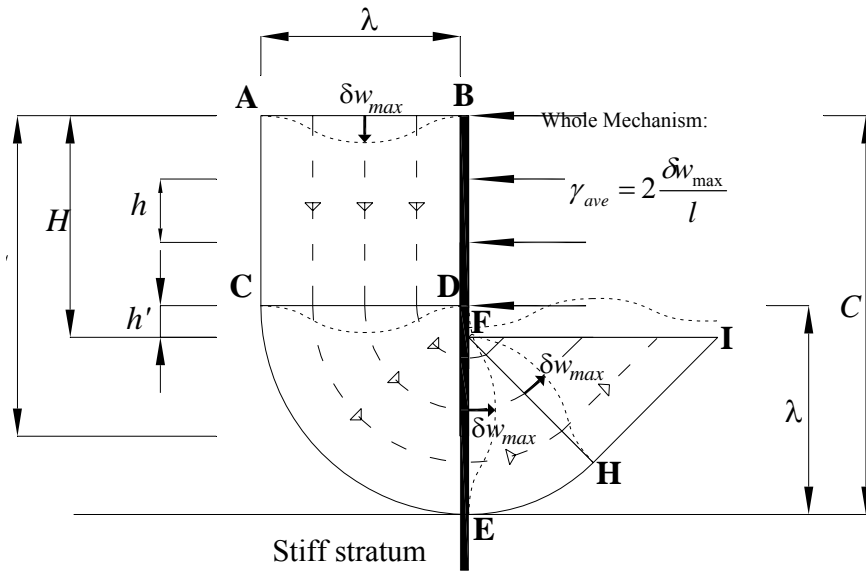


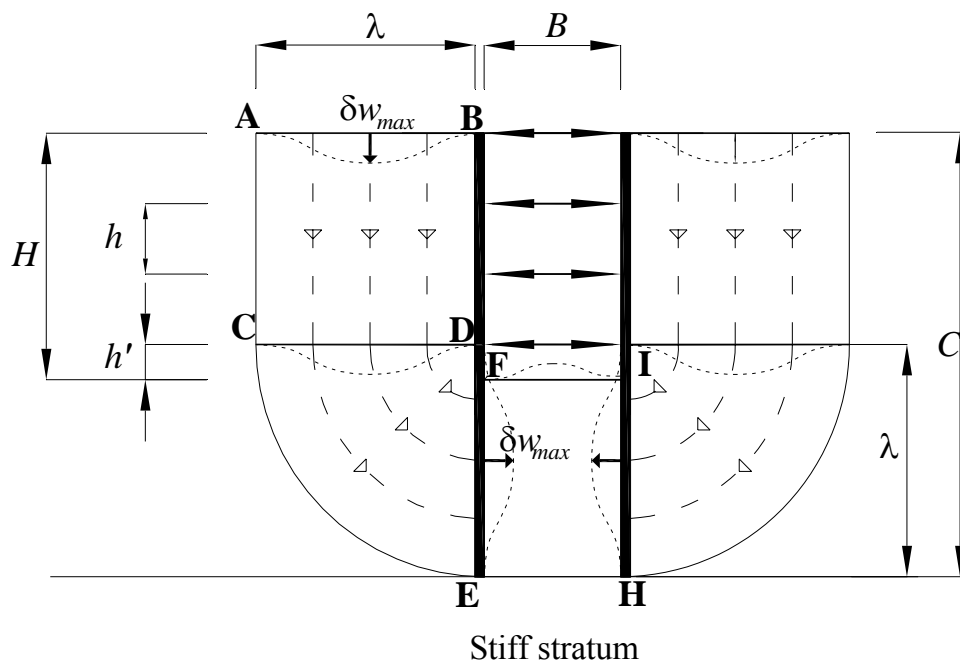
Figure 4.34 A comparison of wall displacement and ground settlement on Tests with different prop stiffness

4.4.2.8 Proposed incremental deformation mechanism for wall bulging

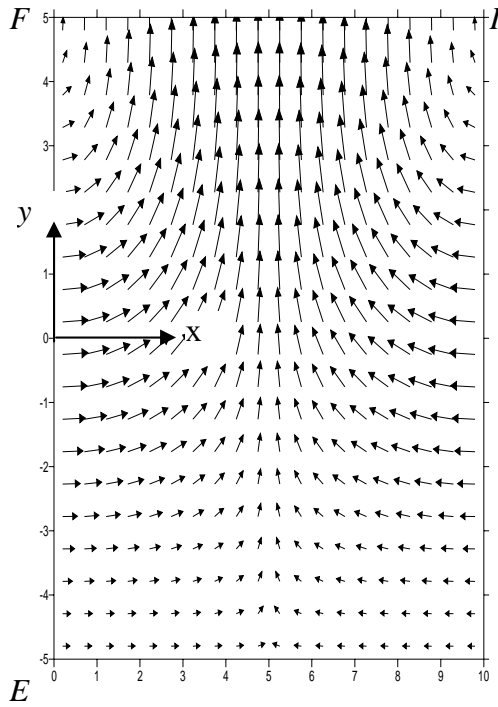
The original mechanism of Osman and Bolton (2006) shown in [Figure 4.35\(a\)](#) only applied to wide excavations (i.e. $2\sqrt{2}(\alpha s - h') \leq B$); narrow excavations (i.e. $2\sqrt{2}(\alpha s - h') > B$) called for the development of the alternative mechanism of [Figure 4.35\(b\)](#). The deformation mechanism inside zone EFHI is defined in [Figure 4.35\(c\)](#). The assumed mechanism satisfied the zero volumetric strain condition throughout so that undrained movement is guaranteed everywhere inside the mechanism. In [Chapter 5](#), the mechanism is adopted to convey the kinematics of the staged deep excavation process.



(a) Incremental displacement field for wide excavation (after Osman and Bolton, 2006)



(b) Incremental displacement field for narrow mechanism



$$\left\{ \begin{aligned} \delta w_y &= \frac{\lambda \times \delta w_{max}}{4B} \left(\pi + \frac{2\pi y}{\lambda} + \sin\left(\frac{2\pi y}{\lambda}\right) \right) \left(\sin\left(\frac{\pi x}{B}\right) \right) & (4.5) \\ \delta w_x &= \frac{\delta w_{max}}{2} \left(1 + \cos\left(\frac{2\pi y}{\lambda}\right) \right) \left(\cos\left(\frac{\pi x}{B}\right) \right) & (4.6) \end{aligned} \right.$$

where

λ = Wavelength of cosine

δw_{max} = Maximum incremental wall displacement

B = Width of excavation

(c) Displacement field in Zone EFHI

Figure 4.35 Proposed deformation mechanism

4.4.3 Soil strains

This section presents the profiles of volumetric and engineering shear strain distributions within the soil during the excavation process. Strains are calculated based on the PIV displacements presented in the previous section. A co-rotational deformation formulation is used allowing rotation, translation and distortion, thereby eliminating numerical instability associated with small gauge length, and separating rigid body rotation from deformation (White, 2002).

Strains can be visualized using the Mohr circle of strain as shown in [Figure 4.36](#).

Since the PIV displacement data was obtained from two different cameras, it is difficult to obtain a complete strain profile directly from the PIV method suggested by White et al. (2003). A new mesh for soil patches has to be built and the displacement data of the patches needs to be obtained by the linear interpolations. By applying the small strain formulation, all necessary strain components ($\epsilon_{xx}, \epsilon_{zz}, \epsilon_{xz}$) can be obtained and used to obtain volumetric strains and engineering shear strains.

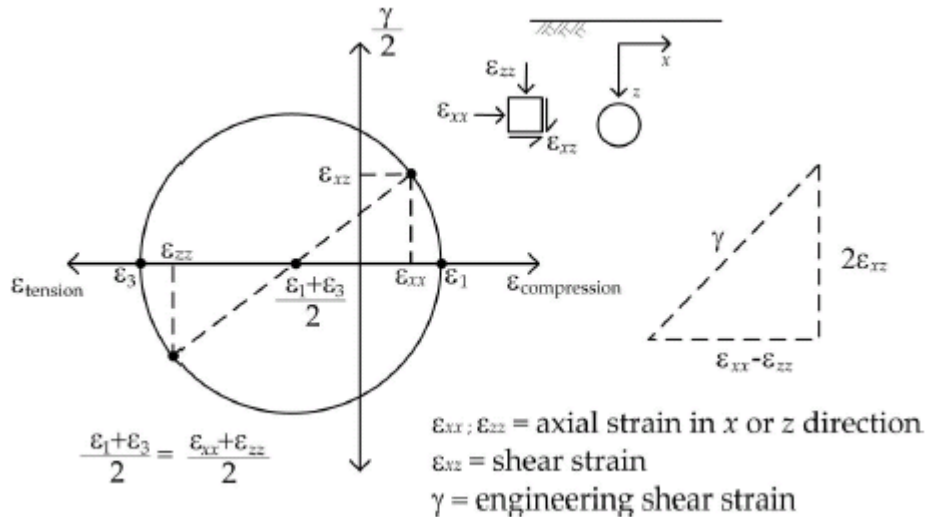


Figure 4.36 Mohr circle of strain

The calculation of strain is highly vulnerable to errors in PIV displacement data. Errors evolve as a result of the level of accuracy of PIV data considering very small movement and more obviously from the difficulties associated with stitching PIV data from different pictures together. The standard deviation in pixel space for the present calibration procedure is about 0.3 pixels which correspond to 0.1mm error in model scale (or 6mm in prototype scale at 60g).

4.4.3.1 Volumetric stain calculation

Volumetric strain (ϵ_v) was defined as the sum of strain in xx , yy and zz directions. Since the strain level in the yy direction is zero for the plane strain condition, the volumetric strain is calculated as follows:

$$\epsilon_v = \epsilon_{xx} + \overset{0}{\cancel{\epsilon_{yy}}} + \epsilon_{zz} \quad (4.7)$$

Figure 4.37 shows a typical volumetric strain map of an excavation in shallow clay for a final excavation depth of 5.4m. It is shown that for the final stage of excavation in shallow clay with short drainage paths the volumetric strain component is below

1%. This implies a nearly undrained condition for an excavation which finished in half an hour in model time. Similar results were obtained for other excavation tests.

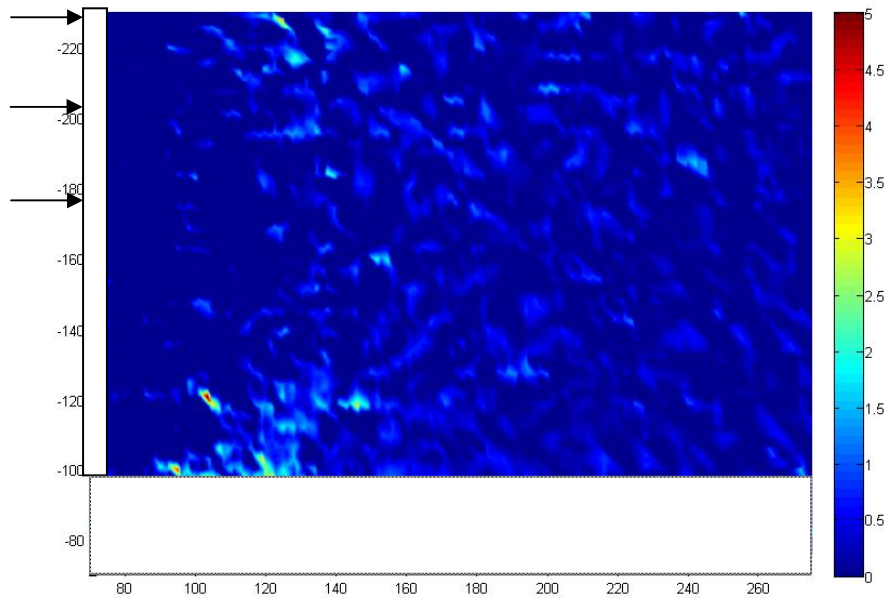


Figure 4.37 Development of volumetric strain for excavation depth of 5.4m (Final stage of test SYL07)

4.4.3.2 Engineering shear strain calculation

The engineering shear strain is a useful quantity to understand the mechanism by which interaction between the retaining structure and the soil can be addressed. For plane-strain conditions, shear strain, ε_{xz} , and the engineering shear strain, γ , can be visualized using the Mohr circle of strain. The engineering shear strain can be calculated using the following equation:

$$\gamma = \sqrt{(\varepsilon_{xx} - \varepsilon_{zz})^2 + (2\varepsilon_{xz})^2} \quad (4.8)$$

Figure 4.38 (a), (b) and (c) show the engineering shear strain map on the active side for excavation depths of 1.08m, 3.24m and 5.40m, respectively for test SYL07.

For an excavation depth of 1.08m, the wall behaved as a simple cantilever; then the first layer of props was introduced, and slightly pre-loaded. Due to the increase in lateral stress near the soil surface, some shear strain concentration happened near the wall crest on the retained side.

When the excavation depth had increased to 3.24m, the 2nd layer of props was introduced. A shear zone developed near the wall toe as a result of wall rotation about the crest of the retaining wall. The average shear strain level was the about 1%.

After installation of the third layer of props, any further movement must be deep-seated. Clearly, a deep seat soil movement developed. A shear band developed from the wall toe and extended upwards towards the soil surface. It is interesting that the width of the shear band develops as it extends above the elevation of the lowest prop towards the soil surface, alongside a zone with smaller shear strain next to the retaining wall above the lowest prop. This observation echoes the discussion in the previous section about the formation of the arching mechanism below the lowest strut since the major principal stresses are directed towards the lowest strut level, while an underlying compressive soil arch transfers loads onto the propped section of the wall.

For the other two flexible wall cases, [Figure 4.38](#) and [Figure 4.39](#) show the distribution of soil engineering shear strain for an excavation depth of 5.4m in [Tests SYL05](#) and [SYL06](#), respectively. For [Test SYL05](#), the depth to the stiff layer (18m in prototype) is about two times the length of the wall (9.6m in prototype). The depth of the mechanism extended deep into the clay layer and the settlement trough is accordingly wider. On the contrary, the depth of the mechanism is controlled by the fixed base layer for [Test SYL06](#) and the width of the settlement trough narrows down to a length of one wall depth.

Data of the cases from **Test SYL04 (Figure 4.39)** and **SYL05 (Figure 4.41)** offer the opportunity of examining the difference in mechanism when comparing with excavation cases with a rigid wall and a flexible wall. Due to the rigidity of the retaining wall, wall flexure below the lowest prop location is the main deformation mechanism (**Test SYL04**). A very thin shear band developed at the toe of the wall and extended towards the soil surface. In contrast to the behaviour of soil around a flexible wall, no soil arch forms as a result of the rigidity of the displacement boundary which suppresses bulging of the wall.

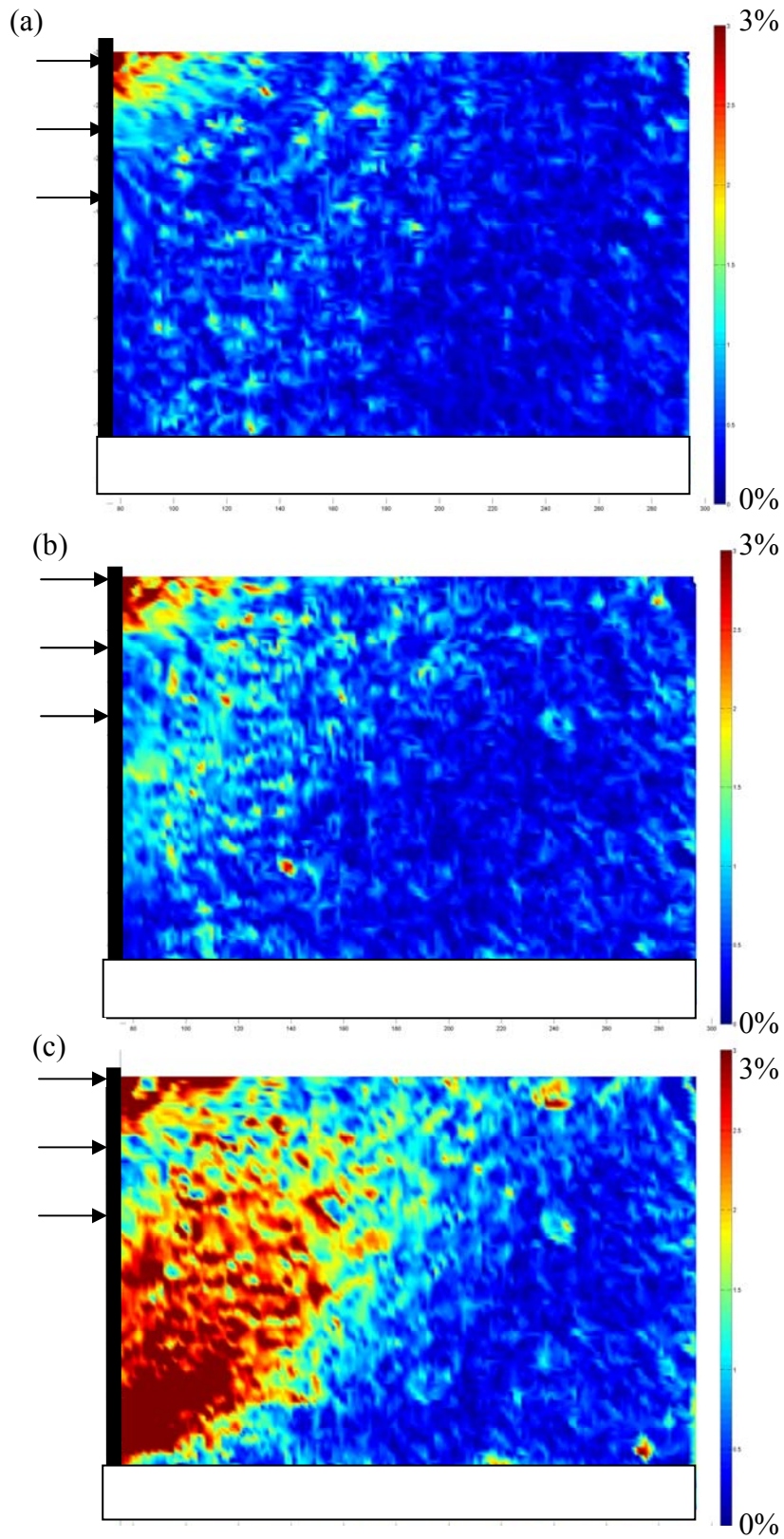


Figure 4.38 Engineering shear strain plots on active side for Excavation depth of H=1.08m, H=3.24m and H=5.40m for Test SYL07

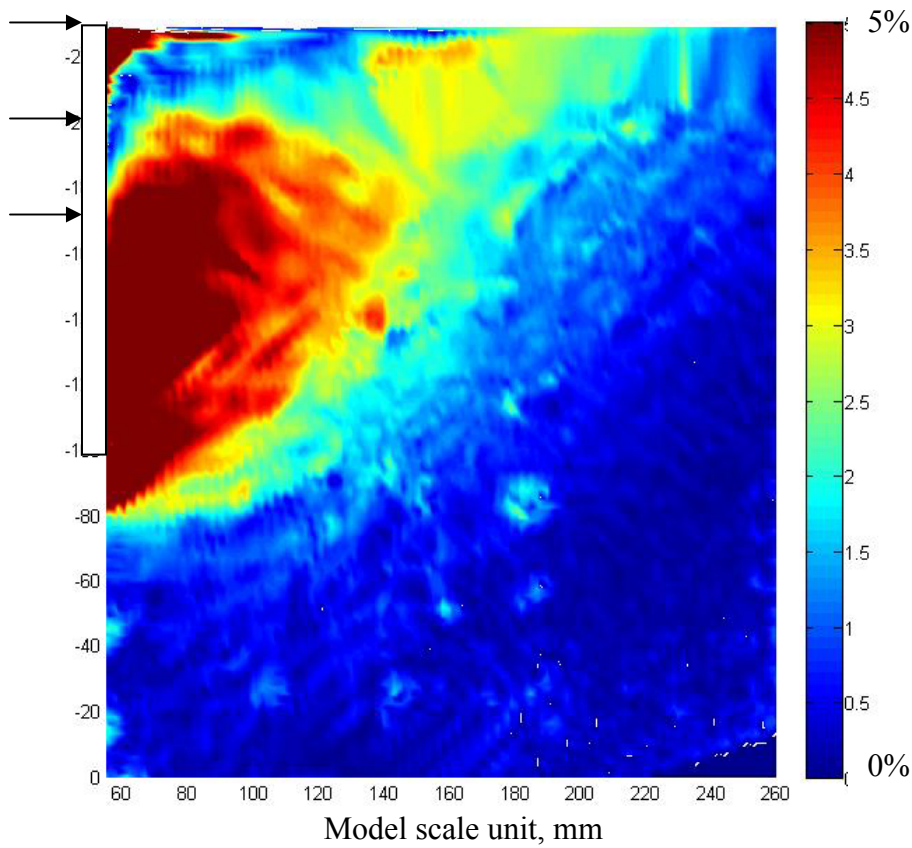


Figure 4.39 Engineering shear strain plots excavation depth of H=5.40m for excavation in deep clay using flexible wall (Test SYL05)

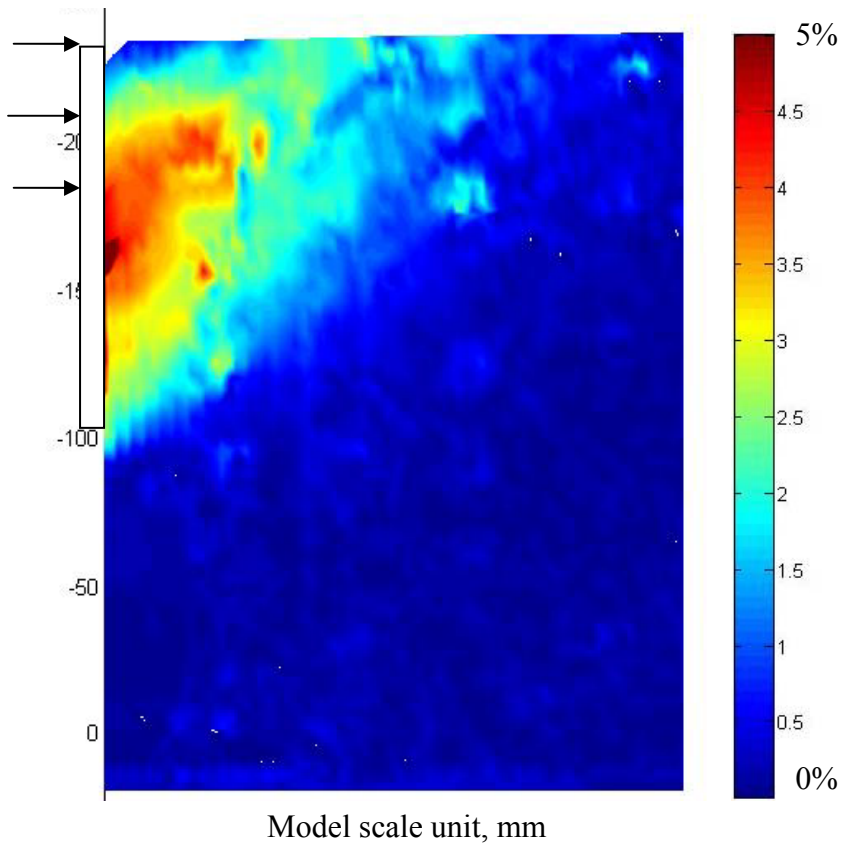


Figure 4.40 Engineering shear strain plots excavation depth of H=5.40m for excavation in deep clay using flexible fixed-base wall (Test SYL06)

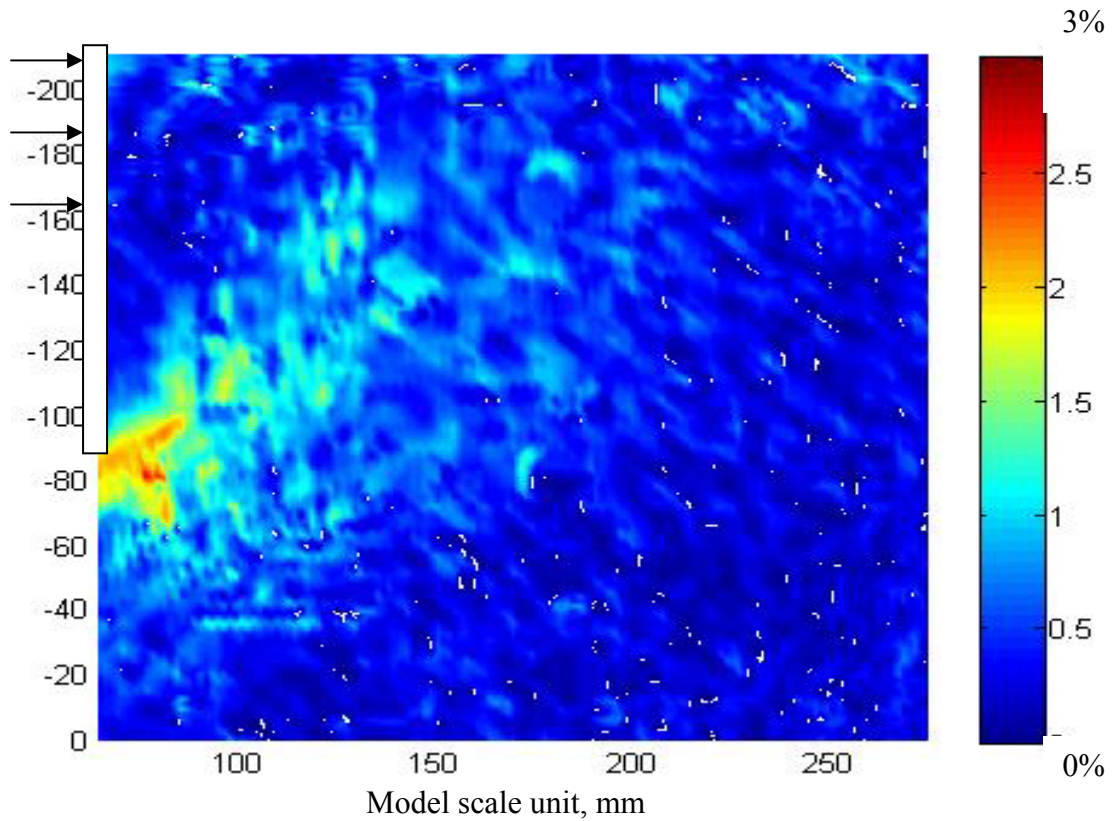


Figure 4.41 Engineering shear strain plots excavation depth of H=5.40m for excavation in deep clay using a rigid wall with rigid props (Test SYL04)

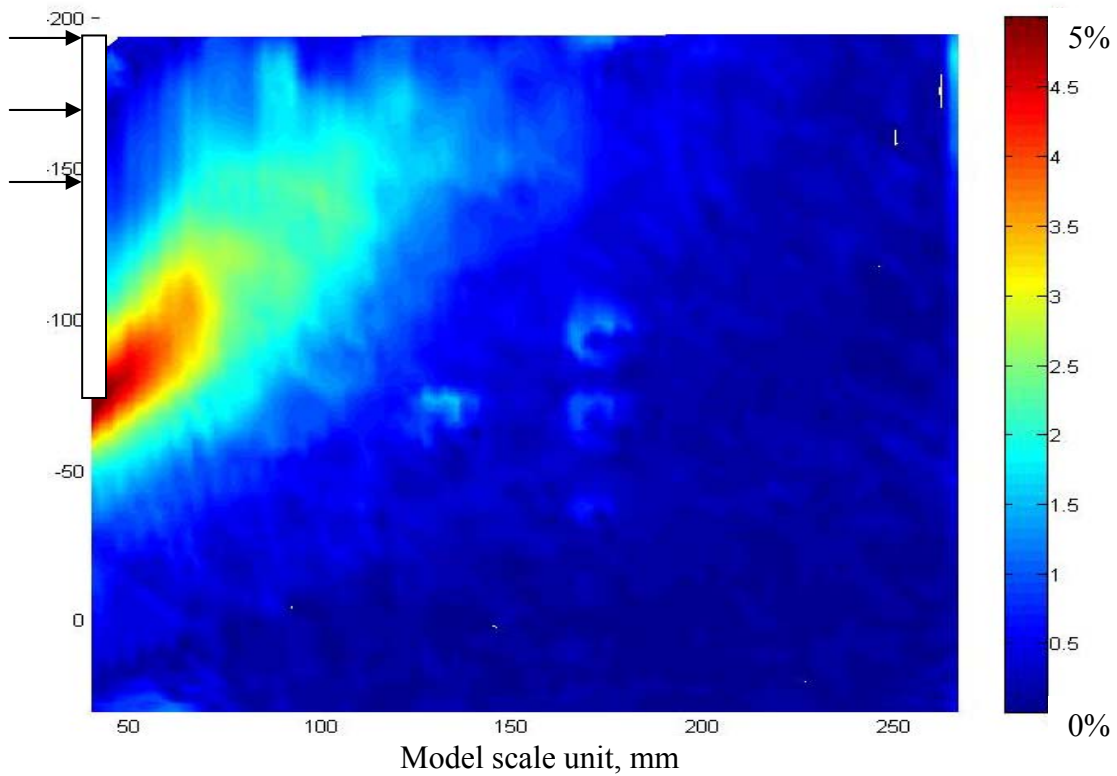


Figure 4.42 Engineering shear strain plots excavation depth of H=5.40m for excavation in deep clay using a rigid wall with soft props (Test SYL03)

4.4.3.3 Validation of the energy conservation principle

By conservation of energy of a geo-structural mechanism, the total loss of potential energy of the soil (ΔP) must balance the total work done in shearing the soil (ΔW) and the total elastic strain energy stored in bending the wall (ΔU_1) and in compressing the props (ΔU_2).

$$\Delta P = \Delta W + \Delta U_1 + \Delta U_2 \quad (4.9)$$

The potential energy loss on the active side of the wall and the potential energy gain of soil on the passive side can be calculated easily. The net change of gravitational potential energy (ΔP) is given by the sum of the potential energy changes for each soil patch:

$$\Delta P = \sum_{i=1}^n \left[\int_{Area} \gamma_{sat}(i) \delta w_y(i) dA \right] \quad (4.10)$$

where $\delta w_y(i)$ is the vertical component of displacement of soil in the i^{th} soil patch; $\gamma_{sat}(i)$ is the saturated unit weight of soil in the i^{th} soil patch.

While calculating the engineering shear strain, soil elements are formed as triangles linking three neighbouring patches. The total work done ΔW in shearing the soil is given by summing for each element:

$$\Delta W = \sum_{i=1}^n \left[\int_{Area} c_{mob}(i) |d\gamma(i)| dA \right] \quad (4.11)$$

where $c_u(i)$ is the undrained shear strength of soil in the i^{th} element; $d\gamma(i)$ is the shear strain increment of soil in the i^{th} element; and the corresponding mobilized strength ratio is given by the stress-strain relation defined by the simple power law obtained in

[Chapter 3, section 3.9.7](#) as follows:

$$\frac{c_{mob}}{c_u} = \left(\frac{\gamma}{\gamma_u} \right)^a \quad (4.12)$$

,where the γ_u and a parameters are found to be 5% and 0.33. The work done per unit area in the element is basically calculated as the area under the stress strain curve.

The total elastic strain energy stored in the wall, ΔU_1 , can be evaluated by repeatedly updating the deflected shape of the wall. It is necessary to do this since U is a quadratic function of displacement.

$$\Delta U_1 = \int_0^s \frac{EI\kappa^2}{2} dx = \int_0^s \frac{M^2}{2EI} dx \quad (4.13)$$

where E and I are the elastic modulus and the second moment of area per unit length of wall, and s is the length of the wall below the lowest prop.

The total elastic energy stored in the props, ΔU_2 , can be estimated by calculating the sum of the product of the displacement of prop after installation and the maximum prop force at different elevations.

$$\Delta U_2 = \sum_{i=1}^n \frac{F_i w_i}{2} \quad (4.14)$$

where F_i is the maximum prop force after installation and w_i is the corresponding compressive displacement.

Following the strain map created by the PIV data, a work map is calculated. **Figure 4.42** shows the total work done per metre at model scale by the soil around an excavation in shallow clay using a flexible wall (SYL07) at different stages of excavation. The total work done at different stages is calculated by **Equation 4.11**. On

the other hand, the total potential energy change by the soil elements at different stages is evaluated by Equation 4.10 and the distribution is plotted in Figure 4.43. The wall bending elastic energy and the prop compressive elastic energy are examined by Equation 4.13 and 4.14, respectively. Ideally, the potential energy change (ΔP) should be equal to the sum of work done by shearing of the soil, the elastic energy stored in the retaining structure ($\Delta U_1 + \Delta U_2 + \Delta W$) assuming minimal boundary friction at interfaces of solid boundaries and soil. Except for the first excavation stage of Test SYL07, the calculated potential energy change is within 25% of the calculated work done on the soil structure system. For the first excavation stage, since the fine measurement of displacement from the PIV data is prone to error due to control markers calibration and photo stitching, the difference between ΔP and $\Delta U_1 + \Delta U_2 + \Delta W$ is as large as 53%. Similar analyses have been carried out for Test SYL06 and SYL05. Their contour map for potential energy change and the work done by the shearing of the wall are shown in Figure 4.44 and Figure 4.45, respectively. The variation of the potential energy change and work done by the soil structure system is plotted on Figure 4.46. The difference of the energy terms is less than 30%. Table 4.2 summarizes the results of the studies.

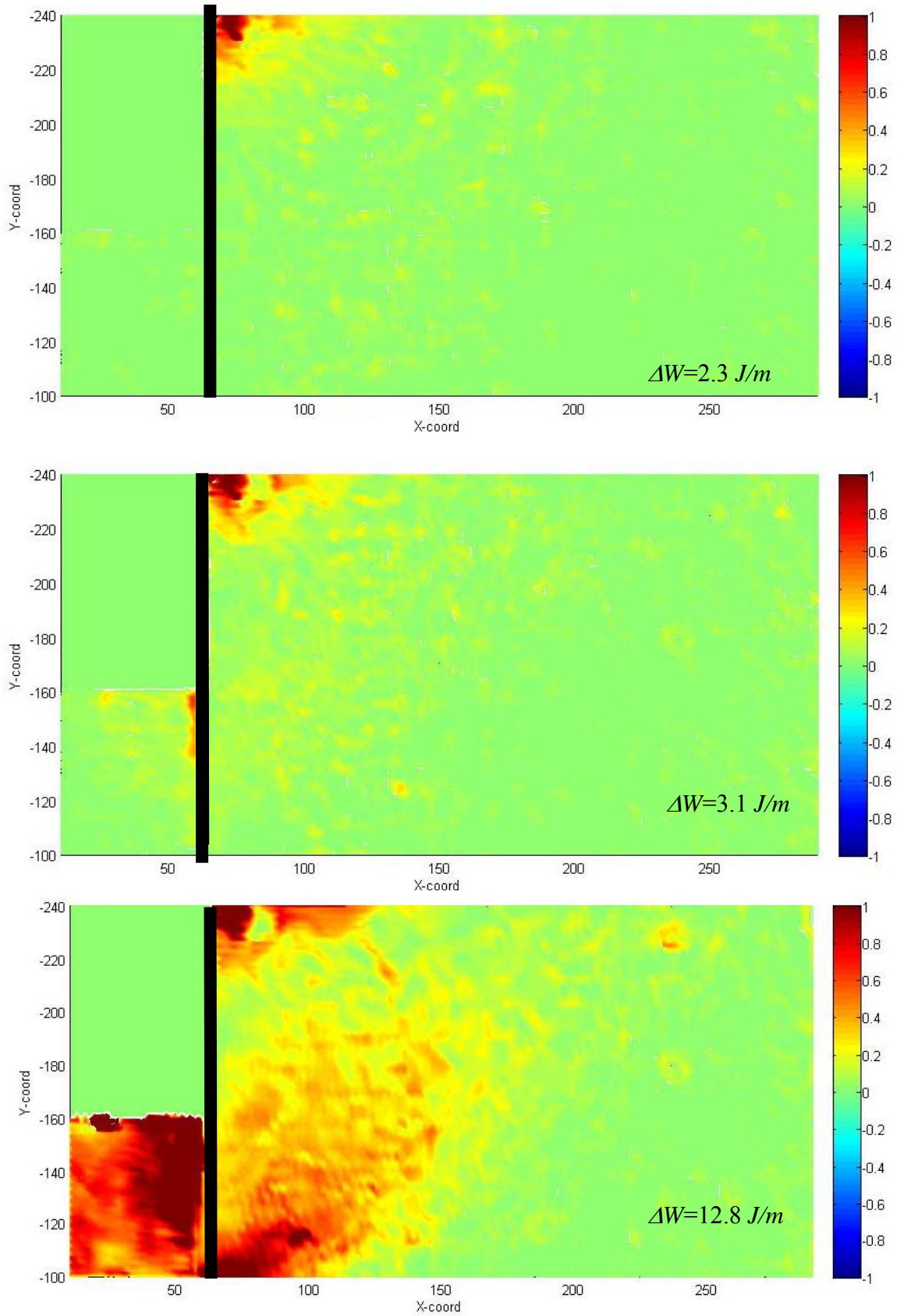


Figure 4.42 Work done in excavation depth of 1.08m, 3.24m and 5.40m for TEST SYL07

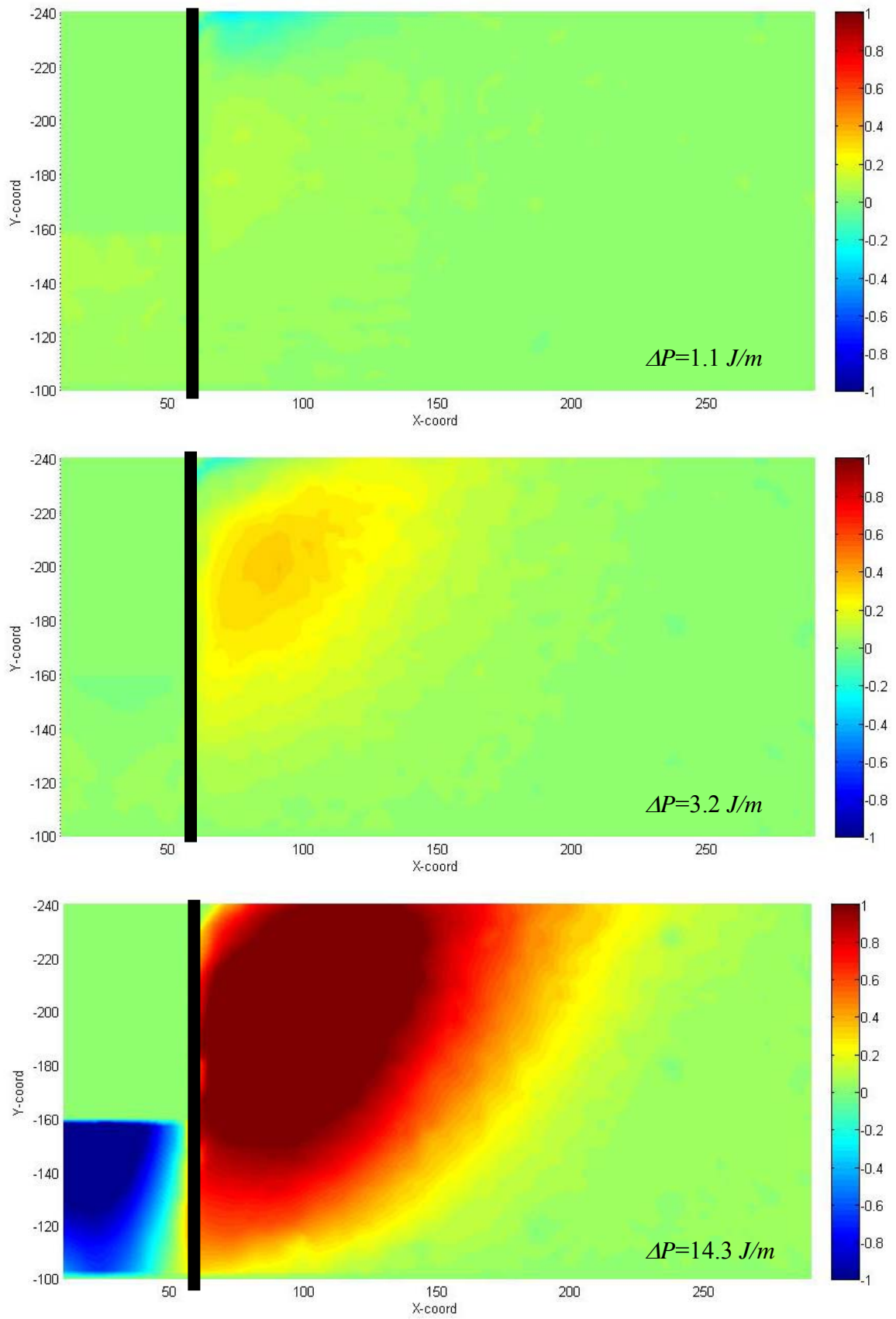


Figure 4.43 Potential energy change for excavation depth of 1.08m, 3.24m and 5.40m for Test SYL07

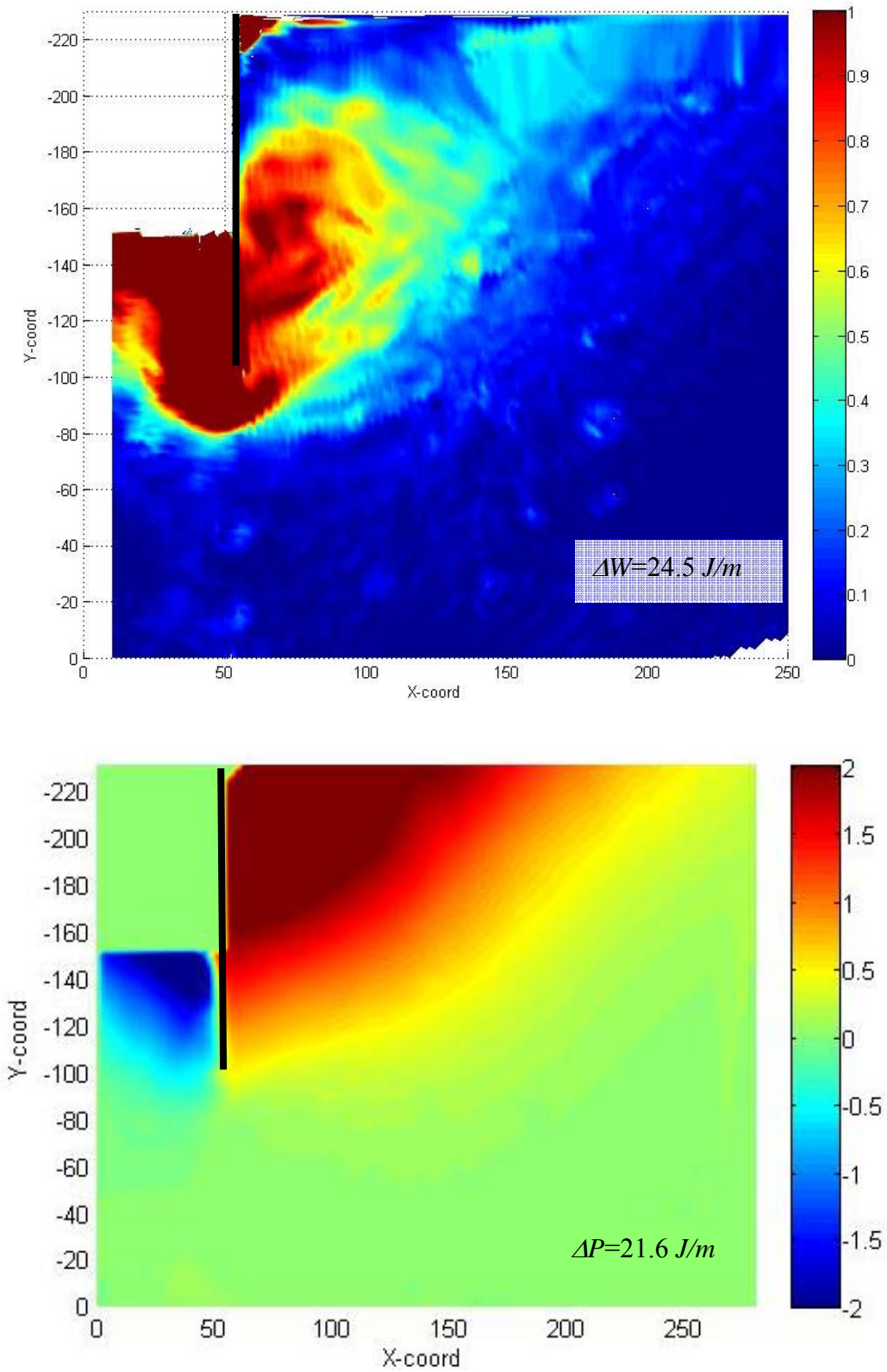


Figure 4.44 Work done and potential energy change for excavation depth of 5.40m for Test SYL05

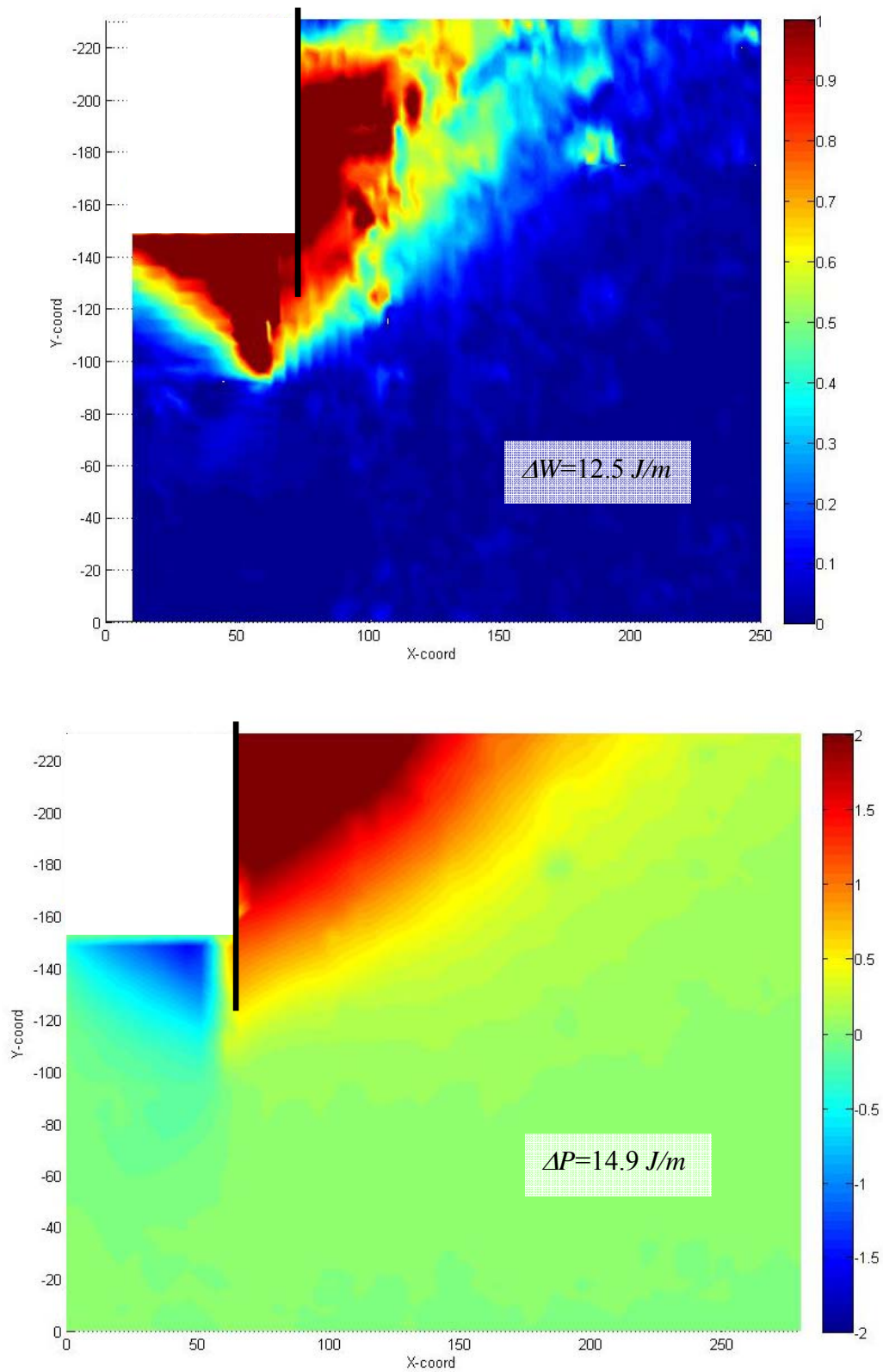


Figure 4.45 Work done and potential energy change for excavation depth of 5.40m for Test SYL06

Table 4.2 A summary of calculated energy terms for different tests

Test & stage	ΔU_1 (J/m)	ΔU_2 (J/m)	ΔW (J/m)	$\Delta W + \Delta U_1 + \Delta U_2$ (J/m)	ΔP (J/m)	% error
SYL07 1	0.0067	0.03	2.3	2.33	1.1	-52.86
2	0.98	0.08	3.1	4.16	3.2	-23.10
3	1.10	0.19	12.8	14.09	14.3	1.49
SYL06 3	0.10	0.17	24.5	24.77	21.6	-12.80
SYL05 3	2.40	0.16	12.5	15.06	14.9	-1.06

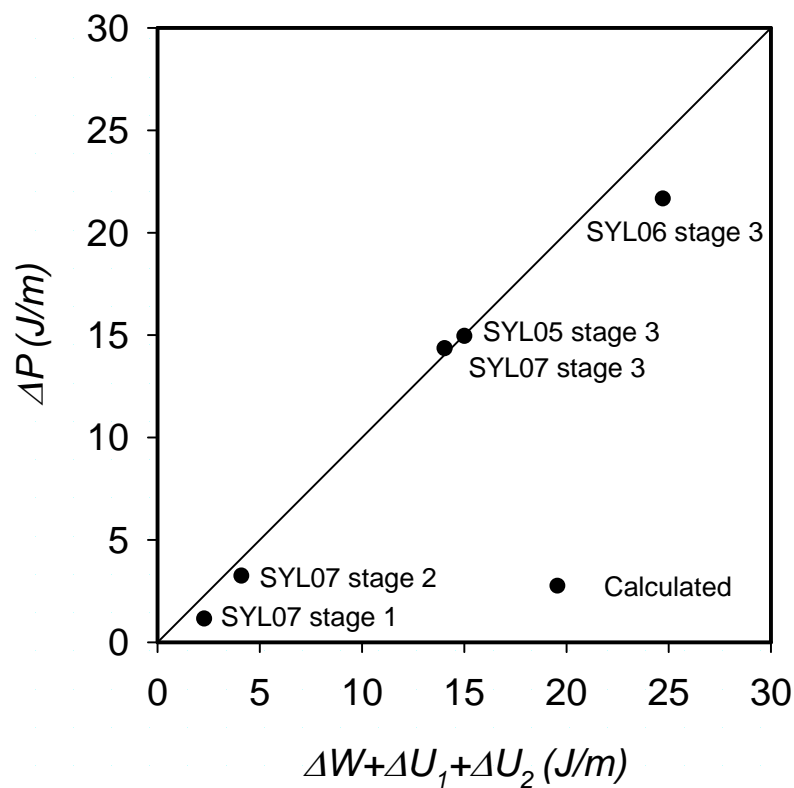


Figure 4.46 Variation of potential energy change with work done by the soil structural system

4.5 Observed performance in long term after excavation

The design of retaining walls for deep basements can be greatly influenced by the hydraulic boundary conditions, especially where there is a flow of water outside and inside the excavation. The flow pattern influences the distribution of earth pressure and water pressure leading to questions arising about the long term stability of the wall and the stability of the excavation floor, where bulk heave or local piping may occur, depending on the particular soil conditions.

With the benefit of the scaling factor of n^2 for consolidation problems in the centrifuge, the long term behaviour of the retaining wall system is investigated. Dissipation of excess pore water pressure is allowed due to water discharge to or from the two drainage boundaries at the base of the soft clay and at the ground surface. That eventually leads to a constant seepage condition around the wall toe. Swelling and softening of soft clay is expected on the excavation side owing to the removal of the over-burden stress on the excavation side and the lowering of the ground water table, which in turn leads to the redistribution of total horizontal stress on the wall and the possibility of a hydraulic failure.

The studies reveal, firstly, the effect of wall toe location away from the high pressure drainage stratum (Test SYL05 and SYL07) and then the effect of a jet grout base slab near the wall toe (Test SYL06) on the long-term destabilizing influence of a high-pressure aquifer close to the toe of the wall. Figure 4.47 shows the locations of the pore pressure transducers (PPTs) for each test. It is noted that the location of the water table is kept at ground level throughout the test by connecting the bottom and top drainage holes to a standpipe with an overflow mechanism.

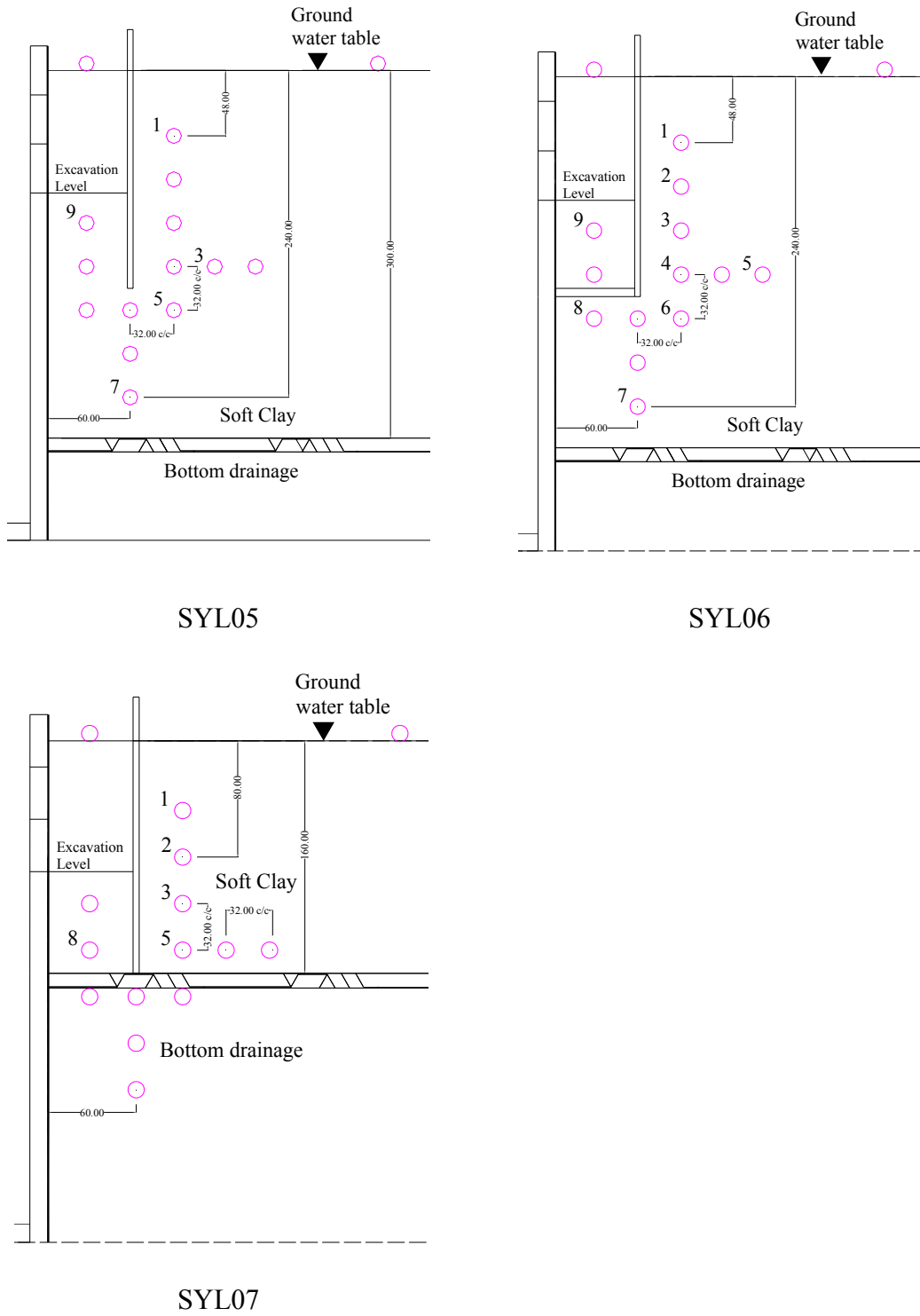
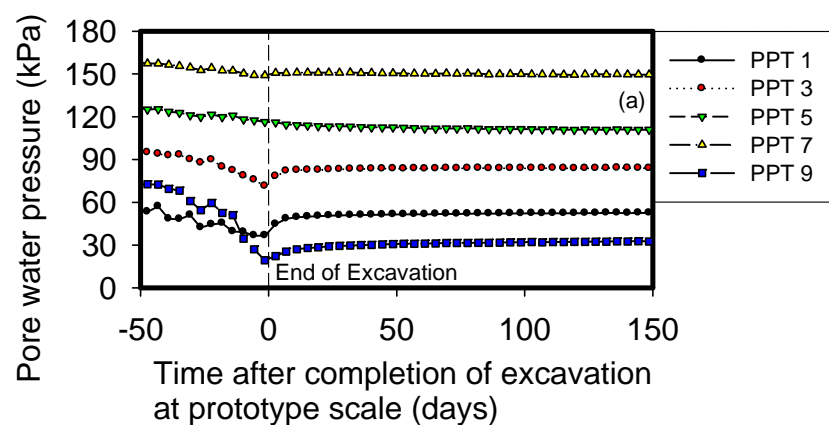


Figure 4.47 Schematic diagram showing locations of PPTs

4.5.1 Pore pressure response

Excess pore water pressure is a result of both stress removal and undrained shearing with zero volume change. The variations of pore pressure for Test SYL05, SYL06 and SYL07 were plotted on Figure 4.48. In general, as shown in Figure 4.48(a) for PPTs located on the retained side at shallow depths, the drop in pore water pressure during excavation is more significant. This could be ascribed to both the generation of negative excess pore water pressure by shearing in over-consolidated clay and greater horizontal stress removal before introduction of propping. Deeper PPTs on the retained side, on the other hand, show less build-up in negative excess pore water pressure presumably owing to positive excess pore pressure by shearing of the deeper, normally consolidated clay which can counteract the smaller reduction of stress. PPT 8 & 9 in the excavation pit experience the greatest decrease in pore pressure due to the removal of the vertical overburden stress. Very similar observations were made by a coupled numerical finite element analysis carried out by Ou and Lai (1994) using a non-linear soil model hyperbolic cam clay. Similar trends are shown in Figure 4.48 (b) and (c) for Test SYL06 and Test SYL07.



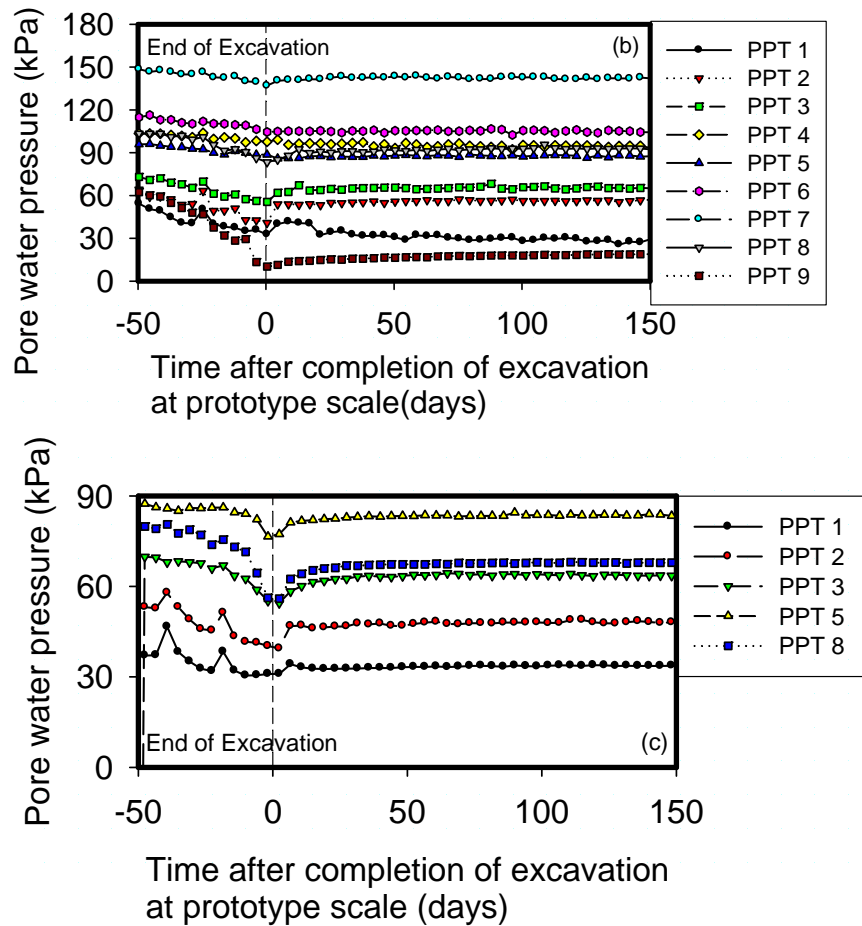


Figure 4.48 Pore pressure responses after excavations for (a) Test SYL05 (b) Test SYL06 and (c) Test SYL07

A phase of dissipation of excess pore water pressure followed the end of excavation. The drainage path of the particular location of the PPTs governs the rate of excess pore pressure dissipation accordingly. In general, all the readings stabilize corresponding to the development of steady seepage condition after 200 days at prototype scale for all tests.

For conventional design purposes, estimation of factor of safety for braced excavations is defined with respect to failure by piping and heave. However, the effect on the safety of the excavation of the reduction in available passive soil resistance and of the increase in active soil pressure due to seepage must also be

considered. It is of vital importance to look into the details of soil permeability and transient flow properties, ground stratification and hydrological conditions.

For the present studies, the bottom drainage layer was maintained with a high water table at the original ground surface. This is the worst representative case of an excavation site where there is a high pressure water aquifer located just below the soft clay stratum. Design against hydraulic failure then becomes a critical issue for engineers.

The distributions of water pressure against depth for **Test SYL05, SYL06 and SYL07** are plotted in **Figure 4.49(a), (b) and (c)**, respectively. As shown in **Figure 4.49(a) and (c)**, the pore water pressure on the retained side recovers to slightly lower than its original level due to downward seepage. Most importantly, the pore water pressure inside the excavation drops in the short term due to unloading and remains low in the long term due to the drawdown of water table in the pit. For the case of **Test SYL06 (Figure 4.49(b))**, the effect of seepage is minimized due to the placement of the impermeable slab representing a grout layer at the base which isolates the excavation pit.

The factor of safety against hydraulic uplift is defined by Terzaghi by the ratio between the submerged unit weight inside the pit and the upward vertical seepage force neglecting shear forces at the vertical soil wall interface.

$$FS_{hydraulic\ uplift} = \frac{\text{Overburden effective stress at wall toes}}{\text{Uplift seepage force}} = \frac{(\gamma_{sat} - \gamma_w)}{i\gamma_w} \quad (4.15)$$

where i is the upward hydraulic gradient.

This factor of safety should be comfortably greater than 1 according to CIRIA 580 report (Williams and Waite, 1993).

The critical hydraulic gradient (i_{crit}) at failure is accordingly defined as ratio between submerged unit weight of soil to the unit weight of water, for clay, i_{crit} is around 0.6.

Figure 4.50(a) presents the possible flow net pattern for Test SLY05, in which the drop in water head mainly occurs inside the excavation pit with an average hydraulic gradient (i) of 0.55 which is only slightly smaller than the critical hydraulic gradient (i_{crit}) of 0.6 ($FS_{hydraulic\ uplift}=1.05$). Since the upward hydraulic gradient is an inverse function of the distance between excavation level and the high pressure aquifer, the much shallower depth of the aquifer in Test SYL07 produces average $i=1.28$ as seen in Figure 4.50(c), $FS_{hydraulic\ uplift}=0.47$) would cause higher risk of a hydraulic uplift failure in the excavation pit. Notwithstanding this, no hydraulic uplift failure occurred in any test, even in the long term, possibly as a result of friction against the wall.

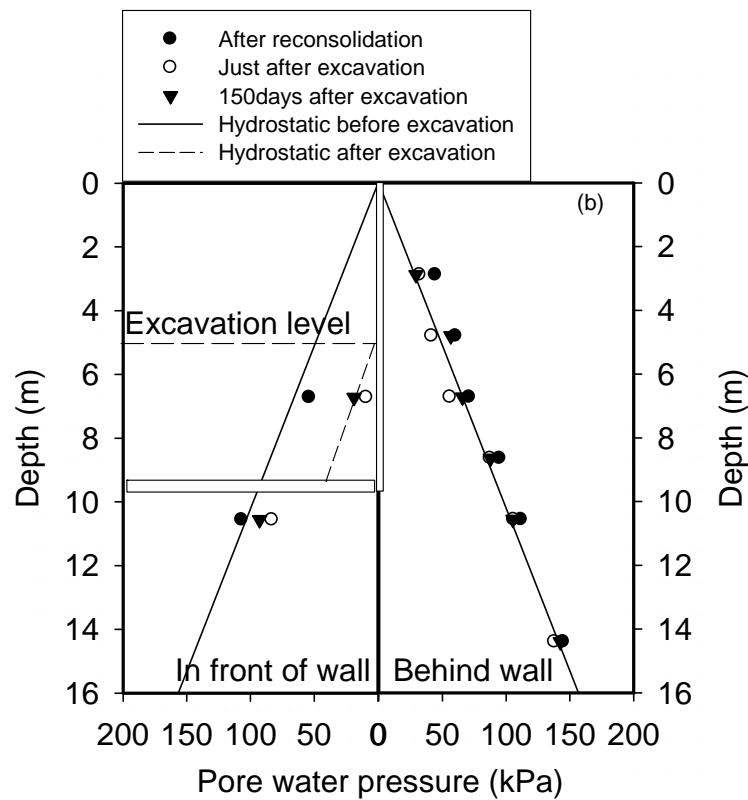
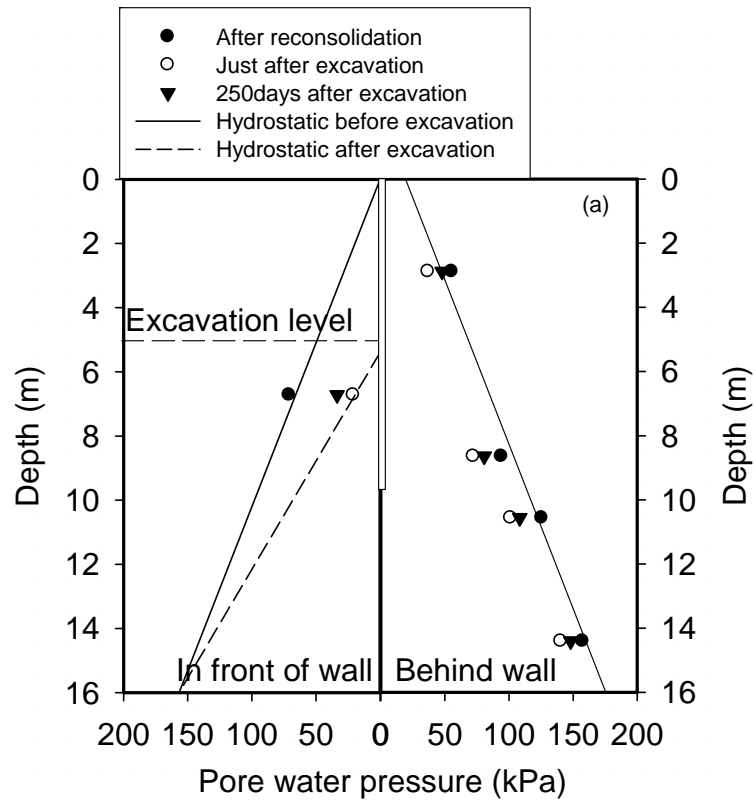
4.5.2 Wall deflection and ground settlement

In view of the hydrological conditions of different tests in long term, the accompanying soil deformation characteristics are investigated. For the case of an excavation wall floating in deep clay (Test SYL05), softening of soil occurs in the pit during the development of long term seepage accompanying the dissipation of negative excessive pore pressure. This leads to minor wall toe kick-out below the lowest prop as shown in Figure 4.51 (a). The additional movement amounts to 20% of the short-term movement induced in the construction process. It is observed that the corresponding additional ground settlement is also within 20% of the excavation induced settlement. The lateral extent of the zone of long term settlement due to wall toe movement was limited to a zone within one times the excavation depth (H).

In the extreme condition in which the excavation is carried out above a shallow high pressure aquifer (Test SYL07), major wall toe kick-out movement occurs below the lowest prop as a result of the high hydraulic gradient in the passive zone (Figure 4.52)). The additional wall toe movement is about 1.5 times the maximum excavation-induced wall lateral displacement. The development of the deformation is shown in Figure 4.54. Initially, base heave and wall bulging characterize the deformations before the full development of constant seepage condition at 150 days after the excavation. (Figure 4.54(a)). An even more significant chimney type of failure mechanism is observed 600 days after the excavation. (Figure 4.54(b)).

In practice, it is important to explore mitigation techniques such as the introduction of a grout base slab (Test SYL06) to minimize the seepage-induced softening of soil in the passive zone (Figure 4.50(b), $i \approx 0$) and to introduce lateral restraint to the wall toe. As a result, in Test SYL06, no kick-out failure is observed in the long term and only consolidation settlement occurs due to dissipation of excavation-induced excess pore

pressures. Further research should be carried out to investigate the efficiency of actual improved soil in reducing long term ground deformations after excavation.



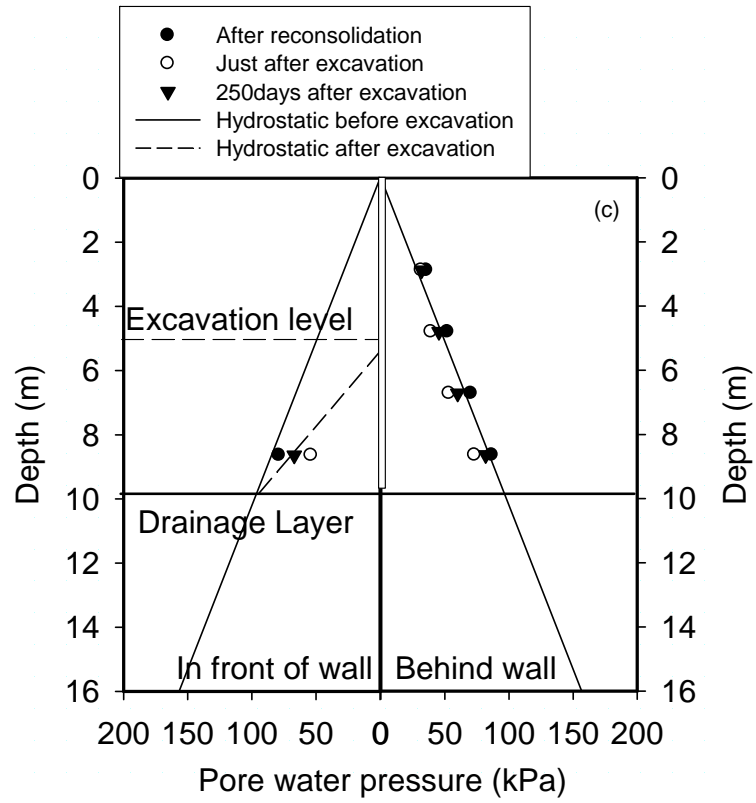
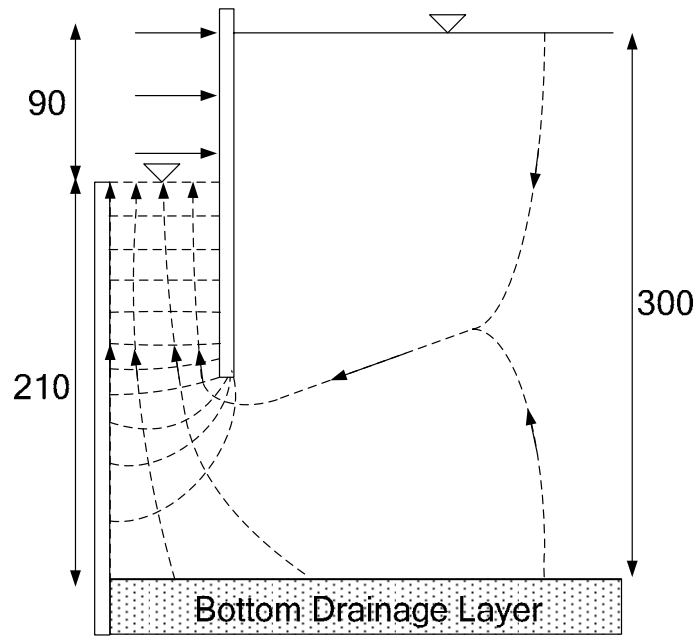
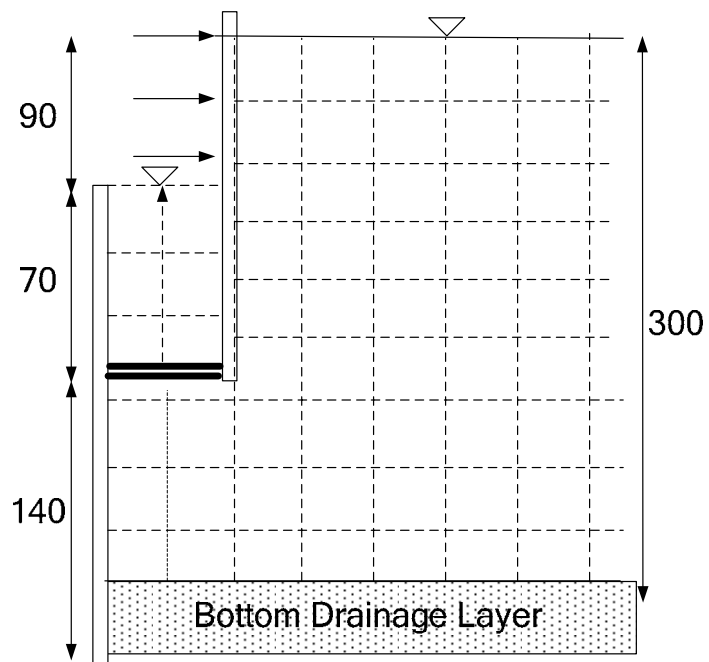


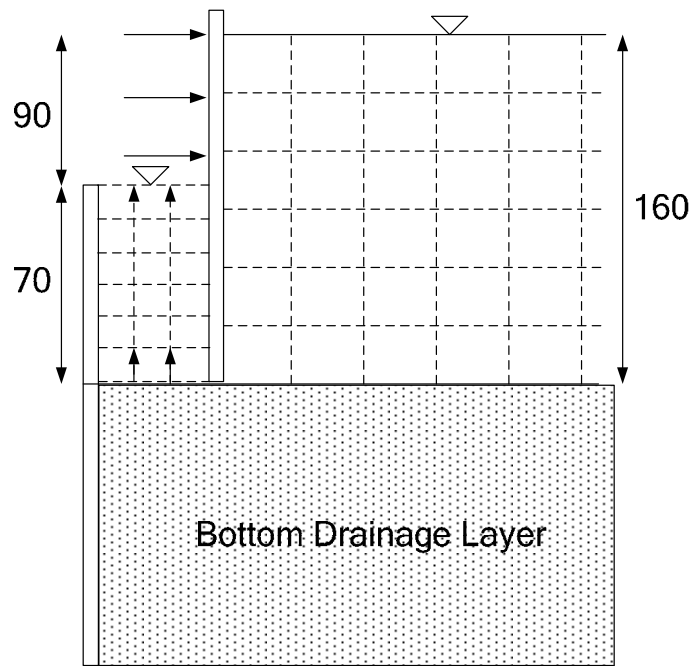
Figure 4.49 Pore pressure distributions against depth for (a) Test SYL05 (b) Test SYL06 and (c) Test SYL07



(a) Test SYL05

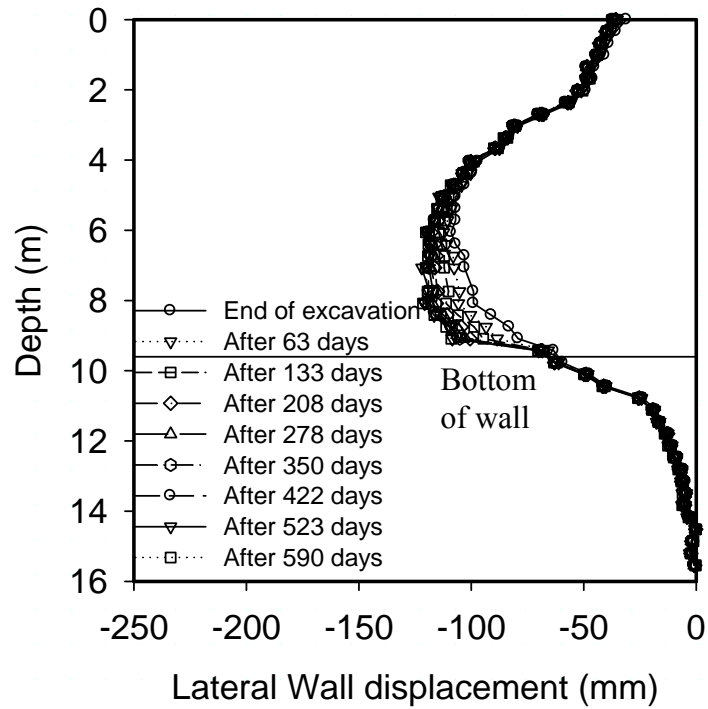


(b) Test SYL06

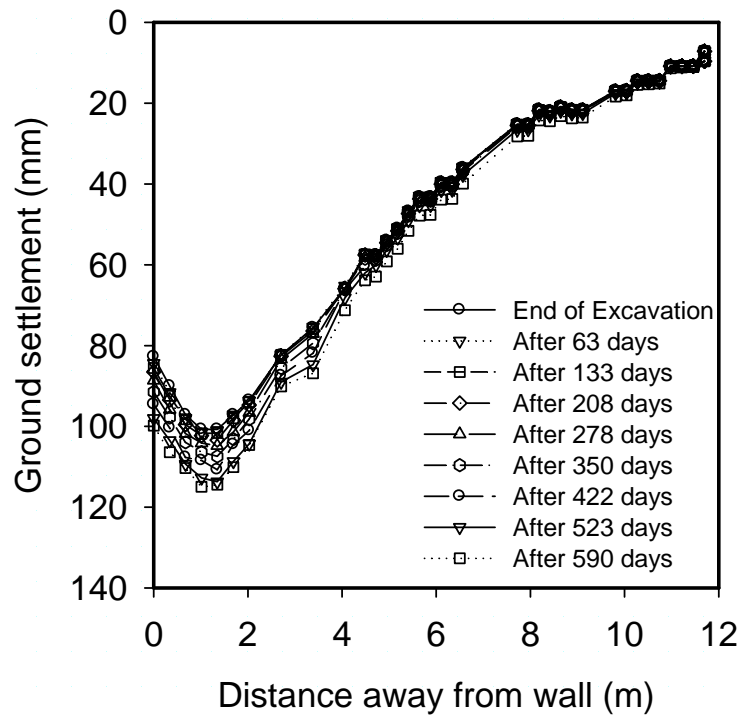


(c) Test SYL07

Figure 4.50 Simplified flow nets for (a) Test SYL05 (b) Test SYL06 and (c) Test SYL07



(a)



(b)

Figure 4.51 Development of long-term (a) lateral wall displacement and (b) ground surface settlement (Test SYL05)

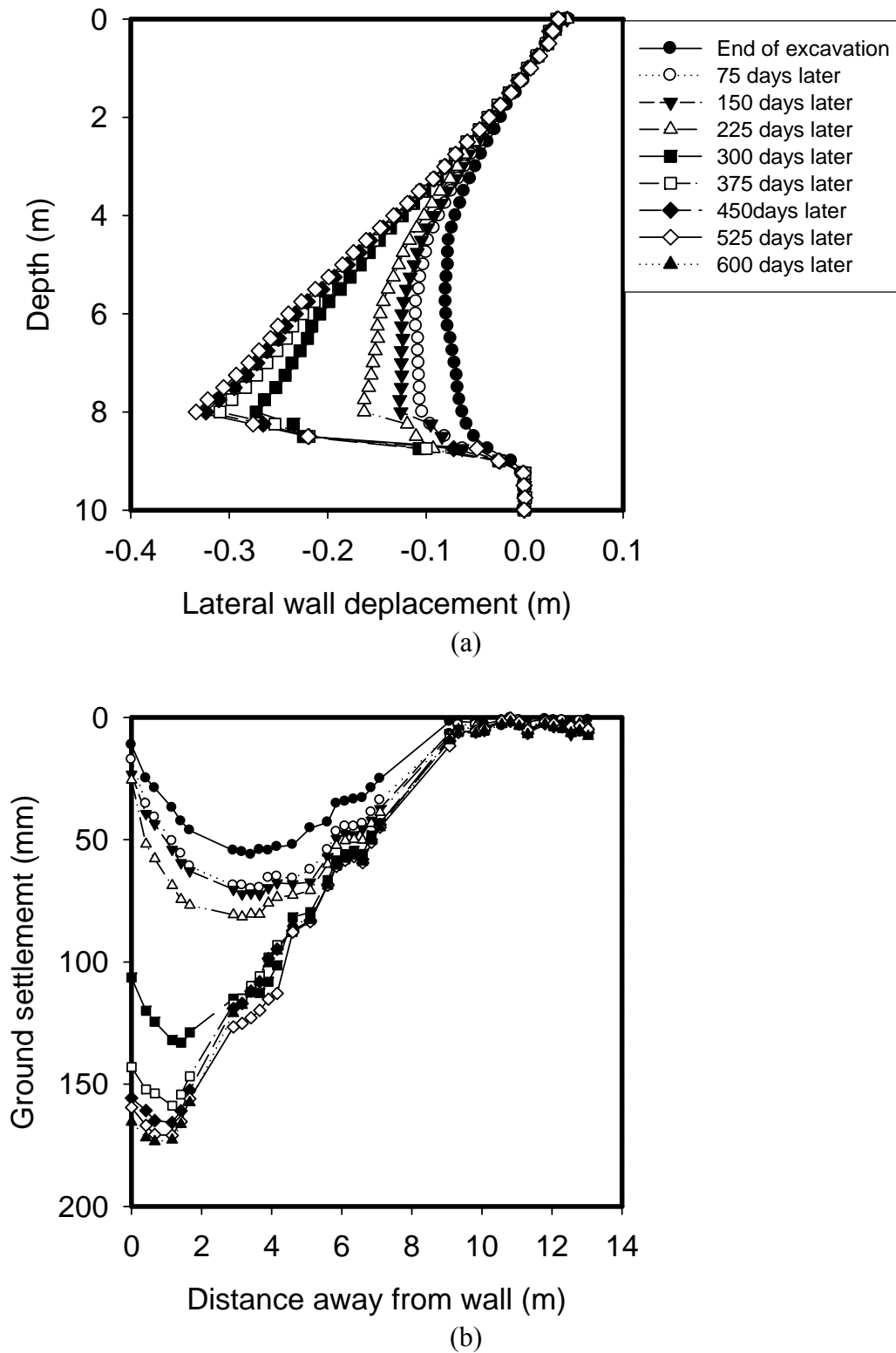
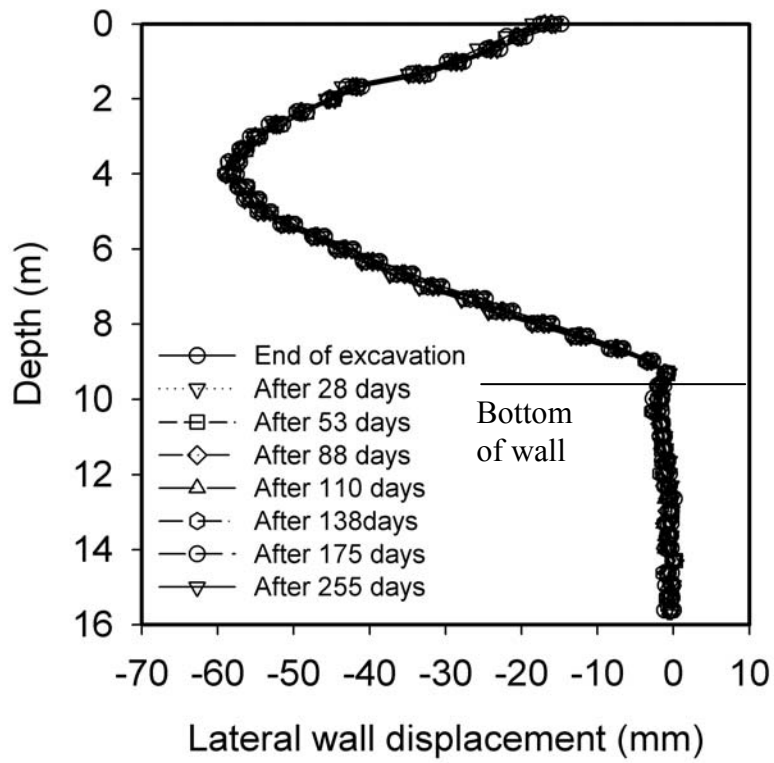
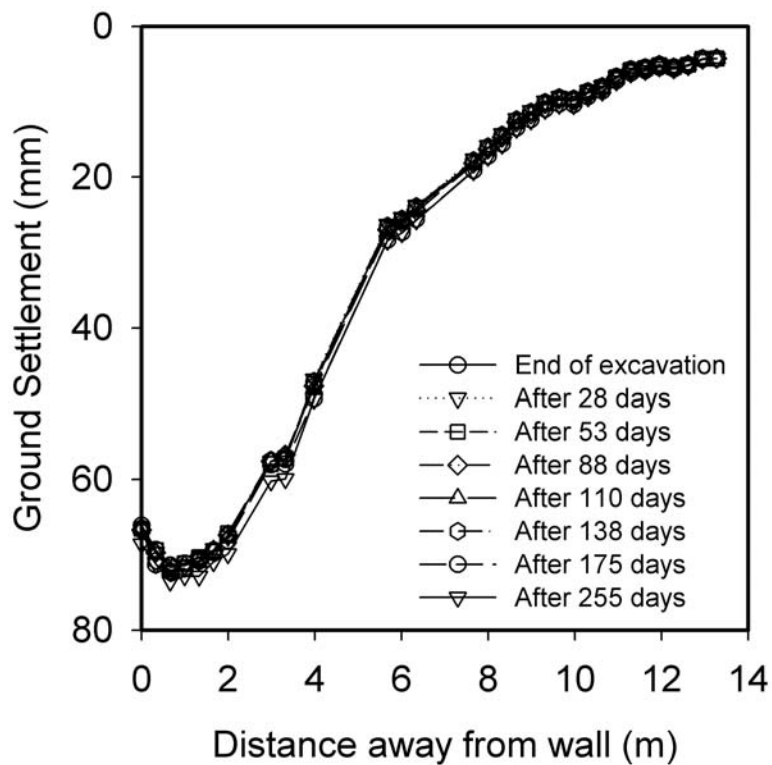


Figure 4.52 Development of long-term (a) lateral wall displacement and (b) ground surface settlement (Test SYL07)

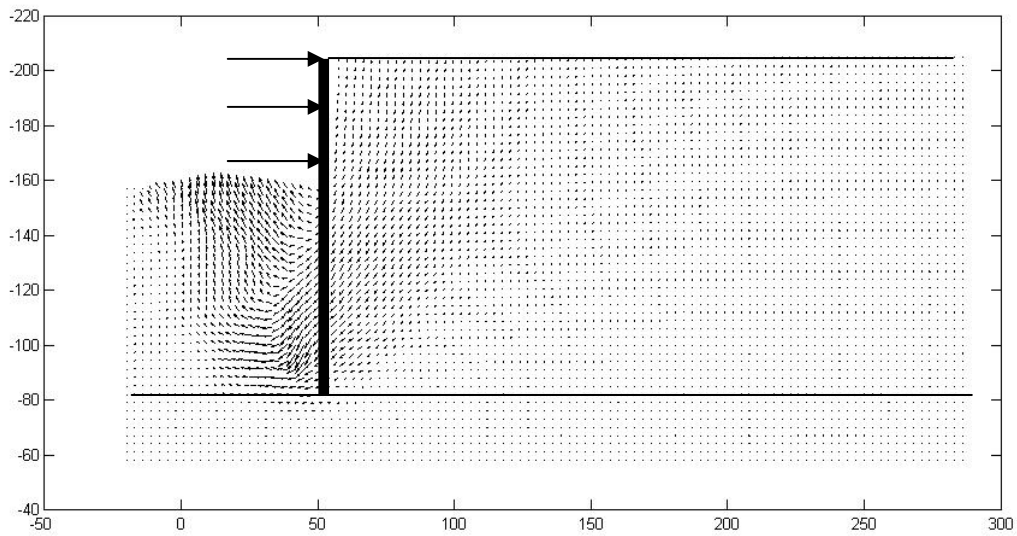


(a)

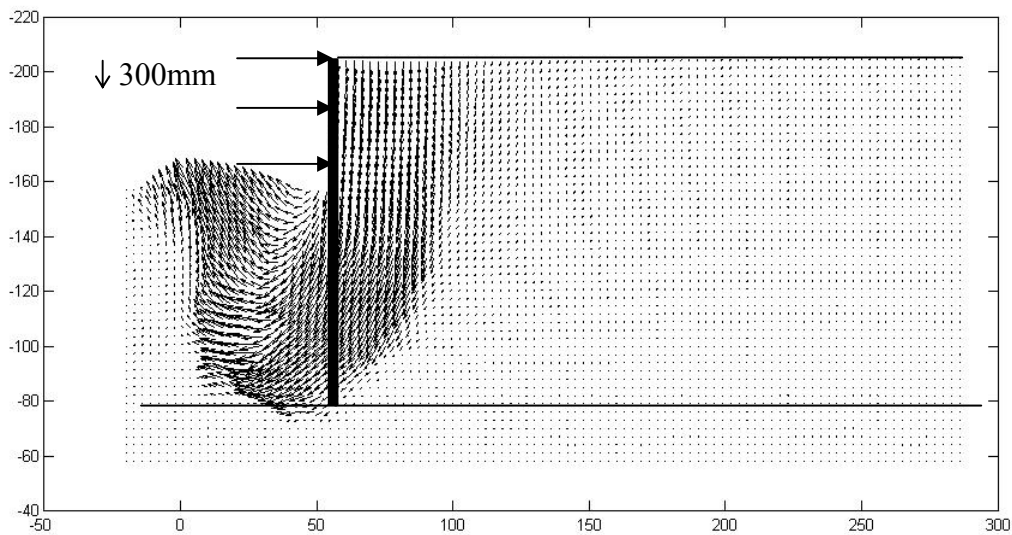


(b)

Figure 4.53 Development of long-term (a) lateral wall displacement and (b) ground surface settlement for Test SYL06



(a) Before wall toe kick-out (150days after excavation)



(b) After wall toe kick-out (600 days after excavation)

Figure 4.54 Long term deformation mechanism in Test SYL07 (a) before wall toe kick out (b) after wall toe kick out

4.6 Summary and discussion

With the aid of different instrumentation, the performance of various model excavations was monitored. Changes in prop loads, pore pressures, total earth

pressure, ground settlement and bending moment in the retaining wall were closely monitored before, during and after the centrifuge in-flight excavation process.

Pre-excavation behaviour suggests that there are very minor pre-excavation wall movements and bending moments after 90% dissipation of excess pore water pressure, as proven by pore water pressure measurement (PPTs), ground displacement measurement (LVDTs) and PIV observations. The accuracy of the PIV technique is also cross-checked by the use of linear variable transformers. Comparable results were obtained by the two monitoring techniques and plane strain testing was confirmed.

Short term excavation behaviour was intended to be undrained and excavation was accordingly completed within 40 minutes at model scale (100days at prototype scale). Approximately zero volumetric strain is observed by PIV measurements.

- During excavation, negative excessive pore water pressure due to vertical unloading was reduced by positive excess pore water pressure due to undrained shearing. A decrease in rate of increase in negative excess pore pressure in the passive zone developed for the more flexible wall system due to more extensive shearing. On the other hand, very small excess pore water pressure developed on the retained side for all tests.
- Empirical estimation by Peck's envelope underestimates apparent earth pressure for a stiff support system by 30% in relation to the build-up of a vertical arching mechanism. Maximum strut force develops at the lowest strut location in the step before the installation of the next level. Struts at a higher elevation experience stress relief. These observations confirm the formation

of a vertical arching mechanism and horizontal load redistribution. Reducing the bending stiffness of the wall or the axial stiffness of the props caused a reduction in apparent earth pressures. Results show that only cases of excavation with a flexible support system agree reasonably well with Peck's recommendations.

- Total earth pressure results reveal that the K_o condition is reached after re-consolidation. In the process of excavation, decrease in total pressure is observed at depth due to the absence of lateral restraint below the lowest propping level. As the excavation depth goes deeper, the rate of decrease in passive total pressure is more obvious revealing the importance of soil excavation in-flight for simulating excavation in the centrifuge.
- By assuming that the total vertical stress is dominated by the overburden weight of the soil, effective stress paths were developed for soil elements at different locations. Soil elements in the passive zone follow very similar effective stress paths as the theoretical PSP stress path. A soil element on the active side will follow PSA initially and then experience shear at reducing mean effective stress offering evidence of the development of an arching mechanism.
- The rate of mobilization of shear strength is insignificant for soil elements around excavations with a rigid supporting system. For excavations with flexible retaining system, the rate of mobilization of a soil element at mid depth of the wall is more significant than for shallower and deeper depths.
- Positive bending moment developed in the short term during the cantilever excavation stage. Large negative bending moments are generated in the propped excavation stage. The maximum bending moment registered in a

flexible wall excavation is higher than that of a rigid wall excavation due to the difference in deformation mode of the system.

- The incremental wall deformation profile generally follows the cosine bulge equation suggested by O'Rourke (1993). New deformation mechanisms can be considered by simplifying the observed mechanism with respect to governing parameters such as wall toe fixity condition and excavation geometry. Averaged soil strains mobilized in the system were below 2%, reiterating the importance of the small to medium strain stiffness for excavation problem.
- Clough et al. (1989)'s approach for estimating wall lateral displacement in relation to factor of safety overestimates wall deformation by a factor of at least 1.5, indicating that the consideration of small strain stiffness and the incremental nature of the construction process should be incorporated even in simple design methods.
- Comparing deformation results for excavations in different depths of clay, the undrained maximum wall displacement was found not to be sensitive to change in depth of clay. Settlement profiles get narrower with smaller depth of clay as the deformation mechanism is limited by the depth of the soft layer.
- A flexible wall with its toe fixed by a base slab only allows bulging as the deformation mode, and limits the development of shear strain to about 1.3%.
- Reduction of strut stiffness increases the wall deflection above the excavation level whereas excavation-induced wall movement below excavation level was not influenced by strut stiffness. Softer prop response gives a deformation mechanism with a narrower settlement trough.
- Strain maps have been generated using the PIV technique, close-range photogrammetry and small strain analysis. The strain map for cantilever

excavation shows an approximately 45 degree triangular shear zone on both retained and excavation sides. The strain map for the propped stage shows shear bands initiating from the wall toe and the depth of shear zone extending upwards towards the lowest props, suggesting the existence of a zone with a smaller shear strain on the retained side. This may show signs of development of vertical arching mechanism.

- Validation of the conservation of the energy in the excavation process is achieved through carefully defined calculations. The total loss of potential energy of the soil is shown to be balanced by the total work done in shearing and total elastic strain energy stored in the structures with an error of at most 30%. This gives a crucial basis for the extensive development of the mobilizable strength design method to include structural effects.

Long-term design of retaining walls is greatly influenced by the hydraulic boundary conditions, especially the water flow around the supporting wall and into the pit. Pore water pressure on the retained side recovered to a level slightly lower than its hydrostatic condition within 200 days in prototype time due to seepage. The seepage-induced hydraulic gradient in an excavation pit is an inverse function of the distance of excavation level from a high pressure aquifer, determining possible long-term failure against hydraulic uplift, and the tendency of the wall toe to kick out. Minor toe kick-out was observed in the test with a deep clay bed. Base heave and wall bulging are the major modes of deformation in the long-term seepage condition just as they were in short-term behaviour. For excavation in a shallow clay bed above an artesian aquifer, base heave and wall bulging are magnified due to transient flow up to 150

days after excavation whereas a much more damaging chimney type of failure mechanism is observed 225 days after the excavation.

Introduction of a base grout slab to prop the wall toe minimizes the seepage effect in the passive soil zone. The method is observed to be effective in causing less softening of soil in passive zone and supporting the wall toe. No wall toe kick out failure and little lateral long term movement is observed.

These centrifuge test observations provide a good basis for understanding the problem, and point towards new theories which will assist in geotechnical design.

CHAPTER 5

AN EXTENDED MOBILIZABLE STRENGTH DESIGN METHOD FOR DEEP EXCAVATION

5.1 Introduction

The Mobilizable Strength Design (MSD) method has developed following various advances in the use of plastic deformation mechanisms to predict ground displacements: (Milligan and Bransby, 1975; Bolton and Powrie, 1988; Bolton et al. 1989, 1990a, 1990b). MSD is a general, unified design methodology which aims to satisfy both safety and serviceability requirements in a single calculation procedure, contrasting with conventional design methodology which treats stability problems and serviceability problems separately. In the MSD method, actual stress-strain data is used to select a design strength that limits ground deformations, and this is used in plastic soil analyses that satisfy either equilibrium conditions or energy conservation principles without the use of empirical safety factors.

Simple plastic mechanisms are used to represent the working state of the geotechnical system. These mechanisms represent both the equilibrium and deformation of the various soil bodies, especially at their junction with the superstructure. Then, raw stress-strain data from soil tests on undisturbed samples, taken from representative

locations, are used directly to link stresses and strains under working conditions. Constitutive laws and soil parameters are unnecessary. The MSD approach has been successfully implemented for shallow foundations (Osman and Bolton, 2005), cantilever retaining walls (Osman and Bolton, 2004), tunneling-induced ground displacements (Osman et al, 2006) and also the sequential construction of braced excavations which induce wall displacements and ground deformations (Osman and Bolton, 2006).

Consider the imposition of certain actions on a soil body, due to construction activities such as stress relief accompanying excavation or to loads applied in service. The MSD method permits the engineer to use simple hand calculations to estimate the consequential ground displacements accounting for non-linear soil behavior obtained from a single well-chosen test of the undisturbed soil.

The MSD approach firstly requires the engineer to represent the working states of the geotechnical system by a generic mechanism which conveys the kinematics (i.e. the pattern of displacements) of the soil due to the proposed actions. Analysis of the deformation mechanism leads to a compatibility relationship between the average strain mobilized in the soil and the boundary displacements.

The average shear strength mobilized in the soil due to the imposed actions is then calculated, either from an independent equilibrium analysis using a permissible stress field (equivalent to a lower bound plastic analysis), or from an equation balancing work and energy for the chosen mechanism (equivalent to an upper bound plastic analysis). Recent work on MSD by Klar and Osman (2008) has extended the application of the principle of energy conservation. This is further extended to deep excavations in the current work, following Bolton et al. (2008), in which changes of gravitational potential energy and structural strain energy are included in the

formulation. Next, the location of one or more representative soil elements is then selected, basing this judgment on the soil profile in relation to the location and shape of the selected mechanism. The centroid of the mechanism can serve as a default location if a single location is to be employed. Stress-strain relationships are then obtained from appropriate laboratory tests on undisturbed soil samples taken from the selected locations and carried out with precise strain measurements. Equivalent in-situ tests such as self-boring pressuremeter tests can alternatively be carried out. The mode of deformation in the soil tests should correspond as closely as possible to the mode of shearing in the MSD mechanism. Otherwise, anisotropy should somehow be allowed for.

Finally, the mobilized shear strength required for equilibrium under working loads is set against the representative shear stress-strain curve in order to obtain the mobilized soil strain, and thereby the boundary displacements of the simplified MSD mechanism.

5.2 Application of MSD for deep excavation

Osman and Bolton (2006) showed for an in-situ wall supporting a deep excavation that the total deformation can be approximated as the sum of the cantilever movement prior to propping, and the subsequent bulging movement that accretes incrementally with every sequence of propping and excavation.

A method for estimating the cantilever movement had been suggested earlier in Osman and Bolton (2004). It begins by considering the lateral earth pressure distribution for a smooth, rigid, cantilever wall rotating about a point some way above its toe, in undrained conditions. A simple mobilized strength ratio is introduced to characterize the average degree of mobilization of undrained shear strength throughout the soil. By using horizontal force and moment equilibrium equations, the

two unknowns – the position of the pivot point and the mobilized strength ratio – are obtained. Then, a mobilized strain value is read off from the shear stress-strain curve of a soil element appropriate to the representative depth of the mechanism at the mid-depth of the wall. Simple kinematics for a cantilever wall rotating about its base suggests that the shear strain mobilized in the adjacent soil is double the angle of wall rotation. Accordingly, for the initial cantilever phase, the wall rotation is estimated as one half of the shear strain required to induce the degree of mobilization of shear strength necessary to hold the wall in equilibrium. Osman and Bolton (2004) used FEA to show that correction factors up to about 2.0 could be applied to the MSD estimates of the wall crest displacement, depending on a variety of non-dimensional groups of parameters ignored in the simple MSD theory, such as wall flexibility and initial earth pressure coefficient prior to excavation.

A typical increment of bulging, on the other hand, was calculated in Osman and Bolton (2006) by considering an admissible plastic mechanism for base heave. In this case, the mobilized shear strength was deduced from the kinematically admissible mechanism itself, using virtual work principles. The energy dissipated by shearing was said to balance the virtual loss of potential energy due to the simultaneous formation of a subsidence trough on the retained soil surface and a matching volume of heave inside the excavation. The mobilized strength ratio could then be calculated, and the mobilized shear strain read off from the stress-strain curve of a representative element, as before. The deformation is estimated using the relationship between the boundary displacements and the average mobilized shear strain, in accordance with the original mechanism.

The MSD solutions of Osman and Bolton (2006) compared quite well with some numerical simulations using the realistic non-linear MIT-E3 model, and various case

studies that provided field data. However, these initial solutions are capable of improvement in three ways that will contribute to their applicability in engineering practice.

(i) The original mechanism assumed a relatively wide excavation, whereas cut-and-cover tunnel and subway constructions are likely to be much deeper than their width. The MSD mechanism therefore needs to be adapted for the case in which the plastic deformation fields for the side walls interfere with each other beneath the excavation.

(ii) The structural strain energy of the support system can be incorporated. This could be significant when the soil is weak, and when measures are taken to limit base heave in the excavation, such as by base grouting between the supporting walls. In this case, the reduction of lateral earth pressure due to ground deformation may be relatively small, and it is principally the stiffness of the structural system itself that limits external ground displacements.

(iii) Progressively incorporating elastic strain energy requires the calculation procedure to be fully incremental, whereas Osman and Bolton (2006) used total energy flows to calculate the results of each stage of excavation separately. A fully incremental solution, admitting ground layering, will permit the accumulation of different mobilized shear strengths, and shear strains, at different depths in the ground, thereby improving accuracy.

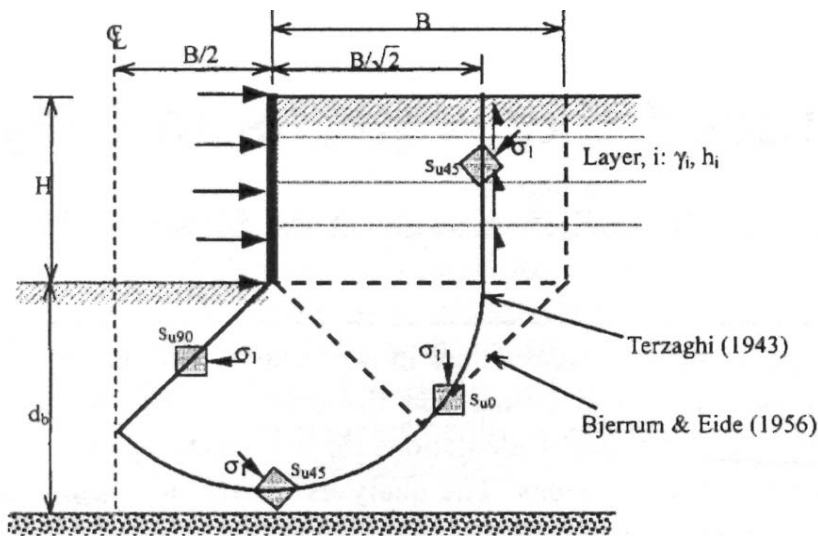
It is the aim of this chapter to introduce an enhanced MSD solution that includes these three features. This is then compared with existing FEA and some case histories of braced excavation. It will be suggested that MSD provides the ideal means of harvesting FEA simulations for use in design and decision-making.

5.3 Plastic failure mechanism

Limit equilibrium methods are routinely used in stability calculations for soft clay which is over-idealised as rigid-plastic. Slip surfaces are selected as the assumed focus of all plastic deformations. Failure mechanisms should be kinematically admissible, meaning that unwanted gaps and overlaps should not be produced. Furthermore, in the case of undrained shearing of clays, a constant-volume condition should be respected at every point. A consequence is that undrained plane-strain failure mechanisms must comprise only slip planes and slip circles. The soil on such failure surfaces is taken to mobilize its undrained shear strength divided by a safety factor, to maintain the mechanism in limiting equilibrium under the action of gravity, and any other applied loads. Calculated in this way, the safety factor literally offers an estimate of the factor by which the strength of the soil would have to drop before the soil construction would collapse. Such estimates might err either on the high side or the low side, depending on the particular assumptions that were made.

In the case of base heave in braced excavations, plastic solutions were derived from slip-line fields based on the method of characteristics. Such solutions comprise both slip surfaces, as before, and plastic fans which distribute plastic strains over a finite zone in the shape of a sector of a circle. Notwithstanding these zones of finite strain, the additional presence of slip surfaces still restricts the application of these solutions to the prediction of failure. Furthermore, no such solution can be regarded automatically as an accurate predictor of failure, notwithstanding their apparent sophistication. All that can be said is that they will lead to an unsafe estimate of stability. Their use in practice can only be justified following back-analysis of actual failures, whether in the field or the laboratory.

Two typical failure mechanisms as suggested by Terzaghi (1943) and Bjerrum and Eide (1956) are shown in **Figure 5.1**. They have each been widely used for the design of multi-propped excavations. Terzaghi (1943) suggested a mechanism consisting of a soil column outside the excavation which creates a bearing capacity failure. The failure is resisted by the weight of a corresponding soil column inside the excavation and also by adhesion acting along the vertical edges of the mechanism. Bjerrum and Eide (1956) assumed that the base of the excavation could be treated as a negatively loaded perfectly smooth footing. The bearing capacity factors proposed by Skempton (1951) are used directly in the stability calculations and are taken as stability numbers, $N = \gamma H/c_u$. Eide et al. (1972) modified this approach to account for the increase in basal stability owing to mobilized shear strength along the embedded length of the rigid wall.



a) Without wall embedment
(principal stress directions after Clough & Hansen, 1981)

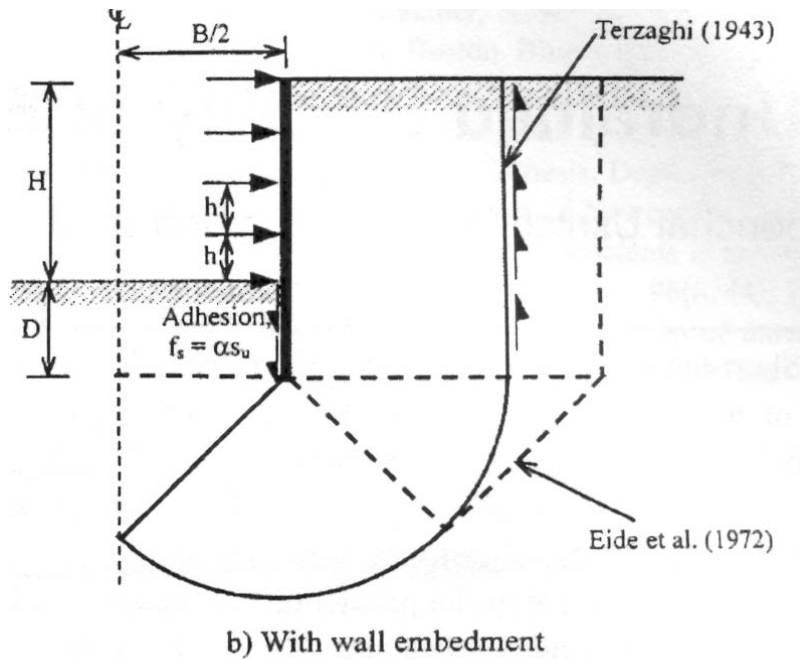


Figure 5.1. Conventional basal stability mechanism and notation (after Ukritchon et al., 2003)

O'Rourke (1993) further modified the basal stability calculations of Bjerrum and Eide (1956) to include flexure of the wall below the excavation level. It was assumed that the embedded depth of the wall does not change the geometry of the basal failure mechanism. However, an increase in stability was anticipated due to the elastic strain energy stored in flexure. This gave stability numbers that were functions of the yield moment and assumed boundary conditions at the base of the wall.

Ukritchon et al. (2003) used numerical limit analysis to calculate the stability of braced excavations. Upper and lower bound formulations are presented based on Sloan and Kleeman (1995) and Sloan (1988), respectively. The technique calculates upper bound and lower bound estimates of collapse loads numerically, by linear programming, while spatial discretization and interpolation of the field variables are calculated using the finite element method. No failure mechanism needs to be assumed and failure both of the soil and the wall are taken care of. However, both soil

and wall are again assumed to be rigid perfectly plastic so the failure mechanism includes a plastic hinge at the lowest level of support.

All these collapse limit analyses provide useful guidance on the possible geometry of plastic deformation mechanisms for service conditions. But the key requirement for MSD mechanisms is that displacement discontinuities (slip surfaces) must be avoided entirely. In that way, small but finite ground displacements are associated at every internal point with small but finite strains.

5.4 Geo-structural mechanism

Consider now the *deformations* of a multi-propped wall supporting a deep excavation in soft, undrained clay. At each stage of excavation the incremental displacement profile (Figure 5.2) of the ground and the wall below the lowest prop can be assumed to be a cosine function (O'Rourke,1993) as follows:

$$\delta w = \frac{\delta w_{\max}}{2} \left(1 - \cos\left(\frac{2\pi y}{\lambda}\right) \right) \quad (5.1)$$

Here δw is the incremental wall displacement at any distance y below the lowest support, δw_{\max} is its maximum value, and λ is the wavelength of the deformation, regarded as proportional to the length s of the wall below the lowest level of current support:

$$\lambda = \alpha s \quad (5.2)$$

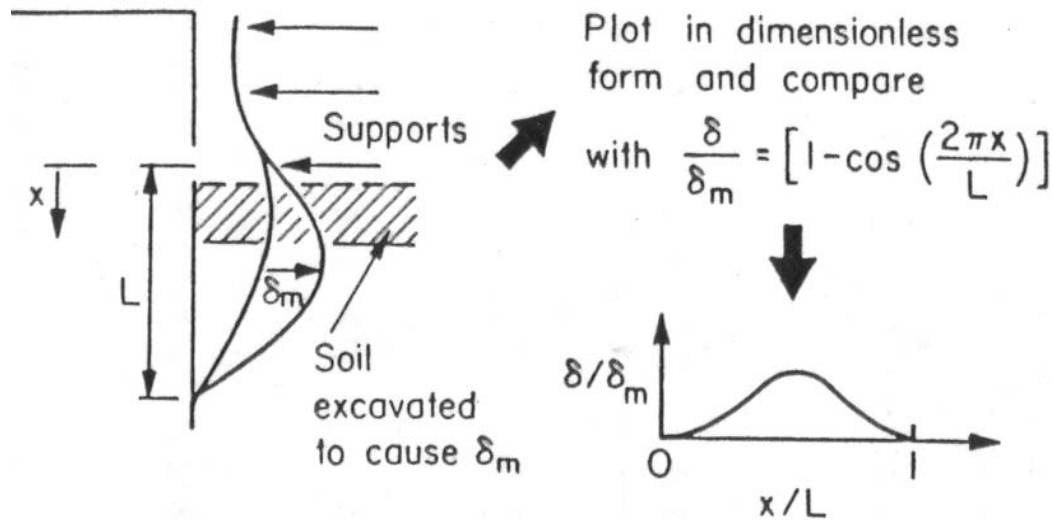


Figure 5.2. Incremental displacements in braced excavation (after O'Rourke, 1993)

O'Rourke (1993) defined the wavelength of the deformation as the distance from the lowest support level to the fixed base of the wall. Osman and Bolton (2006) suggested a definition for the wavelength of the deformation based on wall end fixity. For walls embedded into a stiff layer beneath the soft clay, such that the wall tip is fully fixed in position and direction, the wavelength was set equal to the wall length ($\alpha = 1$). For short walls embedded in deep soft clay, the maximum wall displacement occurs at the tip of the wall so the wavelength was taken as twice the projecting wall length ($\alpha = 2$). Intermediate cases were described as restrained-end walls ($1 < \alpha < 2$).

However, these definitions applied only to very wide excavations. When a narrow excavation is considered, the wavelength will be limited by the width of the excavation. In addition, in the case of the partially restrained wall, the depth of a relatively stiff soil stratum may also limit the depth of the deformation pattern.

An incremental plastic deformation mechanism conforming to Equation 5.1 was proposed by Osman and Bolton (2006) for a wide multi-propped excavation in clay. In this mechanism, the wall is assumed to be fixed incrementally in position and

direction at the lowest prop, implying that the wall has sufficient strength to avoid the formation of a plastic hinge. The wall and soil are deforming compatibly and the soil deformation also follows the cosine function of Equation 5.1. The dimensions of this mechanism depend on the wavelength λ .

Figure 5.3(a) shows the complete displacement field for the mechanism proposed by Osman and Bolton (2006). The solution includes four zones of distributed shear which consist of a column of soil adjoining the excavation above the level of the lowest prop, a circular fan zone centred at the lowest prop, another circular fan zone with its apex at the junction of the wall and the excavation surface and a 45 degree isosceles wedge below the excavation surface. It is required that the soil shears compatibly and continuously with no relative sliding at the boundaries of each zone. The dotted lines with arrows show the direction of the flow. Along each of these lines the displacement is constant and is given by the cosine function of Equation 5.1. It is assumed that the zone outside the deformation zones is rigid. This mechanism is simple, but it only applies to wide excavations. In the case of a narrow excavation, the width of the triangular wedge could be bigger than the actual width of the excavation. In view of this, a new mechanism for narrow excavations is proposed in **Figure 5.3(b)**. The mechanism in the passive zone (zone EFHI) is replaced. The new mechanism meets the condition for undrained shearing, which means that the volumetric strain remains zero throughout the zone.

In the original solution of Osman and Bolton (2006), soils were assumed to be homogenous. The average shear strain increment in each zone was calculated by taking the derivative of the prescribed displacement equation. Then, the undrained shear strength ($c_{u,mob}$) mobilized at any location for any excavation height was expressed using a single mobilization ratio β ($\beta = c_{u,mob}/c_u$) to factor the strength

profile. With the use of the virtual work principle, the plastic work done by shearing of the soil was equated to the virtual change of gravitational potential energy of the soil. A β factor was then found so that a corresponding mobilized shear strain could be read off from the chosen stress-strain curve. The incremental displacement was then calculated by the correlation between the average shear strain increment and the incremental wall displacement.

This approach offered a straightforward way to estimate the bulging displacement of the retaining wall. However, the approach requires refinement in order to include additional features that are significant in deep excavations. Firstly, the approach did not consider the elastic strain energy stored in the support system. Secondly, it is common to find a non-uniform soil stratum with undrained shear strength varying irregularly with depth. Furthermore, the geometry of the deformation mechanism changes as the construction proceeds, so the representation of mobilization of shear strength through the whole depth, using a single mobilization ratio, is only a rough approximation. In reality there will be differences in mobilization of shear strength at different depths for calculating incremental soil displacement. Lastly, the original mechanism of Osman and Bolton (2006) shown in [Figure 5.3\(a\)](#) only applied to wide excavations (i.e. $2\sqrt{2}(\alpha s - h') \leq B$); narrow excavations (i.e. $2\sqrt{2}(\alpha s - h') > B$) called for the development of the alternative mechanism of [Figure 5.3\(b\)](#). A new fully incremental calculation method will be introduced accordingly.

5.4.1 Deformation pattern in different zones

From [Figure 5.3](#), the soil is assumed to flow parallel to the wall at the retained side above the level of the lowest support (zone ABDC) and the incremental displacement

at any distance x from the wall is given by the cosine function of Equation 5.1, replacing y by x .

By taking the origin as the top of the wall, the deformation pattern of retained soil ABDC is given in rectangular coordinates as follows:

$$\delta w_y = -\frac{\delta w_{\max}}{2} \left(1 - \cos\left(\frac{2\pi x}{\lambda}\right)\right) \quad (5.3)$$

$$\delta w_x = 0 \quad (5.4)$$

In fan zone, CDE, by taking the apex of the fan zone as the origin

$$\delta w_y = \frac{\delta w_{\max}}{2} \left(1 - \cos\left(\frac{2\pi\sqrt{x^2 + y^2}}{\lambda}\right)\right) \left(\frac{-x}{\sqrt{x^2 + y^2}}\right) \quad (5.5)$$

$$\delta w_x = \frac{\delta w_{\max}}{2} \left(1 - \cos\left(\frac{2\pi\sqrt{x^2 + y^2}}{\lambda}\right)\right) \left(\frac{y}{\sqrt{x^2 + y^2}}\right) \quad (5.6)$$

For fan zone EFH in very wide excavations as indicated in **Figure 5.3(a)**, by taking the junction of the wall and the current excavation level as the origin:

$$\delta w_y = \frac{\delta w_{\max}}{2} \left(1 - \cos\left(\frac{2\pi\left[h + \sqrt{x^2 + y^2}\right]}{\lambda}\right)\right) \left(\frac{x}{\sqrt{x^2 + y^2}}\right) \quad (5.7)$$

$$\delta w_x = \frac{\delta w_{\max}}{2} \left(1 - \cos\left(\frac{2\pi\left[h + \sqrt{x^2 + y^2}\right]}{\lambda}\right)\right) \left(\frac{y}{\sqrt{x^2 + y^2}}\right) \quad (5.8)$$

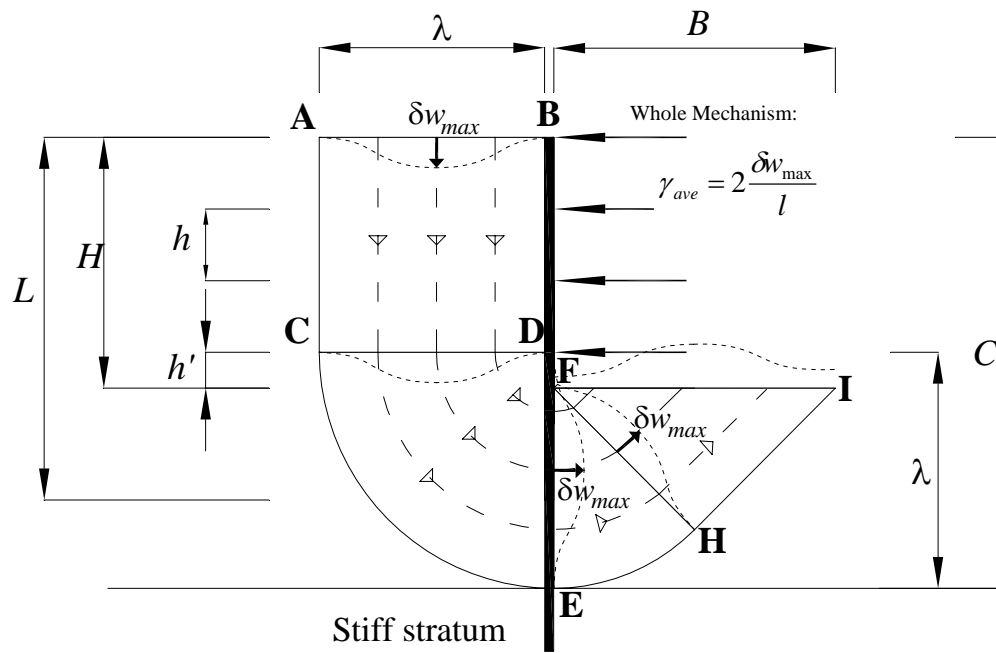
For the triangular zone FHI in very wide excavations, again taking the junction of the excavation and the wall as the origin:

$$\delta w_y = \delta w_x = \frac{\sqrt{2}\delta w_{max}}{4} \left(1 - \cos \left(\frac{2\pi \left[h + \frac{\sqrt{2}}{2}(x-y) \right]}{\lambda} \right) \right) \quad (5.9)$$

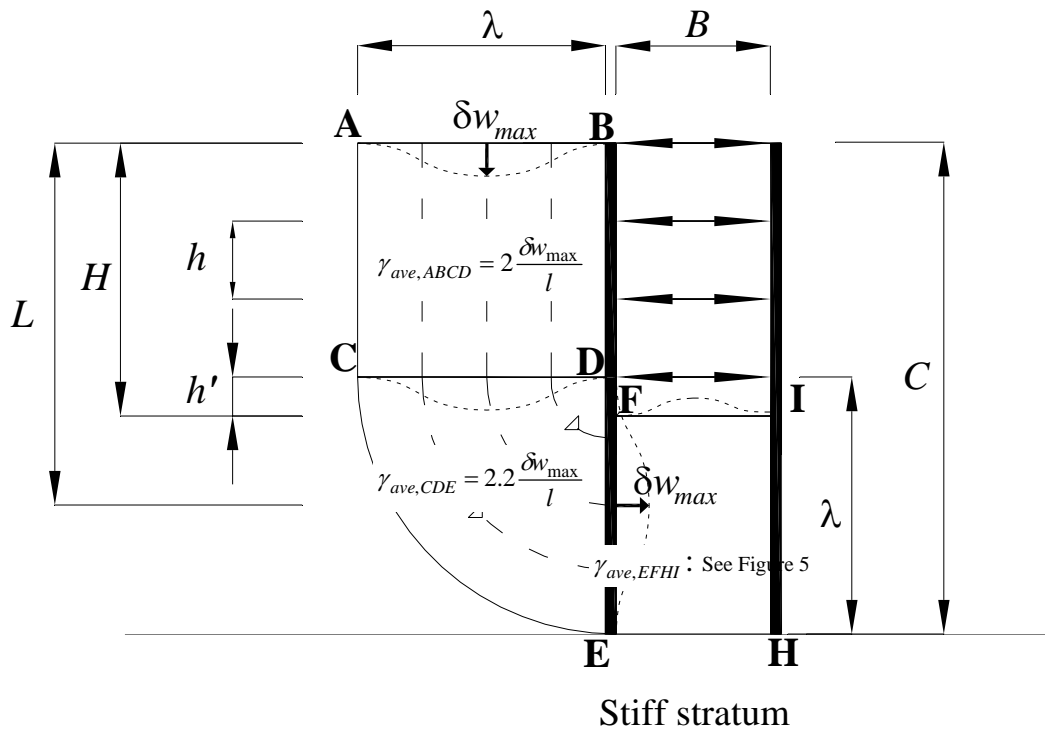
For narrow excavations as shown in **Figure 5.3(b)**, a rectangular zone EFHI of 2D shearing is now proposed. The origin is taken as the mid-point of FE, mid-wavelength in the excavation, at the wall.

$$\delta w_y = \frac{\lambda \times \delta w_{max}}{4B} \left(\pi + \frac{2\pi y}{\lambda} + \sin \left(\frac{2\pi y}{\lambda} \right) \right) \left(\sin \left(\frac{\pi x}{B} \right) \right) \quad (5.10)$$

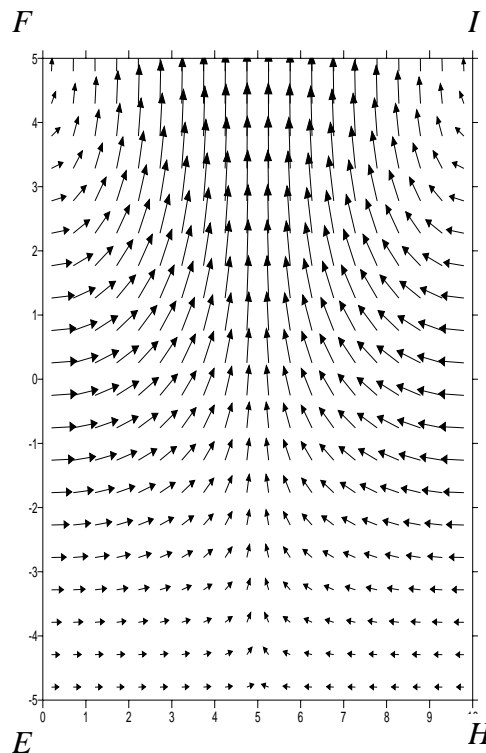
$$\delta w_x = \frac{\delta w_{max}}{2} \left(1 + \cos \left(\frac{2\pi y}{\lambda} \right) \right) \left(\cos \left(\frac{\pi x}{B} \right) \right) \quad (5.11)$$



(a) Incremental displacement field for wide excavation



(b) Incremental displacement field for narrow excavation



(c) Incremental displacement field for narrow excavation in zone EFHI

Figure 5.3 Incremental displacement fields

In order to get more accurate solutions, it is supposed that the soil stratum is divided into n layers of uniform thickness \bar{t} (Figure 5.4). The average shear strain $\delta\gamma(m,n)$ is

calculated for n layers in m excavation stages. The incremental engineering shear strain in each layer is calculated as follows:

$$\delta\gamma(m,n) = \frac{\int \left(\sqrt{\left(\frac{\partial w_x}{\partial y} + \frac{\partial w_y}{\partial x} \right)^2 - 4 \frac{\partial w_x}{\partial x} \frac{\partial w_y}{\partial y}} \right) dVol}{\int dVol} \quad (5.12)$$

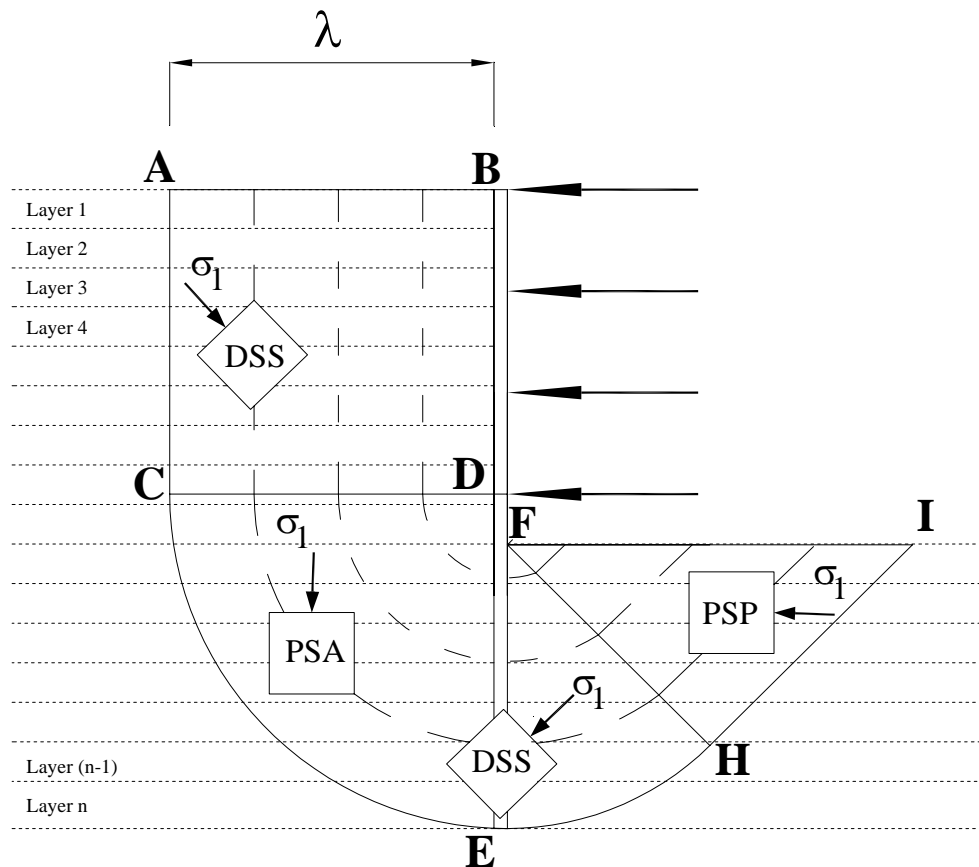


Figure 5.4 Mobilizable shear strength profile of an excavation stage in a layered soil

In order to get a better idea of the deformation mechanism, the relationship between the maximum incremental wall displacement and the average shear strain mobilized in each zone of deformation should be obtained. On the active side of the excavation, the spatial scale is fixed by the wavelength of deformation λ , and all strain components are proportional to $\delta w_{max}/\lambda$. The average engineering shear strain increment γ_{mob} mobilized in the deformed soil can be calculated from the spatial

average of the shear strain increments in the whole volume of the deformation zone.

For a wide excavation i.e. **Figure 5.3(a)**, the average shear strain is equal to $2\delta w_{max}/\lambda$.

For a narrow excavation, the average shear strain (γ_{ave}) of active zone ABCD and fan zone CDE is $2\delta w_{max}/\lambda$ and $2.23\delta w_{max}/\lambda$, respectively, while γ_{ave} in the passive zone

EFHI depends both on the wavelength λ of the deformation and the width B of the excavation. The relationship between the normalized average shear strain in EFHI and

the excavation geometry is shown in **Figure 5.5**. The correlations are as follows:

$$\frac{\gamma_{ave}}{2w_{max}/B} = 0.38\left(\frac{2\lambda}{B}\right) + 0.61 \quad \text{for } \frac{\lambda}{B} \geq 1 \quad (5.13)$$

$$\frac{\gamma_{ave}}{2w_{max}/B} = 0.98\left(\frac{2\lambda}{B}\right)^2 - 3.16\left(\frac{2\lambda}{B}\right) + 3.83 \quad \text{for } \frac{\lambda}{B} \leq 1 \quad (5.14)$$

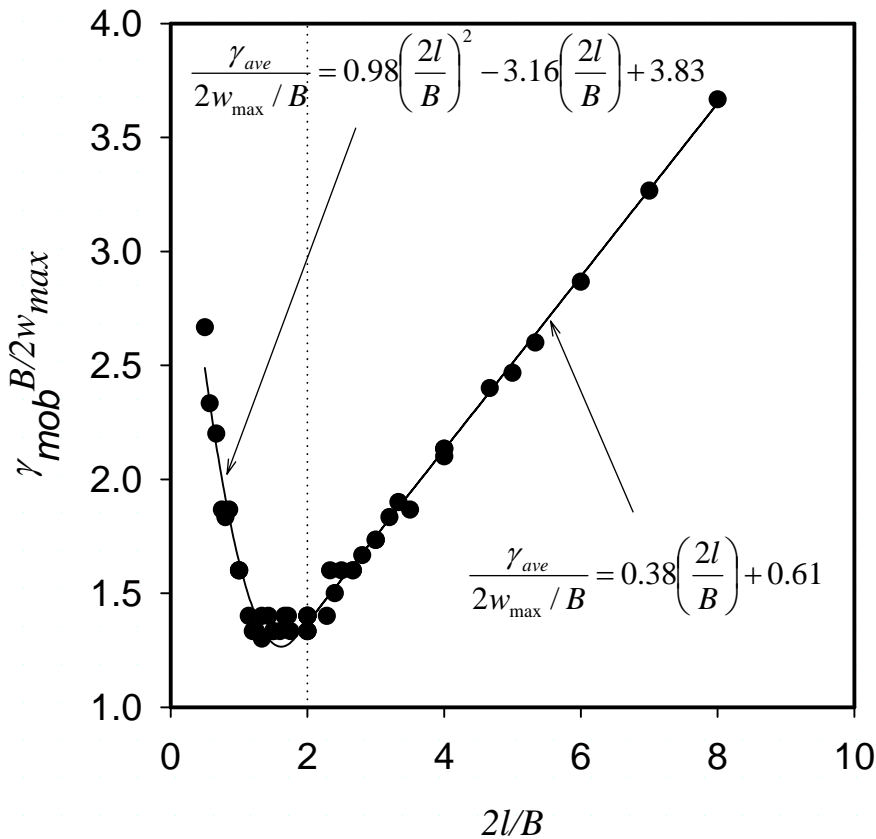


Figure 5.5 Correlation between normalized average shear strain and excavation geometry for a narrow excavation

Apart from the first excavation stage, all subsequent deformation mechanisms must partially overlay the previous ones (Figure 5.6). Due to the non-linearity of soil it is important to calculate the accumulated mobilized shear strain in each particular layer of soil in order to correctly deduce the mobilized shear strength of that layer. This is done by an area average method described as follows:

$$\gamma(m,n) = \frac{d\gamma(m,n) \times A(m,n) + \gamma(m-1,n) \times A(m-1,n)}{A(m,n)} \quad (5.15)$$

where $\gamma(m,n)$ is the total shear strain of the n^{th} layer in the m^{th} excavation stage, and $A(m,n)$ is the area of deformation in the n^{th} layer in the m^{th} excavation stage.

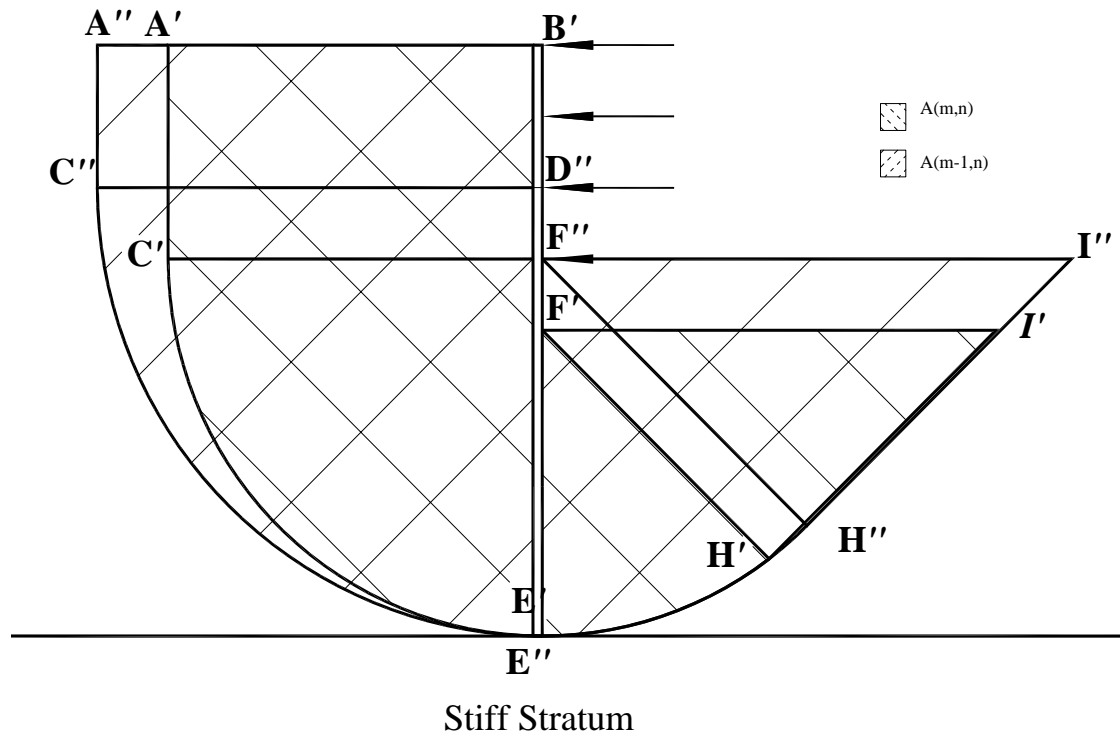


Figure 5.6 Overlapping of deformation field

With the help of some suitable stress-strain relation for the soil (discussed in the following section), the mobilized strength ratio $\beta(m,n)$ at excavation stage m for soil layer n can be found.

5.5 Shear strength mobilized in mechanism

In soft clay, the undrained shear strength generally varies with depth, and with orientation of shear direction. The strength matrix $c_{mob}(m,n)$ mobilized for excavation stage m for layer n can be expressed using a matrix $\beta(m,n)$ on the appropriate undrained shear strength profile. Regarding orientation, anisotropy of soft soil can be a significant factor for excavation stability. For example, Clough & Hansen (1981) show an empirical factor based on the observation that triaxial extension tests give roughly one half the undrained shear strength of triaxial compression, with simple shear roughly half way between. **Figure 5.4** shows the orientation of the major principal stress direction within the various zones of shearing in the assumed plastic mechanism for wide excavations, and indicates with a code the soil test configuration that would correctly represent the undrained shear strength of at the specific orientation. For locations marked DSS the assume directions of shearing are either vertical or horizontal, so the ideal test on a vertical core is a direct simple shear test. In areas marked PSA and PSP, shearing takes place at 45 degrees to the horizontal and these zones are best represented by plain strain active and passive tests, respectively. Since the undrained shear strength of the direct simple shear test is roughly the average of that of PSA and PSP, the relative influence of the PSA and PSP zones is roughly neutral with respect to direct simple shear. As a result, the design method for braced excavation can best be based on the undrained shear strength of a direct simple shear test. A similar decision was made by O'Rourke (1993).

The equilibrium of the unbalanced weight of soil inside the mechanism is achieved by mobilization of shear strength. For each excavation stage, the mobilization of shear strength for each layer is obtained by the following:

$$c_{u,mob}(m,n) = \beta(m,n)c_u(n) \quad (5.16)$$

where $c_{u,mob}(m,n)$ is the mobilized undrained shear strength for layer n in excavation stage m ; $c_u(n)$ is the undrained shear strength for layer n ; and $\beta(m,n)$ is the mobilized strength ratio for excavation stage m and soil layer n .

5.6 Incremental energy balance

By conservation of energy, the total loss of potential energy of the soil (ΔP) must balance the total work done in shearing the soil (ΔW) and the total elastic strain energy stored in bending the wall (ΔU).

$$\Delta P = \Delta W + \Delta U \quad (5.17)$$

The potential energy loss on the active side of the wall and the potential energy gain of soil on the passive side can be calculated easily. The net change of gravitational potential energy (ΔP) in the m^{th} stage of construction is given by the sum of the potential energy changes in each layer:

$$\Delta P_m = \sum_{i=1}^n \left[\int_{\text{volume}} \gamma_{\text{sat}}(m,i) dw_y(m,i) dVol \right] \quad (5.18)$$

where $\delta w_y(m,i)$ is the vertical component of displacement of soil in the i^{th} layer for the m^{th} stage of construction; $\gamma_{\text{sat}}(m,i)$ is the saturated unit weight of soil in the i^{th} layer for the m^{th} construction. The total change in potential energy ΔP from the start of excavation is thus simply given by

$$\Delta P = \sum_{m=1}^M \Delta P_m \quad (5.19)$$

This procedure can obviously be simplified if all soil layers are of equal density.

Since there are no displacement discontinuities, the total work done in shearing the soil is given by summing for each layer:

$$\Delta W = \sum_{i=1}^n \left[\int_{Volume} \beta(m,i) c_u(m,i) |d\gamma(m,i)| dVol \right] \quad (5.20)$$

where $c_u(m,i)$ is the undrained shear strength of soil in the i^{th} layer for the m^{th} construction; $d\gamma(m,i)$ is the shear strain increment of soil in the i^{th} layer for the m^{th} construction; and the corresponding mobilized strength ratio is given by:

$$\beta(m,i) = \frac{c_{u,mob}(m,i)}{c_u(m,i)} \quad (5.21)$$

The total elastic strain energy stored in the wall, ΔU , can be evaluated by repeatedly updating the deflected shape of the wall. It is necessary to do this since U is a quadratic function of displacement:

$$\Delta U = \frac{EI}{2} \int_0^s \left[\frac{d^2 w_x}{dy^2} \right]^2 dy \quad (5.22)$$

where E and I are the elastic modulus and the second moment of area per unit length of wall, and s is the length of the wall in bending. L can be the length of wall s below the lowest prop.

By assuming the cosine waveform equation (Equation 5.1), the strain energy term can be shown to be as follows:

$$\Delta U = \frac{\pi^3 EI \delta w_{max}^2}{\lambda^3} \left(\frac{\pi s}{\lambda} + \frac{\sin(\frac{4\pi s}{\lambda})}{4} \right) \quad (5.23)$$

where λ is the wavelength of deformation, δw_{max} is the maximum deflection of the wall in each excavation increment.

5.7 Calculation procedures for fixed toe walls

The following calculation procedure is programmed in Matlab 2006b.

1. At each stage of excavation, a maximum deformation w_{max} , which is bounded by an upper and a lower bound, is assumed. The soil stratum is divided into n layers. The areas on both the active side and the passive side in each layer are calculated.
2. For each layer, with the help of the numerical integration procedure in Matlab, the mobilized shear strain and the change in potential energy on both active and passive sides in different zones is calculated, (Equation 5.18). The total mobilized shear strain is updated according Equation 5.15.
3. With the use of a suitable stress-strain curve (e.g. Simple shear stress-strain data in [Figure 5.7](#)), the mobilized strength ratio β can be found.

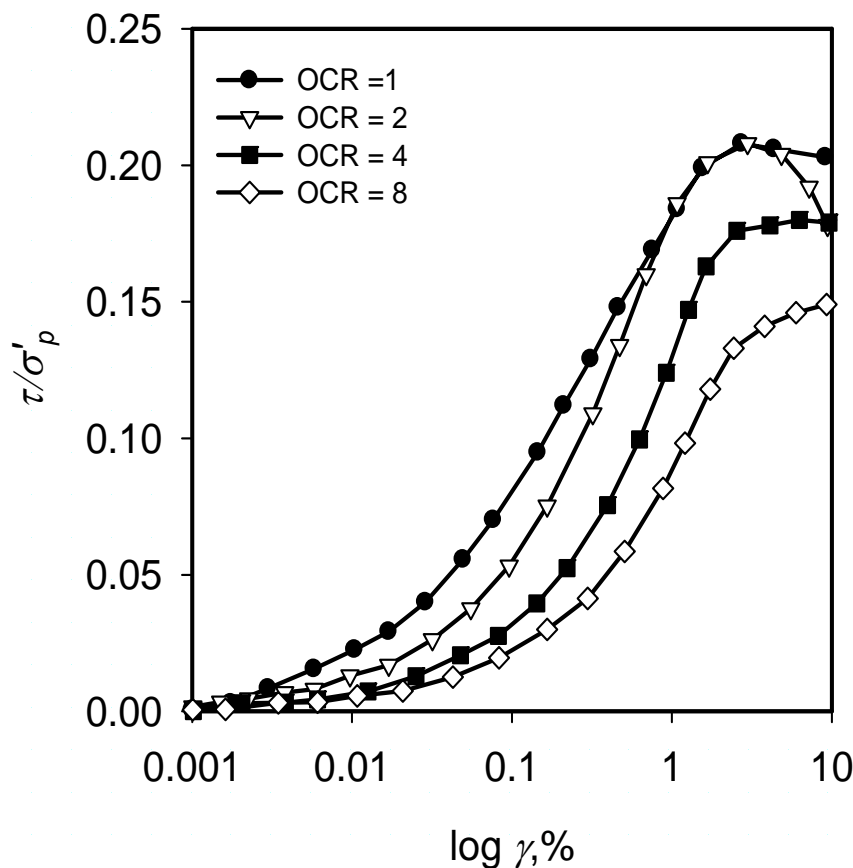


Figure 5.7. Stress-strain response for K_0 consolidated undrained DSS tests on Boston blue clay (After Whittle, 1993)

4. The total change in potential energy, work done on the soil and the elastic bending energy stored in the wall can be calculated by Equations 5.19, 5.20 & 5.22, respectively.
5. By considering the conservation of energy of a structure in static equilibrium, the sum of work in the soil and stored energy in the wall must balance the total change in potential energy. To facilitate solving the solution, an error term is introduced as follows:
$$\text{Error} = \Delta W + \Delta U - \Delta P \quad (5.24)$$
6. When the error is smaller than a specified convergence limit, the assumed deformation is accepted as the solution; otherwise, the method of bisection is employed to obtain another trial maximum displacement, and the error term is calculated again using steps 1 to 5.
7. The incremental wall movement profile is then plotted using the cosine function of Equation 5.1.
8. The cumulative displacement profiles are obtained by accumulating the incremental movement profiles.

5.8 Comparison with finite element analysis

The finite element method can provide a framework for performing numerical simulations to validate the extended MSD method in evaluating the performance of braced excavations. However, finite element analysis of retaining walls is potentially problematic. One of the most difficult problems is the constitutive model used for the soil. The stress-strain relationship can be very complicated when considering soil stress history and anisotropy (Whittle, 1993).

The validation of the extended MSD method is examined by comparing its predictions with results of comprehensive FE analyses of a plane strain braced excavation in Boston Blue Clay carried out by Jen (1998). In these analyses, the MIT-E3 constitutive model is used (Whittle, 1987), based on Modified Cam clay (Roscoe and Burland 1968). However, several modifications had been made to include small strain non-linearity, soil anisotropy and the hysteretic behaviour associated with reversal of load paths. Whittle (1993) also demonstrated the ability of the model to accurately represent the behaviour of different clays when subjected to a variety of loading paths.

An example of MSD calculation

The following example shows the extended MSD calculation of wall deflections for a 40m deep wall retaining clay to 17.5m depth creating an 80m wide excavation. The construction sequence comprises the following steps:

- 1 The soil is excavated initially to an unsupported depth (h) of 2.5m.
- 2 The first support is installed at the ground surface.
- 3 The second level of props is installed at a vertical spacing of 2.5m, and 2.5m of soil is excavated.

The undrained shear strength of the soil is expressed by the relationship suggested by Hashash and Whittle (1996) for Boston Blue Clay (BBC) as follows:

$$c_u = 0.21[8.19z + 24.5]kPa \quad (5.25)$$

The cantilever mode of deformation and the bulging movements are calculated separately using the mechanism of Osman & Bolton (2006) and the extended MSD method as described above. The total wall movements are then obtained by adding the bulging movements to the cantilever movement following Clough et al. (1989).

5.8.1 Wall deflection

Cantilever movement

By solving for horizontal force equilibrium and moment equilibrium about the top of the wall, the mobilized shear stress (c_{mob}) is found to be 11.4kPa. The mobilized strength ratio β is 0.29. With the help of direct simple shear stress-strain data for Boston blue clay by Whittle (1993) (Figure 5.7), the mobilized strain is read off for an appropriate pre-consolidation pressure σ'_p and an appropriate OCR. The mobilized shear strain (γ_{mob}) is found to be 0.2%. The corresponding wall rotation is therefore found to be 0.1%, giving a displacement of 39mm at the top of the wall.

Bulging movement

The first support is installed at the top of the wall. The length of the wall below the support is 40m. By adopting an iterative calculation procedure, and using the deformation mechanism for a narrow excavation, the magnitude of bulging movement at each stage of excavation can be obtained. Then, the incremental bulging movement profile in each stage is plotted using the cosine function based on the corresponding wavelength, which reduces as each level of props is placed. The total wall movement is obtained by superimposing the cantilever movement with all of the bulging movements for the successive stages of excavation. Figure 5.8(a) shows the deformation profiles of the accumulated wall. MSD predicted deeper maximum bulging displacements than the FEA of Jen (1998). The maximum wall deflection predicted by MSD for an excavation depth of 17.5m is 115mm, which corresponds to 0.66% of the excavation depth. This underestimates the FEA by a factor of 1.2.

5.8.2 Bending moment

Comparisons of the bending moments in the retaining wall obtained from FEA and from MSD by a simple finite difference method are shown in [Figure 5.8\(d\)](#). Despite the fact that the position of the MSD predicted maximum bending moment occurs at a deeper level, the magnitude of the maximum bending moment compares very well with the computed result. A design envelope for bending moment is proposed based on MSD predictions and accounting for the changes in profile as excavation proceeds. This gives the designer of a concrete diaphragm wall an apparently successful approximate criterion for the design of steel reinforcement cages necessary for preventing plastic hinge formation.

5.8.3 Ground settlement and base heave

The final displacement profiles of ground settlement are obtained by summing up the incremental settlements in each stage of excavation and are given in [Figure 5.8\(b\)](#). The maximum ground settlement predicted by MSD is 117mm, which over-predicts the FEA by a factor of 1.3. Both the maximum predicted and computed settlement troughs occur at 20m (about 1.14H) behind the diaphragm wall.

Although the MSD results underestimate FEA settlement computations for separations $2H < x < 4H$, it should be recalled that FEA generally predicts settlement troughs that are shallow and wider than reality. MSD may therefore provide a useful boundary for engineers assessing the serviceability of existing structures or services adjacent to deep excavations. In addition, the MSD prediction of base heave at different stages of excavation is compared with computed results in [Figure 5.8\(c\)](#). The maximum base heave predicted by MSD is 64mm, which over-predicts FEA by a factor of 1.1.

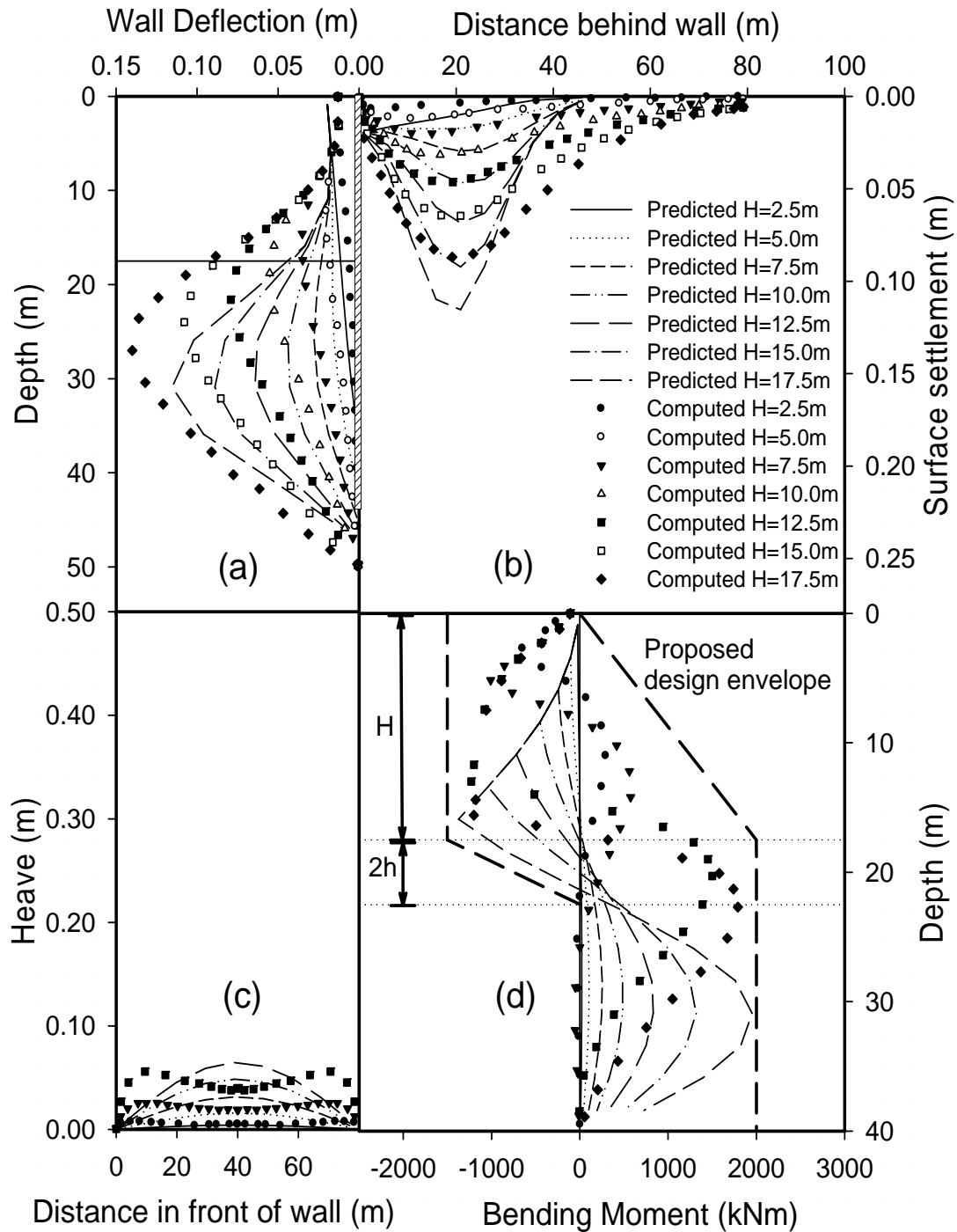


Figure 5.8 Comparison of MSD predicted and computed wall performance: MSD prediction compared with FEA by Jen (1998)

5.9 Validation MSD calculation with case histories in Singapore

The extended MSD method is verified against three case histories of excavations in Singapore marine clay. The new features of layered soil and bending stiffness of the wall would be implemented. Reasonable predictions can be obtained. This

demonstrates the practicality of application of MSD method in the deep excavation problem.

The typical non-linear stress-strain behaviour of Singapore marine clay given by Wong and Broms (1989)(Figure 5.9) is obtained by fitting hyperbolic curve over triaxial stress-strain data using FE. The relationship between stress and strains is given by the hyperbolic formulation as follows:

$$\sigma_1 - \sigma_3 = \frac{\varepsilon_1}{a + b\varepsilon_1} \quad (5.26)$$

,where σ_1 and σ_3 are the major and minor principal stresses respectively and ε_1 is the major principal strain. The parameter a and b are estimated by plotting the triaxial data in $(\sigma_1 - \sigma_3)$ vs ε_1 space. The initial Young's modulus $E_i = 1/a$ and at large strain the deviator stress reaches $(\sigma_1 - \sigma_3)_{ultimate} = 1/b$. The practical failure deviator stress is a fraction of the ultimate stress, $(\sigma_1 - \sigma_3)_{ultimate}$. The expression for Young's modulus E_t can be expressed as:

$$E_t = \left[1 - \frac{R_f (\sigma_1 - \sigma_3)}{2c_u} \right]^2 E_i \quad (5.27)$$

where c_u is the undrained shear strength.

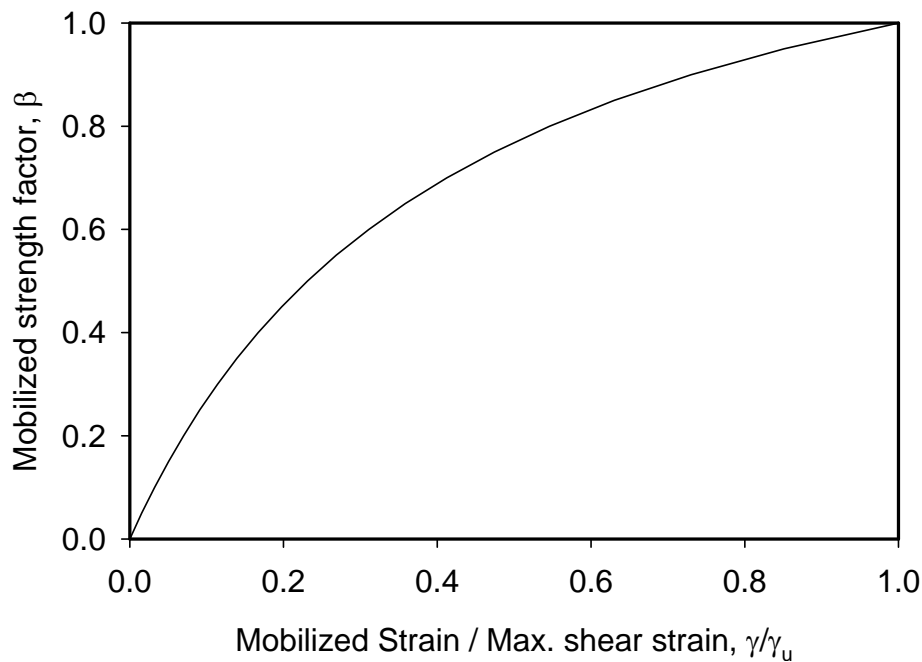


Figure 5.9 Stress strain relationship of Singapore marine clay

Case 1: A braced sheet-pile excavation of 2-level basement in soft marine clay

A narrow excavation of a two-level basement of a sub-structure in soft marine clay in Singapore is investigated. The excavation area measured 110m by 70m is supported by relatively flexible sheet pile wall (Type YSPIII) with a sectional modulus of 1310 cm³/m. The depth of excavation varied from 6.4m to 7.5m. The sheet pile wall was supported by three levels of bolted struts. The vertical spacing varied from 1.4m to 1.8m. The length of the sheet pile ranged from 12m to 24m. The subsoil profile consists of two layers of soft marine clay deposit of a considerable thickness. The detailed description of construction sequence and instrumentations are given in Tan *et al.* (1985). The soil profile of the excavation site is shown in [Figure 5.10](#).

In this analysis, two cases of the sheet pile wall with length of 12m and 24m in layered soils are considered. The measured profiles of lateral displacement are shown in [Figure 5.11\(a\) & \(b\)](#) at various excavation stages at two inclinometers (I-2 and I-9) are chosen for comparison. From measured results from inclinometer I-2, a relatively

large lateral wall displacement of 330mm is observed at an excavation depth of 6.8m due to the considerable extent of the depth of soft clay. While at inclinometer of I-9, the maximum lateral wall displacement was significantly smaller due to the relatively shallow depth of soft clay. Owing to the lack of published actual stress strain data from the site, the simulated stress-strain behavior of Wong and Broms(1989) is used in the MSD calculation. Wong and Broms (1989) assumed $R_f = 0.7$, $E_i = 200c_u$ and $c_u = 15\text{kPa}$. The undrained shear strength of soft clay is assigned to layers at different depths accordingly. The calculated MSD deflection profiles are plotted in the same figure for comparison. Comparisons of maximum lateral deflections between measured data and predicted results are made. A less than twenty percents difference between estimated and computed wall displacement can be obtained. In general, a reasonable estimation of wall displacement can be obtained from stress strain data without the use of FE provided that an appropriate stress strain curve is used.

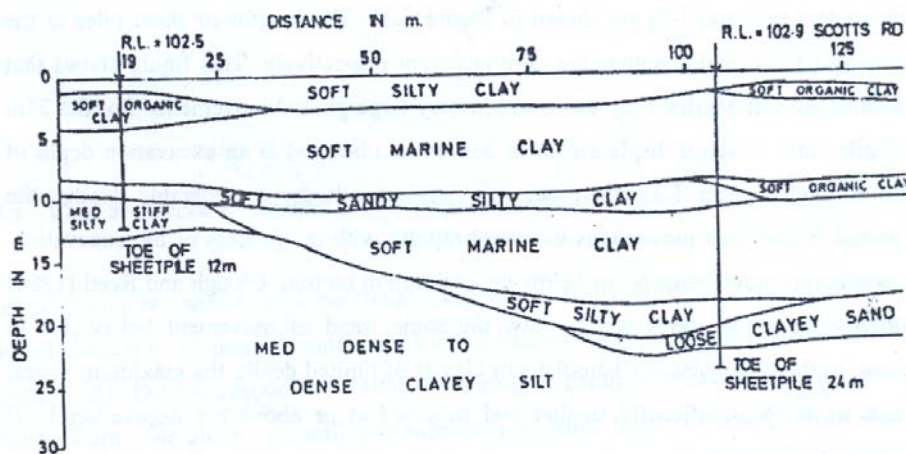


Figure 5.10 Soil profile of excavation site following Tan *et al.* (1985)

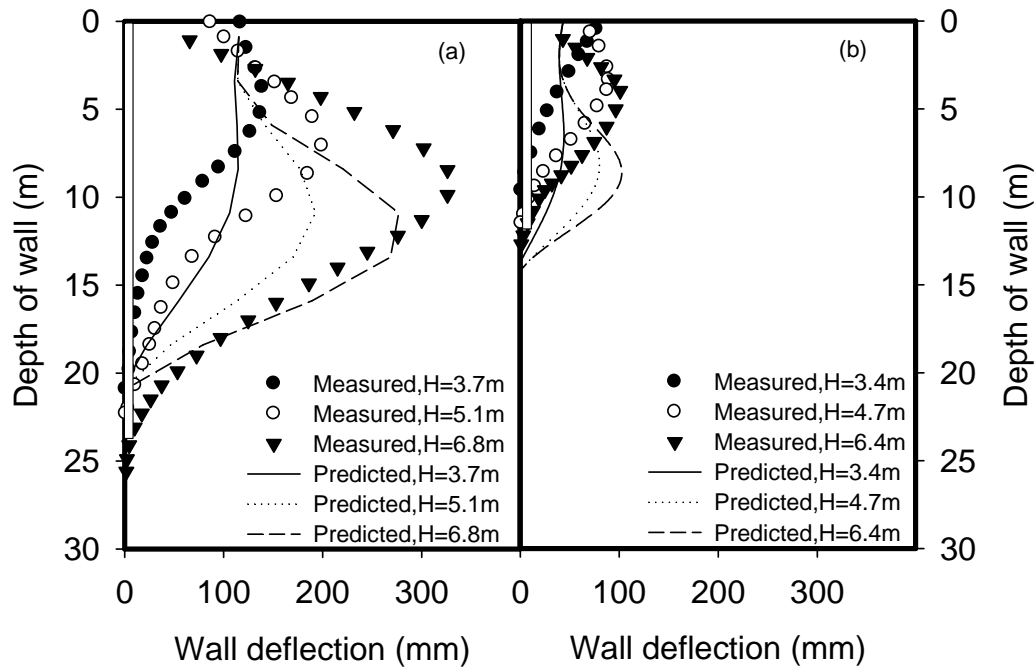


Figure 5.11 MSD Prediction and measured lateral displacement (a) a long wall $L=25\text{m}$ (b) a short wall $L=12.5\text{m}$

Case 2: Excavation of a deep basement in Singapore marine clay supported by diaphragm wall

The construction of the new headquarters of the United Overseas Bank in Singapore, UOB Plaza, included excavation of a 3 level basement. The site is underlain by up to 30m of soft marine clay over hard bouldery clay. The sides of the excavation were supported by diaphragm walls up to 1.2m thick and 35m deep. The basement was constructed using three level of propping with an average prop spacing of 3.5m. The maximum excavation depth is 10 to 12m.

The soil conditions were investigated by boreholes, in-situ vane shear and piezocone tests to establish the shear strength of the soft clay. A desiccated clay layer with a c_u of above 60kPa is sandwiched by a very soft layer of lower marine clay with a c_u of 22kPa and a layer of lower marine clay with a c_u of 50kPa. The water level was located close to the ground surface. For details of the construction method, readers

may refer to Wallace *et al.* (1992). The properties of the soil are summarized in [Figure 5.12](#).

The lateral movement of the diaphragm wall was monitored by inclinometer I111. The inclinometer was installed to the toe of the diaphragm wall which was embedded about 7m into residual soil and hard bouldery clay. Thus, it is assumed that movement of the bottom of the wall toe was zero. The measured movements for a typical diaphragm wall section are shown in [Figure 5.13](#). The relatively small movement is primarily due to the high stiffness of the retaining wall system. The construction sequence was clearly defined and closely supervised with care control of excavation, prompt insertion of prop and preloading. Numerical simulation by FREW is also included for comparison. In general, the computed values over-predicted the lateral wall displacement, which is primarily due to the choice of soil stiffness. On the other hand, MSD prediction results slightly under-predicted the lateral movement at the last stage of excavation owing to the rigid prop assumption. The predicted and computed ground settlement troughs are shown in the figure for comparison. In general, the immediate settlement trough right after the excavation predicted by MSD method agrees well with the computed results.

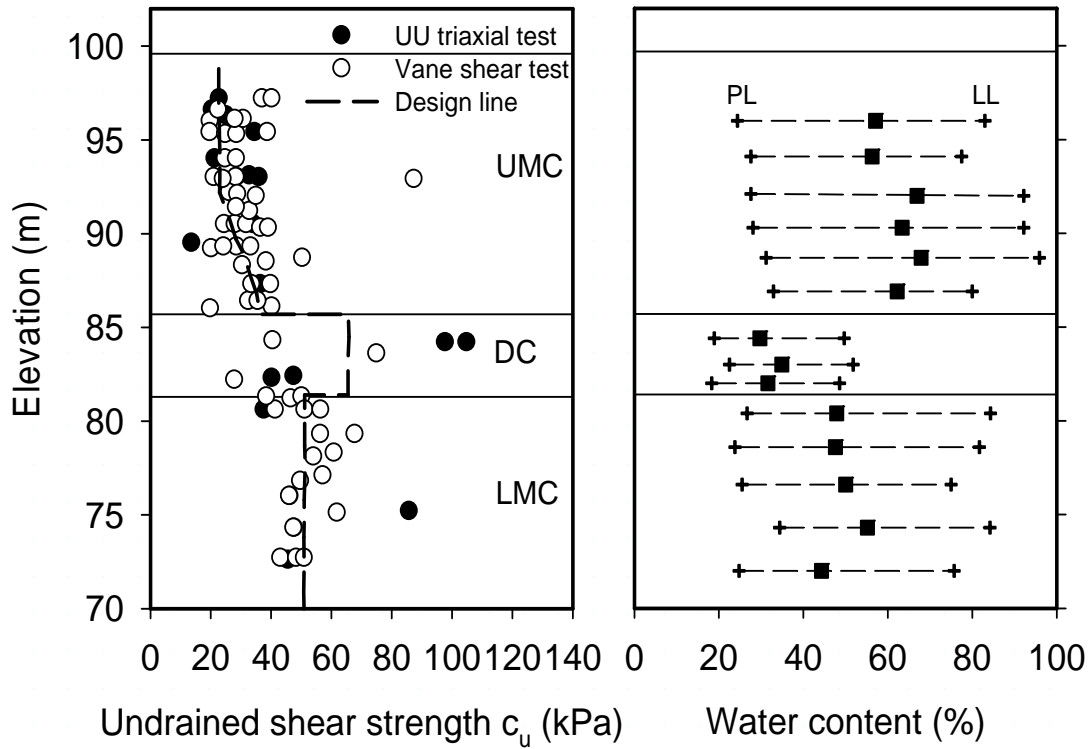


Figure 5.12 Properties of Marine clays from site investigation following Wallace *et al.* (1992)

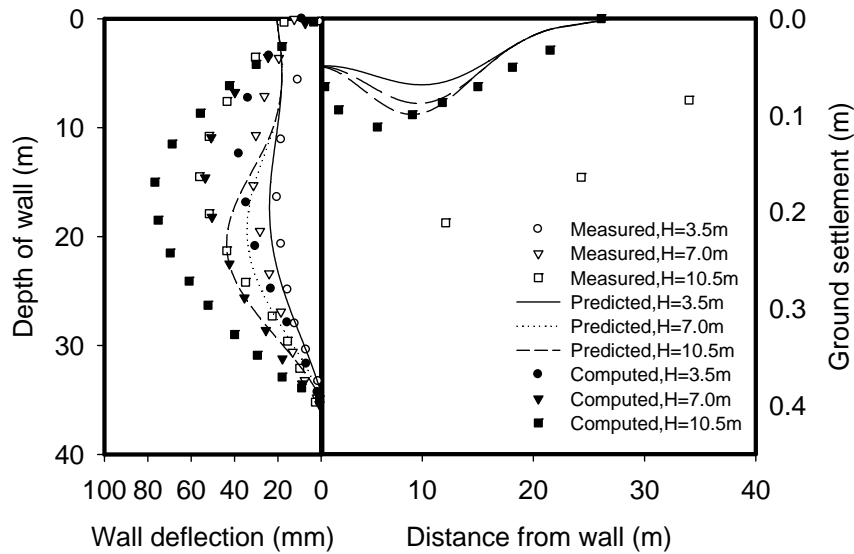


Figure 5.13 Predicted and measured displacement profile at different stage of excavation: MSD predictions compared with measurement and FEA prediction by FREW (Wallace *et al.*, 1992)

Case 3: Excavation of Newton station supported by a 0.8m thick diaphragm wall

The Newton station is about 180m long, 21m wide and 20m deep supported by diaphragm walls embedded 7m into a stiffer layer of completely decomposed granite. The station forms parts of the Singapore metro line and is located below Scotts Road adjacent to the Newton Circus junction with the Bukit Timah Road. The excavation was supported firstly by a 2m-thick heavily reinforced roof slab at an excavation depth of 2.6m for the first stage. Then, it was supported by hangers and trusses at an excavation depth of 7.5m for the second stage and finally a base slab at an excavation depth of 14.5m. Site investigation was conducted by laboratory tests on core taken by thin-wall tube sampler and insitu cone penetration tests. The ground conditions of the site comprise soft marine clay up to 20m deep with a water content of more than 80% overlying fluvial sands and clays which are underlain by completely decomposed granite. The undrained shear strength of the marine clay varies from 14kPa at the clay surface to 18kPa at the bottom of the clay stratum. The marine clay properties are shown in Figure 5.14. For details of the construction method, readers may refer to Nichoson (1987). The properties of the marine clay are summarized in [Figure 5.14](#)

The lateral displacement of the diaphragm wall was monitored by inclinometer I3 for the roof, concourse and base slab stage of excavation. The measured and predicted lateral wall displacement profiles are shown in [Figure 5.15](#). The computed results by Nichoson (1987) are also included for comparison. The prediction gives comparable results with the measured data. It works as well as the result generated by the finite element method. However, the measured maximum wall displacement below ground surface occurs at a higher location than the predicted results. This major discrepancy is ascribed partly to the soft propping response in the field, and partly to the MSD calculation assuming that the top props fix the wall in position and in direction. In

future, the routine for the first level of props should be modified to permit wall rotation about the props. Similarly, predicted immediate ground surface settlement behind the wall shows a comparable result with FEA. The effect of subsequent consolidation settlement can be seen by the measured ground settlement. The settlement points in the field settled 100mm more than those predicted for the immediate undrained condition within a month.

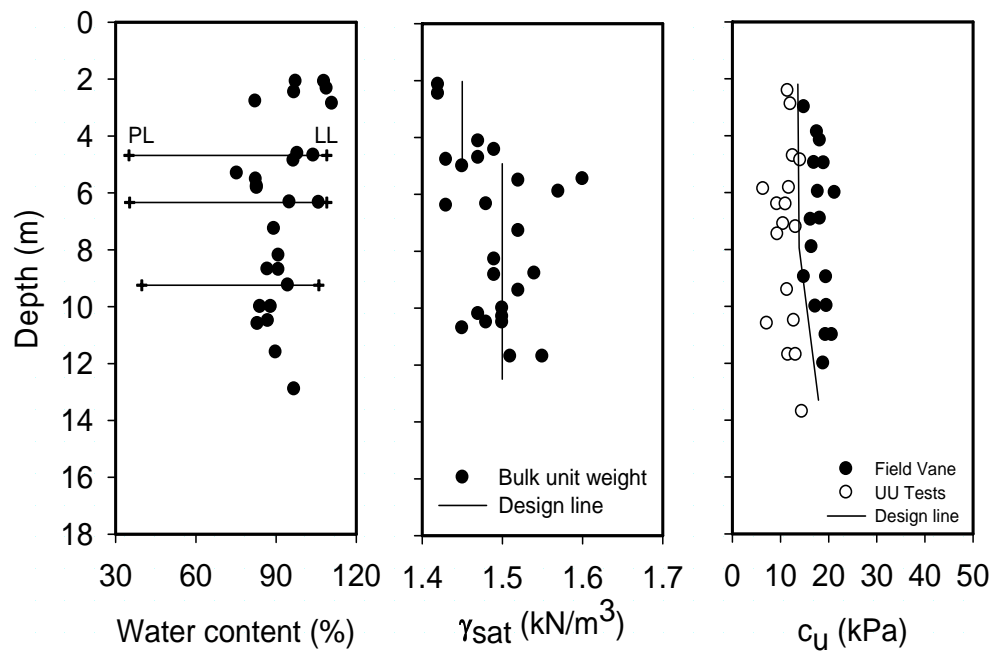


Figure 5.14 Marine clay properties following Nichoson (1987)

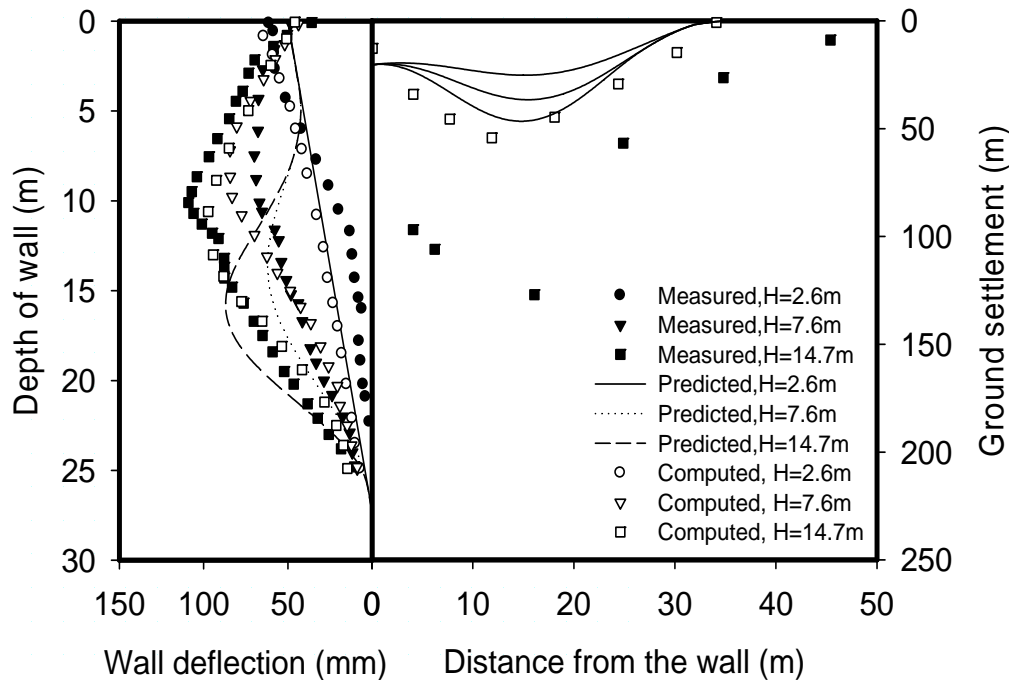


Figure 5.15 Measured and predicted displacement profile at different stages of excavation: MSD predictions compared with measurement and FEA prediction by BILL (Nicholson, 1987)

The extended MSD method is introduced to calculate the maximum wall displacement profile of a multi-propped fixed-base wall retaining an excavation in soft clay. Comparison of the MSD prediction with a numerical experiment carried out by Jen(1998) reveals the capability of the solution to make predictions within 30% of the computed lateral wall displacements. The back-analysis of excavations in Singapore marine clay validates the capability of the new method in dealing with excavations with different wall stiffness, wall length, various soil strata and also different excavation sequences. In the following section, the solution will be extended to applications with excavations in soft clay supported by ‘floating’ walls.

5.10 Calculation procedures for excavation supported by floating walls

In the previous section, the MSD formulation only applies to fixed-toe retaining systems, in which the wall toe is keyed into an underlying stiff stratum. The following section deals with retaining systems ‘floating’ in a thick soft clay deposit. There are

two stages of calculation for an excavation supported by retaining walls with free wall-toe conditions, i.e. floating walls. In the first stage, a MSD prediction is made without considering the elastic energy stored in the structural support system. The following iterations estimate the deep-seated bulging movement assuming zero wall bending stiffness and a wavelength of deformation λ_1 for mechanism ABFIHECA; the kick-out displacement of the wall toe can then be found. This ends the first stage of calculation. In the second stage, the elastic stored energy in the wall is introduced in the formulation. In order to strike an energy balance again, the wavelength of deformation (newly named as λ_2 in stage 2) is allowed to increase. This action induces changes in both potential energy and work done due to shearing in the soil mass above the wall toe (mechanism A'B'FIH'E'C'A). Iterations are carried out until the new energy balance is attained. The modification to the deformation mechanism after introduction of the elastic energy term is shown in [Figure 5.16](#).

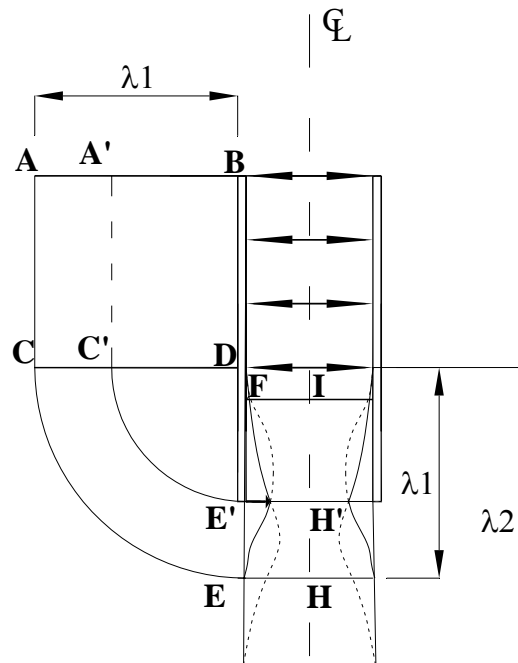


Figure 5.16 Modification to deformation mechanism after introduction of elastic energy stored in the wall to formulation

Here are the details of the new iteration scheme:

Stage I Estimating kick-out displacement at wall toe without consideration of wall stiffness

1. At each stage of excavation, a maximum deformation w_{max} and a wavelength λ_1 (usually within a range of 1.1s to 1.5s, where s is the depth of unsupported wall below the current lowest prop level) are assumed. In addition, the wall stiffness is set to zero to simulate a fully flexible wall. The areas on both the active side and the passive side in each layer are calculated.
2. Repeat steps 2 – 6 for the formulation with a fixed base to obtain maximum wall displacement and the kick-out displacement at the wall toe.

Stage II Estimating actual wall displacement with consideration of wall stiffness

1. Introduction of elastic wall energy term into the formulation upsets the energy balance achieved in stage I.
2. By increasing the wavelength of deformation λ_2 , changes in potential energy and work done by shearing of soil within the deformation mechanism above the wall toe are induced.
3. For each layer, the mobilized shear strain on both active and passive sides in different zones is calculated, (Equation 5.12). The actual total mobilized shear strain is updated according to Equation 5.15.
4. With the use of a suitable stress-strain curve (e.g. Simple shear stress-strain data in Figure 5.7), the mobilized strength ratio β can be found.
5. The total change in potential energy, work done on the soil and the elastic bending energy stored in the wall can be calculated by Equations 5.19, 5.20 & 5.22, respectively.

6. By considering the conservation of energy of a mechanism above the wall toe in static equilibrium, the sum of change in work done in the soil and stored energy in the wall must balance the total change in potential energy. To facilitate solving the solution, an error term is introduced as follows:

$$\text{Error} = (\Delta W_1 - \Delta W_2) + \Delta U - (\Delta P_1 - \Delta P_2) \quad (28)$$

where ΔW_1 and ΔW_2 represents the work done in soils for stage 1 and 2, respectively. ΔP_1 and ΔP_2 represents the potential energy change in soils for stage 1 and 2, respectively. ΔU is the elastic energy stored in the wall.

7. When the error is smaller than a specified convergence limit, the assumed deformation is accepted as the solution; otherwise, the wavelength is increased again, and the error term is calculated again using steps 1 to 6.
8. The incremental wall movement profile is then plotted using the cosine function of Equation 5.1 using wavelengths λ_1 and λ_2 .
9. The cumulative displacement profiles are obtained by accumulating the incremental movement profiles.

5.11 Comparison with finite element analysis

5.11.1 Effect of width of excavation

The effect of excavation width on predicted ground movements is the focus of this section. Underground transportation systems often have excavation widths ranging from 25m (a subway station) to 60m (an underground highway). The most widely used design charts generally incorporate the effect of excavation width in the estimation of factor of the safety against base heave (Bjerrum and Eide, 1956) or as a multiplication factor in estimating the maximum settlement (Mana and Clough, 1981).

The scope of the excavation analyses match those carried out by Jen(1998) and are shown in **Figure 5.17**. In the analyses, the excavation was carried out in undrained conditions in a deposit of normally consolidated Boston Blue Clay with depth C taken to be 100m. A concrete diaphragm wall of depth $L = 40\text{m}$, and thickness 0.9m, supported by rigid props spaced at $h = 2.5\text{m}$, was taken to support the simulated excavation. The excavation width was varied from 20m to 60m. The wavelength of deformation for MSD prediction is chosen according to the $\lambda = \alpha s$ rule, where s is the length of wall below the lowest propping and α was taken to be 1.5. Computed results by Jen (1998) are used for comparison. Full details of the analysis procedures, assumptions and parameters are given in Jen (1998). In the following section, only results of wall deformation will be taken for comparison.

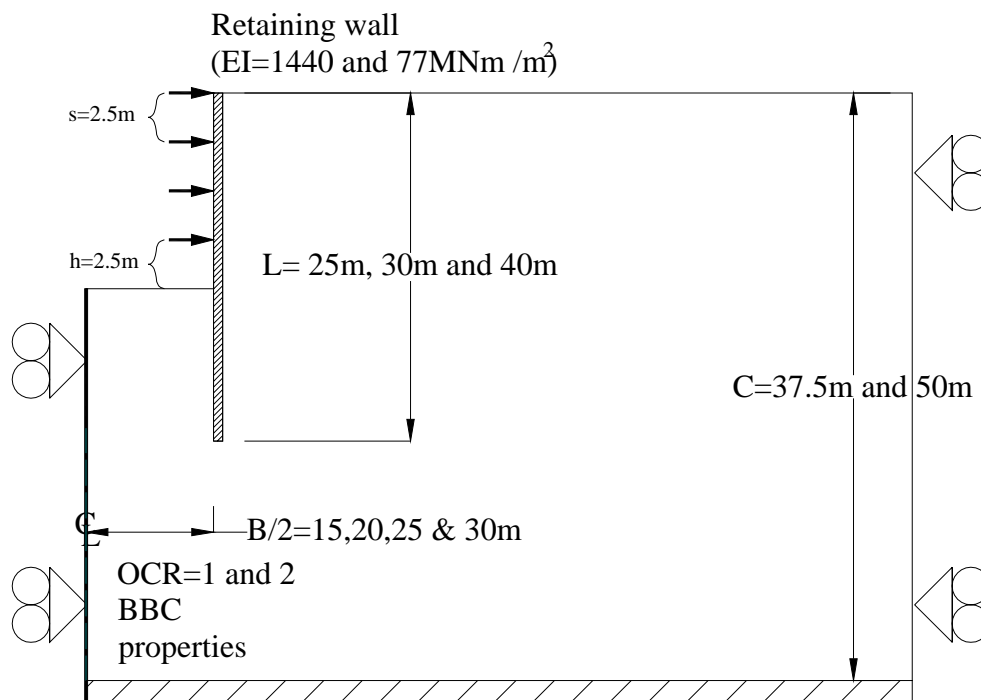


Figure 5.17 Scope of studies carried by Jen (1998)

Figure 5.18 shows the wall deflection profile with different excavation widths at an excavation depth of 17.5m, as calculated by the extended MSD method and the MIT-

E3 model. The MSD predicted results fall within 5% of the FEA computations, and show the same factor increase of about 1.5 as the width of the excavation increases from 30m to 60m. The shapes of the deflected wall given by MSD and FEA are very similar.

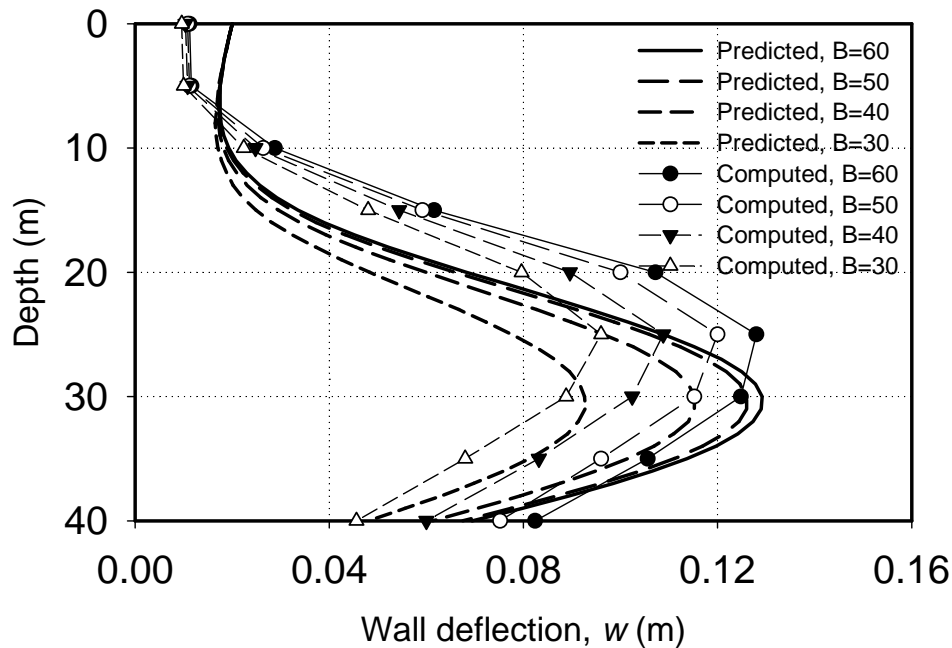


Figure 5.18 Wall deflection profile of different excavation widths at $H = 17.5\text{m}$

5.11.2 Effect of bending stiffness of the wall

In general, structural support to excavations is provided by a wall and bracing system. Soldier piles and lagging, sheet piles, soil mix and soldier piles, drilled piers (secant piles), and reinforced concrete diaphragm walls are examples of wall types that have been used to support excavations. The various types of wall exhibit a significant range of bending stiffness and allowable moment. Support walls composed of soldier piles and sheet piles are generally more flexible and capable of sustaining smaller lateral loads than the more rigid drilled piers and reinforced diaphragm walls.

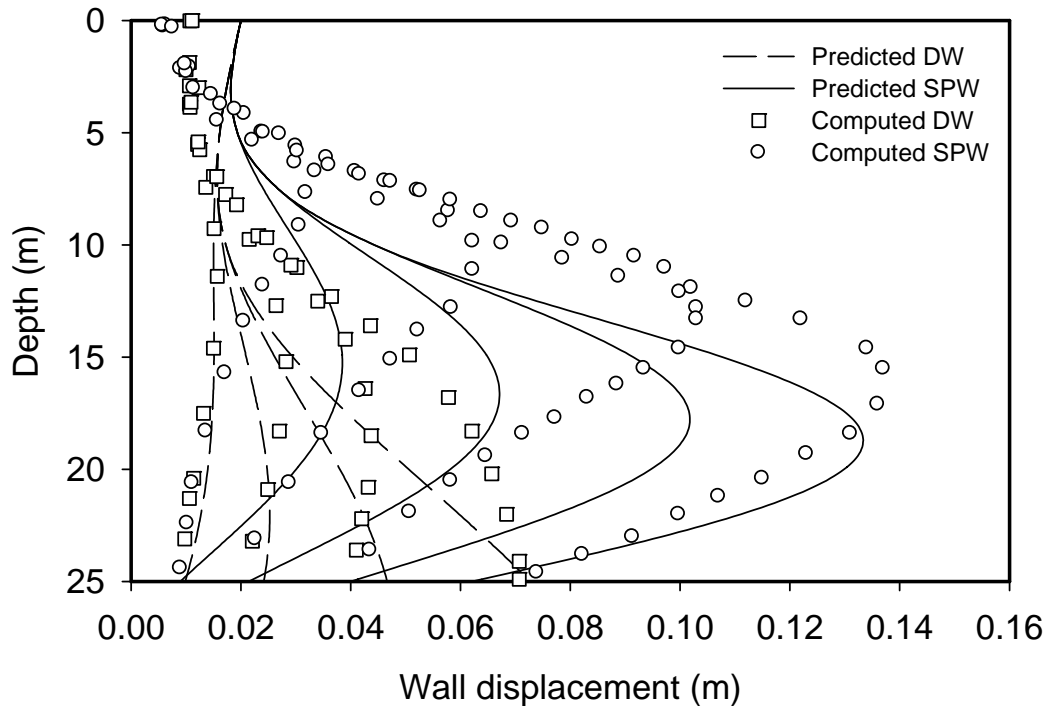


Figure 5.19 Deflection profiles of walls with various bending stiffness

The preceding sections have all assumed a 0.9m thick concrete diaphragm wall with elastic bending stiffness $EI = 1440\text{MNm}^2/\text{m}$. Although it is possible to increase this bending stiffness by increasing the wall thickness and reinforcement, or by using T-panels (barrettes), most of the walls used in practice have lower bending stiffness. For example, the typical bending stiffness of sheet pile walls is in the range of 50 to 80 MNm^2/m . This section assesses the effect of wall bending stiffness on the excavation-induced displacements.

Excavation in soft clay with a width of 40m supported by a wall of depth 25m and of two bending stiffness ($EI = 1440$ and $70 \text{MNm}^2/\text{m}$) are studied. Results generated by the MSD method and FEA are compared. **Figure 5.19** presents the deflection profiles of the excavations predicted by extended MSD and the MIT-E3 model. As the bending stiffness of the wall decreases, there is a change in the overall shape of the wall; the maximum wall deflection increases and its location migrates towards the excavated grade. At $H = 12.5\text{m}$, the maximum wall displacement is 71mm for the

concrete diaphragm wall with the maximum deflection located at 12.5 m below the excavation level, while the result for the most flexible sheet pile wall shows 132mm of maximum wall deflection occurring at 2.5m below the excavation level. In addition to this, changes in wall stiffness also affect the transition from a sub-grade bending mode to a toe kicking-out mode. As the wall stiffness decreases, the influence of embedment depth reduces, and hence the tendency for toe kick-out to occur is less. Again, a fairly good agreement can be seen when comparing extended MSD results and numerical results by the MIT-E3 model, though kinks are usually found at the wall toe in the numerical predictions, which implies localization of large shear strains developed beneath the wall toe.

5.11.3 Effect of the depth of bearing stratum

The depth to bedrock, C , is an important component of the excavation geometry. The preceding analyses have assumed a deep clay layer with bedrock located at $C = 100\text{m}$ which represents a practical upper limit on C . In practice, however, the clay layer is usually less than 100m deep. The following results focus on the discussion of the geometrical parameter C . The analysis involves plane strain excavation in normally consolidated Boston blue clay supported by a 0.9m thick concrete diaphragm wall with rigid strut supports spaced at 2.5m.

The wall deflection profiles for excavations predicted by both MSD and MIT-E3 with two depths of the clay stratum ($C = 35\text{m}$ and 50m) are compared in [Figure 5.20 \(a\) and \(b\)](#).

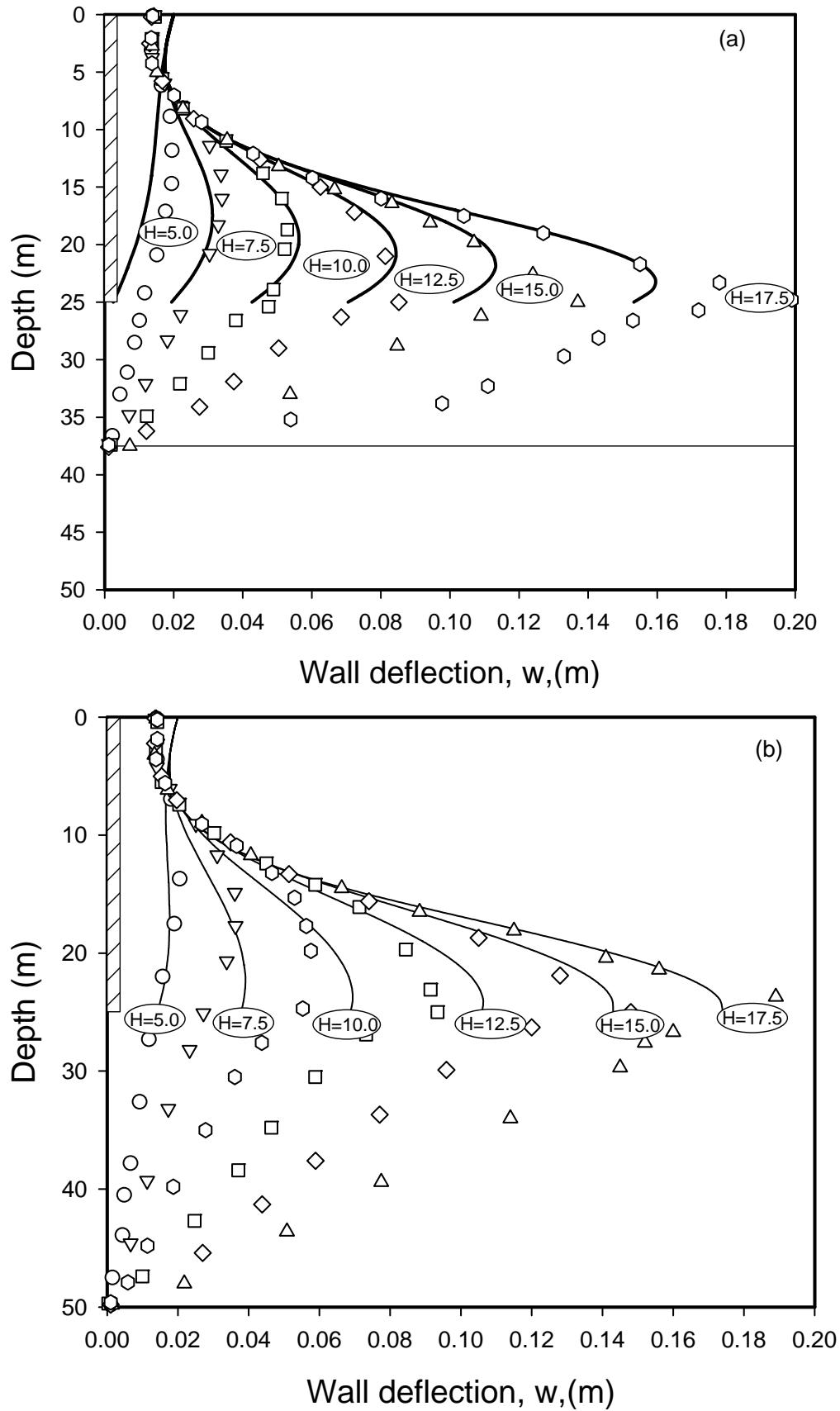


Figure 5.20 Wall deflection profiles of excavation with different depths to the firm stratum: solid lines- MSD prediction, Icons- FEA by Jen (1998) (a) shallow clay C=37.5m (b) deep clay C=50m

The depth of the firm stratum would only affect wall deformations below the excavated level, hence the largest effects can be seen at the toe of the wall. For situations where the wavelength of deformation is restricted less by excavation width than by the depth of the firm stratum ($B > C$), the magnitude of maximum wall deflection increases with the depth of the firm stratum (C). The MSD method predicts a smaller kick-out displacement of the toe of the wall since the size of the deformation mechanism would be limited by the depth of the stiff stratum. The increase in incremental wall deflection decreases in later stages of excavation when H increases from 12.5m to 17.5m due to the reduction of wavelength of deformation. On the other hand, when the depth of the firm stratum is much larger than the width of the excavation ($B < C$), the depth of the bed rock has a minimal effect on the magnitude of wall deflection. Results by FEA by Jen (1998) (Figure 5.18) also showed the same observation. Despite the shortcoming of MSD not being able to model the precise shape of wall, the maximum wall deflection is predicted reasonably well. The net difference in maximum wall displacement between MSD and the full FEA is generally less than 20%.

5.11.4 Effect of clay stratum with different strength or OCR

The influence of soil stress history on excavation-induced ground movements was one of the important parameters evaluated by Jen (1998) which studied embedded walls in Boston Blue Clay with different OCR profiles. In this section, two cases of 40m-deep diaphragm walls embedded in a clay stratum with OCR of 1 and 2, respectively, supporting a 20m deep and 80m wide excavation, are investigated. The undrained shear strength profile is idealized to be increasing linearly with depth for both cases in

which the slope of variation is 1.7kPa/m and 3.4kPa/m, respectively, for OCR=1 and OCR=2.

Two wall deflection profiles of excavations supported by diaphragm walls in a clay stratum with two different OCRs (OCR=1 and OCR=2) are shown in [Figure 5.21 \(a\) and \(b\)](#).

The effect of the stress history and strength profile is firstly the influence on the degree of mobilization of shear strain and hence the magnitude of maximum wall movements. The higher the over-consolidation ratio (OCR), the higher the undrained shear strength and undrained stiffness of the soil are. More work is done by a stiffer soil in the undrained shearing process to balance the potential energy loss of soils within the geo-structural mechanism. Although the MSD wall deflection profile predicts a lower location of the maximum wall deflection, the magnitude of the results predicted by MSD method are within 30% of the FEA results. The maximum wall deflection of an excavation with a depth of 12.5m doubled when the OCR ratio of the soil fell from 2 to 1. The location of the maximum wall movement has a tendency of shifting downwards towards the wall toe as the OCR of soils decreases. This implies a transition of the wall deformation mode from bulging to 'kick-out' mode so that a longer wall should be used to resist the kick-out of the wall toe. This phenomenon will be explained in next section.

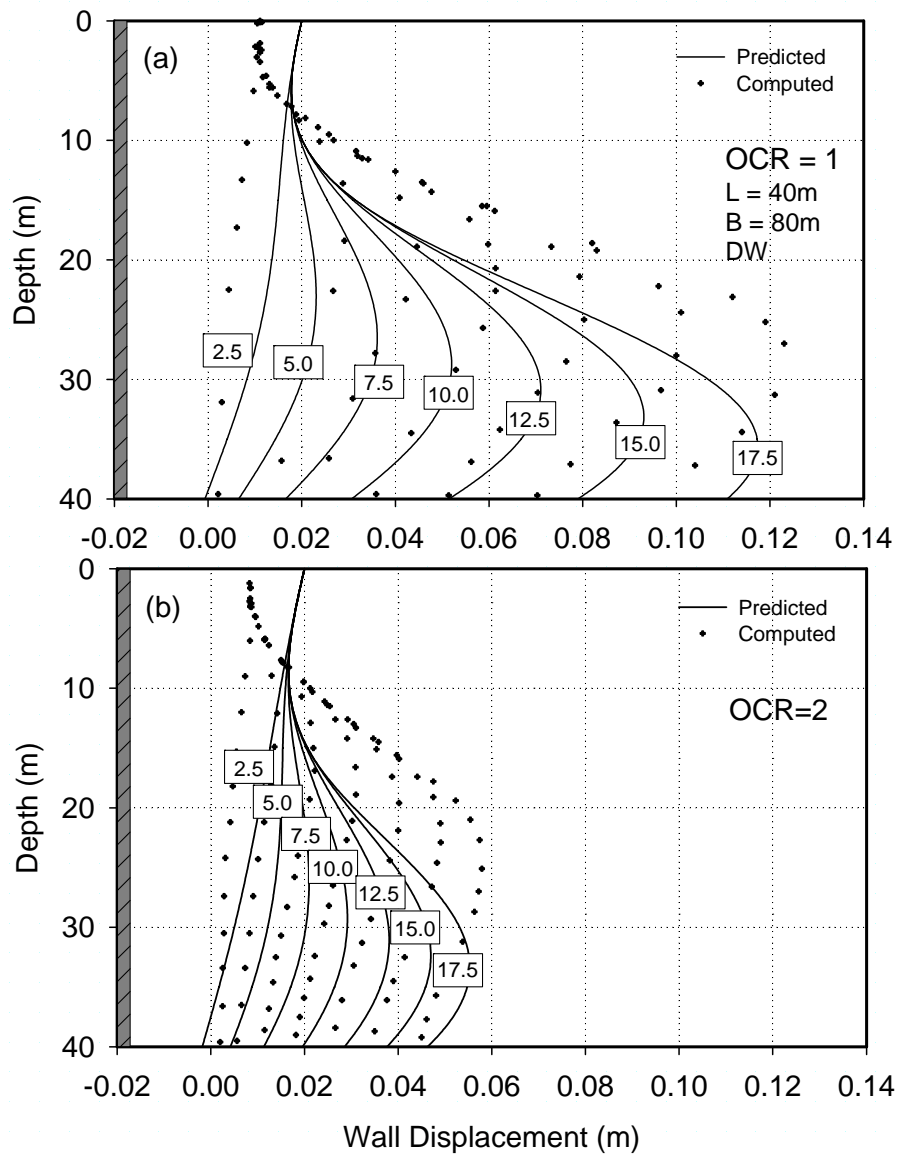


Figure 5.21 Deflection profiles of walls embedded in soil profiles of different stress histories

Figure 5.22 shows the MSD predictions for wall deflection of excavations in soils with different OCRs supported by either a 0.9m-thick concrete diaphragm wall (DW) or a sheet pile wall (SPW). By increasing the wall stiffness, maximum wall displacement decreases by about 45% for walls embedded in soils with OCR of 1 and 2. Apparently, the use of a stiff structural support system for reducing wall displacements in soft soil (OCR=1) is more efficient than in stiffer soils (OCR>1). For an excavation process with a particular geometry, allowing for a potential energy

loss in the soil, a stiffer soil mass does more work to maintain the stability of the excavation so that less elastic energy is stored in the support system. **Figure 5.23** shows the variation of normalized maximum wall movement with system stiffness ($\eta = \frac{EI}{\gamma_w s^4}$) defined by Clough (1989). The MSD prediction lines represent two cases of excavation with the same excavation geometry as defined in **Figure 5.21** in soils with different OCR ratio supported by “floating” walls with different stiffness. Data points of excavations in both soft ($c_u < 75\text{kPa}$) and stiff clays ($c_u > 75\text{kPa}$) from an empirical database collected by Moormann (2004) are included for demonstration purposes. Despite the scatter of the data points, the effect of an increase in system stiffness on reducing ground movement is more prominent for soft soils. A similar trend was shown by the MSD predictions. Further research could be carried out to address the suitability of applying the present approach to soils with higher stiffness such as London Clay.

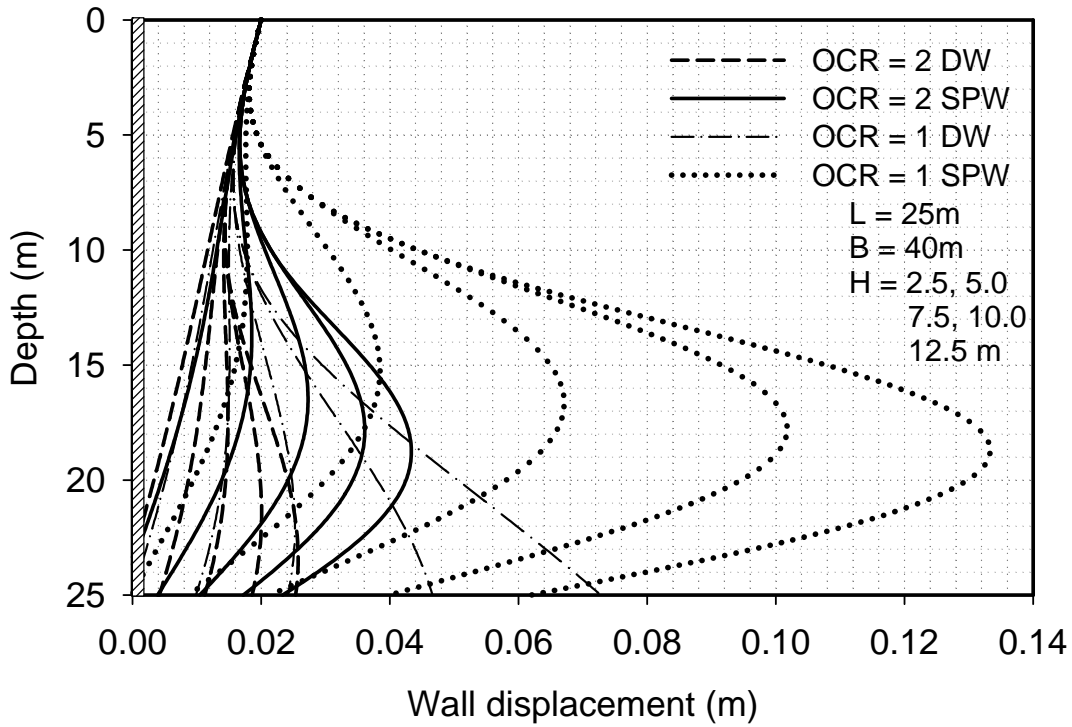


Figure 5.22 Deflection profiles of diaphragm wall and sheet pile wall embedded in soil profiles of different stress histories

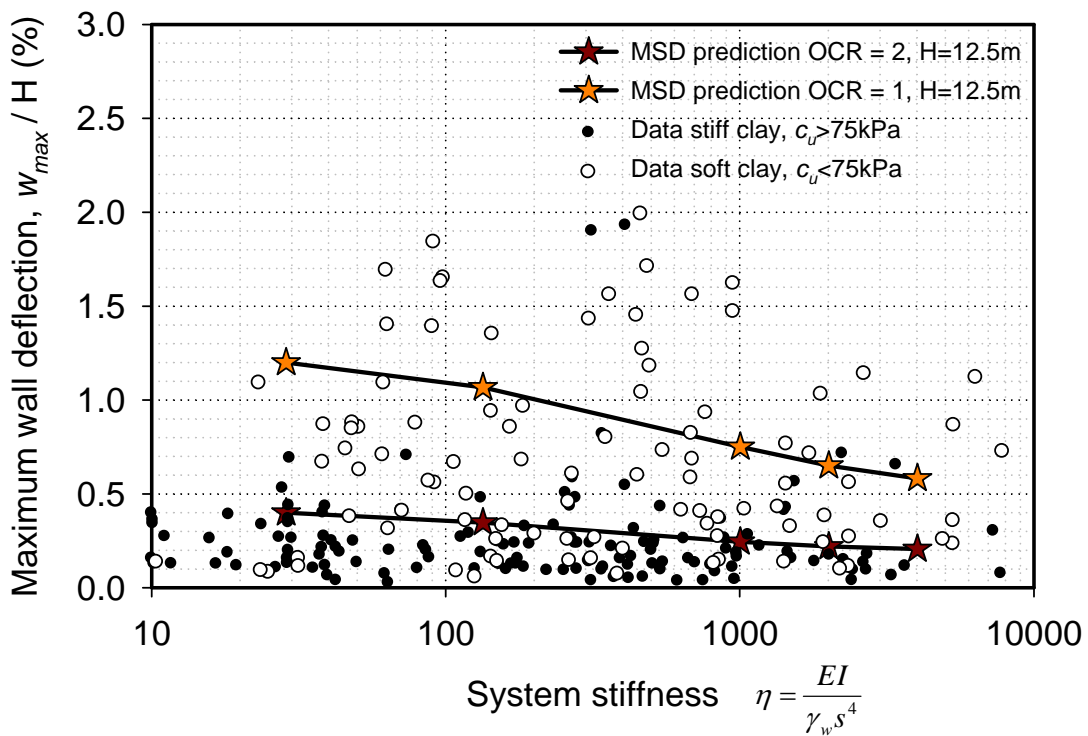


Figure 5.23 Variation of normalized maximum wall deflection with system stiffness following Moormann (2004)

5.11.5 Effect of embedded wall length

Wall length is one of the geometrical factors affecting the behaviour of a supported excavation. Previous analyses were done by Osman and Bolton (2006). The studies showed that the wall end condition should be assumed to be free ($\lambda=2$) for short wall where the clay is soft at the base and the embedded length is not long enough to restrain the movement at the tip of the wall: “Kick-out” deformation mode. For long walls ($L=40\text{m}$), the embedded depth was assumed to be sufficient to restrain wall movement at the wall base. Bulging wall deformation is usually observed for excavation supported by long walls. Although, the effect of structural stiffness was not included in their original formulation, similar observations were made by Hashash and Whittle (1996) in their numerical simulations.

In this section, the effect of the embedded wall length will be considered. Excavations with a width of 40m supported by a 0.9m thick diaphragm wall with varying length ($L=25, 30, 40\text{m}$) are studied. Figure 5.24 shows the wall displacement profiles against depth with different lengths of wall. For an excavation depth below 5m, the wall deformation shapes for all wall lengths are very similar. For an excavation depth of 7.5m onwards, the 25 deep wall exhibited kick-out due to the small embedded depth. A similar situation happens for the 30m deep wall when the excavation depth reaches 12.5m, whereas for the 40m deep wall a bulging deformation mode remains dominant. Similar trends are shown by numerical simulations carried out by Jen (1998). Kick-out happens at excavation depth of 10m and 15m for 25m and 30m deep walls, respectively, although the kick-out of the wall toe happens in a more subtle fashion than with the MSD predictions.

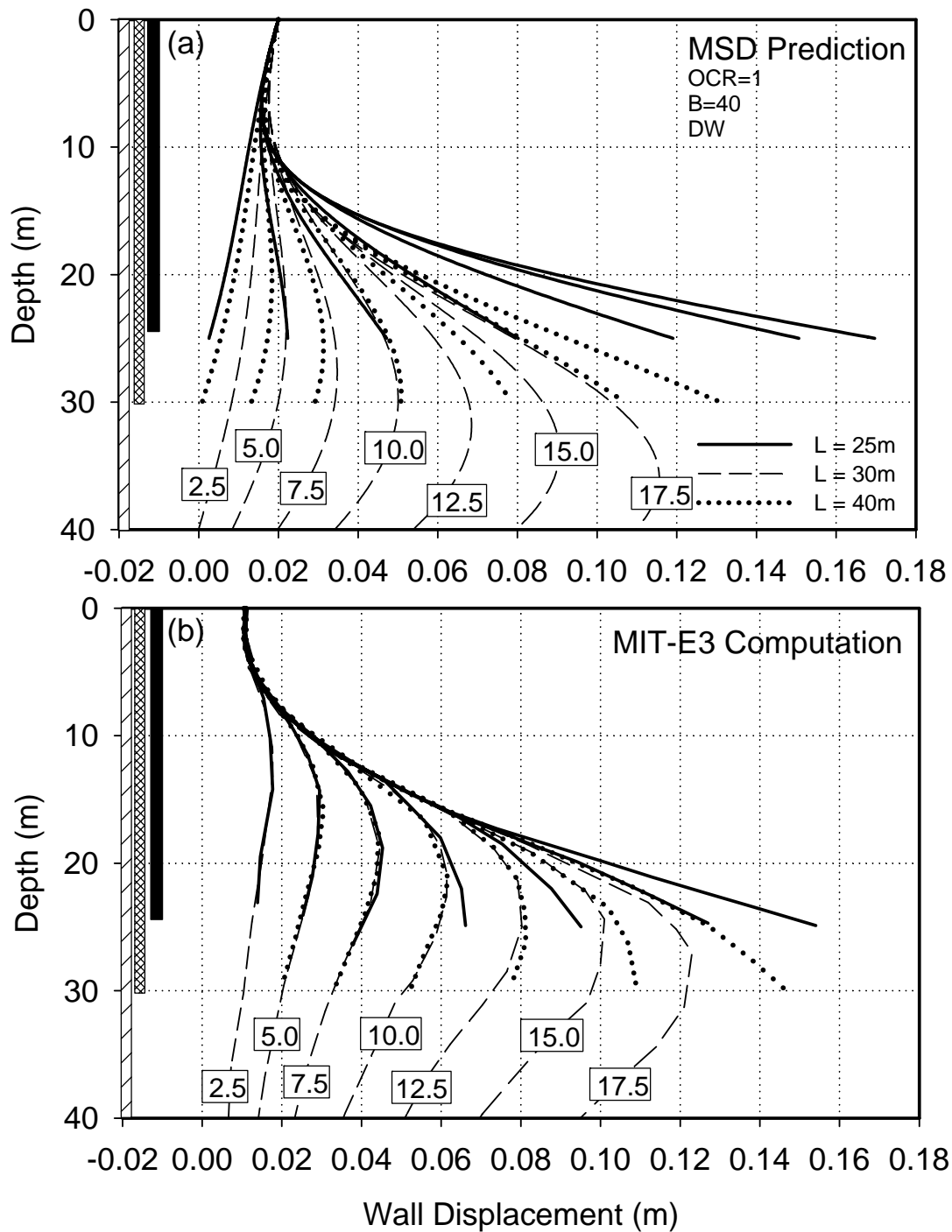


Figure 5.24 Deflection profiles of diaphragm walls with different wall lengths embedded in soft soil

To sum up, the new MSD formulation for floating walls captures the general behaviour of braced excavations accounting for effect of excavation with narrow geometry, variation in width, wall embedded depth wall stiffness and also soil stress

histories. The maximum ground movements predicted by MSD fall within 30% of the FEA computation of Jen (1998).

5.12 Comparison with observed results in centrifuge tests

Results of two centrifuge tests, modelling a rigid floating wall (SYL04) & a flexible floating wall (SYL05), were analyzed by the new floating wall MSD formulations. The MSD predicted wall displacement profiles are plotted against depth in Figure 5.25. The measured results are plotted as icons in the same figure for comparison. The MSD prediction of the stiff wall is very good: the right shape and the predicted maximum within 30% of the observation. The MSD prediction of the flexible wall is less satisfactory presumably due to the contrast between MSD's perfect props and the softer props used in the centrifuge tests, and the use in MSD of a stiff wall for the cantilever phase for prediction.

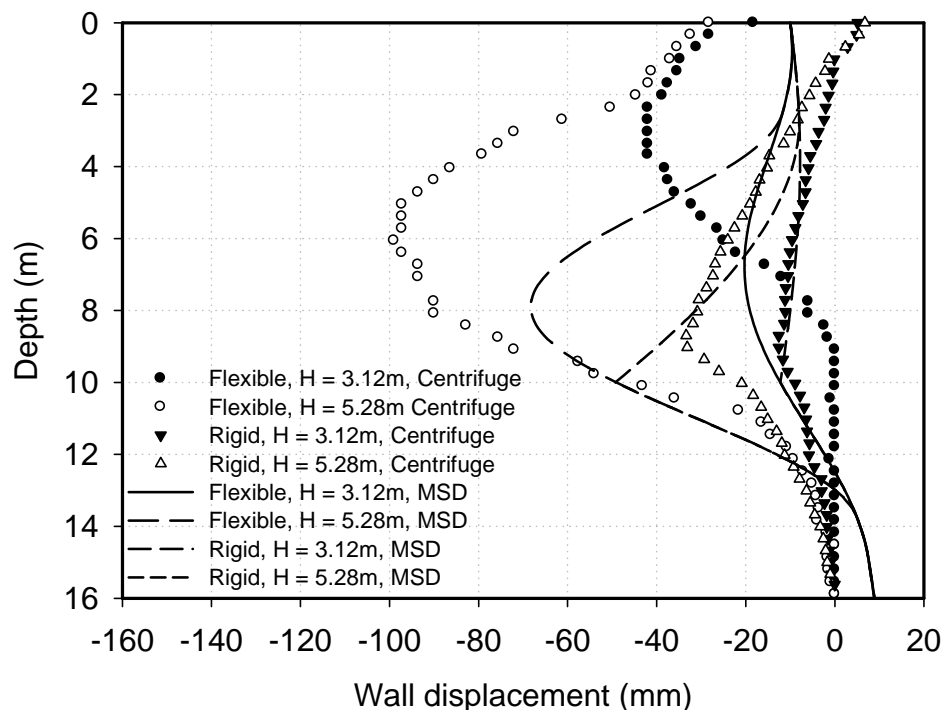


Figure 5.25 Comparison of the deflection profiles by MSD predictions with actual measured displacement in centrifuge tests

5.13. Summaries and discussions

An improved MSD method has been introduced to calculate the displacement profile of a multi-propped wall retaining an excavation in soft clay, which is taken to involve undrained soil behavior during construction. As with the earlier MSD approach, each increment of wall bulging, generated by excavation of soil beneath the current lowest level of support, is approximated by a cosine function. The soil is divided into layers in each of which the average shear strain increments are compounded so that the mobilized strength ratio in each layer can be tracked separately as excavation proceeds, using normalized stress-strain data from DSS tests matched to the soil properties at mid-depth of each layer. The incremental loss in potential energy associated with the formation of a settlement trough, due to wall deformation and base heave, can be expressed as a function of those ground movements at any stage. By conservation of energy, this must always balance the sum of incremental work done in shearing the soil and the incremental storage of elastic strain energy in bending the wall. By an iterative procedure, the developing profile of wall displacements can be found.

A reasonable agreement is found between predictions made of fixed-toe wall displacements, ground settlements, base heave and bending moments using this extended MSD method and the FEA results of Jen (1998) who created full numerical solutions using the MIT-E3 soil model. Although there were some discrepancies in the precise location of the point of maximum bulges, the slope of the wall profile was broadly correct and the magnitude of the maximum displacement was 20% under-predicted by MSD computed with the FEA values. The magnitude of maximum settlement was 30% over-predicted by MSD compared with FEA, which also gave a characteristically wide settlement trough that may not reflect the true field situation.

Maximum wall bending moments produced by MSD corresponded quite closely to FEA computations, although the computed location of the maximum value was significantly higher.

In cases of excavations supported by floating walls, a modified iteration scheme is implemented in two stages of calculation. The first stage estimates the kick-out wall toe displacement assuming zero bending stiffness of the wall. The second stage introduces the elastic bending energy in the wall to the energy balance equation recalculating lateral wall displacement profiles of the wall. The new calculation accounts for the effect of embedded wall length, depth of stiff bearing layer, bending stiffness of wall, excavation width and over-consolidation ratio of soils. The results are compared with the FEA results of Jen (1998) who created full numerical solutions using the MIT-E3 soil model and the centrifuge test SYL04(rigid wall) and SYL05(flexible wall). In general, the MSD predictions fall within 30% of the actual results by both FEA and experiments.

It is proposed that this relatively straightforward MSD analysis, which can be performed within an hour or two by a design engineer, could be a useful tool in taking key design decisions, even if it serves as a precursor to more elaborate FEA.

CHAPTER 6

DATABASE OF MOVEMENTS DUE TO DEEP EXCAVATION IN SOFT SOIL

6.1 Introduction

The MSD procedure for estimating ground deformations due to deep excavations has been seen to be capable of accounting reasonably well for factors such as ground stratification, wall stiffness and boundary conditions, which should be known at the design stage. Other factors, such as the actual construction sequence in space and time and the workmanship involved in fixing struts, will only emerge during construction.

With the aim of gaining a better understanding of the actual ground deformations induced by deep excavations, a database of 155 international well-documented case histories was collected, each of which has been published in geotechnical journals, international conference proceedings, national technical reports, or dissertations. The main focus of these cases was on the deformation of walls supporting deep excavations in soft to firm clays (i.e. $c_u < 75\text{kPa}$). For each case history, relevant information was extracted and analyzed, considering major factors such as soil properties, groundwater conditions, excavation geometry, stiffness of structural support system, construction method and ground deformation responses. Extensive tabulated explanations and full references are attached and shown in Table 6.1.

6.2 Traditional interpretation of field data

This section uses the new database to demonstrate the rather limited efficacy of current ways of presenting wall deformation data. In [Figure 6.1](#), the maximum horizontal wall displacement w_{max} is plotted against the excavation depth H with different icons used for different structural support systems. The values of maximum horizontal displacement scatter over a very wide range, showing that there is no simple linear relationship between horizontal wall displacement and excavation depth, even for a specific wall type. For 55% of the cases, of which the majority are supported by diaphragm walls, the maximum displacement w_{max} is less than 0.5% H . whereas 26% of the cases show maximum displacements lying between 0.5% H and 1% H . Only in 19% of the cases, always involving sheet pile wall excavations, are the maximum wall displacements greater than 1% H . It is evident that the stiffness of the support system has a significant influence on the horizontal wall displacements notwithstanding the scatter in [Figure 6.1](#).

Mana and Clough (1981) plotted the normalized maximum horizontal displacement w_{max}/H against factor of safety against base heave (FOS) defined by Terzaghi (1943) and this is shown for the new database in [Figure 6.2](#). [Figure 6.2](#) also shows the limits suggested by Mana and Clough for cases of excavation in soft soil supported by sheet pile walls. In general, the normalized horizontal displacement of walls from the new database decreases with increasing FOS as expected. Although the majority of the cases fall within the suggested limits, the measured wall movements for a typical FOS=1.5 scatter between $w_{max}/H=0.2\%$ and 2.8%, demonstrating that there is no simple dependence of normalized wall movement with the FOS based on the soil strength alone. The traditional calculation of FOS does not account for governing factors such as soil stiffness and the structural stiffness of the support system.

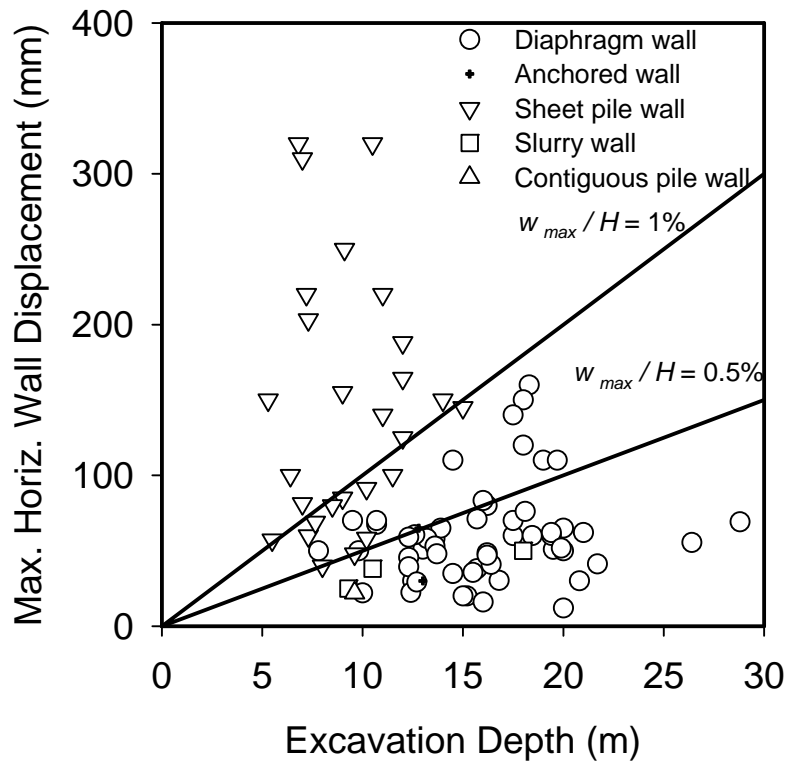


Figure 6.1 Normalized horizontal wall displacement with different support system

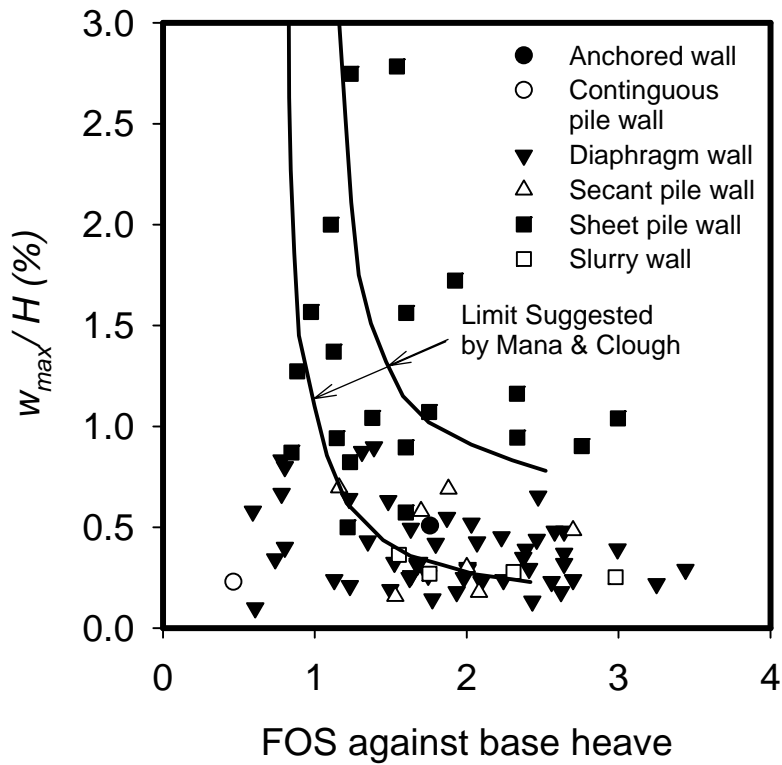


Figure 6.2 Variation of normalized horizontal wall displacement following Mana and Clough (1981) approach

The normalized maximum horizontal wall displacement is plotted in [Figure 6.3](#) versus the system stiffness (η) as defined by Clough et al. (1989).

$$\eta = \frac{EI}{\lambda_w h^4} \quad (26)$$

where EI is the flexural stiffness of the wall, h is the representative vertical spacing between supports, and γ_w is the unit weight of water. Again the data for the cases scatter in a wide range with no simple dependency of the wall displacement on the system stiffness, although the chart suggested by Clough et al.(1989) may be roughly consistent with regard to the dual influence of the system stiffness and factor of safety against base heave. A calculated safety factor of about 1 could lead to observed maximum wall displacements w_{max}/H as low as 0.1%, even though the value expected by Clough et al. was about 1% even for the stiffest support system. Similar observations were made with other databases by Moorman (2004) and Long (2000). Apparently, the factor of safety against base heave is not an ideal measure to quantify ground movements due to deep excavation, even when the wall stiffness is accounted for. Soil stiffness is also significant, as will now be demonstrated.

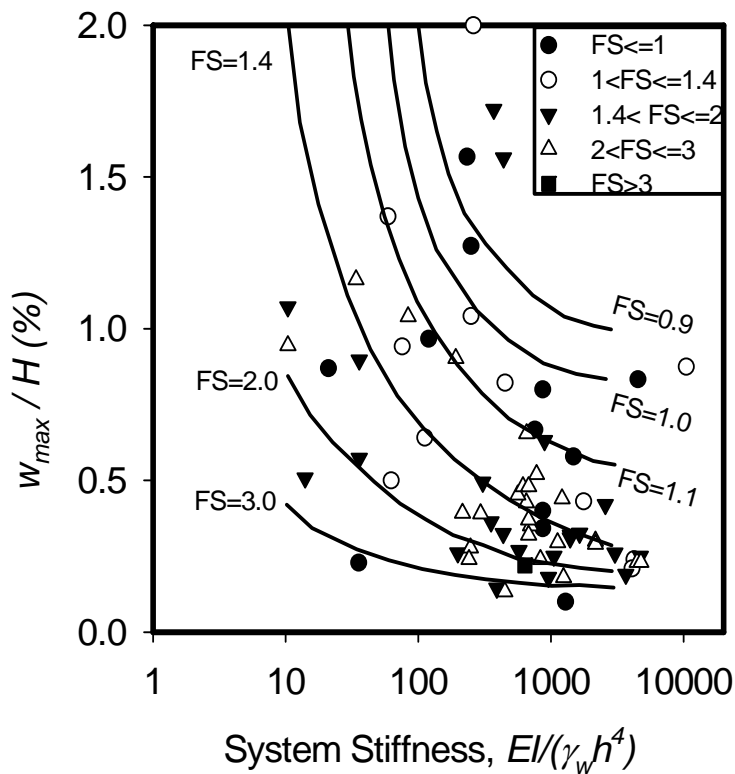


Figure 6.3 Variation of maximum horizontal wall displacement with System stiffness defined by Clough et al. (1989) and factor of safety against base heave.

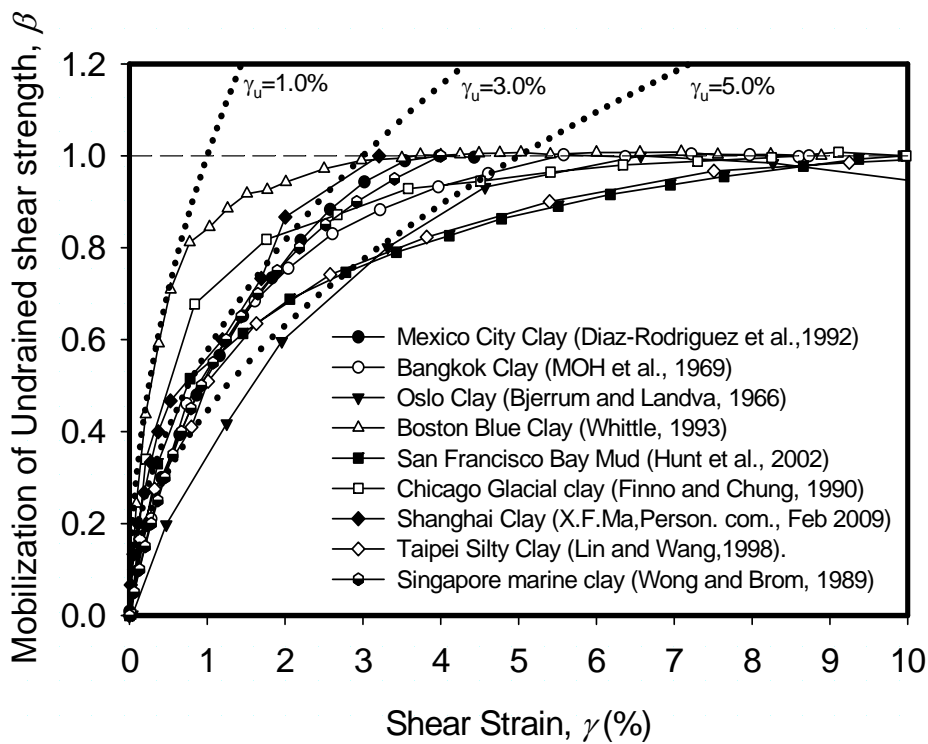


Figure 6.4 Stress Strain relationship of soft clay worldwide (mainly DSS data)

6.3 Performance of MSD method in estimating deformations around deep excavations

A total of 110 out of 155 case histories were so fully documented that an analysis could be conducted with the incremental form of the MSD method taking careful consideration of ground stratification, system stiffness, excavation geometry including excavation depth and breadth, depth to stiff layer, undrained shear strength profile and soil stiffness, for each particular case study.

Figure 6.4 shows the degree of mobilization β of shear strength versus strain in tests reported for the nine soils concerned. The actual test data are compared with parabolic stress strain curves featuring strain to mobilize peak strength $\gamma_u=1\%$, 3% and 5%. The excavation case-specific information from the database was used directly in MSD to predict maximum wall displacements for each stage of excavation, which are compared with authors' reported observations in Figure 6.5. Results show a correlation coefficient $R^2=0.83$ about the line 1:1, with a coefficient of variation of 0.24. More than 90% of the MSD predictions, typically for each of 4 excavation levels, fell within 30% of the corresponding observations. Considering the lack of any detailed account of soil anisotropy, the field performance of MSD is evidently quite satisfactory.

6.4 Simplified relationship between wall deflections and mobilization of soil strength

Following the logic of MSD, a simplified but sound way of analyzing data from the *whole* database can now be introduced. According to the requirement of soil-structure compatibility and the kinematic mechanisms involved in deep excavations the wall

deflection w_{max} can be related to the average shear strain γ_{ave} in the adjacent soil mass by the following:

$$w_{max} \approx \lambda \gamma_{ave} / 2 \quad (6.1)$$

where λ is the typical wavelength which defines the size of the zone of deformation. For the field case studies, which were all on excavations with fixed-based walls, the wavelength is always limited by the depth of the soft clay stratum. In other words, it is defined at any stage as the distance between the lowest prop level and the base of the clay stratum. Due to the incremental nature of a multi-prop excavation, the average wavelength can be taken as:

$$\lambda_{ave} \approx C - (H - h) / 2 \quad (6.2)$$

where C and H are the depth of clay stratum and ultimate excavation depth, respectively, and h is the vertical prop spacing.

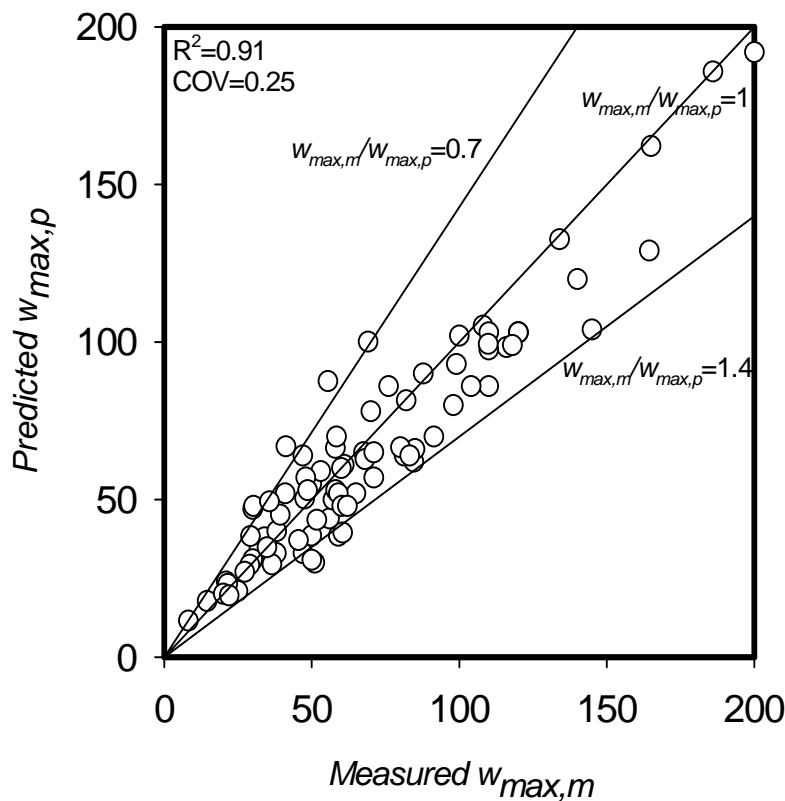


Figure 6.5 Comparison between measured and predicted lateral wall displacement by MSD

The second element of MSD is to relate the shear strain to the mobilization of soil strength by considering the shear stress-strain properties of representative soils. A Mobilization Factor was defined in the UK code of practice on Earth Retaining Structures (BS 8002,1994) as follows:

$$M = \frac{c_u}{c_{mob}} = \frac{1}{\beta} \quad (6.3)$$

The degree of strength mobilization is controlled by shear strain, through the stress-strain relation.

Shearing within the retained soil mass is characterized by principal stress rotation and is best approximated by data from direct simple shear tests. The use of undrained direct simple shear tests is well developed for geotechnical engineering design in soft ground construction (e.g. Ladd and Foott, 1974). **Figure 6.4** summarizes the mobilized shear strength ratio β obtained mainly from undrained DSS tests on a variety of soft clays worldwide. For $\beta < 0.8$, these clays are well described by a parabolic relation:

$$\frac{\gamma}{\gamma_u} = \left(\frac{c_{mob}}{c_u} \right)^2 = \left(\frac{1}{M} \right)^2 \quad \text{for } M \geq 1.25 \quad (6.4)$$

where γ_u is a reference strain obtained by extrapolating approximately parabolic small strain data to intersect the peak strength asymptote. These curves, superimposed on the data in **Figure 6.4**, tend to fall within a range of γ_u from 1% to 5%. For high plasticity normally consolidated clays like Oslo clay, the reference strain value can be larger than 5% whereas the shear strength of low plasticity lightly over-consolidated Boston Blue clay is mobilized at a smaller reference strain of about 1%. When the reference strain is used to normalize the small strain power-law stiffness of soil, a simple relation can be obtained from equation (6.1), (6.2), (6.3) and (6.4) to define a normalized displacement factor ψ for deep excavations as follows:

$$\psi = \frac{2w_{\max}}{\lambda_{ave}\gamma_u} = \frac{2w_{\max}}{(C - (H - h)/2)\gamma_u} \quad (6.5)$$

The approximate parabolic fitting, for $\beta \leq 0.8$ ($M \geq 1.25$) in [Figure 6.4](#) permits a further prediction

$$\psi = \left(\frac{1}{M}\right)^2 \quad \text{for } M \geq 1.25 \quad (6.6)$$

The records of field displacements from the database of Table 6.1 permit the direct calculation of displacement factor ψ from Eq. (6.5) where the characteristic shear strain γ_u is known. We might expect that ψ will vary between 0 and 1, and that it will decrease as the stiffness of the support system increases. The newly extended MSD theory enables a prediction to be made of the variation of ψ with the system stiffness ($\eta = EI/\gamma_w h^4$). An MSD chart of ψ versus η for various values of excavation depth to depth of stiff layer ratio (H/C) and calculated for a typical soft clay strength profile and a stress-strain curve with $\gamma_u = 3\%$, is given in [Figure 6.6\(a\)](#). Although the present analysis does not consider other factors such as consolidation effects, corner effects and also workmanship, the MSD trend lines are broadly consistent with the field data. However, it should be noted that when the parabolic stress-strain approximation leads to calculated values ψ in excess of 0.64, the field measurements can significantly exceed the MSD prediction, (the square icons lying above the uppermost MSD prediction in [Figure 6.6\(a\)](#)). [Figure 6.6\(b\)](#) repeats the MSD prediction of ψ versus η , but for selected values of $\gamma_u = 1\%$, 3% and 5% . It should be noted that γ_u is embodied in the definition of ψ itself, through Eq. (6.5). Accordingly, although γ_u is found in [Figure 6.6](#) not to influence very strongly the predicted displacement factor ψ , at least for flexible walls ($\eta \leq 10^2$), the predicted wall displacement remains *proportional* to γ_u through eq.(6.5).

As discussed above, a warning is included in [Figure 6.6](#) against using the simple parabolic prediction of displacement factor ψ in the case of $\psi_{MSD} > 0.64$, corresponding to $M < 1.25$ or $\beta < 0.8$. Note however that $\psi_{MSD} > 0.64$ corresponds to $w_{max}/H \approx 1\%$ for a typical excavation, which would generally be thought to be excessive in any event, requiring a redesign of the scheme.

If an engineer wants to design a structure to support an excavation with a specified excavation geometry in soil with a stress-strain curve that can be estimated, and if the permissible wall deflection is specified, the equivalent normalized displacement factor ψ can be deduced. The required system stiffness can then be read off from the trend lines in [Figure 6.6\(b\)](#). For instance, to design a 20m deep excavation in a 30m thick very soft soil with a reference strain (γ_u) of 3% and a maximum permissible lateral wall movement of 100 mm, simple calculations (Eq. 6.5) would tell the engineer that the displacement factor should be about 0.33. From the design trend line, a support system with a system stiffness (η) of 1170 is recommended and this will be found to correspond to a 0.8 m thick diaphragm wall with a support spacing of about 3m (giving $\eta \approx 1230$). Although the present approach shows that the displacement factor is not sensitive to change in the system stiffness ranging from a sheet pile wall to a nominal diaphragm wall, the chart is very useful in giving preliminary assessments of ground deformations around excavations.

This approach can provide approximate but reasonably robust answers to key design questions in a sensible industry timescale. For example:

- Should the base of the wall be propped, such as by jet-grouting, prior to excavation?
- Will a particular construction sequence cause the soil to strain so much that it could indulge in post-peak softening?

This opportunity should lead engineers to consider soil stiffness as a key factor in the design of deep excavations, and to request accurate stress-strain data accordingly.

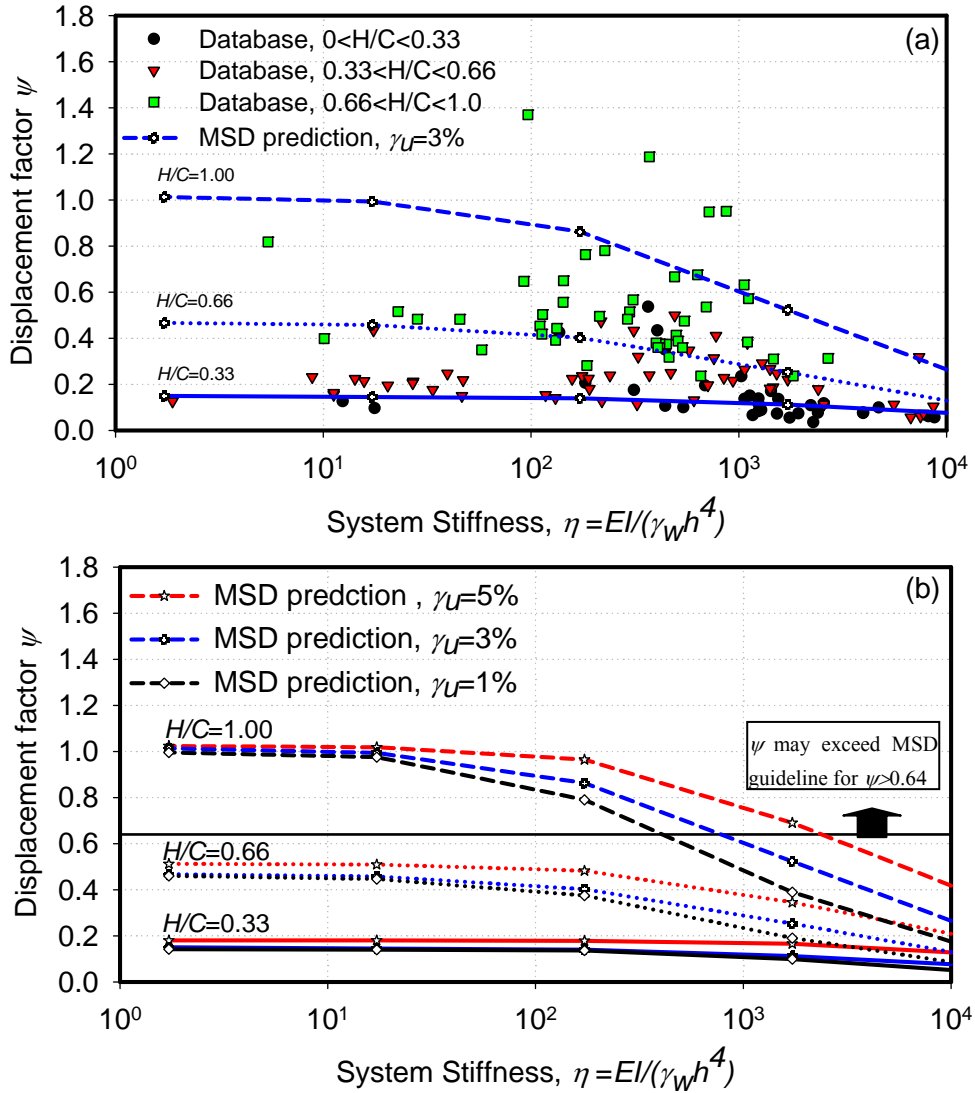


Figure 6.6 Variation of displacement factor ψ with system stiffness defined by Clough (1989) (a) Data and MSD prediction for $\gamma_u = 3\%$, (b) MSD prediction for $\gamma_u = 1\%$, 3% and 5%

6.5 Non-dimensional analysis of deep excavation case histories

Whilst MSD can confidently be used to make site-specific predictions and perform preliminary design of serviceability, it will also be helpful to use MSD concepts to derive better dimensionless groups to chart data from field case studies, and to assist understanding and decision-making prior to any detailed analysis.

Consider first the normalization of maximum wall displacement w_{max} itself. MSD shows us, as in [Figure 5.8](#), that the initial excavation to fix the top row of props generally produces relatively small movements at the crest in the cantilever phase of wall rotation or bending. The most significant deformations for a fixed-base wall arise from later stages of construction when the wall bulges below the lowest props. Elastic beam theory applied to the mechanism then teaches us that the change of net pressure necessary to produce a bulge of amplitude w_{max} over a wavelength λ will be

$$\Delta p \propto w_{max} \frac{EI}{\lambda^4} \quad (6.7)$$

This can be normalised with respect to the reduction in vertical earth pressure $\rho g H$ due to excavation. Accordingly, a structural response ratio S can be defined:

$$S = \frac{w_{max} EI}{\rho g H \lambda^4} \quad (6.8)$$

Whilst MSD permits λ to reduce progressively as props are placed deeper, a design chart might simply characterise the average situation, and an average λ value will be

taken here as the distance between the middle props and the base of the deforming clay.

We will define

$$\text{Average } \lambda = D - 0.5H \quad (6.9)$$

and we will use this value in Equation 6.7.

Now consider the various system parameters that might modify the structural response ratio. It is proposed that they can best be visualized in combination as a soil-structure stiffness ratio R :

$$R = \frac{c_u}{\gamma_u} \frac{c_u}{\rho g H} \frac{\lambda^3}{EI} \quad (6.10)$$

where λ is again taken as the average value during the whole excavation process, and where the value of c_u is selected to represent the strength at mid-depth of the soft clay layer. The rationalization is as follows. The ratio c_u/γ_u is the secant shear modulus just as peak strength is reached. For a parabolic shear stress-strain curve we obtain the secant modulus mobilised at any earlier stage:

$$G = \frac{c_{mob}}{\gamma} = \frac{c_u}{\gamma} \left(\frac{\gamma}{\gamma_u} \right)^{0.5} = \frac{c_u}{\gamma_u} \left(\frac{\gamma_u}{\gamma} \right)^{0.5} \quad (6.11)$$

We can also write this as:

$$G = \frac{c_u}{\gamma_u} \frac{c_u}{c_{mob}} = \frac{c_u}{\gamma_u} M \quad (6.12)$$

representing the shear modulus increasing at higher values of M and correspondingly smaller strains. Now, the average mobilisation factor M in the soil should be of the following form:

$$M \propto \frac{c_u}{\rho g H} \quad (6.13)$$

governing the “factor of safety” of an undrained excavation. It follows from (6.12) and (6.13) that the mobilised soil secant modulus:

$$G \propto \frac{c_u}{\gamma_u} \frac{c_u}{\rho g H} \quad (6.14)$$

which is recognisable as the first two terms on the right hand side of Equation 6.10. The final term (λ^3/EI) is simply the inverse of wall bending stiffness per unit axial length, expressed in consistent units. Equation 6.10 therefore represents the non-dimensional soil-structure stiffness ratio for soil with a parabolic stress-strain curve up to (c_u, γ_u) . The new database can now be used to investigate the relationship between structural response ratio S and soil-structure stiffness ratio R : see [Figure 6.7](#) where this is shown on log-log axes to capture the enormous range of wall stiffness between sheet-piles and thick diaphragm walls. Very remarkably, the field data fit an exactly inverse relationship (i.e. the slope equals -1.00), with a coefficient of determination of 0.964. This can be written as

$$\log_{10} S = -2.6 - \log_{10} R \quad (6.15)$$

and rationalized to give:

$$SR \approx \frac{1}{400} \quad (6.16)$$

within an uncertainty factor of 2.9 (calculated as 2 standard deviations) according to [Figure 6.7](#). The same relationship emerges from the predicted wall displacements using MSD: see [Figure 6.8](#).

Substituting for S and R from equations 6.8 and 6.10, respectively, we can define a normalised displacement factor Ω such that:

$$\Omega = SR = \frac{w_{\max}}{\lambda} \frac{1}{\gamma_u} \left(\frac{c_u}{\rho g H} \right)^2 = \frac{1}{400} \quad (6.17)$$

Notably, the wall bending stiffness has now cancelled out. Figures 6.7 and 6.8, together with equations 6.16 and 6.17, have shown that wall stiffness may have a negligible influence on the amplitude of wall bulging due to excavation in the case of wall fixed at their base. This seems to be valid for EI ranging within 4 orders of magnitude between sheet-piles and reinforced concrete diaphragms, representing 110 braced retaining walls from around the world.

Equation 6.17 enables the engineer to estimate maximum wall displacement w_{\max} using knowledge only of excavation depth H, clay depth D to a stiff stratum (to calculate λ from equation 6.9), soil density γ_{sat} and shear strength c_u at mid-depth 0.5D, and the reference strain γ_u required for peak strength which can be estimated from plasticity index according to Vardanaga & Bolton (2010). But the possible variation by a factor of

up to 2.9 must not be forgotten. This is emphasized in [Figure 6.9](#) where the normalized displacement factor Ω is plotted on a linear scale against a non-dimensional structural system stiffness η where:

$$\eta = \frac{EI}{\rho_w g \lambda^4} \quad (6.18)$$

The arithmetical average value of Ω for the field data plotted in [Figure 6.9](#) is 0.003, but the range is about 0.001 to 0.008. It must be recognized that much of this scatter arises from the desire in these charts to represent the excavation construction process in terms of a single mechanism of dimension. If the engineer is prepared to take another few hours establishing the possible construction sequence and excavation stages, and performing a cumulative MSD calculation on a spreadsheet, then the scatter of 110 jobs reduces from a factor of about 2.9 (see [Figure 6.7](#)) to a factor of about 1.4 (see [Figure 6.5](#)). Most of this remaining uncertainty is thought to arise from the difficulty of selecting representative values of undrained shear strength c_u and reference strain γ_u . It would be easy to accept that c_u might be uncertain within 10% so that c_u^2 varies within a factor of 1.2. And while the plots in [Figures 6.7 and 6.8](#) benefitted from an estimate of γ_u based on the data of site-specific direct simple shear (DSS) tests, shown in [Figure 6.4](#), the uncertainty factor must again have been about 1.2. A larger uncertainty would have had to be accepted if γ_u had been estimated from plasticity index, of course.

It is interesting to use equation 6.17 to develop an expression for the more familiar term w_{max}/H :

$$\frac{w_{max}}{H} \approx \frac{\gamma_u}{400} \frac{\lambda}{H} \left(\frac{\rho g H}{c_u} \right)^2 \quad (6.19)$$

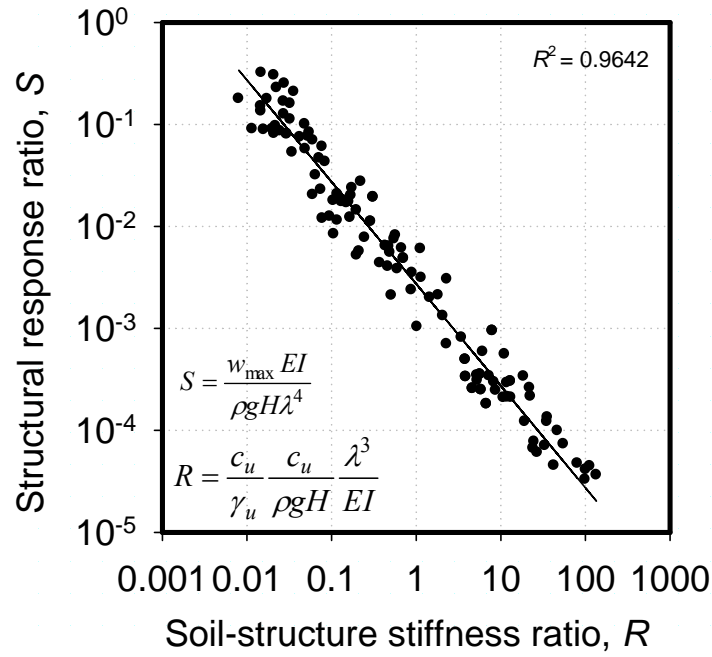


Figure 6.7 Field data plotted on log S versus log R

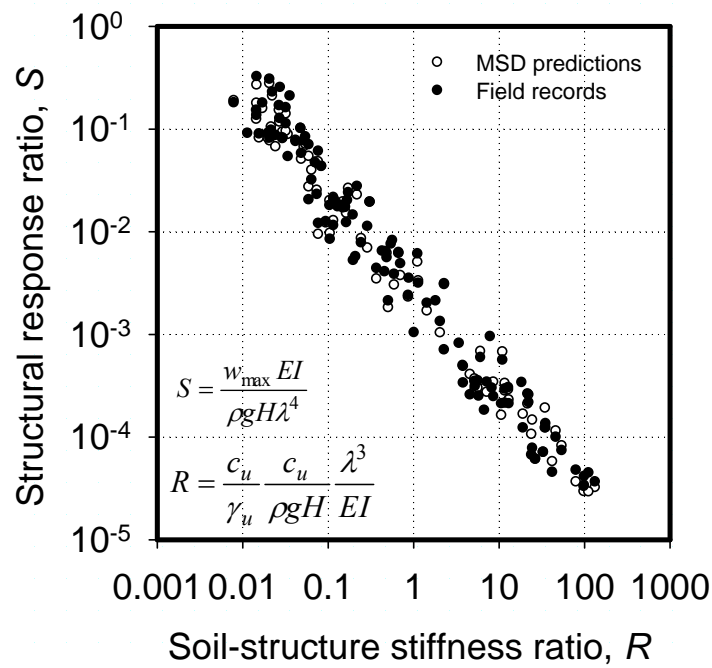


Figure 6.8 Field data and MSD predictions plotted on log S versus log R

6.5.1 Normally consolidated clays

Let us now estimate the undrained strength at mid-depth of “soft” clay. Considering normally consolidated high plasticity clay with a high water table:

$$c_u = 0.3 \sigma'_v = 0.3 (\gamma - \gamma_w) gD/2 \quad (6.20)$$

Taking the corresponding density $\rho \approx 1500 \text{ kg/m}^3$, and making the necessary substitutions:

$$\frac{w_{\max}}{H} \approx \frac{\gamma_u \lambda H^2}{400 H D^2} 400 \approx \gamma_u \frac{H(D-0.5H)}{D^2}$$

$$\frac{w_{\max}}{H} \approx \gamma_u \frac{H}{D} \left(1 - 0.5 \frac{H}{D}\right) \quad (6.21)$$

For example, if $H/D = 2/3$ such that $\lambda = H$, and $\gamma_u = 3\%$, we find:

$$\frac{w_{\max}}{H} \approx 0.44 \gamma_u \approx 1.3\% \quad (6.22)$$

Bolton et al (2008) showed that the average shear strain mobilised in the soil around a bulging wall is

$$\gamma_{\text{average}} \approx 2 \frac{w_{\max}}{\lambda} \quad (6.23)$$

for relatively wide excavations ($B \geq \lambda$), and somewhat larger in the passive zone between the walls for narrow excavations ($B < \lambda$). Combining (6.19) and (6.23), we find

$$\gamma_{average} \approx \frac{\gamma_u}{200} \left(\frac{\rho g H}{c_u} \right)^2 \quad (6.24)$$

Using the same wall geometry as in (6.21) and (6.22) we find that for typical braced excavations in normally consolidated high-plasticity clay:

$$\gamma_{average} \approx \frac{\gamma_u}{200} 400 \frac{H^2}{D^2} \approx 0.89 \gamma_u \quad (6.25)$$

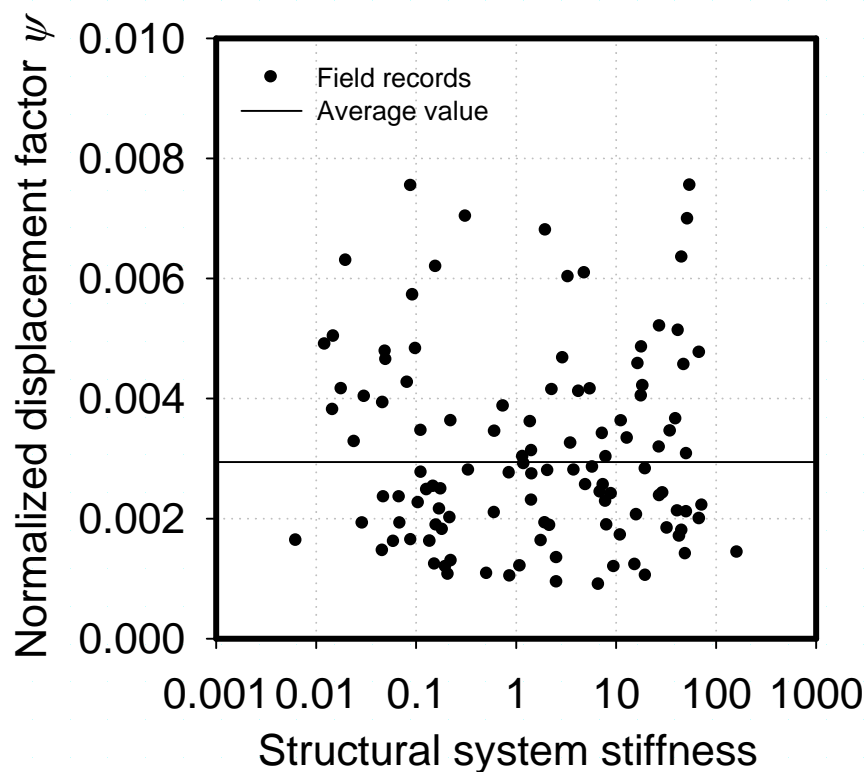


Figure 6.9 Field data plotted on normalized displacement factor versus structural system stiffness

However, shear strains vary within the assumed deformation mechanism up to a maximum which is $\pi/2$ times the average. And there must ultimately be a tendency to develop a thin slip zone adjacent to the wall. These considerations must lead us to expect first a loss of secant stiffness, and then a drop in strength below the peak, as large deformations develop behind a wall in normally consolidated clay. The rate of wall bulging and ground subsidence would then start to exceed the initial predictions of equation 6.19, and might result in structural failure. And although the foregoing calculations were predicated on undrained behaviour, the tendency of soil beneath the excavation to swell and soften due to stress relief would compound the problem. It should be considered essential to monitor the wall profile continuously during the excavation of normally consolidated clays.

6.5.2 Over-consolidated clays

If the strength of the clay at its mid-depth was double the normally consolidated value, equation 6.17 suggests that the wall displacements would correspondingly be reduced by a factor of 4. On the other hand, over-consolidated clays are heavier, and if the bulk density was 25% higher, the wall displacements would be 25% larger. It is not yet clear whether over-consolidation reduces the reference strain γ_u , so this will be regarded as being unchanged. The estimated maximum wall displacement in this “firm” clay, in the same excavation scenario as that examined for “soft” clay in (6.20) to (6.22), would therefore be:

$$\frac{W_{\max}}{H} \approx 0.14 \gamma_u \approx 0.4\% \quad (6.26)$$

The useful notion of parabolic stress-strain curves, and the application of dimensional analysis, has allowed us to estimate that wall displacements in firm clays could well be about one third those of the same type of soil, had it been normally consolidated. This offers a straightforward explanation for why it is normally consolidated clays that have caused greatest anxiety, even where braced reinforced concrete diaphragm walls have been used to support the sides.

6.6 Implication on design of retaining wall

These bulging displacements must apparently be regarded as unavoidable, even if a typical diaphragm wall is used. The evidence of Figure 6.7 suggests that a secant-pile wall or a sheet-pile wall might fare just as well if it were correctly braced or anchored. Measures such as exceptional wall thickness, barrettes or buttresses would be needed to enhance the structural stiffness beyond that of any of the walls in the new database ($R < 0.01$; $\eta > 100$) if bulging was to be suppressed. Only then might the structural strain energy increase to the point where ΔW_{wall} becomes significant compared with ΔW_{soil} in the energy balance equation, and only then might the trend-line of structural response in Figures 6.7 and 6.8 curve below the linear regression line established for walls in the existing database. These postulations also agree with incremental MSD predictions for fixed based wall. However, the current study does raise the question of whether heavy duty diaphragm walls are necessary or efficient, especially in over-consolidated soils. An alternative structural design philosophy in stiff clays would be to accept the wall displacements and curvatures implied by equation 6.19, and to create a well-integrated structure with a wall that was as thin as possible, to minimise bending strains. Of course, other constraints must be met, such as ease of construction, connection to supports, water-tightness, Key-in criteria for the wall toe and the walls' possible role in

vertical load-bearing. More efficient scheme of reducing ground movement around deep excavation for soft clay would be ground improvement techniques such as jet grouting and deep mixing methods.

6.7 Conclusions

In order to assess the capability of MSD to produce useful wall displacement predictions in actual field conditions, a new database has been created of 155 case histories of walls which could be taken to be fixed in a hard layer at their toe, but otherwise retaining soft to firm clays. This is a much larger database than has previously been collected. It was shown that incremental MSD analyses were capable of making predictions of maximum wall movement in 90% of these cases within 30 % of the actual field values.

Since MSD is semi-analytical, it could also be used to generate a more rational normalization of maximum excavation-induced wall displacement,

$$\psi = \frac{2w_{max}}{(C - (H - h)/2)\gamma_u}$$
. This normalization recognizes that if all details of excavation

geometry, wall stiffness and support remain the same, w_{max} should be proportional to the size of the ground deformation mechanism induced by the various stages of excavation, and also to the characteristic soil strain γ_u defined by the intersection of the non-linear stress-strain curve extended to meet the peak strength asymptote.

A new chart of ψ versus normalized system stiffness $\eta = EI/\gamma_u h^4$ was used to demonstrate that MSD could correctly capture the trend of wall displacements increasing with ratio of excavation depth to depth of stiff layer (H/C), but which could be controlled by increasing wall stiffness EI for very stiff walls system. It has also been confirmed that a representative soil shear-strain curve is necessary in order to make good ground movement predictions. The re-defined characteristic soil shear strain γ_u is

a promising index parameter that might be taken to lie between 1% for low-plasticity over-consolidated clays and 5% for high plasticity normally consolidated clays.

New dimensionless groups have been defined using MSD concepts and used to analyze 110 cases of deep excavations. The new database can now be used to investigate the relationship between structural response ratio S and soil-structure stiffness ratio R where this is shown on log-log axes to capture the enormous range of wall stiffness between sheet-piles and thick diaphragm walls. Very remarkably, the field data fit an exactly inverse relationship (i.e. the slope equals -1.00), with a coefficient of determination of 0.964. The stiffness of fixed base walls seems to have a negligible influence on the magnitude of the wall bulging displacements due to deep excavation over a wide range of wall stiffness from sheet pile walls to ordinary reinforced concrete diaphragm walls. A comparison between ground deformations of the same excavation scenarios in either soft normally consolidated clay or over-consolidated clay shows a halve in undrained shear strength profile would triple the normalized wall bulging movements. This explains why it is the normally consolidated clays that caused great anxiety even though reinforced diaphragm walls were used to support the sides. If the wall bulging movements are to be suppressed by introducing a very stiff wall system, a very heavily reinforced thick wall with buttresses might be used. An alternative structural design philosophy might be to use a thin wall, and accept the bulging displacement and curvature, whilst minimizing bending strains and cracks.

There is a need for monitoring to check the progress of wall displacements during excavation, allowing c_u and γ_u to be updated by MSD back-analysis, and checking that the “workmanship” of propping is adequate. If w_{max}/H approaches $0.5\gamma_u$, a normally consolidated clay will be approaching its peak strength.

Table 6.1 Summary of Case Histories (Reference list: Page R-10 & R-11)

Case Histories	Location	C_u (kPa)	H (m)	C (m)	B (m)	Wall type	EI (Kpa)	Support config.	s (m)	L (m)	w_{max} (mm)	Max. Settlement (mm)	λ	r_u	FOS against Base heave
						Diaphragm									
Singapore	1 UOB Plaza Singapore	30 (vane)	13	30	16	wall	4320000	Mutiprop	4.00	36	56	130	23.5	4	1.35
	2 CTC Singapore	20 (vane)	12	37	30	Sheet pile wall	57440	Mutiprop	2.00	30	188	150	17.5	4	0.97
						Diaphragm									
	3 Newton Singapore	18 (vane)	15	12	21	wall	2500000	Topdown	3.63	30	110	220	17.7	4	
	4 MOE I2	18 (vane)	6.8	24	70	Sheet pile wall	45436	Mutiprop	1.70	24	320	400	21.6	4	1.61
	5 MOE I9	18 (vane)	6.4	12	70	Sheet pile wall	45436	Mutiprop	1.60	12	100	?	8.8	4	1.60
						Diaphragm									
	6 Singapore Bugis	40 (vane)	18	30	?	wall	4320000	Mutiprop	2.29	50	160	250	24.7	4	1.31
	7 H'Fok A Singapore	15 (vane)	7.3	19		Sheet pile wall	75700	Mutiprop	1.83		60		15.3	4	1.23
		10-15													
	8 Singapore CBD	(Vane)	15	17		Sheet pile wall	70000	Mutiprop	2.50		145		9.5	4	
						Diaphragm									
	9 Singapore Parking	Soft	9.5	12		wall	540000	Mutiprop	5.90		70		7.2	4	
	Singapore Esplanade Car					Diaphragm									
	10 park	30	11	30	65	wall	2279200	Mutiprop	3.50	35.5	67.5		24.8	4	1.48
						Diaphragm									
	11 MRT NE line construction	23	18	22	21	wall	980000	Mutiprop	2.90	26	60		19.2	4	0.74
	12 MOE Building	15	7	18	70	Sheet pile wall	45436	Mutiprop	2.30	24	310		16.5	4	1.21
	13 Rochor Complex	25	5.3	24	95	Sheet pile wall	45436	Mutiprop	1.80	24	150		21.3	4	2.65
						Diaphragm									
	14 Syed Alwi Project	17	7.8	20	28	wall	414000	Mutiprop	3.90	20	50		12.1	4	1.23
						Diaphragm									
	15 Lavender MRT Station		16	18	23	wall	1916666	Mutiprop	2.60	28	38		20.2	4	
						Diaphragm									
	16 CCL project	15	20			wall	1916666	Mutiprop	1.00		12		13	4	

Chapter 6 Database of movements due to deep excavation in soft soil

					Diaphragm										
17	PYL station	20	19	30	wall	1916666	Mutiprop	3.00	50	110		30.5	4	0.59	
					Diaphragm										
18	MBT station	25	18	25	wall	981333	Mutiprop	3.00	45	120		21	4	0.78	
					Diaphragm										
19	Bugius station	25	18	33	wall	3312000	Mutiprop	2.60	54	150		23.5	4	0.78	
					Diaphragm										
20	Little India shallow clay	25	18	28	wall	981333	Mutiprop	2.90	35	70		19.2	4	0.80	
					Diaphragm										
21	Little India deep clay	25	18	35	wall	981333	Mutiprop	2.90		140		26.2	4	0.80	
	Davidson avenue, San Francisco														
22	Francisco	20	9.1	18	Sheet pile wall	76700	Mutiprop	2.28	13.7	250		25	3	1.24	
	Davidson avenue, San Francisco, failure														
23	Francisco, failure	20	7.3	30	Sheet pile wall	76700	Mutiprop	3.65	13.7	203.2		17	3	1.54	
	MUNI metro turnback project				Diaphragm										
San Francisco	24	50	14	34	wall	1397250	Mutiprop	3.40	44	58		28.2	3	2.07	
	Embarcadero III project				Sheet pile wall	76700	Mutiprop	4.60	27	150		23	3	1.75	
	Chicago project				Sheet pile wall	76700	Mutiprop	4.50	21	85		15.5	2	2.33	
	Chicago NW U				Anchored wall	76700	Anchor	4.30	19	65		12.6	2	1.76	
	Chicago subway				Anchored wall	1397250	Anchor	4.30	20	30	25	8	2		
	Chicago site C North				Sheet pile wall	76700	Mutiprop	2.75	15.3	57.2		13.4	2	3.00	
	Chicago site C West				Sheet pile wall	76700	Mutiprop	3.45	15.3	81.3		12.7	2	2.33	
	Chicago site E east				Slurry wall	848030	Mutiprop	3.50	18	38.1		10.9	2	1.55	
	Chicago site E west				Slurry wall	848030	Mutiprop	3.10	16.5	25		11.5	2	1.75	
	Chicago site F east				Sheet pile wall	76700	Mutiprop	3.40	16.5	91.4		11.4	2	1.60	
	Chicago site F north				Sheet pile wall	76700	Mutiprop	3.40	16.5	58.4		11.4	2	1.60	
Chicago	35	Chicago HDR4 I	24	12	16	Sheet pile wall	76700	Mutiprop	3.00	19.5	164.4	254	12	2	1.13
Boston Blue clay	36	BBC Case histroy	90	18	24	Slurry wall	808593	Mutiprop	3.60	28	50		15	1	2.31
	BBC Post Office square garage II, Boston				Diaphragm										
	garage II, Boston				wall	1397250	Mutiprop	3.68	25.6	30		14.6	1	1.78	

Chapter 6 Database of movements due to deep excavation in soft soil

	38	MIT stata center	80	13	36	Diaphragm wall	1397250	Mutiprop	4.33	15	51	23.5	1	2.99		
	39	Don Bosco school ,boston	75	15	30	Diaphragm wall	1397250	Mutiprop	3.60	24	20	17.5	1	2.43		
	40	State street	70	20	31	Diaphragm wall	848030	Mutiprop	3.90	25.5	50.8	18.2	1	1.75		
						Continious pile										
Taipei	41	Taiwan China Airline	45	9.6	9	62	wall	18850	Mutiprop	2.40	16.7	22	22	4.2	3	0.46
	42	Taiwan Power	47	16	21	60	Diaphragm wall	540000	Mutiprop	3.24	22	80	56	12.9	3	1.63
	43	Taiwan Quen-Ming	47	11	23	51.6	Diaphragm wall	540000	Mutiprop	2.68	17	70	35	17.6	3	2.47
	44	Taiwan Chi-Ching		14	30	80	Diaphragm wall	857500	Topdown	2.78	28	65	65	23.0	3	
	45	Taiwan Tax center	25-50	7.6	30	54	Sheet pile wall	40000	Mutiprop	1.90	16	69	41	26.1	3	2.76
	46	Taiwan Far-east	60	20	32	63.8	Diaphragm wall	857500	Topdown	3.33	32.9	65	65	22	3	1.69
	47	Taiwan Formosa	25-70	18	22	35	Diaphragm wall	1280000	Mutiprop	2.64	31	60	42	12.7	3	1.52
	48	Taiwan New Cathay life	50-130	21	28	42.4	Diaphragm wall	857500	Mutiprop	2.63	33	62	31	17.5	3	2.41
	49	Taiwan TNEC		20	46		Diaphragm wall	1507000	Mutiprop	3.30	35	110	80	25.1	3	
	50	NTUH	70	16	40	140	Diaphragm wall	981333	Anchor	3.14	27	71	20.1	3	2.23	
	51	TCC	67.5	13	33	230	Diaphragm wall	414000	Anchor	3.13	24	30	18.7	3	2.70	
	52	TCAC	65	20	35	93	Diaphragm wall	3312000	Anchor	2.50	38	50	32	3	1.63	
	53	Post office		10	42	29.3	Diaphragm wall	447000	Bottom-up	2.50	18	22	22	3	3.25	

54	Hsinkuang	16	55	33.4	Diaphragm wall	709000	Bottom-up	2.67	27	83.2	32.5	3	2.03
55	Sinyi	12	46	49.3	Diaphragm wall	447000	Bottom-up	2.46	21.5	45.51	26.1	3	2.64
56	Taiwan Sugar	13	45	35	Diaphragm wall	1059000	Bottom-up	2.64	28	58.08	35.4	3	2.46
57	Tai kai	13	48	54.1	Diaphragm wall	447000	Bottom-up	2.52	22	60.48	26.7	3	2.58
58	Tai Gas	18	46	35.5	Diaphragm wall	2067000	Topdown	2.59	40	76.02	50.9	3	1.80
59	Tzuchyang	14	46	36.4	Diaphragm wall	709000	Bottom-up	3.40	28	53.04	35.2	3	2.39
60	Capital	12	50	24.6	Diaphragm wall	447000	Bottom-up	2.46	23	59.04	28.3	3	2.64
61	Electronics	14	36	36	Diaphragm wall	709000	Bottom-up	2.74	28.5	47.95	35.9	3	2.37
62	Baisern	12	37	41.2	Diaphragm wall	447000	Bottom-up	2.46	25	39.36	31.3	3	2.64
63	MRT-1	17	45	16	Diaphragm wall	1059000	Bottom-up	2.80	30	30.24	36.6	3	1.93
64	MRT-2	16	52	19	Diaphragm wall	1059000	Bottom-up	2.73	30	41	36.8	3	1.98
65	MRT-3	12	48	21	Diaphragm wall	2067000	Topdown	3.10	36.5	22.32	41.8	3	2.62
66	MRT-4	16	45	20	Diaphragm wall	2067000	Topdown	2.70	33	48.6	41.4	3	2.01
67	Subway-1	15	46	12.3	Diaphragm wall	1059000	Bottom-up	2.90	26	34.8	31.7	3	2.24
68	Subway-2	19	45	15	Diaphragm wall	2751000	Bottom-up	3.23	30	60.14	35.3	3	1.68
69	Subway-3	19	50	15	Diaphragm	2751000	Bottom-up	3.23	30	62.08	35.3	3	1.68

Chapter 6 Database of movements due to deep excavation in soft soil

					wall										
					Diaphragm										
70	Subway-4		16	50	20	wall	2067000	Topdown	2.70	33	46.98		41.4	3	2.01
					Diaphragm										
71	Subway-5		16	46	18.4	wall	3572000	Bottom-up	2.58	31	35.65		38.7	3	2.10
					Diaphragm										
72	Subway-6		13	46	17.6	wall	3572000	Bottom-up	2.54	27	29.21		34.1	3	2.56
					Diaphragm										
73	Subway-7		20	46	17.6	wall	3572000	Bottom-up	2.84	27	51.74		30.5	3	1.63
					Diaphragm										
74	Subway-8		29	50	25.7	wall	3572000	Bottom-up	2.62	51	69.12		62.1	3	1.13
					Diaphragm										
75	Subway-9		26	50	20	wall	3572000	Bottom-up	2.64	49	55.44		60.3	3	1.23
					Diaphragm										
76	Subway-10		22	50	17.2	wall	3572000	Bottom-up	2.71	39	41.23		47.6	3	1.50
77	Vaterland 1	25	11	16		Sheet pile wall	76800	Mutiprop	2.00		220	270	10.5	5	1.11
78	Vaterland 2	20	11	16		Sheet pile wall	73800	Mutiprop	2.00		140	260	10.5	5	0.88
79	Vaterland 3	34	12	26		Sheet pile wall	73800	Mutiprop	2.00		125	114	20	5	1.38
					Diaphragm										
80	Bank of Norway	20	16	18		wall	2500000	Mutiprop	3.20		16		10	5	0.61
81	Christiana	?	9.6	23		Sheet pile wall	483600	Mutiprop	3.00		48	100	18.2	5	
82	Enerhaughen	20	8	17		Sheet pile wall	45000	Mutiprop	2.50		40	106	13	5	1.22
83	Telecom	20	8.5	10		Sheet pile wall	35850	Mutiprop	2.25		80	93	5.75	5	1.14
84	Gronland 2	20	12	26		Sheet pile wall	76800	Mutiprop	3.75		100	178	20.2	5	0.85
Oslo	85	Gunnerus	35	11	18	Sheet pile wall	82350	Mutiprop	2.00		320	600	12.7	5	1.62
Mexico City	86	Mexico city	25	9	20	Sheet pile wall	50640	Mutiprop	1.80		155		15.5	4	1.92
					Diaphragm										
	87	BangKok A	9.8	15		wall	1378420	Mutiprop	3.10		50		10.1	4	
Bangkok clay	88	BangKok E	7.2	12		Sheet pile wall	50000	Mutiprop	1.80		220		8.4	4	
Shanghai		Senmao International				Diaphragm							16.0		
clay	89	Building	18	25		wall	2500000	Multi-prop	4.4	30	129		5	3	

90	Ocean Building	13	14	Diaphragm wall	1280000	Multi-prop	3.3	26.9	42	7.3	3	
91	Shanghai Telegraph Building	12	15	Diaphragm wall	540000	Multi-prop	4.3	20.5	24.5	8.7	3	
92	Underground garage of Shimao Binjiang Garden	9	11	Diaphragm wall	540000	Multi-prop	4.7	20.8	42	6.7	3	
93	The standard section of People Square Station in M8 Line	13	19	Diaphragm wall	1280000	Multi-prop	3.3	25	72.4	12.7	3	1.87
94	The extreme section of People Square Station in M8 Line	15	19	Diaphragm wall	1280000	Multi-prop	3.8	28	30.5	11.8	3	
95	Shanghai Waitan Jingcheng Building	12	14	Diaphragm wall	1280000	Multi-prop	3.7	24	106	7.45	3	
96	New Shanghai International Building	13	24	Diaphragm wall	1280000	Multi-prop	4.5	26	83.1	17.3	3	
97	Shanghai Stock Building	12	15	Diaphragm wall	1280000	Multi-prop	4.9	20.9	107.7	9.2	3	1.39
98	Waitan Store	10	12	Diaphragm wall	1280000	Multi-prop	3.5	21	29	7.1	3	
99	Shanghai Construction Building	11	15	Diaphragm wall	1280000	Multi-prop	4.4	21.5	16.9	9.5	3	
100	Shanghai Nanyang Square	16	16	Diaphragm wall	2500000	Multi-prop	4.7	30.5	45.5	8.45	3	3.44
101	Shanghai Theater	10	13	Diaphragm wall	2500000	Multi-prop	4.5	23.6	79	7.8	3	
102	Shanghai Financial Square Building	13	15	Diaphragm wall	1280000	Multi-prop	3.9	25	58	8.15	3	
103	Lansheng Building	13	14	Diaphragm wall	1280000	Multi-prop	4.2	26	40	7.4	3	
104	China Coal Building	12	13	Diaphragm	1280000	Multi-prop	4.3	26	130	7.3	3	

				wall									
				Diaphragm									
105	New World Store	13	13	wall	1280000	Multi-prop	3.7	23	14.2		6.75	3	
				Diaphragm									
106	Shanghai City Building	11	12	wall	1280000	Multi-prop	4.3	21	37		6.5	3	
	Shanghai Pacific Ocean			Diaphragm									
107	Sqaure	10	12	wall	540000	Multi-prop	4.2	20	27		6.4	3	
	Shanghai Food &			Diaphragm									
108	Entertainment City	15	24	wall	1280000	Multi-prop	4.3	30	59		16.4	3	
	Luwan District 110 Office			Diaphragm									
109	Building	11	14	wall	1280000	Multi-prop	4.5	22	66.3		7.8	3	
	Zhaofeng World Trade			Diaphragm									
110	Building	12	13	wall	1280000	Multi-prop	4.0	24	38.4		6.6	3	
	Pacific Ocean			Diaphragm									
111	Sqaure-second stage	11	13	wall	1280000	Multi-prop	4.1	20	35.6		7.48	3	
	Tangchen Financial			Diaphragm									
112	Building	13	15	wall	1280000	Multi-prop	3.5	25	118.3		8.3	3	
	The library of Tongji			Diaphragm							23.3		
113	University	9	28	wall	540000	Multi-prop	2.2	16.5	27		5	3	
	Shengkang Liaoshi			Diaphragm									
114	Building	11	15	wall	1280000	Multi-prop	3.3	22.3	89		9.39	3	
	The stardard section of the			Diaphragm									
	open excavation interval in												
115	M6 Line	15	16	wall	1280000	Multi-prop	3.3	28	71.2		8.3	3	
				Secant pile									
116	Shanghai Yindu Building	10	10	wall	965700	Multi-prop	3.5	20.5	17.55		4.95	3	2.08
				Secant pile									
117	Pudong Yuandong Building	11	14	wall	919700	Multi-prop	4.5	23	23.3		8.8	3	
				Secant pile									
118	Huaneng Union Building	13	14	wall	2260000	Multi-prop	3.7	26	21		7.45	3	1.53
119	Gorden Magnolia Square	10	17	Secant pile	1567300	Multi-prop	8.3	23.2	30.76		11.6	3	

					wall									
	Shanghai	Jiangshan			Secant pile									
120	Building		12	18	wall	1471900	Multi-prop	3.8	28.5	57		12.1	3	2.7
					Secant pile									
121	Wanbao Garden Square		9	13	wall	808800	Multi-prop	4.0	17	53		8.15	3	
					Secant pile									
122	Some building in Pudong		8	11	wall	700000	Multi-prop	3.6	19.5	36.5		6.5	3	
					Secant pile							11.2		
123	Union Square		11	17	wall	1279900	Multi-prop	4.8	25	40.4		5	3	
	Dongyin	Huayuan-The			Secant pile									
124	second phrase		10	13	wall	698500	Multi-prop	4.3	21	31		8.15	3	
					Secant pile									
125	Wandu Building		12	17	wall	1490000	Multi-prop	4.8	26	40.1		10.8	3	
	Kunyang	International			Secant pile									
126	Business Square		7	10	wall	602880	Multi-prop	4.6	18	57		5.85	3	
	The west side of the excavation site of Zhaofeng City Building (The first phrase)				Secant pile									
127			8	11	wall	919700	Multi-prop	7.1	16	27.6		7.05	3	
					Secant pile									
128	Shanghai Kaikai Square		8	15	wall	602880	Multi-prop	4.1	18	75.3		10.6	3	
	Large People Stage				Secant pile									
129	Building		11	14	wall	1016520	Multi-prop	5.3	21.5	49.9		8.5	3	
	Swimming Pool in Jingan				Secant pile									
130	Sports Centre		8	10	wall	768320	Multi-prop	4.1	18	46		6.35	3	
	The east district of Hongqiao International				Secant pile									
131	Square		12	13	wall	146500	Multi-prop	6.2	26.5	42.6		7.13	3	
					Secant pile							7.72		
132	East Huaihai Apartment		13	14	wall	1795800	Multi-prop	6.7	25.4	75		5	3	
					Secant pile									
133	Shanghai Haipu Centre		9	14	Secant pile	634610	Multi-prop	4.5	22	32		9.5	3	

	Shanghai Yinhe Hotel			pile wall									
	The main building of the			Continguous									
149	branch of Jinjiang Hotel	9	13	pile wall	364560	Multi-prop	9.1	22	100		8.15	3	
	The Boarding Corridor in												
	the second stage of Pudong			Continguous									
150	Airport	7	14	pile wall	264600	Multi-prop	6.6	12	35		10.4	3	
	The south end of Shanghai			Soil Mixing									
151	New World Square	10	14	wall	231500	Multi-prop	3.3	20	25.2		9.3	3	2.98
				Soil Mixing									
152	Some building in Shanghai	7	12	wall	69300	Multi-prop	3.5	12	27.5		8.36	3	
	Shanghai Minhang Centre			Soil Mixing									
153	Hospital	8	11	wall	22500	Multi-prop	7.5	12	80		7.05	3	
	Chengkai High Technology			Soil Mixing							6.82		
154	Business Centre	8	11	wall	339110	Multi-prop	4.2	17.5	51.5		5	3	
				Soil Mixing									
155	Shenhai Building	7	12	wall	306600	Multi-prop	3.7	12	28		7.9	3	

CHAPTER 7

CONCLUSIONS AND FUTURE DEVELOPMENTS

7.1 Introduction

To minimize both the risk of catastrophic failure (ultimate limit state) of deep excavation construction and of structural damage (serviceability limit state), the design of deep basements should be carried out by detailed deformation analysis and checked against some simple empirical and analytical methods. A detailed understanding about the deformation and load transfer mechanism around the construction process is required.

This thesis addresses the problem of predicting ground movement around a deep excavation construction process firstly by making physical observations of small scale centrifuge models, secondly by analyzing the field records of properly monitored constructions, and thirdly by extending the mobilizable strength method for deformation analysis based on this physical evidence. The main focus of the study is on observing deformation mechanisms which are incorporated into a simple strain-based analytical design tool for excavation-induced wall lateral displacements. This chapter reviews the achievements of this work and also points out the possibility for further development.

7.2 Achievements

7.2.1 Development of a novel technique for deep excavation in centrifuge tests

The development of the experimental apparatus and testing procedures was detailed in Chapter 3. A newly developed actuation system, in which the construction sequence of propping is precisely designed, facilitated the process of in-flight excavation in the centrifuge. The method was proven to give more realistic initial ground conditions before excavation, with minimal pre-excavation bending and displacement of the wall. During the excavation, the actual removal of soils provided a more accurate way of simulating passive soil resistance compared with the draining of heavy fluid as a mean of stress removal. The test package was designed such that tests could be performed in a quasi-plane strain condition and observed through a Perspex window such that digital images could be taken of the soil using the PIV technique.

Undrained triaxial tests with local strain measurements were carried out to characterize soil stress strain behaviour at strains as low as 0.01%. Promising results were obtained by using a parabolic function to represent the non-linear small strain behaviour of Kaolin. This created a crucial basis for MSD analysis.

7.2.2 Observations from small scale centrifuge model tests

With the aim of characterizing the soil structure interaction of the deep excavation problem, small scale well-instrumented centrifuge model tests of deep excavation in soft clay were carried out. Pre-excavation, short-term and long-term soil behaviour relating to pore water pressure, total pressure, ground settlements and wall displacements were studied. Here are some of the key observations:

- Negative excess pore water pressure due to vertical unloading is reduced by positive excess pore pressure generated from undrained shearing. Smaller

negative excess pore pressures for more flexible structures developed due to more intensive shearing.

- Empirical estimation using Peck's apparent earth pressure envelope underestimated the observed results of excavation cases with rigid support by 30%. The observed results for flexible support agreed quite well with the empirical method.
- Maximum strut force is observed at the lowest strut location and stress relief is observed at previous strut levels, which implies a horizontal stress redistribution within the system. This observation is more eminent in flexible system.
- Total earth pressure measurements decreased non-linearly as excavation went deeper. This emphasizes the importance of excavating real soil in-flight for proper simulation of passive resistance of soil in the excavation pit.
- Stress path analysis for the excavation process showed that the soil elements in the passive zone below excavation level follow stress paths as a plane strain passive (PSP) shear mode, whereas the soil elements on the active side generally follow plane strain active (PSA) stress paths initially and then experience a tendency to stress rotations.
- Incremental wall deformation profiles generally followed O'Rourke's (1993) cosine bulge equation. New deformation mechanisms were postulated with respect to the wall toe fixity condition and excavation geometry.
- The effect of excavation in a shallow clay bed was investigated. The settlement profiles show a tapering-off trend as the extent of the deformation mechanism is limited by the shallow depth of soft layer.

- Validation of the conservation of energy term newly proposed in the MSD analysis process was also checked for the centrifuge model. The total loss of potential energy of the soil is shown to be balanced by the sum of the total work done in shearing and the total elastic strain energy stored in structures with an error of at most 30%. This gives a crucial basis for the extensive development of the mobilizable strength design method.
- The long-term design of a retaining wall should take the hydraulic boundary conditions into account. Seepage induced hydraulic gradient due to a high pressure aquifer below the excavation pit was found to be the determining factor for the observed base heave and wall toe kick-out failure. Introduction of an insitu base slab plate to model a zone of jet grout acting as a prop at the wall toe and to minimize the recharge effect to soften soil in the passive zone, was successful.

7.2.3 Extended mobilizable strength design method for deep excavation

An improved MSD method has been introduced to calculate the displacement profile of a multi-propped wall retaining an excavation in soft clay, which is taken to involve undrained soil behavior during construction. As with the earlier MSD approach, each increment of wall bulging, generated by excavation of soil beneath the current lowest level of support, is approximated by a cosine function. The incremental loss in potential energy associated with the formation of a settlement trough, due to wall deformation and base heave, can be expressed as a function of those ground movements at any stage. By conservation of energy, this must always balance the sum of incremental work done in shearing the soil and the incremental storage of elastic

strain energy in bending the wall. By an iterative procedure, the developing profile of wall displacements can be found.

A reasonable agreement was found between predictions made of **fixed-toe** wall displacements, ground settlements, base heave and bending moments using this extended MSD method and the FEA results of Jen (1998), who created full numerical solutions using the MIT-E3 soil model. Although there were some discrepancies in the precise location of the point of maximum bulges, the slope of the wall profile was broadly correct and the magnitude of the maximum displacement was 20% under-predicted by MSD computed with the FEA values. The magnitude of maximum settlement was 30% over-predicted by MSD compared with FEA, which also gave a characteristically wide settlement trough that may not reflect the true field situation. Maximum wall bending moments produced by MSD corresponded quite closely to FEA computations, although the computed location of the maximum value was significantly higher.

In cases of excavation supported by **floating** walls, a modified iteration scheme was implemented in two stages of calculation. The new calculation accounts for the effect of embedded wall length, depth of stiff bearing layer, bending stiffness of wall, excavation width and over-consolidation ratio of soils. The results are compared with the FEA results of Jen (1998), who created full numerical solutions using the MIT-E3 soil model, and the centrifuge test SYL04(rigid wall) and SYL05(flexible wall). In general, the MSD predictions fall within 30% of the actual results by both FEA and experimental evidence.

It is proposed that a relatively straightforward MSD analysis which could be performed within an hour or two by a design engineer, could be a useful tool in taking key design decisions, even if it serves as a precursor to more elaborate FEA.

7.2.4 Database of ground movements of deep excavation in soft soil

In order to assess the capability of MSD to produce useful wall displacement predictions in actual field conditions, a new database has been created of 155 case histories of walls which could be taken to be pinned in a hard layer at their toe, but otherwise retaining soft to firm clays. It was shown that incremental MSD analyses were capable of making predictions of maximum wall movement in 90% of these cases within 40 % of the actual field values.

Since MSD is semi-analytical, it could also be used to generate a more rational normalization of maximum excavation-induced wall displacement,

$$\psi = \frac{2w_{\max}}{(C - (H - h)/2)\gamma_u}$$

This normalization recognizes that if all details of excavation geometry, wall stiffness and support remain the same, w_{\max} should be proportional to the size of the ground deformation mechanism induced by the various stages of excavation, and also to the characteristic soil strain γ_u defined by the intersection of the non-linear stress-strain curve extended to meet the peak strength asymptote.

A new chart of ψ versus normalized system stiffness $\eta = EI/\gamma_w h^4$ was used to demonstrate that MSD could correctly capture the trend of wall displacements increasing with ratio of excavation depth to depth of stiff layer (H/C), but which could be controlled by increasing wall stiffness EI for very stiff floating wall systems. It has also been confirmed that a representative soil shear-strain curve is necessary in order to make good ground movement predictions. The re-defined characteristic soil shear strain γ_u is a promising index parameter, which might be taken to lie between 1% for over-consolidated low-plasticity clays and 5% for high plasticity normally consolidated clays.

New dimensionless groups have been defined using MSD concepts and used to analyze 110 cases of deep excavation. The new database was used to investigate the

relationship between new definitions of structural response ratio S and soil-structure stiffness ratio R , shown on log-log axes to capture the enormous range of wall stiffness between sheet-piles and thick diaphragm walls. Very remarkably, the field data for fixed-based walls fit an exactly inverse relationship (i.e. the slope equals -1.00), with a coefficient of determination of 0.964. Wall stiffness for fixed-base walls seems to have a negligible influence on the magnitude of the wall bulging displacements due to deep excavation, over a range of wall stiffness from sheet pile walls to ordinary reinforced concrete diaphragm walls. Figure 7.1 summarizes the findings on the influence at wall stiffness EI in the cases of floating wall and fixed base walls. A comparison between ground deformations for excavation scenarios in either soft normally consolidated clay or over-consolidated clay shows a reduction in undrained shear strength profile by half would triple the normalized wall bulging movements of fixed base walls. This explains why it is normally consolidated clays that cause the greatest anxiety even where reinforced diaphragm walls are used to support the sides. If the wall bulging movements are to be suppressed by introducing a very stiff wall system, very heavily reinforced thick walls with buttresses might be used. An alternative structural design philosophy might be to use thin walls to accept the bulging of the wall as inevitable and to minimize bending strain and the development of cracks.

Monitoring is required to check the progress of wall displacements during excavation, allowing c_u and γ_u to be updated by MSD back-analysis, and checking that the “workmanship” of propping is adequate. If w_{max}/H approaches $0.5\gamma_u$, a normally consolidated clay will be approaching its peak strength, bringing the soil close to failure. Setting a limit for the ratio of w_{max}/H observed during construction may be rational in relation to avoidance of damage to the support system, and existing

structures near the excavation, and so that the construction team retains the ability to controlling the rate of deformation by preventing soil from approaching too close to its mobilization of peak strength.

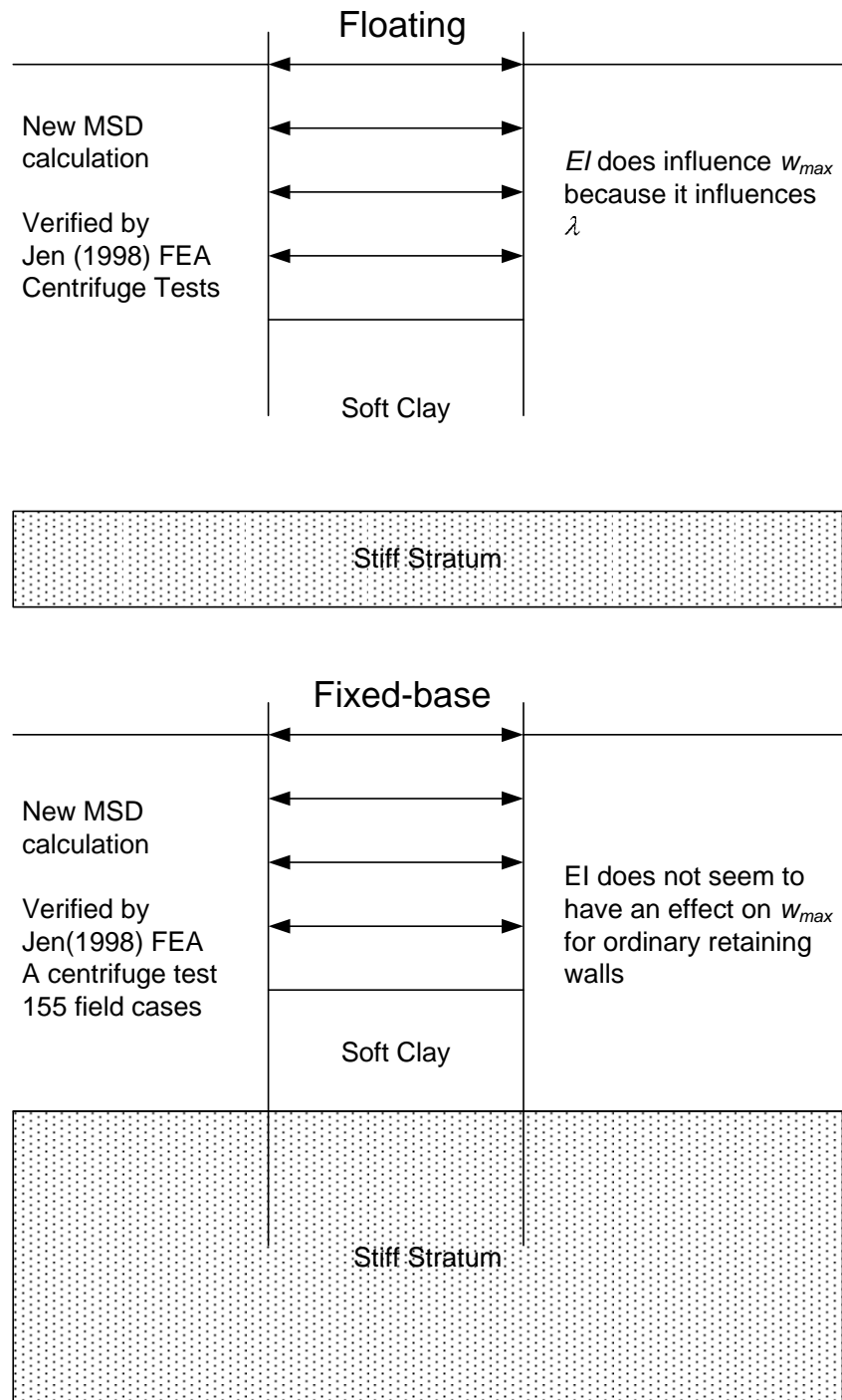


Figure 7.1 A summary of findings on the influence at wall stiffness EI in the cases of floating wall and fixed base walls

7.3. Future developments

- The development of the novel testing technique using small scale centrifuge model test will lead to studies on the effect of excavation on existing nearby buildings and buried structures such as tunnels, pipelines and foundations. It is believed that the buried structures usually strengthen the ground. Engineers would expect smaller ground movements are induced by excavation. However, stringent and conservative criteria are usually imposed on the allowable ground movement to protect serviceable structures. More research can be carried out to find the actual mechanism involved so as to improve the current design guidelines.
- The present MSD method predicts undrained excavation-induced movement, the zero volume change assumption prevents its application to mechanisms associated with volume change such as clay under consolidation, or to excavation in sand. For sandy material, the typical behaviour involves stress-dependent stiffness and dilatancy, making the choice of an appropriate stress-strain relation difficult. Further work has to be carried out on investigating a simple way of characterizing drained soil stress strain behaviour.
- Technical improvements can be made to MSD, especially in respect of the early phase of excavation. The cantilever phase could be treated as flexible and the wall could be regarded as pinned at the first level of props when the next stage of excavation is being estimated.

REFERENCES

Addenberooke, T.I., Potts, D. M. and Dabee, B. (2000). Displacement flexibility number for multi-propped retaining wall design. *Journal of Geotechnical and Geo-environmental engineering*, Vol. 126, No. 8, August, 2000, pp 718-726.

Adrian R.J. (1991). Particle imaging techniques for experimental fluid mechanics. *Annual review of fluid mechanics* 23:261-304

Askegaard, V. (1961). Measurement of pressure between a rigid wall and a compressible medium by mean of pressure cell. *Acta Polytechnica Scandinavica, Civil Engineering and Building Construction Series*, No.11 Copenhagen: Technical University of Denmark.

Arulnathan, R., Boulanger, R.W. Riemer, M.F. (1998). Analysis of bender element. *ASTM Geotechnical Testing Journal*, Vol. 21, No. 2, pp. 120-131.

Azevedo, R.F. (1983). Centrifuge and analytical modelling of excavation in sand. Ph.D thesis, University of Colorado, Boulder.

Bjerrum, L. and Eide, O. (1956). Stability of strutted excavation in clay. *Geotechnique*, 5(1): 7-17.

Bjerrum, L. and Landva, A. (1966). Direct simple-shear test on a Norwegian quick clay. *Geotechnique*, 16(1), 1-22.

Bolton, M.D. and Powrie, W. (1988). Behaviour of diaphragm walls: retaining walls prior to collapse. *Geotechnique*, 37(3),pp 335-353.

Bolton, M.D., Powrie W. and Symons, I.F. (1989). The design of stiff in-situ walls retaining overconsolidated clay. *Ground engineering*, 22(8),pp 44-48.

Bolton, M.D., Powrie, W. and Symons, I.F. (1990a). The design of stiff in-situ walls retaining over-consolidated clay part 1, short term behaviour. *Ground Engineering*, 23(1), pp34-39.

Bolton, M.D., Powrie, W. and Symons, I.F. (1990b). The design of stiff in-situ walls retaining over-consolidated clay, part II, long term behaviour. *Ground Engineering*, 23(2), pp 22-28.

Bolton, M.D. and Stewart, D.I. (1994). The effect on propped diaphragm walls of rising groundwater in stiff clay. *Geotechnique* 44, No.1, 111-127.

Bolton, M. D., Lam, S.Y. and Osman, A.S. (2008). Supporting excavations in clay-from analysis to decision-making. Special Lecture, 6th *International Symposium of Geotechnical Aspects of Underground Construction in Soft Ground*. April, Shanghai.

Bowles, J.E. 1988. Foundation analysis and design. 4th ed., McGraw-Hill Book Company, New York.

Brignoli, E. & Gotti, M. (1992). Misure della velocità di onde elastiche di taglio in laboratorio con l'impiego di trasduttori piezoelettrici. Riv. Ital. Geotec. 26, No. 1, 5-16.

Brignoli, E.G.M., Gotti, M. and Stokoe, K.H. (1996). Measurement of shear waves in laboratory specimens by means of piezoelectric transducers. Geotechnical Testing Journal, Vol. 19, PT.4, pp.384-398.

Burland, J.B., and Hancock, R.J.R. (1977). Underground carpark at the House of Commons, London: Geotechnical aspects. The Structural Engineer, No. 2, Volume 55, 87-100.

Burland, J.B. (1989). Ninth Laurits Bjerrum Memorial lecture: "Small is beautiful."- the stiffness of soils at small strains, Canadian Geotechnical Journal, vol.26, pp 499-516.

Caspe, M.S. (1966). Surface settlement adjacent to braced open cuts, Journal of Soil Mechanics and Foundation Division, ASCE, 92(SM4): 51-59.

Chua, H.Y. (2006). Horizontal arching of earth pressure on retaining structures. Ph.D Thesis, University of Cambridge.

Clayton, C.R.I., and Bica, A.V.D., (1993). The design of diaphragm-type boundary total stress cells, Geotechnique 43, No.4, pp 523-535.

Clough, G.W. and Hansen, L.A. (1981). Clay anisotropy and braced wall behaviour. ASCE Journal of Geotechnical Engineering, 107(7), pp 893-913.

Clough, G.W. and O'Rourke, T. D., (1990). Construction induced movements of in situ walls. In Proc. Design and performance of earth retaining structure, ASCE Special conference, Ithaca, New York, pp 439-470.

Clough, G.W., Smith, E. W. and Sweeney, B. P.(1989) Movement control of excavation support system by iterative design. Foundation Engineering Current Principles and Practices, Vol.2 ASCE, New York, NY, 1989, pp.869-882.

Cuccovillo, T. and Coop, M. R. (1997). "The measurement of local axial strains in triaxial tests using LVDTs". Geotechnique, 47, No. 1, 167-171.

Diaz-Rodriguez, J.A., Leroueil, S. and Aleman, J.D. (1992). Yielding of Mexico City clay and other natural clay. J. Geotech. Div. ASCE, Vol.118, No.7, July, 1992.

Dyvik, R. and Madhus, C. (1985). Lab measurements of G_{max} using bender-elements. In Proceedings of the ASCE Conference on Advances in the Art of Testing Soils Under

Cyclic Conditions, Detroit, 24 Oct., pp. 186–196.

Eide, O., Asa, G. and Josang, T. (1972). Special application of cast-in-place walls for tunnels in soft clay. Proceedings of 5th European Committee for Standardization (ECS). Brussels, Belgium. pp 485-497.

Elshafie, M. (2008). Effect of building stiffness on excavation-induced displacements. Ph.D thesis, University of Cambridge.

Finno, R.J., Atmatzidis, D.K., and Perkins, S.B. (1989). Observed performance of a deep excavation in clay. J. Geotech. Engng Div. Am. Soc. Civ. Engrs 115, No. 8, 1045-1064.

Finno, R.J. and Chung, C.K. (1990). Stress strain strength responses of compressible Chicago Glacial clays. J. Geotech. Div. ASCE, Vol.118, No.10, October, 1992.

Furuya, E., Tsukagoshi, H. and Inoue, H. (1988), “Design of Dry Jet Mixing Method”, Proc. 23rd JSSMFE, pp.2273-2274.

Gaba, A. R. (1990), “Jet grout at Newton Station, Singapore”, 10th Southeast Asian Geotechnical Conference, Taipei.

Goh, A.T.C. (1994). Estimating basal heave stability for braced excavation in soft clay. Technical note, Journal of Geotechnical Engineering, Vol. 120, No.8, August, 1994, 1430-1436.

Goldberg, D.T., Jaworski, W.E., and Gordon, M.D. (1976). Lateral support systems and underpinning. Rep. FHWA-RD-75-128, Federal Highway Administration, Washington D.C.

Haigh, S.K., Houghton, N.E., Lam, S.Y., Li, Z. and Wallbridge, P.W. (2010). Development of a double-axis servo- actuator for novel centrifuge modeling. 7th International conference of Physical Modeling in Geotechnics. pp.239-244

Haigh, S.K. and Madabhushi, S.P.G. (2002). Dynamic centrifuge modeling of the destruction of Sodom and Gomorrah. International conference on physical modeling in geotechnics, St. John’s Newfoundland, Canada, July 2002.

Hansmire, W.H., Russell, H.A., Rawnsley, R.P., and Abbott, E.L.(1989). Field performance of structural slurry wall. J.Geotech. Engng Div. Am. Soc. Civ. Engrs 115, No. 2, 141-156.

Hashash, Y. M. A., and Whittle, A. J. (1996). Ground movement prediction for deep excavations in soft clay. J. Geotech. Eng., 122(6), pp.474-486.

Hashash, Y.M.A. and Whittle, A.J. (2002). Mechanism of load transfer and arching for braced excavations in clay. J. Geotech. And Geoenviron. Engrg, Vol. 128, No. 3, March 1, 2002, pp.187-197.

- Hsi, J.P. & Yu, J.B.Y. (2005). Jet grout application for excavation in soft marine clay. Proc. Of 16th ICSMGE, 12-16 Sept., Osaka, Japan. Vol. 3, 1485-1488.
- Hsieh P. G. and Ou, C.Y.(1998). Shape of ground surface settlement profiles caused by excavation. Canadian Geotechnical Journal, Vol. 35,1004:1017
- Hunt, C. E., Pestana, J. M., Bray, J. D., and Riemer, M. (2002). "Effect of pile driving on static and dynamic properties of soft clay." J. Geotech. Geoenviron. Eng., 128(1), 13–24.
- Ikuta, Y., Maruoka, M., Aoki, M., Sato, E. (1994). Application of the observational method to a deep basement excavated using the top-down observation method. Géotechnique, 44(4): 655-664.
- Jen, L. C. (1998). The design and performance of deep excavation in clay. Ph.D thesis, MIT.
- Jamiolkowski, M., Ladd, C.C., Germaine, J.T., and Lancellotta, R. (1985). New developments in field and laboratory testing of soils. Proc. of 11th ICSMFE. Vol.1, 1985, pp57-153.
- Kimura, T., Takemura, J., Hiro-oka, A., Okamura, M. and Park, J. (1994). Excavation in soft clay using an in-flight excavator. Centrifuge 94, Balkema, Rotterdam.
- Kimura, T., Takemura, J., Hiro-pka, A. Suemasa, N. and Kouda, N. (1993), Stability of unsupported and supported vertical cuts in soft clay. 11th SEAGC, Singapore, pp 61-70.
- Klar, A. and Osman, A.S. (2008). Load-displacement solutions for pile and shallow foundations abased on deformation fields and energy conservation. Geotechnique 58(7), 581-589.
- Kok, Y. L. (2006). Investigating the Mechanical Behaviour of Two Residual Soils from Malaysia. PhD thesis, University of Cambridge, UK.
- Lambe, T.W. (1973). Predictions in Civil Engineering. Géotechnique, Vol. 23, No. 2, 149-202.
- Lambe, T.W. (1967). Stress path method, J. Getech. Engrg. Div. ASCE, Vol. 93. No.6, pp309-331.
- Lee, S.L. and Yong, K.Y. (1991), "Grouting in Substructure Construction", Guest Lecture, Proc. 9th Asian Reg. Conf. On SMFE, December, Bangkok, Thailand, Vol.2.
- Leong, E.C., Yeo, S.H. and Rahardjo, H. (2005). Measuring shear wave velocity using bender elements. Geotechnical Testing Journal, Vol. 28, no.5, pp.488-498.
- Liao, H. J. and Tsai, T. L. (1993), Passive Resistance of Partially Improved Soft Clayey

Soil, Proc 11th SEAGC, Singapore, pp.751-756.

Lim, G. T. (2003). Stabilization of an excavation by an embedded improved soil layer. Ph.D thesis, National University of Singapore.

Lin, H.D. and Wang, C.C. (1998). Stress strain time function of clay. J. Geotech. & Geoenviron. Engrg, ASCE, Vol. 124, No. 4, April, 1998.

Liu, G. B. and Wang, Z.W. (2005). Observed performance of a deep multi-strutted excavation in Shanghai soft clays. J. Geotech. & Geoenviron. Engrg, ASCE, Vol. 131(8), 1004-1013.

Loh, C.K., Tan, T.S. and Lee, F.H. (1998). Three dimensional excavation tests in the centrifuge. Centrifuge 98, Tokyo.

Long, M. (2001). Database for retaining wall and ground movements due to deep excavation. J. Geotech. & Geoenviron. Engrg, ASCE, Vol. 127(3),203-224

Lyndon, A. and Schofield, A.N. (1970). Centrifuge model test of short term failure in London clay, Geotechnique 20, No.4, pp.440-442.

Madabhushi, S.P.G., Houghton N.E., and Haigh S.K. (2006). A new automatic sand pourer for model preparation at University of Cambridge. Proc. ICPMG'2006, Hong Kong, pp 217-222.

Malone, A., Ng, C.W.W. & Pappin, J. (1997a). Invited discussion paper: Displacements around deep excavations in completely decomposed granite. Proc. 14th Int. Conf. Soil Mech. & Fdn. Engrg., Hamburg. Vol.4, 2325-2328.

Mana, A. I. and Clough, G. W. (1981). Prediction of movements for braced cuts in clay. J. Geotech. Engrg, ASCE, 107(6): 759-777.

McNamara, A.M. and Taylor, R.N. (2002). Use of heave reducing piles to control ground movements around excavations. Proceedings of ICPMG 2002, 847-852.

Mihashi, M., Tachibana, T. and Motoyama, S. (1987), "Measure of deformation and effect of large scale excavation on soft ground near the housing situation", Journal of JSCE, pp.295-302.

Milligan, G.W.E. and Bransby, P.L. (1976). Combined active and passive rotational failure of a retaining wall in sand. Geotechnique, 26(3), 473-494.

Moh, Z.C., Nelson, J.D. and Brand, E.W. (1969). Strength and Deformation behaviour of Bangkok clay. ICSMFE VII, Mexico, 1969, pp.287-295.

Moormann, C. (2004). Analysis of wall and ground movement due to deep excavation in soft soil based on a new worldwide database. Soils and Foundations, Vol. 44, No. 1, 87-98.

- Ng, C. W.W., (1998). Observed Performance of multi-propped excavation in stiff clay. *J. Geotech & Geoenviron. Engrg.* Vol.124 (9). pp. 889-905.
- Ng, C.W.W. (1999). Stress paths in relation to deep excavations. *J. Geotech. & Geoenviron. Engrg, ASCE.* Vol. 125, No. 5. 357-363.
- Ng, C. W.W., Simpson, B., Lings, M.L. and Nash, D.F.T. (1998). Numerical analysis of a multi-propped excavation in stiff clay. *Canadian Geotechnical Journal*, Vol. 35:115-130.
- Nicholson, D.P. (1987) The design and performance of the retaining walls at Newton Station, Proc. Conf. Singapore MRT, April 1987, Singapore, pp.147-154.
- O'Rourke, T.D. (1981). Ground movements caused by braced excavations. *J. Geotech. Engng Div. Am. Soc. Civ. Engrs* 107, GT9, 1159-1178.
- O'Rourke, T.D. (1993). Base stability and ground movement prediction for excavations in soft clay. *Retaining structures*, Thomas Telford, London, 131-139.
- Osman, A. S. (2004). Prediction ground displacement in clay during construction. Ph.D thesis, University of Cambridge
- Osman, A. S. & Bolton, M. D. (2004). A new design method for retaining walls in clay, *Canadian Geotechnical Journal*, 41(3): 453-469.
- Osman, A. S. and Bolton, M. D. (2006). Ground movement predictions for braced excavations in undrained clay. *J. Geotech. & Geoenviron. Engrg., ASCE*, Vol. 132, No. 4, April 1, 2006.
- Ou, C. Y. Hsieh, P.G. and Chiou, D.C. (1993). Characteristics of ground surface settlement during excavation. *Canadian Geotechnical Journal*, Vol 30, pp. 758-767.
- Ou, C.Y. and Chiou, D.C. and Wu, T.S. (1996). Three dimensional finite element analysis of deep excavations. *Journal of geotechnical engineering*, Vol 122, No.5, May,1996, pp337-345.
- Ou, C.Y. and Lai, C.H. (1994). Finite element analysis of deep excavation in layered sandy and clayed soil deposit. *Canadian Geotechnical Journal*, Vol. 31,204-214.
- Ou, C.Y., Liao, J.T. & Cheng, W.L. (2000). Building response and ground movements induced by a deep excavation, *Geotechnique*, 50(3): 209-220.
- Ou, C.Y. and Wu, T.S. (1996), "Evaluation of material properties for soil improvement in excavation", Proc. of IS-Tokyo '96 / 2nd Int. Conf. on Ground Improvement Geosystems, Tokyo, vol.1, pp.545-550.
- Peck, R. B., (1969). Deep excavation and tunneling in soft ground. In Proc. of 7th

ICSMFE, State-of-the-Art volume, Mexican City, pp.225-290.

Powrie, W. (1986). The behaviour of diaphragm walls in clay Ph.D thesis, University of Cambridge.

Powrie, W. and Li, E.S.F. (1991) Finite element analyses of an in situ wall propped at formation level, *Geotechnique*, Vol. 41, No. 4, pp. 499-514.

Richard, D.J. and Powrie, W. (1998). Centrifuge tests on doubly propped embedded retaining walls in over-consolidated kaolin clay. *Geotechnique* 48, No. 6, 833-846.

Rowe, P.W. (1952) Anchored sheet pile walls. *Proc. ICE*. 1:27-70.

Sanchez-Salinero, I., Roesset, J.M. & Stokoe, K. H. (1986). Analytical studies of body wave propagation and attenuation. Report GR 86-15, University of Texas, Austin.

Shirlaw, N. (2005). Invited special lecture: Deep excavations. *Proc. 5th Int. Sym. On Geotechnical Aspects of Underground Construction in Soft Ground*. Pre-print volume, 1-16.

Shirley, D.J. (1978). An improved shear wave transducer. *Journal of the Acoustical Society of America*, 63(5): 1643–1645.

Simpson, B. (1992). Retaining structures: Displacement and design. 32nd Rankine Lecture. *Geotechnique* 42, No.4, 541-576.

Skempton, A.W. (1951). The bearing capacity of clays. *Proc. Building Research Congress*, London, 180-189.

Sloan, S.W. (1988). Lower bound limit analysis using finite elements and linear programming. *Int. J. Numer. Analyt. Method. Geomech.*, 12(1), 61-77.

Sloan, S.W. and Kleeman, P.W.(1995). Upper bound limit analysis using discontinuous velocity fields. *Compu. Methods Appl. Mech. Eng.*, 127, 293-314.

Take, W.A. (2002). The influence seasonal moisture cycles on clay slopes. PhD thesis, University of Cambridge.

Takemura, J., Kondoh, M., Esaki, T., Kouda and M. Kusakabe. (1999). Centrifuge model tests on double propped wall excavation in soft clay. *Soils and Foundations*, Vol. 39, No. 3, 75-87, June 1999.

Tan, S.B., Tan, S. L. and Chin, Y.K. (1985) A braced sheetpile excavation in soft Singapore marine clay, 11th Int. Conf. Soil Mech. Fdn. Engrg, Vol.3, pp.1671-1674.

Tanaka, H. (1993), “Behavior of braced excavations stabilized by Deep Mixing Method”, *Soil and Foundations*, JSSMFE, vol.33, No.2, pp.105-115.

and pressure distribution data. Vicksburg: US Army Engineer Waterways Experiment Station.

Terzaghi, K. (1943). Theoretical soil mechanics, John Wiley, New York

Taylor, R.N., 1995, Centrifuges in modeling principles and scale effects. Geotechnical centrifuge technology, Taylor R.N. (editor), Blackie Academic and Professional.

Terzaghi, K. and Peck, R. B.,(1967). Soil Mechanics in engineering practice, John Wiley and Sons, Inc., New York, Toronto, London. pp.729.

Terzaghi, K., (1943). Theoretical soil mechanics, John Wiley & Sons, Inc., New York, N.Y.

Trollope. D.H. and Lee, I.K., (1961). The measurement of soil pressures, Proceedings of Fifth International Conference on soil mechanics and Foundation Engineering, Vol.2, pp 493-499.

Uchiyama, N. and Kamon, M. (1998), “Deformations of buttress type ground improvement and untreated soil during strutted excavation in clay”, 2nd Int. Conf. on Ground Improvement Techniques, 8-9 Oct. 1998, Singapore.

Ukritchon, B., Whittle, A.J. and Sloan, S.W.(2003). Undrained stability of braced excavation in clay. J. Geotech. & Geoenviron. Engrg., ASCE, Vol. 129, No.8, August 1, 2003.

Ulrich, E.J. (1989). Internally braced cuts in over-consolidated soils. J. Geotech. Engeng Div. Am. Soc. Civ. Engrs 115, No. 4, 504-520.

Vardanega, P.J. and Bolton, M.D. (2010). The stiffness of clays and silts. Geotechnique. (under review)

Viggiani, G. and Atkinson, J. H. (1995). Stiffness of fine-grained soil at very small strains. Geotechnique, 45, No.2, 249-265.

Viggiani, G. and Atkinson, J.H. (1995). Interpretation of bender element tests. Geotechnique, 45, No.1, 149-154.

Wallace, J.C. and Long, M.M.(1992) Retaining wall behavior for a deep basement in Singapore marine clay, Proc. Conf. Retaining Structures, July 1992, Cambridge, pp.195-204.

Wang, Z. W., Ng C. W. W. and Lui, G. B, (2005). Characteristics of wall deflection and ground surface settlements in Shanghai. Canadian Geotechnical Journal, Vol. 42, 1243-1254

Weiler Jr., W.A. and Kulhawy, F.H.,(1982). Factors affecting stress cell measurements in soil, Journal of the geotechnical engineering division, Proceedings of the ASCE, Vol.

108. GT12, pp 1529-1545.

White D.J., Take W.A, Bolton M.D. (2001a) Measuring soil deformation in geotechnical models using digital images and PIV analysis. Proceedings of the 10th International Conference on Computer Methods and Advances in Geomechanics. Tucson, Arizona. pp 997-1002 pub. Balkema, Rotterdam.

White D. J., Take W.A, Bolton M.D. & Munachen S.E. (2001b) A deformation measuring system for geotechnical testing based on digital imaging, close-range photogrammetry, and PIV image analysis. Proceedings of the 15th International Conference on Soil Mechanics and Geotechnical Engineering. Istanbul, Turkey. Pp 539-542. pub. Balkema, Rotterdam.

White, D.J. (2002). An investigation into the behaviour of pressed-in piles. Ph.D thesis, University of Cambridge.

White, D.J. and Take, W.A. (2002). GeoPIV: Particle image Velocimetry (PIV) software for use in geotechnical testing, Technical Report CUED/D-SOILS/TR322, October 2002, University of Cambridge.

White, D.J. Take, W.A. and Bolton M.D. (2003). Soil deformation measurement using Particle Image Velocimetry (PIV) and Photogrammetry. *Geotechnique* 53(7): 619-631.

Whitman, R. V., Johnson, E. G., Abbott, E. L., & Becker, J. M. (1991). Field instrumentation plays vital role in deep excavation project. Proc., Geotech. Engrg. Congress, Geotech. Spec. Publ. No. 27, ASCE, 1, 173-184.

Whittle, A. J. (1993). Evaluation of a constitutive model for over-consolidated clays. *Geotechnique*, 43(2): 289-313.

Williams, B P and Waite, D (1993). The design and construction of sheet piled cofferdams, Special Publication 95, CIRIA, London

Wong I. H., Poh T. Y. and Chuah.H. L., (1997). Performance of excavations for depressed expressway in Singapore, *J. Geo. & Geoenv. Engrg.*, Vol. 123 (7). pp617-625.

Wong, K.S. and Broms, B.B. (1989). Lateral wall deflections or braced excavation in clay. *J. Geotech. Engrg.*, Vol. 115, No.6, June, 1989,pp.853-870.

Wong, K.S., Goh, A.T.C., Jaritngam, S. and Chang, L.J.D. (1998), Optimization of jet grout configuration for braced excavation in soft clay”, Proc. 2nd Int. Conf. on Ground Improvement Techniques, Singapore.

Wong,I. H., Poh, T. Y. and Chuah, H. L.(1997). Performance of excavations for depressed expressway in Singapore. *J Geotech. & Geoenviron. Engrg.*, Vol. 123(7), 617-625.

Zhao. Y.. Gafar. K.. Elshafie. M.Z.E.B.. Deeks. A.D.. Knappett. J.A. & Madabhushi.

S.P.G. (2006). Calibration and use of a new automatic sand pourer. Proc. of ICPMG 2006, pp265-270.

List of references for case histories:

- Aas, G. (1985). Stability problems in a deep excavation in clay. Norwegian Geotechnical Publication No. 156, Norwegian Geotechnical Institute, Oslo.
- Balasubramaniam, A.S., Bergado, D.T., Chai, J.C. and Sutabur, T.(1991). Deformation analysis of deep excavations in Bangkok. Proc. 13th int. Conf. Soil Mech. Found. Engrg., Vol.2, Balkema, Rotterdam, The Netherlands, 909-915.
- Becker, J.M. and Haley, M.X. (1990) Up-down construction decision making and performance. In Proc. Of the design and Performance of earth retaining structures, Geotech. Publ. No. 25, ASCE, New York, 170-189.
- Becker, J.M. and Haley, M.X. (1990) Up-down construction decision making and performance. In Proc. Of the design and Performance of earth retaining structures, Geotech. Publ. No. 25, ASCE, New York, 170-189.
- Broms, B.B., Wong, I.H. and Wong, K.S.(1986). Experience with finite element analysis of braced excavations in Singapore. Proc. 2nd Int. Symp. On Numer. Methods in Geomechanics, Balkema, Rotterdam, The Netherlands, 309-324.
- Chua, T.S., Lew, M., Rama, V. and Phua, H.L. (2008). Robust earth retaining wall system to control ground movement and minimize impact on adjacent structures, Int. Conf. on Deep excavation, 2008
- Clough, G.W. and Reed, M.W. (1984). Measured behaviour of braced wall in very soft clay. J. Geotech. Eng. 110(1), 1-19
- Clough, G.W., Smith E.M. and Sweeney, B.P. (1989). Movement control of excavation support systems by iterative design. Foundation Engineering: Current Principles and practices, Vol.2, ASCE, New York, NY, 1989, pp869-882.
- Clough, G.W., Smith E.M. and Sweeney, B.P. (1989). Movement control of excavation support systems by iterative design. Foundation Engineering: Current Principles and practices, Vol.2, ASCE, New York, NY, 1989, pp869-882.
- Davies, R.V. and Walsh, N.M.(1983). Excavations in Singapore marine clays. Proc. Int. Seminar on Constr. Problems in Soft Soils, Nanyang Technological Institute, Singapore
- Finno, E.J., Bryson, S. and Calvello, M. (2002). Performance of a stiff support system in Soft clay. J. Geotech. And Geoenviron. Engrg. Vol128.No.8, pp660-671
- Finno, R.J. and Roboski, J.F. (2005). Three-dimensional responses of a tied-back excavation through clay. J. Geotech. And Geoenviron. Engrg. Vol 131No.3. March 1, 2005.
- Finno, R.J., Atmatzidis, D.K. and Perkins, S.B. (1989). Observed performance of a deep excavation in clay. J. Geotech. Engrg., ASCE, Vol.115, No.8, pp 1045-1064
- Finstad, J.A. (1991). Royal Christianna hotel-basement with permanent sheet pile wall, up and down method. Proc. 4th int. conf. on Piling and Deep found., Deep found. Inst., London.
- Gill, S. A., and Lukas, R. G. (1990). "Ground movement adjacent to braced cuts." *ASCE Proc., Design and Performance of Earth Retaining Structures*, Cornell University, Ithaca, N.Y., No. 25, 471-488.
-
- Halim, D. and Wong, K.S. (2005). Evaluation of modified cam clay parameters for deep excavation analysis. In proc. of Underground Singapore 2005.
- Hsieh, P.G., and Ou, C.Y. (1998). Shape of ground surface settlement profiles caused by excavation. J. Can. Geotech. Vol.35(6), 1004-1017.
- Hulme, T.W., Potter, J., and Shirlaw, N. (1989) Singapore MRT system: Construction. Proc. Instn. Of Civ. Engrs., Vol 86, London, 709-770.
-
- Kok, C.Y. (1985). A braced sheet pile excavation in very soft Singapore marine clay, the MOE building at Scotts Road. Geotechnical Publication by Public Works Department (3): 1-45. Singapore
- Koutsoftas, D.C., Frobenius, P. Wu, C.L., Meyersohn, D. and Kulesza, R. (2000). Deformation during Cut and cover construction of MUNI metro turnback project. J. Geotech. And Geoenviron. Engrg. ASCE. Vol126.No.4, April, 2000
- Kung, G.T.C., Juang, C.H., Hsiao, E.C.L. and Hashash, Y.M.A. (2007). J. Geotech and Geoenviron. ASCE. Vol 133 No.6. 731-747
- Kung, T.C. (2003). Surface settlement induced by excavation with consideration of small-strain behaviour of Taipei silty clay. PhD thesis, National University of Science and Technology, Taiwan.
- Kung, G.T.C., Hsiao, E.C.L. and Schuster, M. and Juang, C.H. (2007). A neural network approach to estimating excavation induced wall deflection in soft clays. Computers and Geotechnics. 34, 385-396

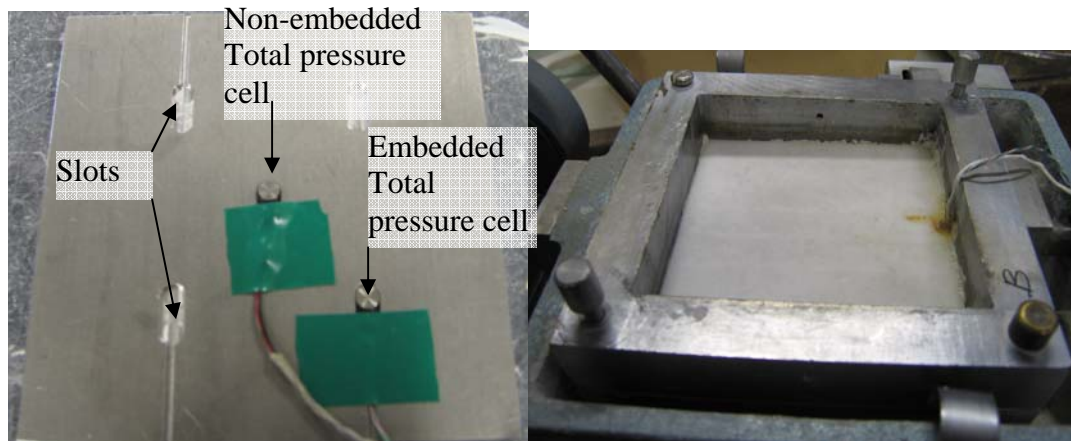
-
- Lambe, T.W., Wolfskill, L.A. and Jaworski, W.E. (1972). The performance of a subway excavation. In proc. Of a speciality conference on performance of earth supported structure. Purdue University, Lafayette, Vol.1, 1403-1424.
- Lee, S.L., Karunaratne, G.P., Lo, K.W., Yong, K.Y. and Choa, V. (1985). Developments in soft ground engineering in Singapore, 11th Int. Conf. Mech. Fdn. Engrg, Vol.3, pp.1661-1666.
- Liao, H.J. and Hsieh, P.G. (2002). Tie-back excavation in alluvial soil of Taipei. J. Geotech and Geoenviron. Engrg. Vol. 128.No.5 MAY1,2002.
- Lim, H.T., Lim, P.H., Kho, C.M. and Osborne, N.M. (2008). Behaviour of stiff earth retaining wall system in soft Singapore Marine Clay. In Proc. of Int. conf. on Deep Excavation 2008. Singapore, 2008
- Lim, K. W., Wong, K.S., Orihara, K. and Ng, P.B. (2003). Comparison of results of excavation analysis using WALLAP, SAGE CRISP, and EXCAV 97. in proc. Of Underground Singapore 2003:83-94, Singapore
-
- Nicholson, D.P. (1987) The design and performance of the retaining walls at Newton Station, Proc. Conf. Singapore MRT, April 1987, Singapore, pp.147-154.
- Norwegian Geotechnical Institute (NGI). (1962). Measurement at a strutted excavation, Oslo subway, Enerhaugen South, km 1982. Technical Report No. 3, Oslo
- Norwegian Geotechnical Institute (NGI). (1962). Measurement at a strutted excavation, Oslo subway, Vaterland 1, km 1373. Technical Report No. 6, Oslo
- Norwegian Geotechnical Institute (NGI). (1962). Measurement at a strutted excavation, Oslo subway, Vaterland 2, km 1408. Technical Report No. 7, Oslo
- Norwegian Geotechnical Institute (NGI). (1962). Measurement at a strutted excavation, Oslo subway, Vaterland 3, km 1450. Technical Report No. 8, Oslo
- Norwegian Geotechnical Institute (NGI). (1962). Measurement at a strutted excavation, Oslo subway, Gronland 2, km 1692. Technical Report No. 5, Oslo
- Norwegian Geotechnical Institute (NGI). (1962). Measurement at a strutted excavation, The new headquarters building for the Norwegian Telecommunications administration, Oslo. Technical Report No. 4, Oslo
- Olsen, M.B. (2001). Measured performance of a large excavation on the MIT campus. SM thesis, Dept. of Civil and Environmental Engineering, MIT, Cambridge, Mass., U.S.
- O'Rourke, T.D. (1993). Base stability and ground movement prediction for excavation in soft clay. Retaining Structures, Thomas Telford, London, 131-139
- Ou, C.Y., Hsien, P.G. and Chiou, D.C. (1993). Characteristics of ground surface settlement during excavation. J. Can. Geotech. Vol. 30.758-767
- Poh, T.Y. and Wong I.H. (2003). Performance of basement excavation for Singapore Esplanade Car park. In proc. of Underground Singapore 2003. pp319-325
- Rodriguez, J.M., and Flamand, C.L. (1969). Strut loads recorded in a deep excavation in clay In proc. 9th ICFMFE, Vol2, 450-467.
- Roti, J.A., and Friis, J. (1985). Diaphragm wall wall performance in soft clay excavation. Proc. 11th int. Conf. Soil Mech. Found. Engrg., Vol 4. 2073-2078.
- Shirlaw, J.N., Tan, T.S. and Wong, K.S. (2006). Deep excavation in Singapore marine clay. In. Proc. Of Geotech. Asp. Of Underground construction in soft ground. Taylor & Francis Group, London.
- Tan, S.B., Tan, S. L. and Chin, Y.K. (1985) A braced sheetpile excavation in soft Singapore marine clay, 11th Int. Conf. Soil Mech. Fdn. Engrg, Vol.3, pp.1671-1674.
- Vuillemin, R.J., and Wong, H. (1991). Deep excavation in urban environment: 3 examples. Proc. 10th Eur. Conf. Soil Mech. Found. Engrg., Vol.2, Balkema, Rotterdam, The Netherlands, 843-847.
- Wallace, J.C., Ho, C.E., Long M.M. (1992), Retaining wall behaviour for a deep basement in Singapore marine clay. Pro. Int. Conf. Retaining struct., Thomas Telford London, 195-204.
- Xu, Z. (2007). Deformation behaviour of deep excavations supported by permanent structure in Shanghai soft deposit. PhD Thesis, Shanghai Jiao Tong University.

APPENDIX A

COMMENTS ON CALIBRATION OF EARTH PRESSURE CELLS

Calibration of the earth pressure cell (EPC) was carried out in a conventional shear box apparatus. The box was a square with 100mm in length. A base plate was designed and fitted into the base with four grooves, which were carefully machined to provide an exact fitting for the pressure cell to fit in. Horizontal spacing between cells was carefully selected according to those recommended by Weiler and Kulhawy (1982). In the present calibration, one cell was put on the metal surface without embedding into the plate and another one was embedded in to the metal plate (Figure A1(a) and (b)). The side walls were greased to reduce friction between clay and metal surface. A piece of porous plastic and filter paper were placed on the top as a drainage boundary. Pressure was added on the top using a lever arm system and a hanger (Figure A1(c)). The clay sample used for testing is speswhite kaolin pre-consolidated to 100kPa in a consolidometer. A digital meter was used to read the electronic signal from the sensors. The electronic signal was plotted with pressure applied in Figure A2 (a) and (b). The clay sample was first loaded to 100kPa, which was the preconsolidation pressure of the sample. Unloading and reloading cycles were then carried out. After that the sample was consolidated to 150kPa and then unloading and reloading cycles followed. The sample was then consolidated to 200kPa and then unloading and reloading cycles followed.

In general, a sensitive and linear response could be obtained for the pressure cell embedded in the base plate, while convex curving response was obtained for the pressure cell sitting on the flat plate without embedding into the metal plate. For details about calibration process of the flat type earth pressure cell, the reader can refer to Chau (2004).



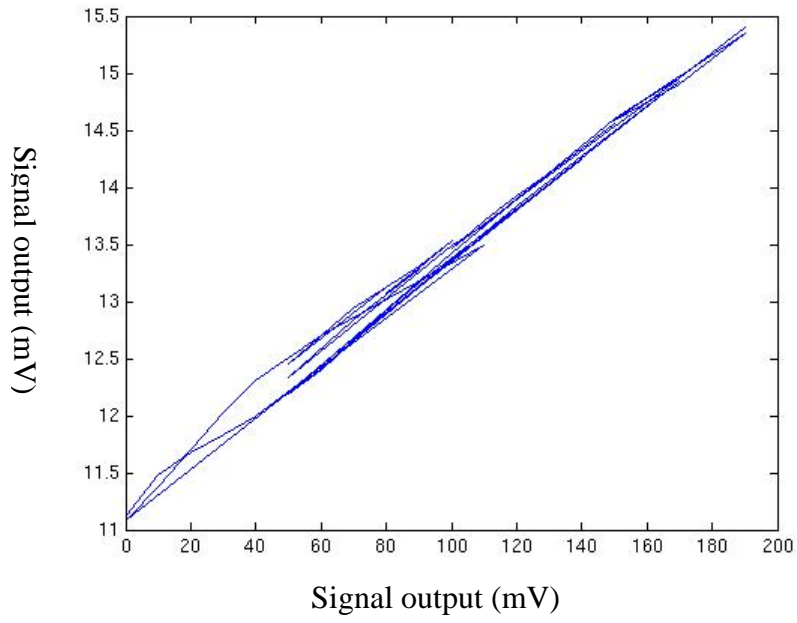
(a) Embedded in flat plate

(b) Conventional shear box

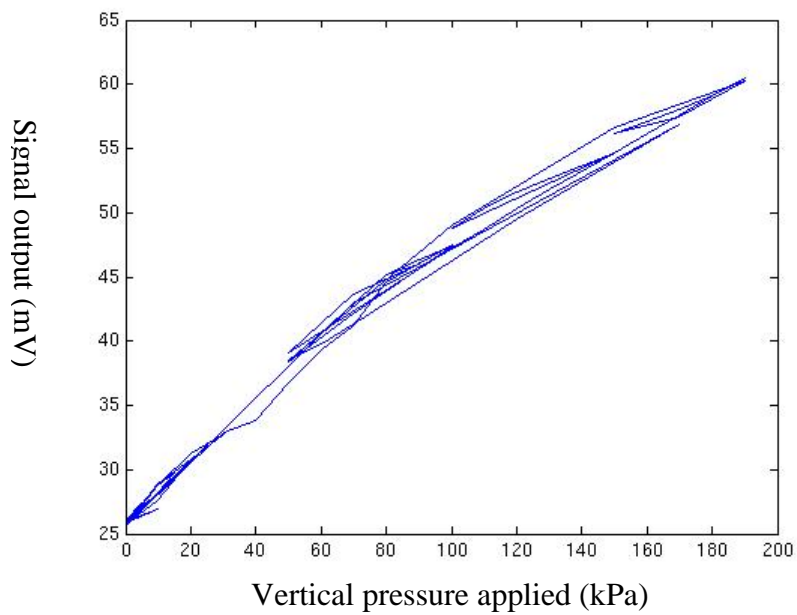


(c) Loading rig

Figure A1 Apparatus for calibration of earth pressure cell



(a) Embedded in slot



(b) Not embedded

Figure A2 Calibration result of earth pressure cell for (a) embedded and (b) not embedded cell